Title
Network Interactions During Spontaneous Activity: Theory and Experiment

Author
Choudhary, Krishna

Publication Date
2021

Peer reviewed|Thesis/dissertation

UNIVERSITY OF CALIFORNIA
Los Angeles

Network Interactions During Spontaneous Activity: Theory and Experiment

A dissertation submitted in partial satisfaction of the requirements for the degree Doctor of Philosophy in Physics

by

Krishna Choudhary

2021

ABSTRACT OF THE DISSERTATION

Network Interactions During Spontaneous Activity:
Theory and Experiment

by

Krishna Choudhary

Doctor of Philosophy in Physics

University of California, Los Angeles 2021

Professor Mayank Mehta, Chair

Higher order functions of cognition rely on the cooperative computations of multiple brain regions. Understanding how these spatially and temporally distributed neural circuits work together remains an important question. Attempts have been made at a computational understanding of these brain circuits and their coordinated activity, but usually involve models requiring thousands of parameters. The explosion of dimensionality trades biophysical accuracy with predictive power and analytic understanding. In this dissertation, I outline a theory of cortical interaction that can explain a variety of phenomena within the *in vivo* brain using only two parameters, and I study the implications of this theory using the cortico-entorhinal-hippocampal circuit *in vivo*.

Briefly, a theory of coordinated interaction between generic cortical networks is developed using only excitation, inhibition, and the adaptation of excitation. By constraining this model onto a 2D parameter space by modulating only the recurrent excitation of the efferent network and the external drive coming in from the afferent network, the theory is able to reproduce over a dozen experimental observations during spontaneous activity *in vivo*. The theory reproduces previously observed phenomena, namely spontaneous persistent activity, which occurs when the efferent networks decouple from the afferent drive and remain active while the afferent network has shut down. The theory goes further to predict a novel phenomena, spontaneous persistent inactivity, when the efferent network remains inactive while the afferent excitation turns on. This has never before been observed experimentally or computationally. We test our theory using simultaneously recording local field potential within the neocortex and membrane potential measurements from individual neurons in the entorhinal cortex. We find that while MEC layer 3 neurons show persistent activity, both MEC and LEC neurons show persistent inactivity.

The advantage of our mean field theory is that its simplicity gives insights into the mechanistic principles behind these decoupling events. Both persistent activity and inactivity arise from the non-linear amplification of afferent network excitation. Through further analysis of the entorhinal cortex, we find that persistent activity is also found in MEC layer 2,

and persistent activity is found in both MEC layer 2 and LEC layer 2.

Given the ubiquity of connections between the entorhinal cortex and the hippocampus, we further analyze hippocampal activity during these persistent activity and inactivity events. We find that specific subfields, namely the Dentate Gyrus granule cells and CA1 inhibitory neurons, also display persistent activity and inactivity. We find that hippocampal activity is modulated by entorhinal persistent activity and inactivity in a fashion that is in line with anatomical observations of the connections between these two brain regions. Additionally, these regions coordinate information transfer within specific oscillation bands unique to each brain region. Our results indicate a new way of understand persistent activity, persistent inactivity, and the functional connectivity between large brain networks during spontaneous activity in the absence of sensory stimulus.

Finally, we show the presence of a unique, 3-Hz oscillation in cells of the lateral entorhinal cortex, dentate gyrus, and hippocampal inhibition. This is not present in neocortical and MEC neurons, suggesting that it is distinct from the theta and delta oscillations studied by others. The findings suggest a functional link between inhibition in the hippocampus and LEC circuits.

This dissertation of Krishna Choudhary is approved.

Robijn Bruinsma
Sotiris Masmanidis
Dolores Bozovic
Mayank Mehta, Committee Chair

University of California, Los Angeles
2021

Dedicated to Nana

ACKNOWLEDGMENTS

First, I would like to thank my advisor, Prof. Mayank Mehta, for allowing me the freedom to pursue problems which I found exciting, and for giving me the opportunity of working with him and his colleagues. I have developed as a scientist mostly due to his close guidance, and will cherish this experience for a lifetime.

I would also like to thank other members of the Mehta lab, especially Jason Moore, Chinmay Purandare, Mina Shahi, Shinali Dhingra, and Karen Safaryan, for their helpful comments during lab meetings, and for making it an overall joy to work in science.

I would like to thank Sven Berberich, who was always only an email away with any questions I had about the experiments, and never lost patience with me no matter how many times I asked for clarification or for additional data.

I would like to thank the committee for being involved with the dissertation. I would particularly like to thank Prof. Bruinsma, whose courses and guidance early in my PhD career led me to discover the beautiful world of biophysics. I would also like to thank Prof. Bozovic for stepping up last minute to be on my committee after unforeseen circumstances.

I would like to thank friends and extended family for their support. I would also like to thank my partner, Joni, for all the mental and moral support that got me through some tough times.

Finally, I would like to thank mom and dad, for their unwavering support all these years. This would not have been possible without you, and is as much your accomplishment as it is mine.

VITA

0.1 Education

June, 2018 ..... Ph.D. Candidate, Department of Physics and Astronomy, UCLA, Los Angeles, CA

May, 2014 ..... B.A. in Physics, with minor in Biophysics, Princeton University, Princeton, NJ

0.2 Research Manuscripts

"Theory of interaction between networks: persistent activity and inactivity *in vivo*", **K. Choudhary**, S. Berberich, T. G. Hahn, M. R. Mehta. KC did theory, simulations, and data analysis. SB and TGH did experiments. MRM participated and supervied all aspects. KC and MRM wrote the paper, with input from SB. *submitted*

"Spontaneous activity *in vivo* reveals functional connectivity in cortico-entorhinal-hippocampal interaction", **K. Choudhary**, S. Berberich, T. G. Hahn, M. R. Mehta. *in prep*

"A novel 3-Hz rhythm in LEC Layer 2, Dentate Gyrus, and Hippocampal Inhibition *in vivo*", **K. Choudhary**, S. Berberich, T. G. Hahn, M. R. Mehta. *in prep*

"Moving bar of light generates angle, distance, and direction selectivity in place cells", C. S. Purandare, S. Dhingra, R. Rios, C. Vuong, T. To, A. Hachisuka, **K. Choudhary**, M. R. Mehta. SD, CSP, RR, CV, TT, AH and KC performed the experiments. *accepted at Nature*

0.3 Awards

"Kaplan Fellowship in Biophysics," July 2017, Center for Biological Physics, UCLA

"SfN Travel Award," July 2018, Brain Research Institute, UCLA

"Departmental Teaching Award," Dec 2016, Dept. of Physics and Astronomy, UCLA

Table of Contents

List of Figures

Figure **Page**

Chapter 1
Introduction

1.1 The role of theory in science

A familiar joke among academic circles about physicists is their tendency to simplify problems to absurd levels, like assuming a cow is a sphere in the zero-gravity environment (Fig. 1.1). Yet despite this derision, physics has been extremely successful in explaining natural phenomena. Some may even argue that this success occurs precisely because physicists tend to approach problems from first principles, and add complexity only when absolutely necessary. This approach to problem solving has been especially productive in the study of many-body systems, or systems with a large number of degrees of freedom. The ideal gas law is a famous example: by assuming that all particles of gas in a room are essentially point-like billiard balls that collide with one another elastically, one can deduce the quantitative relationship between pressure, temperature, and volume. This law successfully describes, to first order, aside range of gaseous substances, from mono-atomic helium to poly-atomic carbon dioxide, and gives intuitive insights into how microscopic behavior of individual constituents, in this case the atoms or molecules of gas itself, can collectively manifest into macroscopic phenomena.

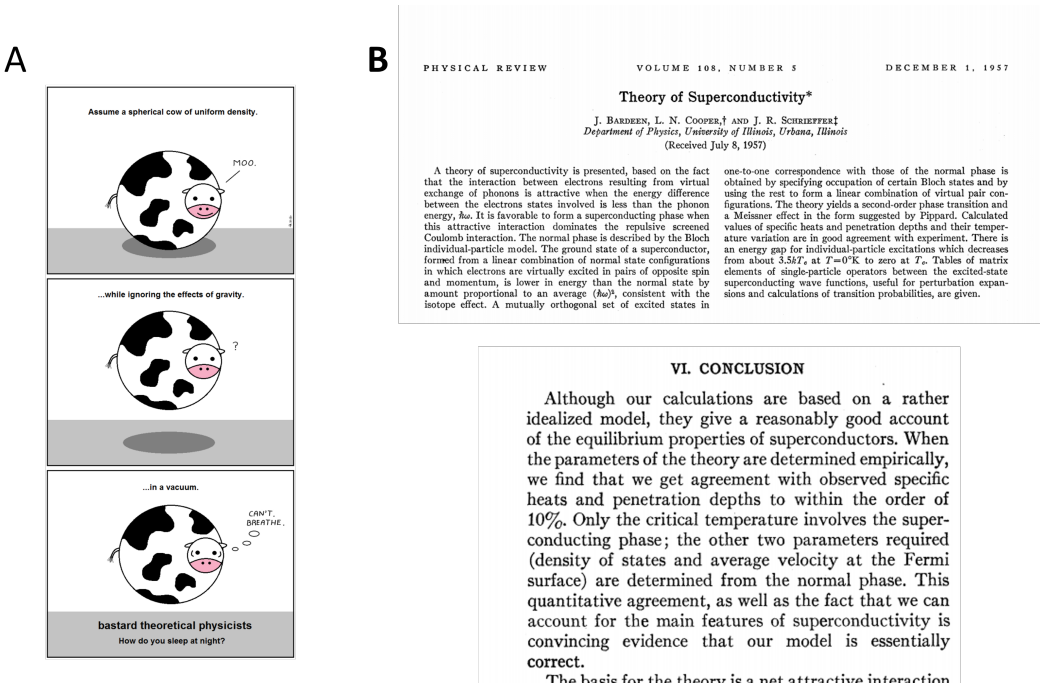

Figure 1.1: A) Cartoon by Abstruse Goose, highlighting how physicists tend to simplify things. B) The BCS superconductivity paper. In the conclusion section, they highlight the simplicity of their theory, and the fact that it can explain quantitatively multiple experimental observations [1].

Many-body physics is full of examples where simplifying assumptions lead to low-dimensional theories that can accurately reproduce numerous experimental observations. A famous example is the BCS theory of superconductivity, which utilizes just three parameters to explain a whole host of phenomena [1]. The success of such theories relies to a large extent on the validity of the simplifying assumptions: it is, for example, completely reasonable to treat every constituent part as completely identical, as every electron is identical, every phonon is identical, and every Ising spin is identical. In biology, however, these fundamental simplifications break down. The theoretical study of neurons and neural networks is marred with the problem of high-dimensionality, as each brain network involves billions neurons, each neuron synapses onto tens of thousands of other neurons, and within each neuron the dynamics of activity involve the operation of millions of constituent parts. Even one of the most celebrated theoretical works in neuroscience, the Hodgkin-Huxley equa-

tions, for example, involve about 17 parameters that must be fit using experimental data, all just to predict the activity of a small constituent part of the neuron itself [2]. Once fit to these parameters, however, the theory allows one to reliably predict experimental results; in particular, one can accurately calculate the speed of propagation of inaction potential along the squid axon once the fitted parameters of conductances and gating variables are known.

Developing a theory that is fundamental in its assumptions but accurately describes biological phenomena is the task.

1.2 Spontaneous Activity: What is it good for?

Another lesson from the discipline of physics is the idea of using simplified experimental preparations to test theories quantitatively. This idea is as old as Galileo himself, who used smooth inclined planes to develop the law of inertia. In modern times, artificial vacuums and experimental preparations near absolute zero can still be used to answer fundamental questions about the nature of constituents. Such isolated systems allow us to accurately test our theories while controlling for outside influence, and are indispensable to research.

The overarching goal of neuroscience is to understand how the brain, consisting of all its different cell types, can manifest thought, cognition, and behavior. One approach used by many is to study the brain under natural conditions and behavior, such as free foraging; another method is to use specific tasks to subject the animal to the same stimuli over multiple reputations. These approaches have been instrumental in establishing the field of systems neuroscience, and while the discipline has had moderate success in describing certain behaviors, it is undeniably deterred by the randomness involved in trial-to-trial variability, and in the underlying complication that cognition, and perhaps even consciousness, introduce.

Another approach, followed in this dissertation, is to study brain networks in isolation; i.e. in the absence of sensory or behavioral input. In this condition, one can study the spontaneous internal activity of neural networks while controlling for influences from the external world. Although the brain is fundamentally a structure that functions to understand and

predict the external world, by disconnecting it entirely from sensory and conscious influence, one can begin to investigate the fundamental states, and thus the fundamental operating principles, of brain networks. In practice, this isolation can be achieved in three ways: using *in vitro* preparations, wherein slices of brain tissue are kept alive under neurophysiological conditions conducive to active neural phenomena, using *in vivo* studies when the animal is subjected to loss of consciousness through anesthesia, and during natural sleep, when the animal is mostly cutoff from outside sensory stimulus.

Spontaneous activity during the absence of sensory or behavioral input is exhibited in many brain structures. Resting state imaging studies in humans have found that ongoing brain activity consumes 20% of the body's energy; further, task-related increases in neuronal metabolism only represents a $< 5\%$ increase compared to baseline levels during the resting state [3]. Despite several decades of research into spontaneous activity, its importance and significance during normal brain function is still poorly understood.

1.2.1 More than just noise

Upon the presentation of identical stimuli, cortical neurons exhibit variability in their responses. While their activity reflects Poisson statistics, one can often extract a signal from the variable responses by averaging over repeated presentations of the stimulus [4, 5]. In doing so, one can remove the effect of the intrinsic dynamics; from a mechanistic point of view, this procedure assumes that the underlying noise is simply a consequence of how inherently noisy biology is, given that almost all brains operate at 300 Kelvin. This interpretation, however, diminishes the meaning of spontaneous activity as simply a nuisance; something the brain has to deal with and overcome, and something that is not helpful in any way.

Spontaneous activity within networks, and even individual neurons, is generated by the synaptic inputs from other coherently activated neurons, and can be observed in the absence of sensory input to be as large as sensory-evoked activity itself [6, 7]. This activity can be correlated across spatial scales, as much as multiple millimeters, and across time scales, from milliseconds to tens of seconds [8]. This spontaneous activity contributes to the underlying

variability of cortical responses to stimuli, and its interaction with the external world can lead to the responses seen in experiments.

1.2.2 Insights into functional connectivity

During development, spontaneous activity is evoked by networks in isolation and is crucial in defining informative properties for individual cells, like receptive fields and tuning curves. The early patterns of connectivity can thus be built without any sensory experience; the activity is thus reflective of the underlying connectivity within the cortex [9, 10]. For example, primary visual cortex orientation maps, where neighboring cells within the visual cortex display tuning towards the orientation of a simple visual stimulus, can interestingly emerge during spontaneous activity as well [11, 12]. Furthermore, the connectivity map unveiled by triggering the activity of other neurons on the activity of a single neuron reveals a pattern that highlights those cortical columns that match the orientation preference of the triggering neuron[13, 14]. The connectivity maps unveiled through this method are confirmed by anatomical and cross-correlation analysis of pairs of single-unit recordings [15]. These results change depending on anesthesia depth, showing that while circuit connectivity highly affects spontaneous activity dynamics, the same network can display different activity patterns dependent on ambient conditions.

At larger spatial scales, imaging and electrophysiological studies across brain regions can be used to find anatomically separate cortical networks observed as covariation of measured activity. Such procedures are commonly referred to as functional connectivity analysis [16, 17]. Functional Magnetic Resonance Imaging (fMRI) can be used to study brain connectivity during resting-state conditions [18, 19]. Spontaneous activity during these conditions can covary with brain state [20], and is relatively stable across a wide range of cognitive states, ranging from wakefulness to light sleep and deep anesthesia.

1.2.3 During Sleep

The most natural form of spontaneous activity occurs when we sleep. Contrary to the popular view, the brain is capable of complex processing of sensory information during

sleep, as first indicated by multiple behavioral experiments in humans [21, 22]. In recent decades, there has been increased interest into the patterns of spontaneous activity evoked during sleep. For example, both the hippocampus and neocortex have been found to replay firing patterns observed during prior behavior [23–28]. This activity replay is likely crucial in the process of memory consolidation, and may form the substrate by which brain circuitry can be structurally reorganized for long term memory storage through synaptic potentiation [29–31]. These replay patterns are not, however, purely related to learning, and likely reflect the activity of local circuits which are already present, since sequences can be observed even before the presentation of stimuli [32]. These patterns are highly altered after the repeated presentation of a stimulus or sequence of stimuli, thereby altering the patterns of subsequent spontaneous activity [33]. According to classic Hebbian learning, persistent interaction between cells can cause long lasting cellular changes [34]. Thus, reverberation of the activity within cell assemblies during spontaneous activity can serve as a substrate for short-term memory formation and long-term learning[35].

1.3 Cortical Oscillations

Ever since the advent of modern electrophysiology, the electrical oscillations within brain tissue have been the subject of extensive research. The first mention is usually attributed to Hans Berger in 1929, who first discovered that the electrical activity of the human brain could be measured through the scalp, i.e. the electroencephalogram, or EEG [36]. In the same study, he also noticed that the EEG signal could display a regular oscillation pattern at about 10Hz when subjects closed their eyes. Since then, neural oscillations have been discovered during behavior, during sleep, and even in isolated slices of brain tissue.

Oscillations can be observed within the membrane potential of individual neurons and in the network activity of large numbers of neurons, suggesting that they can arise at multiple scales, from intrinsic neuronal mechanisms to dynamic interplay between neurons and groups of neurons [37]. The tendency of cortical circuits to oscillate suggest that they could be functioning like central pattern generators, commonly observed in vertebrates,

which comprise of circuits where sensory input provides a drive for a many-body oscillator, like those responsible for respiration, walking, etc [38]. This framework, however, is less applicable to cortical oscillations, since they are weak compared to the overall power spectra, and their bandwidth is very wide. Additionally, spiking behavior of cortical neurons is inherently stochastic, which is qualitatively different from oscillators generated through central pattern generators.

The frequency of cortical oscillations can span from extremely slow (0.5Hz) to extremely fast (500Hz), and can be broken up into many categories.

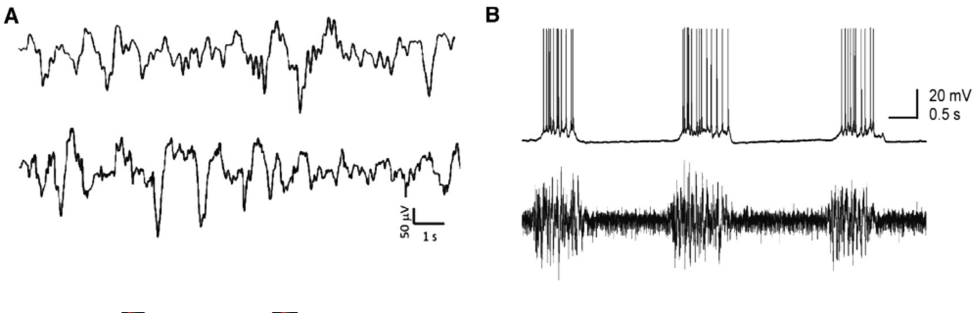

Figure 1.2: Up-Down state oscillations are considered the default activity states of cortical circuits. A) Slow oscillations, the natural sleep version of Up-Down states, recorded with EEG from frontal regions under propofol anesthesia (top trace) and during spontaneous sleep in humans (bottom trace). From [39]. B) Up-Down states recorded *in vitro* intracellularly (top) and extracellularly (bottom) from ferret visual cortex. From [40]

1.3.1 The Slow Waves

During non-rapid-eye-movement (nREM) sleep, under the effect of several anesthetics, and during drowsy or quite-wakefulness periods, EEG/LFP signals are dominated by high amplitude slow fluctuations in the delta band (0.1 to 2 Hz) [7, 32, 41–43]. Within single cells, this pattern of activity is accompanied by alterations between a phase where neurons do not fire, and individual neurons are hyperpolarized, and a phase where they are tonically firing, and individual neurons are depolarized. While the delta oscillations during nREM sleep and the slow oscillations were initially thought to be separate phenomena, recent work

suggests that these are not separate patterns but rather the same [44]. Delta waves have been suggested to have both thalamic and cortical origin, but recent work has shown that thalamic lesions do not completely silence the delta oscillation [45].

Slow waves propagate through the cortex, from the forebrain to the hindbrain, as shown in high-density EEG recordings [46]. These slow waves also propagate in the rodent brain under anesthesia, and can be observed by means of voltage sensitive dyes and electrode arrays [47–50]. Simultaneous intracellular recordings reveal that neighboring cortical neurons undergo synchronous transitions [51]. This synchronization can be effective over several millimeters, supported by horizontal cortico-cortical connections [52, 53]. Evidence for this mechanism comes from studies which show that pharmacological disruption of these connections between neurons can reduce the synchronization of slow waves [54].

1.3.2 Up-Down States as the Default Network Activity

Some studies have suggested that the slow-oscillations expressed within cortical tissues can be considered as the default activity regime of neural networks [55]. Slow oscillations are the emergent activity pattern when the cortex has been functionally disconnected from the outside world, such as during slow wave sleep and deep anesthesia [31, 41, 56, 57]. These oscillations are invariant under different anesthetics, including ketamine-xylazine, propofol, midazolam, halothane, isoflurane, and urethane [39, 58–61]. Furthermore, physical separation of brain tissue preserves the slow oscillation, such as cortical slabs and even random cortical networks *ex vivo* [62–64]. Slow oscillations also occur in specific clinical conditions, such as the "cortical island," which occurs as a result of a traumatic or cerebrovascular disorder [65]. These oscillations are also common in acute ischemic cortical stroke and can persist for months and sometimes even years [66]. Finally, cortical slices in the dish can express slow oscillations in the absence of any chemical or electrical stimulation. These are described in detail in the following sections [67].

1.3.3 Fast Oscillations

In addition to the slow oscillations, neural networks ubiquitously show fast oscillations. These are grouped into the theta (4-8Hz), beta (15-30 Hz), and gamma bands (40-150 Hz), and each of these bands can be broken up into slow and fast subbands. At these frequencies, spikes locked to a certain phase tend to occur in synchrony. Neural synchrony is a potential mechanism by which information can be encoded and transferred, as neurons are sensitive to coincident arrival of input spikes as opposed to asynchronous inputs [68, 69]. This synchrony may play a role in well timed coordination and communication between neural populations simultaneously engaged in cognitive processes.

During awake and sleep states, the EEG of spontaneous activity exhibits fluctuations at high frequencies with low amplitude. Oscillations in the theta band have been associated with spatial memory and navigation [70–72]. Oscillations in the beta band and gamma band have been associated with working memory readout [73–75]. They have also been associated with cognitive processing such as attention, decision making, motor functions, and sensory processing [76–79].

1.4 Up-Down states across the extended brain

Up and Down states are defined by the bi-modality of the membrane potential during the slow-oscillation, with one depolarized phase and one hyperpolarized phase. This was observed *in vivo* for the first time in spiny neurons for the neostriatum of anesthetized rats. Since this discovery, most of the work about Up and Down states have been performed using either anesthetized animals or *in vitro* preparations [41, 80].

In slices showing slow oscillatory activity, intracortical stimulation is able to evoke transitions from Up to Down and Down to Up states [40]. Studies in thalamocortical slices which sustain UDS have shown that both electrical and chemical stimulation to the thalamus during the Down state can induce a transition to the Up state, but not from the Up to the Down state [81, 82]. Many *in vivo* studies have shown that Up-Down transitions can be triggered by sensory stimulation; yet still other studies disagree [47, 83]. This difference

could be explained by anesthesia type and dosage, but further studies are necessary. In any case, it is clear that network activity has a fundamental role in the alteration between the Up and Down states.

1.4.1 In the Cortex

Up and Down states are coincident across most neocortical areas in mammals [84, 85]. Specifically, the rodent barrel cortex (part of the somatosensory cortex) has been extensively used to study the spatio-temporal nature of Up and Down states. The somatosensory cortex is a prototypical primary sensory cortex, consisting of 6 layers. Thalamic input into the somatosensory cortex, which carry information about touch, pressure, temperature, and proprioceptive input, are excitatory but can target both excitatory and inhibitory neurons [86–88].

The entorhinal cortex (EC) connects the parietal, temporal, and prefrontal cortices to the hippocampal formation, and thus forms the interface between the neocortical brain regions, which encode ongoing sensory information and long-term memories, and the hippocampus, which is responsible for long-term memory consolidation [89]. The entorhinal cortex further serves the primary input-output structure for the hippocampus, and can be divided into the lateral and medial subdivisions. Unlike the neocortex, which is tightly linked to the thalamic nuclei, there is no evidence for strong monosynaptic coupling between the thalamus and the EC. However, this does not deter the EC from exhibiting robust UDS, indicating that there are several other motifs of recurrent activity. Previous experimental work has found that Up states in the neocortex likely propagate into the entorhinal cortex. EC neurons show UDS *in vivo*, and gamma oscillations are nested within the Up states. Slices of both MEC and LEC can generate UDS even in the absence of long range inputs [90–92]. Finally, these UDS oscillations in the EC are physically locked to those in the neocortex [93, 94].

1.4.2 Cortico-Hippocampal Interaction and Memory Consolidation

Memory consolidation occurs during neocortical-hippocampal dialogue during slow-wave-sleep, and has been a subject of extensive study [26, 95]. Within the hippocampus, this process has been associated with the sharp-wave-ripple, which consists of high-frequency "ripple" oscillation (150 Hz and above) riding on top of a depolarizing "sharp-wave" event [96]. During these events, a process called "replay" occurs, where cell assemblies active during the waking information-acquiring behavior are reactivated in the same order as in the waking state. One hypothesis is that replay strengthens synaptic connections in the neocortex, thereby mediating a "transfer" of memory from the short term to the long term. In support of this hypothesis is the fact that replay events within the hippocampus and the neocortex are highly correlated, and that impairing sharp wave events in the hippocampus during post-learning sleep reduces memory consolidation [25, 97–100]. Further, strengthening the coupling between sharp wave ripples and cortical events via precisely timed electrical stimulation during ripple events improves memory consolidation[101].

During sleep, especially nREM slow wave oscillations, the sharp-wave-ripples in the hippocampus appear to be closely linked to neocortical Up and Down states . Some studies show that these occur mostly during neocortical Down states, with their peak occurrence happening just before the noeocrtical Down-Up transition [102]. Other studies have suggested that these ripples actually occur during Up states [93, 101]. Regardless, the events in the hippocampus seem tightly coupled to the Up-Down oscillation of the neocortex, and thus the coordination between ripple events and the slow oscillation is likely important for memory consolidation. In this context, the direct input from CA1 to the prefrontal cortex likely plays an important role [103, 104].

Finally, in contrast to the neocortex, the somatosensory cortex, and the entorhinal cortex, the hippocampus does not display clear epochs of Up and Down states. Instead, hippocampal LFP during slow wave sleep exhibits "large irregular activity." Intracellular recordings in rodents reveal unimodal, and not bimodal, distribution of the membrane potential of pyramidal neurons in both CA1 and CA3 [93, 105]. Granule cells in the dentate

gyrus have only skewed distributions, while interneurons are completely phase locked to neocortical UDS [106]. Finally, neurons in the subiculum show bimodality, consistent with its extensive neocortical, paleocortical, and thalamic connectivity [93, 107].

1.5 Persistent Activity and Working Memory

Persistent activity is often considered a neural substrate for working memory, as information can be stored in the sustained firing of cells even after synaptic input has been extinguished. Thus, multiple research efforts have been devoted to understanding the potential mechanisms underlying persistent activity, especially as it relates to working memory [108]. The theories fall into two broad categories: either cell intrinsic mechanisms or network mechanisms. We will focus on the network mechanisms, as the phenomena discussed in this dissertation is most likely not due to intrinsic cellular processes.

1.5.1 Computational Network Models of Persistent Activity

The key challenge in implementing a biophysically realistic model of how networks can sustain working memory is to bridge the timescales involved: while working memory can last seconds to tens of seconds, neuronal responses to external synapses decay within 10-20 ms. Thus, central to these models is the idea that patterns of connectivity must extend these short-term representations into long term activity. One way to achieve this is to store information in so called "attractor states," such that activity patterns converge on these states and remain stable on their own [109].

Spiking neuron models are the most biologically realistic, as real neurons communicate with action potentials. The simplest of these models are integrate and fire neurons; each neuron is characterized by a single parameter, the membrane potential, and when its value achieves the spiking threshold, the neuron fires an action potential and resets its value back to the resting state [110]. More complicated models use the many-compartment idea, where the membrane potential varies across different parts of the cell [111]. Still more complicated models include a range of different ionic currents, with each conductance modeled using

non-linear gating variables akin to the Hodgkin Huxley models [112, 113].

Another method is to not model the dynamical evolution of each neuron's membrane potential, but to compare the total synaptic input into the neuron to a pre-described threshold. If the neuron is receiving inputs above its threshold, it fires a spike in that time bin. These binary neurons models (0 for no spike, 1 for a spike) capture the discrete nature of neuronal responses but ignores the temporal nature in which neurons integrate their inputs, as all inputs co-occur and are coincident in the same time bin [109].

Finally, there are the continuous or rate-coded models. Here, instead if modeling the sequences of action potentials emitted by neurons, the focus is on describing each neuron with a continuous-valued rate variable that changes over time dependent on the synaptic inputs [114, 115]. The parameter here can describe the rate of action potential firing, or the overall activity level of the entire network. The models do not capture the discrete nature of neuronal dynamics, but are much more amenable to mathematical analysis than the spiking or binary models. This type of model will be developed in this dissertation.

1.6 Dissertation Outline

The dissertation is organized as follows. In Chapter 2, I review the basic mean-field techniques and build a mean-field theory of cortical interaction using only excitation and inhibition. In Chapter 3, I outline the *in vivo* experiments that were used to test the theory, and quantify several predictions that are quantitatively tested within the experiment, all yielding stark agreement to theory. In Chapter 4, I extend the ideas of the model to understand how cortical interactions can affect downstream structures, specifically the hippocampus, as it is the major source of input from cortical areas during natural spontaneous activity and is the site of memory consolidation and learning.

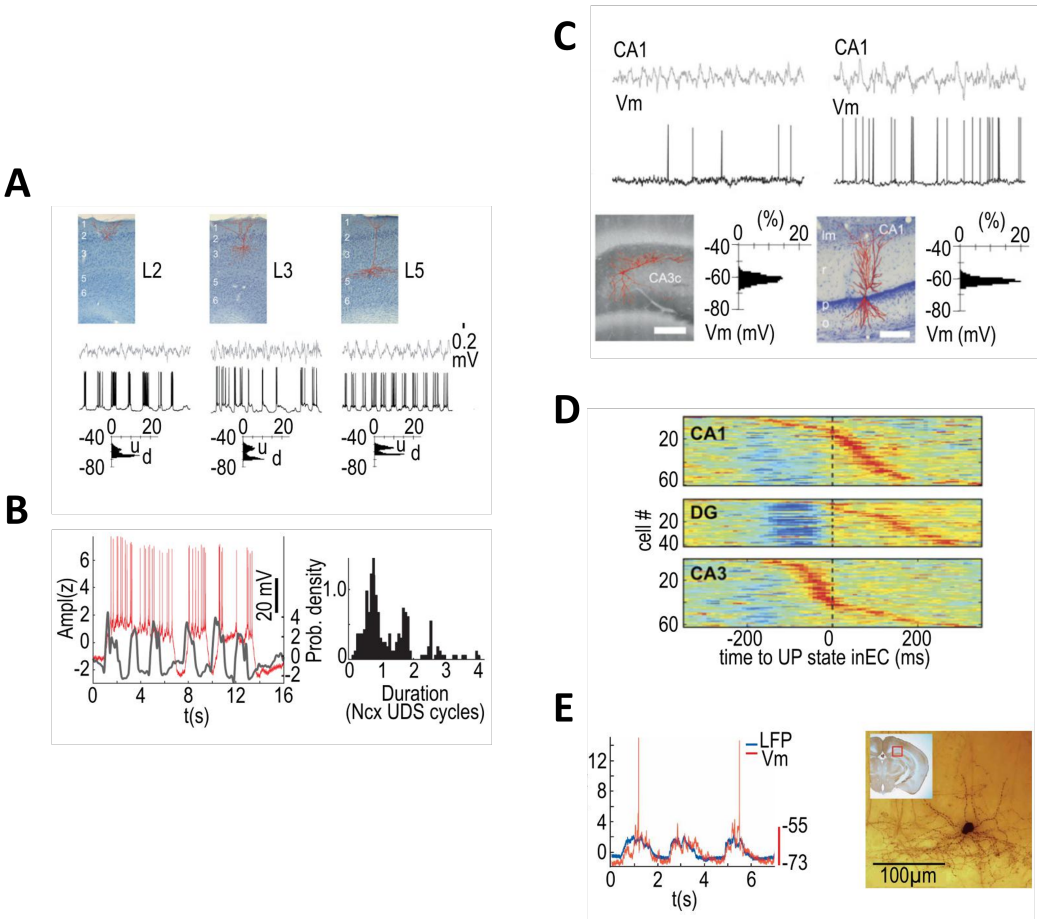

Figure 1.3: Up-Down states in Entorhinal Cortex and Hippocampus. A) Entorhinal cortex intracellular recordings in layer 2,3, and 5 (each column). Top: histology of cell. Top middle: Hippocampal LFP. Bottom middle: Intracellular recording of V_m. Bottom: Histogram of V_m values, showing bimodal distribution. Adapted from [93]. B) Left: Intracellularly recorded Up states in MEC layer 3 pyramidal neurons (red) can outlast one or more neocortical Up-Down state cycles (gray). Right: The duration of these Up states preferentially lasts an integer number of neocortical UDS cycles. Adpated from [94]. C) Intracellular recordings from pyramidal neurons in CA1 and CA3, showing no bimodality. The organization is similar to A. Adapted from [93]. D) Colored coded stacked cross-correlograms of CA1, dentate gyrus (DG), and CA3 neurons (one per row) recorded during slow wave sleep in a naturally sleeping rat, aligned to the Down-Up transition. A clear Down state can be seen only in DG. Adapted for [93]. E) Intracellular membrane potential from hippocampal CA1 layer interneuron (red), showing phase locking with neocortical UDS (gray), along with histological reconstruction. Adapted from [106]

Chapter 2

A mean field theory of network interactions

This chapter outlines the mean field model of excitation, inhibition, and adaptation used to study persistent activity and inactivity throughout. We begin with a brief review of how neural networks work in biological brains. We then use mean field techniques to abstract the long timescale (i.e. > 100 ms) features and develop the equations of motion of a single neural network consisting of excitatory and inhibitory neurons. We then add adaptation to the excitatory neurons and use this formulation to build a simple model of the Up-Down state (UDS) oscillation. Finally, we examine the dynamics of coupled networks, showcasing how such a simple model can yield both persistent activity and persistent inactivity. We explore the physics underlying these phenomena in detail, specifically focusing on falsifiable predictions that can be tested in an *in vivo* experimental setup.

2.1 A brief introduction to the relevant neuroscience

Mammalian brains consist of billions of neurons, the basic unit of the nervous system; the human brain has over 80 billion. Each neuron makes thousands to tens of thousands of connections with other neurons, creating neural networks of vast complexity. The combined activity of all of these neurons creates behavior, cognition, and, somewhere down the line, consciousness. Over the years, experimentalists have advanced our understanding of how the brain works at scales ranging from the action of individual molecules to the activity of the entire brain.

2.1.1 The individual neuron

Despite the varied morphologies of neurons found in the brain, the basic structure of neurons is similar in all living creatures with nervous systems (Fig. 2.1) [116]. Differences between animals is usually in the number of neurons and the complexity of the interconnections. An individual neuron operates by maintaining an electrical potential difference across its cell membrane; when the neuron is at rest (i.e. inactive), a balance of ions (K^+, Na^+, Cl^-, etc.) maintains the intracellular space at a lower voltage compared with the extracellular space (-40 to -70 mV). This non-equilibrium state is maintained through the active expenditure of energy in the form of ATP, which is used to pump ions against their concentration gradient across the membrane.

Neurons are unidirectional systems, having a space for inputs (the dendrites), a space for integration (the soma), and a space for output (the axon and presynaptic terminals). Neurons meet at synapses; the neuron outputting signal is called presynaptic, while the neuron receiving signal is called postsynaptic. When signals come into the dendrites (at the postsynaptic terminal), the intracellular space becomes flooded with ions from the outside of the cell. These ions serve to either depolarize the cell, making the inside less negative in voltage, or hyperpolarize the cell, making the inside more negative. If there are enough depolarizing inputs in the dendrites, the soma voltage increases until a threshold, usually termed the firing threshold. Once this happens, a sequence of reactions initiate a strong, short-lived electrical signal, called the action potential, which propagates down the neuron, through the axon, and towards the neuron's postsynaptic targets. Action potentials are also termed "spikes," and are a signature of the neuron being active at some point in time. After an action potential occurs, the neuron returns to the resting state for some time, called the "refractory period." During this time, active processes within the cell return all ion concentrations to the steady-state value, thereby preparing the cell to fire another action potential in the future.

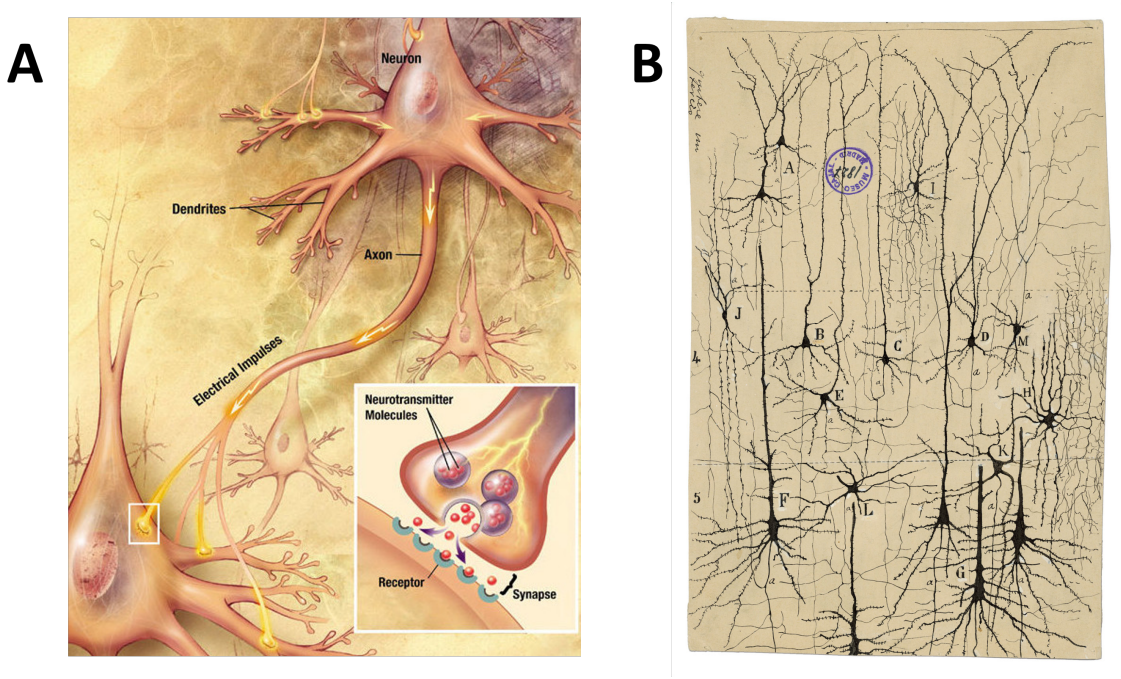

Figure 2.1: A) The basic structure of neurons and their connections, called synapses. Each neuron receives input from other neurons through the dendrites. These signals are integrated in the soma, the cell body. If the inputs integrate above the firing threshold, an action potential is generated, which travels along the axon of the neuron via electrical impulses, governed by the transport of ions across the membrane potential into and out of the neuron. These impulses are called action potentials. The axon terminates on the dendrites of other neurons, which then go through a similar process. The location where the neuron's axon terminates on another neuron's dendrite is called the synapse (inset). The neuron sending the action potential is the presynaptic neuron, while the one receiving is called the postsynaptic neuron. When the action potential reaches the presynaptic terminal from the soma, neurotransmitters are released into the synaptic cleft (space between the pre and postsynaptic terminals). These neurotransmitters then bind to neuroreceptors in the postsynaptic neuron. This generates an excitatory postsynaptic potential (EPSP) that is depolarizing if the signal comes from an excitatory neuron. If it comes from an inhibitory neuron, it is called an inhibitory postsynaptic potential (IPSP) and typically hyperpolarizes the postsynaptic neuron. B) A drawing from Ramon y Cajal's notebook, detailing the diversity of morphologies neurons can have in the mamalian brain. Picture credit: Wikipedia.

2.1.2 Excitation and Inhibition

When a spike arrives at the presynaptic terminal at the end of the axon, the presynaptic neuron releases molecules called neurotransmitters into the space between the presynaptic terminal and the postsynaptic dendrite. Examples of well known neurotransmitters are dopamine, serotonin, and norepinephrine; these are well known for their specific effects on the brain. But the bread and butter of the brain are just two molecules: glutamate and gamma-aminobutyric acid (GABA). When glutamate binds to the receptors on the postsynaptic dendrite, it causes positive ions (like Ca^{2+}) to enter the cell, thereby depolarizing the cell and pushing it towards the firing threshold. Binding of GABA, on the other hand, causes negative ions (like Cl^{-}) to enter the cell, hyperpolarizing it and driving it away from the firing threshold. Thus, glutamate works to "excite" the postsynaptic neuron, while GABA works to "inhibit."

One crucial fact that is seemingly invariant across species is the fact that neurons come in two distinct categories: excitatory and inhibitory. Excitatory neurons release on excitatory neurotransmitters, like glutamate, while inhibitory neurons release only inhibitory ones. The balance between excitation and inhibition is crucial to normal brain function. A brain dominated by glutamate would only be capable of exciting itself in bursts of activity, similar to an epileptic seizure. Conversely, a brain dominated by GABA would be highly inactive. A healthy brain operates in the middle regime, where the opposing forces of excitation and inhibition can generate complex patterns of activity.

2.2 The mean field technique

While studies of individual neurons and their interactions are crucial for understanding brain function at the fundamental level, higher cognitive functions like sensory information processing, learning, memory storage, and pattern recognition involve the concerted activity of large groups of neurons. Approaching these problems at a single cell level can be problematic. Furthermore, while local interactions between nerve cells are largely random, these connections can lead to quite precise long-range interactions. In physics, the

knowledge of the minute details of the system's components are often deemed unnecessary for the understanding of the system as a whole; for example, one does not need to know the identity of every molecule in a container in order to extract the relationship between pressure, temperature, and volume.

2.2.1 The Wilson-Cowan equations

In view of these ideas, it is more fruitful to develop a theory that emphasizes not the individual cell but rather the properties of populations. The cells comprising these populations are assumed to be in close spatial proximity, and their interconnections are assumed to be random, yet dense enough that there is at least one path connecting any two cells within the population. Under these assumptions, we can neglect spatial interactions and deal simply with the temporal dynamics. The relevant variable is then the proportion of cells in the population which are active at any time. We denote this variable by $E(t)$ and $I(t)$ for the excitatory and inhibitory sub-populations, respectively. This approach was first used by Wilson and Cowan [115]; a modified approach is outlined here. Similar works include [117–120].

From single neurons to populations

To find the general equations governing the behavior of $E(t)$ and $I(t)$, we will need two independent expressions for the proportion of sensitive cells (i.e. cells which are not refractory after spiking) and the proportion of cells receiving afferent excitation higher than threshold. Then, if $E(t), I(t)$ represent the proportion of cells active at time t, then at time $t+dt$ these functions will equal the proportion of cells that are sensitive *and* receive enough excitation to become active.

Let us assume all excitatory and inhibitory neurons have the same refractory period, r_E and r_I, respectively. Excitatory neurons which have fired within the time window $[t-r_E, t]$ are then considered refractory at time t, so the proportion of refractory excitatory neurons

is given by

$$E_{refractory} = \int_{t-r_E}^{t} E(t')dt' \tag{2.1}$$

Similarly, for inhibitory neurons, the proportion of refractory cells is

$$I_{refractory} = \int_{t-r_I}^{t} I(t')dt' \tag{2.2}$$

The amount leftover are then the proportion of neurons which are sensitive

$$E_{sensitive} = 1 - \int_{t-r_E}^{t} E(t')dt' \tag{2.3a}$$

$$I_{sensitive} = 1 - \int_{t-r_I}^{t} I(t')dt' \tag{2.3b}$$

We now need an expression for the proportion of each subpopulation that is receiving at least threshold excitation per unit time as a function of the average activity level of each subpopulation; these functions will be called the subpopulation response functions. Note, these functions assume that all neurons in a subpopulation are sensitive. If we assume that the distribution of neural thresholds (θ) within a subpopulation is given by some unimodal function $D(\theta)$, and that all cells recieve the same number of excitatory and inhibitory afferents, then on average all cells will be subjected to the same average excitatory input $x(t)$, and the response function will take on the form

$$\Psi_{E/I}(x) = \int_{0}^{x(t)} D_{E/I}(\theta_{E/I})d\theta_{E/I} \tag{2.4}$$

where the subscript indicates the subpopulation each variable describes. This response function is monotonically increasing, and in the simplest case will be of sigmoid form. This sigmoid shape is intuitively simple: in a population of thresholds, too low excitation will not excite any elements, while too high excitation will excite all elements, but no more. This non-linear relationship has been supported by numerous experimental studies, at the level of dendrites, single cells, and even networks as a whole.

To make equation 2.4 useful, we must find an expression for $x(t)$, the average excitation generated within each cell of a subpopulation. For the excitatory cells, let W_{EE} and W_{IE} represent the average number of excitatory and inhibitory synapses per cell, and if we

assume that individual cells sum their inputs and the effect of stimulation decays with a time course $\alpha(t)$, then the average excitation generated within an excitatory neuron is

$$x_E(t) = \int_{-\infty}^{t} \alpha_E(t-t')[W_{EE}E(t') - W_{IE}I(t')]dt' \tag{2.5}$$

Similarly, for the inhibitory subpopulation, the average excitation within each neuron is

$$x_I(t) = \int_{-\infty}^{t} \alpha_I(t-t')[W_{EI}E(t') - W_{II}I(t')]dt' \tag{2.6}$$

where W_{EI} and W_{II} represent the average excitatory and inhibitory synapses in inhibitory neurons.

We have now find expressions for the proportion of sensitive cells, the subpopulation response functions, and the average excitation within each subpopulation. We can combine these to get the equations of motion for $E(t)$ and $I(t)$. The activities in a subpopulation at time $t+\tau$ will be equal to the proportion of cells which are both sensitive and receive above threshold excitation at time t. If these two conditions are independent, then we have

$$E(t+\tau_E) = \left[1 - \int_{t-r_E}^{t} E(t')dt'\right] \cdot \Psi_E\left(x_E(t)\right) \tag{2.7a}$$

$$= \left[1 - \int_{t-r_E}^{t} E(t')dt'\right] \cdot \Psi_E\left(\int_{-\infty}^{t} \alpha_E(t-t')[W_{EE}E(t') - W_{IE}I(t')]dt'\right) \tag{2.7b}$$

$$I(t+\tau_I) = \left[1 - \int_{t-r_I}^{t} I(t')dt'\right] \cdot \Psi_I\left(x_I(t)\right) \tag{2.7c}$$

$$= \left[1 - \int_{t-r_I}^{t} I(t')dt'\right] \cdot \Psi_I\left(\int_{-\infty}^{t} \alpha_I(t-t')[W_{IE}E(t') - W_{II}I(t')]dt'\right) \tag{2.7d}$$

In real biological networks, there is undoubtedly a correlation between the average excitation within a subpopulation and the fraction of sensitive cells; this can be neglected for highly interconnected networks because of the presence of spatial and temporal fluctuations in the average excitation within the populations. Additionally, thresholds for individual neurons and networks observed in classic experimental works and highly variable [121, 122].

Time Course Graining

For the purposes of our study, we are interested in dynamics of long timescales, much longer than the population update time τ. We can define a new variable:

$$\bar{E}(t) = \frac{1}{2s}\int_{t-s}^{t+s} E(t')dt' \tag{2.8a}$$

$$\bar{I}(t) = \frac{1}{2s}\int_{t-s}^{t+s} I(t')dt' \tag{2.8b}$$

Now, if we assume that $\alpha(t)$ is close to unity for $0 \leq t \leq r$ and 0 for larger t for both E and I subpopulations, then one can replace the integrals in 2.7d with their time-averaged values

$$\int_{t-r}^{t} E(t')dt' \to r\bar{E}(t) \tag{2.9a}$$

$$\int_{-\infty}^{t} \alpha(t-t')E(t')dt' \to k\bar{E}(t) \tag{2.9b}$$

where k is a constant that relates to the time dependence of external synaptic input. We can then expand Eq. 2.7d about $\tau = 0$, yielding

$$\bar{E} + \tau_E\frac{d\bar{E}}{dt} = \left[1 - r\bar{E}\right]\cdot\Psi_E\left(k[W_{EE}E(t') - W_{IE}I(t')]\right) \tag{2.10a}$$

$$\bar{I} + \tau_I\frac{d\bar{I}}{dt} = \left[1 - r\bar{I}\right]\cdot\Psi_I\left(k[W_{EI}E(t') - W_{II}I(t')]\right) \tag{2.10b}$$

Taking the limit as $r \to 0$, and absorbing the constant k into the connectivity constants W_{ij}, we arrive at our final equation for an isolated, connected network of excitatory and inhibitory neurons:

$$\tau_E\frac{dE}{dt} = -E + \Psi_E\left(W_{EE}E - W_{IE}I\right) \tag{2.11a}$$

$$\tau_I\frac{dI}{dt} = -I + \Psi_I\left(W_{IE}E - W_{II}I\right) \tag{2.11b}$$

2.2.2 Adding Adaptation

We now outline the mean-field model equations used in the present work to study the Up-Down state oscillation. The Wilson-Cowan equations, derived in the previous section,

assume that over long timescales each subpopulation is capable of sustained firing, and the memory of the network is only as long as the individual subpopulation time constants τ_E and τ_I. However, experiments have observed that excitatory neurons, but not inhibitory ones, show long-timescale adaptation in both spike-frequency and spike-amplitude. During sustained intracellular current injections, inhibitory neurons can sustain repeated action potentials of equivalent strength; pyramidal neruons, on the other hand, fire bursts of action potentials before slowing down, with each subsequent spike diminishing in amplitude. This phenomena is commonly termed *adaptation*, and has to do with resource depletion and fatigue within excitatory neurons. The addition of this third variable has huge consequences to the temporal activity of the model. The equations of interest are:

$$\tau_E \frac{dE}{dt} = -E + \Psi_E \left(W_{EE}E - W_{IE}I - W_{EA}A + \xi_E + i_E \right) \tag{2.12a}$$

$$\tau_I \frac{dI}{dt} = -I + \Psi_I \left(W_{IE}E - W_{II}I + \xi_I \right) \tag{2.12b}$$

$$\tau_A \frac{dA}{dt} = -A + W_{AE}E \tag{2.12c}$$

These describe the time evolution of the average excitatory $E(t)$ and average inhibitory $I(t)$ activity within a subpopulation, where the excitation is governed by a negative feedback adaptation $A(t)$. The time constants $\tau_E = 10ms$ and $\tau_I = 5ms$ for each subpopulation are much shorter than the adaptation time constant $\tau_A = 300ms$; these values are consistent with experimental data on the time-constants of each neural subtype. ξ is an additional noise current to simulate uncorrelated network fluctuations, and is drawn from a gaussian distribution ($\mu = 0, \sigma = 0.03$). Each subpopulation receives independent noise. Finally, i_E represents inputs coming from outside the entire network itself, either from experimental perturbation or long-range synapses.

As described earlier, the functions $\Psi(x)$ define the population response function, relating the net input excitation x to the proportion of the subpopulation that will be active at that input level. This function is, in simplest form, a nonlinear sigmoid: at extremely low input, none of the neurons are active, at extremely high input, all of the neurons are active, and for medium levels of input, there is a linear relationship between input and proportion of

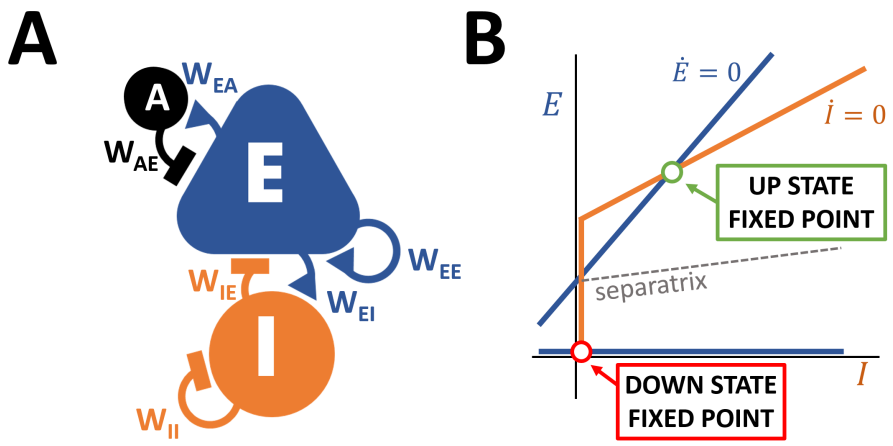

Figure 2.2: A) A single network with excitatory (E) and inhibitory (I) subpopulations, each characterized by the average activity level, a dimensionless number between 0 and 1. Only the excitatory subpopulation shows activity dependent adaptation (A). The connectivity weights are named with convention W_{XY}: from population X to Y. Triangular synapses denote positive weights, while bars indicate negative weights. B) In the E-I phase plane, nullclines for E (blue) and I (orange) for a single E-I network intersect at the stable Up (green circle) and Down (red circle) fixed points. The separatrix (dashed line) separates the two basins of attraction.

neurons active. Assuming we are nowhere near saturation, we can use the simplest possible response function: a threshold linear relationship:

$$\Psi_{E/I}(x) = g_{E/I}(x - \Theta_{E/I})_+ \tag{2.13}$$

where $g_{E/I}$ is the slope of the input/output relationship for each neural population, and $\Theta_{E/I}$ is the minimum input needed to excite any element of the population. Throughout this dissertation, $g_E = 6, g_I = 30$, and $\Theta_E = 0.0517, \Theta_I = 0.2778$. Furthermore, the connectivity parameters are $W_{EE} = 1, W_{II} = 0.083, W_{EI} = 0.166, W_{IE} = 1.66$. For the adaptation variable, $W_{EA} = 0.166, W_{AE} = 1.1$. A schematic of the network is show in Fig. 2.2.

2.3 The Up and Down States

Analyzing Eq. 2.12 in the absence of noise $\xi = 0$ and external input $i_E = 0$ shows that trivially, $E = 0, I = 0$ is a steady state of the system. Intuitively, this makes sense; when both populations are inactive, there is no drive to become active. We identify this situation with the "Down" state from the Up-Down state oscillation.

Since the adaptation parameter is so slow-varying, we can consider a snapshot of the network at a fixed adaptation A^* and consider the state space of all possible realizations of activity E/I. We can solve for the nullclines of each population by setting the derivative of the activity in each population to zero, and solving for E:

$$E = \frac{g_E W_{EI} I + g_E(W_{EA} A^* + \Theta_E)}{g_E W_{EE} - 1} \tag{2.14a}$$

$$E = \frac{(1 + g_I W_{II}) \cdot I + g_I \Theta_I}{g_I W_{IE}} \tag{2.14b}$$

These are the excitation and inhibition nullclines, respectively, and are plotted in Fig. 2.2. In order to have a stable Up state, these two nullclines must intersect at nonzero values of E and I, which is possible under the condition that

$$\Theta_I \geq \frac{g_E W_{IE}}{g_E W_{EE} - g_E W_{EA} W_{AE} - 1} \Theta_E \tag{2.15a}$$

$$g_E \leq \frac{1 + g_I W_{II}}{W_{EE}(1 + g_I W_{II}) - g_I W_E W_{IE}} \tag{2.15b}$$

These conditions are satisfied by our choice of parameters, and ensure that the excitation nullcline is steeper than the inhibition nullcline but has a smaller E-intercept, thus ensuring an intersection. We identify this intersection with the neurological Up state, where both excitatory and inhibitory populations exhibit sustained firing. Its coordinates are

$$E = \frac{W_{EI}\Theta_I - \left[W_{II} + \frac{1}{g_I}\right] \cdot \Theta_E}{W_{EI} W_{IE} - \left[W_{EE} - \frac{1}{g_E} - W_{EA} W_{AE}\right] \cdot \left[W_{II} + \frac{1}{g_I}\right]} \tag{2.16a}$$

$$I = \frac{\left[W_{EE} - \frac{1}{g_E} - W_{EA} W_{AE}\right] \cdot \Theta_I - W_{IE}\Theta_E}{W_{EI} W_{IE} - \left[W_{EE} - \frac{1}{g_E} - W_{EA} W_{AE}\right] \cdot \left[W_{II} + \frac{1}{g_I}\right]} \tag{2.16b}$$

We identify this fixed point with the "Up" state, when both excitatory and inhibitory

populations are firing in a sustained fashion. Finally, there is a third fixed point at

$$E = 0 \tag{2.17a}$$

$$I = \frac{g_E(W_{EA}A^* + \Theta_E)}{g_E W_{EE} - 1} \tag{2.17b}$$

2.3.1 Linear Stability Analysis

If we were to freeze the adaptation level at some particular value A^* and track the fate of the network that starts at arbitrary points on the $E - I$ plane, we will find that every network ends up in either the Up or the Down state (Fig 2.3). The third fixed point, identified by Eq. 2.17, lies exactly on the separatrix, which marks the boundary between the two regions of stability.

The local stability of the Up state can be found by linearizing Eq. 2.12 about the Up state fixed point, found in Eq. 2.16 [123]. If the eigenvalues of the matrix coefficients have a negative real part, the fluctuations from that fixed point will exponentially decrease with time. For our 2D coefficient matrix, this is equivalent to imposing the condition that the determinant of the coefficients matrix is positive and the trace is negative. These conditions yield the following relations between connectivity, time-scale, and gain:

$$\left[W_{II} + \frac{1}{g_I}\right] \cdot \left[W_{EE} + \frac{1}{g_E}\right] \leq W_{EI}W_{IE} \tag{2.18a}$$

$$\tau_I \cdot (g_E W_E E + 1) \leq \tau_E \cdot (g_I W_{II} + 1) \tag{2.18b}$$

These conditions are satisfied by our choice of parameters.

2.3.2 Oscillation via Adaptation

The global stability of each fixed point is inversely related to the distance of the fixed point from the unstable separatrix. The closer each stable fixed point (the Up or Down state) is to the separatrix, the less relatively stable that fixed point becomes, since random noise has a higher chance of kicking the network over the boundary. Notably, the variable A^* is

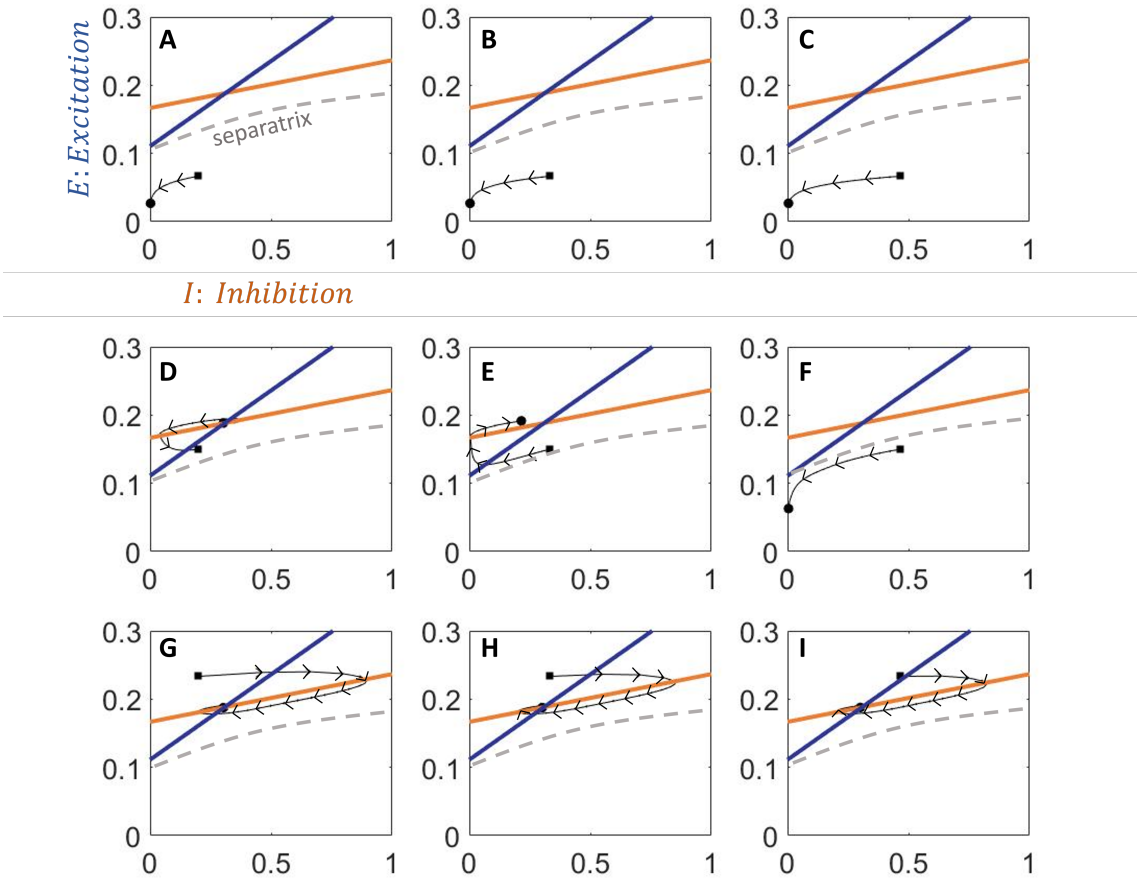

Figure 2.3: The mean field equations define an attractor landscape in the $E-I$ coordinate plane. The mean field model defines two discrete attractors in the $E-I$ coordinate plane. Here we trace the evolution of a single network in the (E, I) coordinate plane from various initial conditions (denoted by the black square) to the final condition (denoted by the circle) in the absence of noise and for fixed adaptation level ($\alpha = 0.5$). The excitation and inhibition null clines are depicted (solid colored lines) along with the separatrix (dotted line). Conditions A,B,C, and F end in the 'Down' state fixed point, while the others end in the 'Up' state fixed point.

simply an additive constant to the excitation nullcline, the dynamics of which determines the positions of intersection for both the stable Up state as well as the separatrix (See Fig. 2.4). As the network remains in the Up state, the adaptation variable increases, effectively shifting the excitation nullcline up. This not only decreases the overall firing rate in the Up state by shifting the fixed point, it also stabilizes the Up state by bringing the separatrix closer to the Up state. A kick from random noise eventually forces the network to transition into the down state. Here, adaptation recovers back to zero, shifting the excitation nullcline down, thereby bringing the separatrix closer to the Down state fixed point; eventually, a noisy kick forces the network into the Up state, where the cycle repeats.

2.4 Coupled Networks

A minimal mean field network supporting UDS has only three crucial, and biologically well-established ingredients: excitation, inhibition, and the adaptation of excitation (but not inhibition). We constructed a mean field theory of two cortical regions, each with its own recurrently connected inhibitory and excitatory populations, as in Fig. 2.2. In isolation, each network exhibits transitions between Up and Down states that are the stable fixed points of the dynamical system of equations. Their stability is inversely related to their distance from the separatrix, a line which defines the boundary between the basins of attraction for each fixed point. The changing, activity-dependent adaptation translates the excitatory nullcline, thereby influencing the relative stability of each state. In this framework, growing adaptation governs the transition from the Up to Down state, while external drive and a falling adaptation governs the transition from Down to Up. Underlying gaussian noise gives the network a "temperature," preventing it from stagnating in a particular state for arbitrarily long time periods. One can use the physical analogy of pendula swinging between two possible states, with adaptation determining the frequency of oscillation (Fig 2.5). For simplicity, quantitative falsifiability, and based on available observations, we assumed that all internal parameters except the recurrent excitation strength W_{EE} are identical across the afferent and efferent networks.

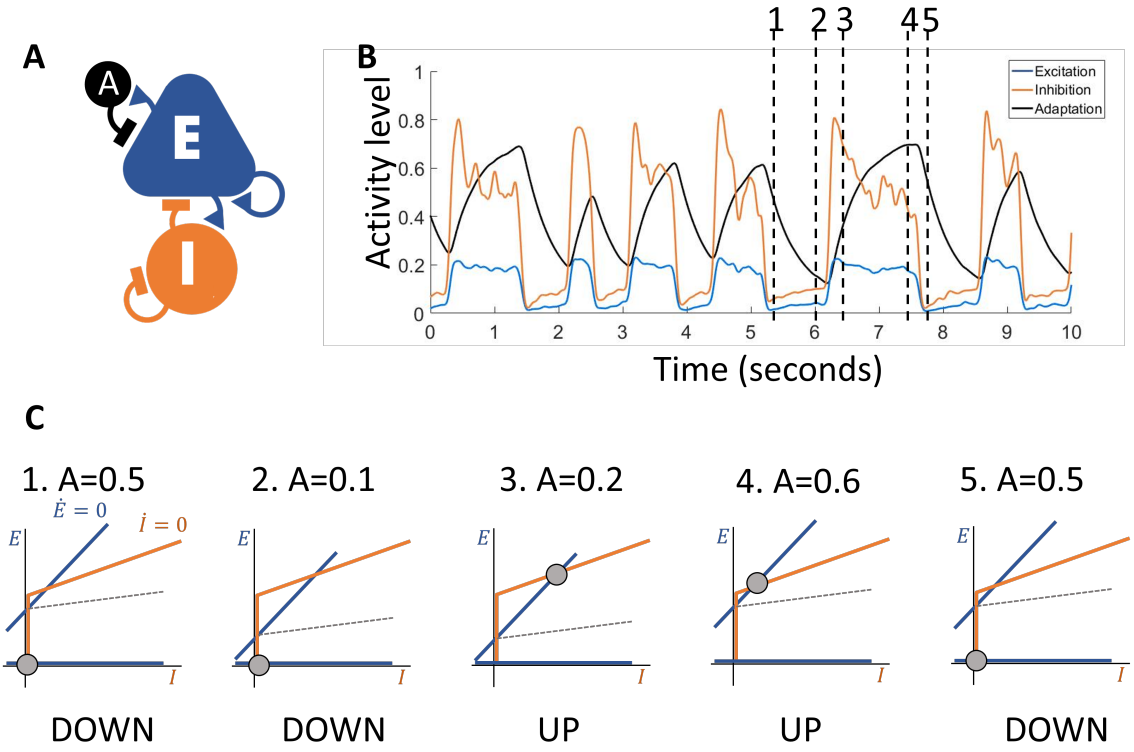

Figure 2.4: A)The Excitation(E)-Inhibition(I)-Adaptation(A) model. B) A sample trace of E, I, and A. C) The time-evolution of the network for one complete UDS cycle (time points in B) can be visualized on the E-I phase space. Nullclines for the E and I variables are plotted in blue and orange, respectively, and denote where the time derivative for that particular variable (E ,I) is zero. Intersections of the nullclines denote equilibrium points where both $\dot{E} == 0$ and $\dot{I} == 0$. There are two stable points, corresponding to the Up state (E,I¿0) and the Down state (E,I=0). These two attractor points form basins of attraction in the E-I plane, with a separatrix (dashed line) denoting the boundary. Under noise, the relative stability of each point is inversely proportional to its distance from this separatrix. An increase in α corresponds to a upwards translation of the E nullcline, making the Up state less stable; a decrease in α corresponds to a downward shift, making the Down state less stable.

2.4.1 Variability of Network Activity during UDS

Further, the afferent network provides a weak excitatory input W_{EXT} into the excitatory population of the efferent network (Fig 2.5). We use W_{EXT} to refer to this synaptic weight from the afferent to the efferent network and W_{INT} to refer to the internal excitatory-excitatory weight in the efferent network (W_{EE} in all equations so far). Effectively, this means that for the efferent network there is an external input into the excitatory population

$$i_E(t) = W_{EXT}(E_A(t) * Z) \tag{2.19}$$

where $E_A(t)$ is the activity of the excitatory population in the afferent network, and Z denotes the fluctuations in the network activity, modeled by an Orstein-Uhlenbeck process centered at 1 and with standard deviation 0.3. Without this noise term Z, the UDS of the afferent network would be a simple square wave, since the 'Up' and 'Down' state fixed points are rigid and show little variation from one UDS cycle to another. This is not biologically realistic, since real networks show considerable variability in activity during UDS (See Fig. 2.6). If the connection strength W_{EXT} between the afferent and efferent excitatory populations is sufficiently strong, the two networks UDS oscillations phase lock, as the transitions between states in the efferent network are no longer due to independent noise but the timed increase and decrease in input coming from the afferent network. Similar to previous results, the connection strength W_{EXT} must be about an order of magnitude smaller than the internal connections W_{INT} in order to show desynchronization [117].

2.4.2 Persistent Activity and Inactivity

What happens when both networks are in the Up state and the afferent input transitions into the Down state? This cuts off afferent input W_{EXT}, immediately shifting the efferent excitation nullcline to the left, thereby destabilizing the efferent Up state. The efferent network can either remain in the Up state through its own recurrent excitation or follow the afferent and transition into the Down state. Instances when the efferent remains in the Up state are termed "spontaneous persistent activity (SPA)" (Fig. 2.7). It follows from

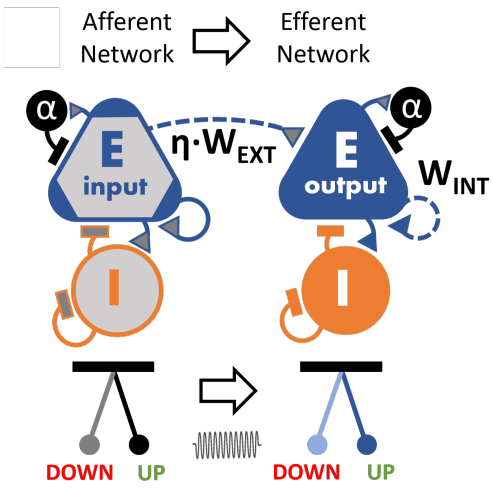

Figure 2.5: The coupled afferent-efferent network. To distinguish between afferent and efferent internal excitation W_{EE}, we refer to the efferent network internal recurrent excitation as W_{INT} for the remainder of this dissertation. There is an additional afferent current being fed to the efferent network. Both networks can sustain UDS on their own, like two coupled pendula. The external connection can be imagined as a unidirectional spring

the stability arguments outlined earlier that by increasing the distance between the Up state fixed point and the separatrix, one can increase the stability of the Up state, thereby increasing the probability that the network will display SPA. If we refer to the excitation nullcline equation [Eq. 2.14], we see that increasing W_{INT} (i.e. W_{EE} in earlier equations) results in the downward scaling of the nullcline: the Up state fixed point shifts to the right, and the unstable fixed point shifts downward. Combined, this has the effect of increasing the stability of the Up state, thus leading to higher probability of SPA.

The converse scenario applies for the Down state, where both networks are in the Down state and the afferent transitions into the Up state. This suddenly increases the input, shifting the excitation nullcline down, destabilizing the Down state. The efferent network can either follow into the Up state or remain in the Down state; the latter case we term "spontaneous persistent inactivity" (SPI: Fig 2.7). The size of downward shift due to the incoming current from the W_{EXT} synapse has a direct consequence on the stability of the Down state: the larger the weight, the more the shift, and thus the more destabilized the DOWN state becomes. Thus, decreasing the synaptic weight W_{EXT} increases the probabil-

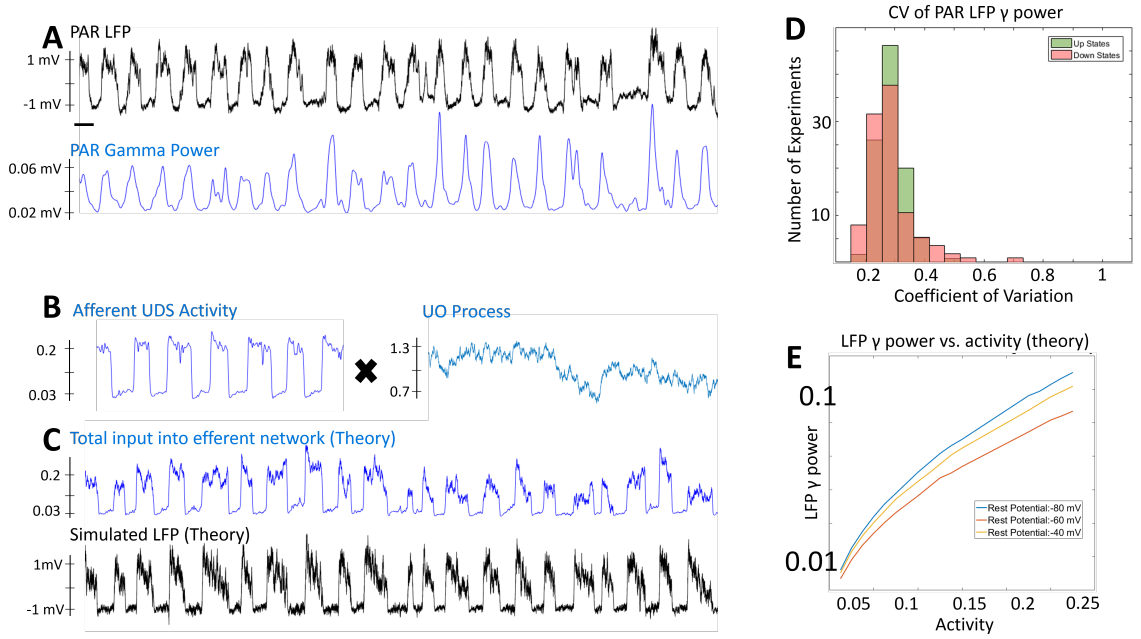

Figure 2.6: A Ornstein-Uhlenbeck process can capture the variability of in vivo gamma activity during UDS. A) In the in vivo experiment, the parietal LFP (black trace) exhibits clear Up-Down states. The filtered gamma power (blue trace: 40-120 Hz) also follows UDS but additionally exhibits fluctuations from one cycle to the next. As a result, some Up states contain higher gamma power than others. The same goes for Down states. B) In our model, the afferent network exhibits Up-Down state oscillations (left). However, the excitation is more regular than in the experiment, since the model equations define the attractor landscape in the E-I coordinate plane, and this landscape is largely unchanged from one UDS cycle to the next. To simulate in vivo variability, we multiply this UDS with a U-O process with mean of 1 and a standard deviation of 0.3. C) The resulting UDS trace shows similar variability compared to the in vivo experiment (the gamma power in A). This is used as the net afferent input into the excitatory population of the efferent network. Simulated LFP (black trace, see Appendix) using poisson-spiking excitatory and inhibitory neurons shows characteristic UDS, similar to experiment, and the variability is not visible, since the low frequency components dominate. D) The coefficient of variation (CV) of the PAR LFP gamma power within the Up states and the Down states is similar in magnitude (Up: 0.29 ± 0.1, Down: 0.31 ± 0.14). Thus, we used a UO process with standard deviation of 0.3. E) Simulated LFP using poisson-spiking excitatory and inhibitory units showed an increase in the gamma band power in the LFP with increasing overall activity level within the network. Depicted are resulting from three different simulations where the neurons are held at three different membrane potential values.

ity of SPI. Indeed, simulations where we modulated both W_{INT} and W_{EXT} confirmed our hypothesis on the dependence of persistent activity and inactivity on these two variables (Fig. 2.8).

2.4.3 Effect of Afferent Fluctuations on SPA and SPI

For our simulations, the size of the afferent network fluctuations, given by the OU process, were chosen such that the standard deviation matches that observed within experiment (Fig. 2.6). To investigate what effect this had on the prevalence of spontaneous persistent activity and inactivity, we reproduced the simulations with different OU process amplitudes (Fig. 2.8). This modulation had virtually no effect on the SPA prevalence, but had huge effects on the SPI; this is likely due to the fact that the Up-Down transition is governed by internal variables, while the Down-Up transition is governed by afferent input. This differential dependence is explored further in the next chapters.

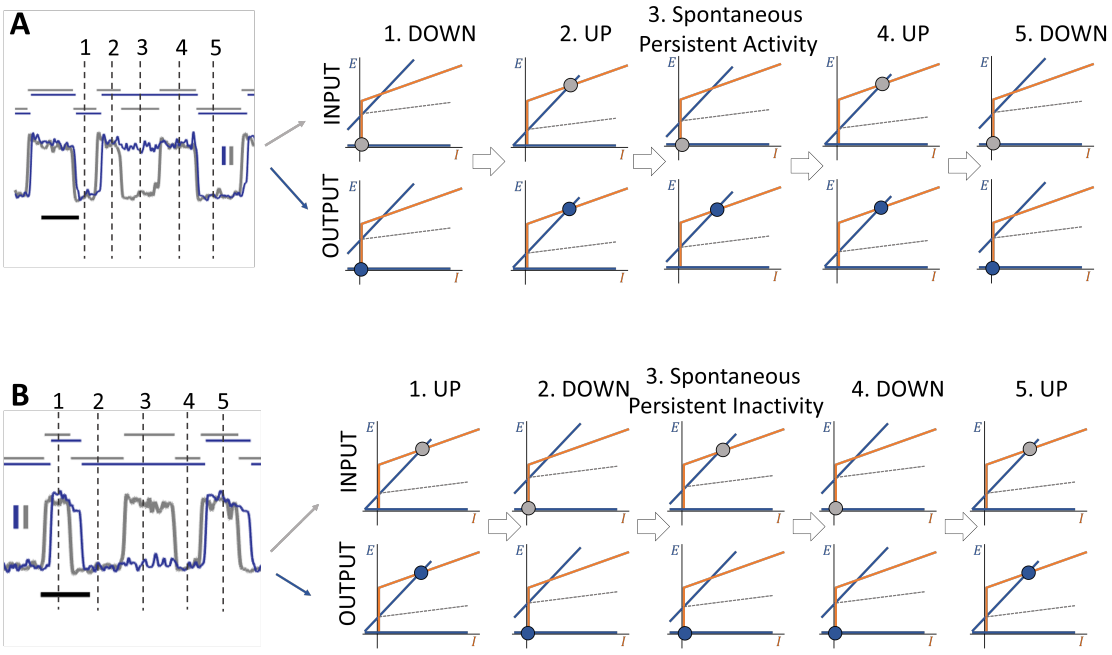

Figure 2.7: SPA and SPI occur when the efferent network persists in its current state and does not follow a state transition in the afferent network. A) Left: SPA occurs when the efferent network (blue) persists in the Up state while the afferent (gray) undergoes a complete Down state. The black scale bar represents 1 sec in time, and the blue and gray scale bars correspond to activity of 0.1. Right: Each network lives in its own E-I coordinate plane. A sudden decrease (from 2-¿3) in the afferent input (an Up-Down transition) translates the efferent output E nullcline upward, destabilizing the Up state and inducing a synchronous transition to the Down state. If the destabilization is not enough (because the decrease was not large, i.e. the afferent Down state has high activity), the efferent network can persist in the Up state on its own, resulting in SPA. B) Similar to A, but showing SPI, which occurs when the efferent network persists in the Down state while the afferent undergoes a complete Up state. A sudden increase in the afferent input (a Down-Up transition) translates the efferent E nullcline downwards, destabilizing the Down state an inducing a transition to the Up state. Again, if the destabilization is not enough (because the afferent Up state has low activity), the efferent network can persist in the Down state, resulting in SPI. Scale bars show time (horizontal black, 1 second) and the amplitude in afferent (vertical gray, 0.1) and efferent (vertical blue, 0.1) network activity.

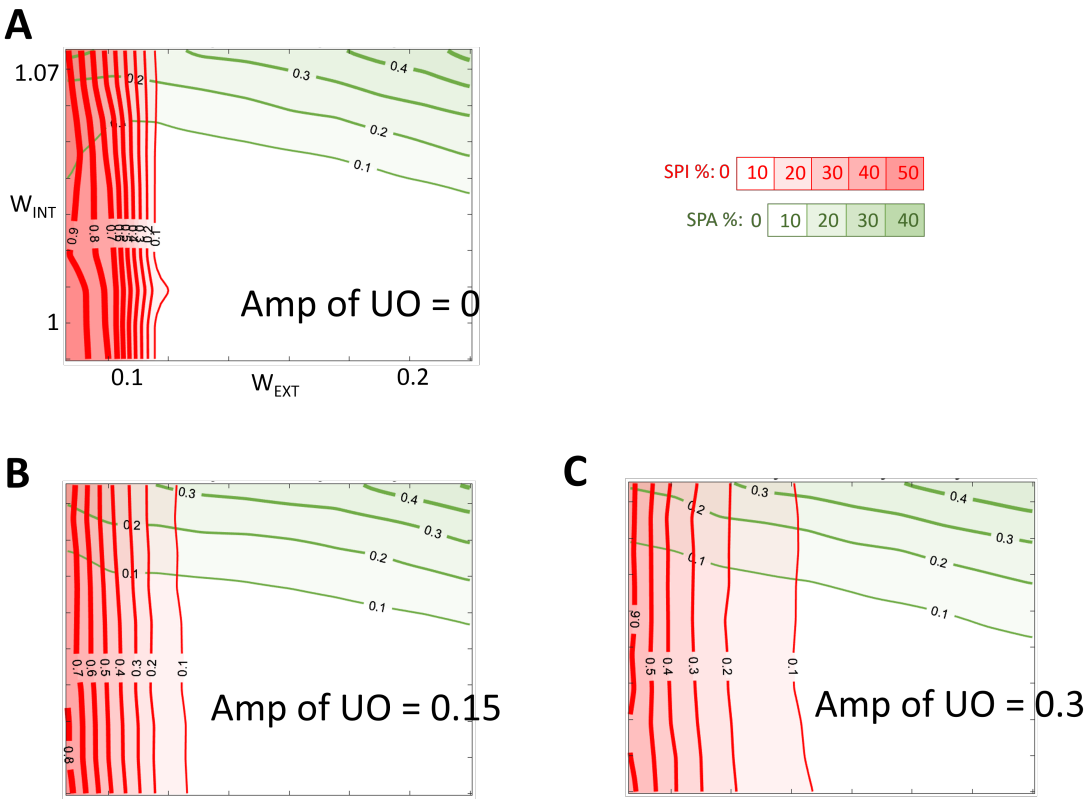

Figure 2.8: The time-averaged prevalence of SPA (green) and SPI (red) observed in a single simulation, created by varying just two variables, W_{EXT} (x-axis) and W_{INT} (y-axis). The contour lines and shaded areas reveal that W_{EXT} has a greater impact on SPA (nearly horizontal green lines), whereas W_{INT} has a greater impact on SPI (nearly vertical red lines). A) In the absence of a UO process, the model still exhibits SPA and SPI. As the UO process variability is increased (B-C), SPI is exhibited by efferent networks with higher W_{EXT}. The variance of the UO process has little effect on the amount of SPA exhibited by the efferent network.

Chapter 3

Persistent Activity and Inactivity in Entorhinal Cortex Layer 3 *in vivo*

Interactions between large brain networks govern all cognition. A mechanistic understanding of these interactions is a major challenge. In the previous chapter, we outlined a simple, analytically tractable, mean field theory of network interactions during the 'Up-Down' state oscillation (UDS). The theory predicts new phenomena: spontaneous persistent activity (SPA) and inactivity (SPI). In this chapter, we confirm these predictions *in vivo* using simultaneously recorded parietal cortical local field potential (LFP) and the membrane potential (V_m) of identified excitatory neurons from several brain areas *in vivo*, especially from layer 3 of the medial (MECIII) and lateral entorhinal cortex (LECIII), which show SPA and SPI. Further, the theory reproduces quantitatively, not just qualitatively, several *in vivo* features, on average and on a cell-by-cell basis using just two variables. We show that the strength of internal excitation within the entorhinal cortex mediates SPA, and the strength of afferent cortical input mediates SPI. The theory predicts, and the experiments confirm, that SPA and SPI are quantized by cortical UDS and result from a nonlinear amplification of small fluctuations in afferent cortical gamma power. Our results further suggest that internal excitation within MECIII is greater than within LECIII. These convergent, theory-experiment results provide a novel way to generate persistent activity, which has been implicated in a wide range of conditions, and persistent inactivity, and help to understand the rich dynamics of interactions between large networks of neurons *in vivo*.

3.1 Introduction and Motivation

Cognition involves interactions between several neural networks, each network containing millions of neurons, each neuron in turn characterized by many microscopic parameters, resulting in billions of parameters for a detailed biological network. But, to develop an analytically tractable theory of the fundamental operating principles, one must use only a few salient variables to both reproduce experimental observations and propose novel predictions that can be tested in simplified experimental preparations that capture the essence. This is analogous to using frictionless inclined planes or artificial vacuums to study the laws of motion in physics. In the previous chapter, we developed a theory of spontaneous persistent activity, a phenomenon implicated in several cognitive functions. Here, we verify the theory *in vivo* during internally generated activity in the absence of external sensory stimuli.

During quiescence, deep sleep, under anesthesia, and in vitro, local neural networks from many brain areas, including cortex, show synchronous, rhythmic activity termed delta oscillations, non-REM sleep oscillations, slow wave sleep (SWS) etc.[41, 124, 125]. The LFP shows rapid transitions between periods of elevated activity (the Up state) and silence (the Down state). The V_m of individual neurons exhibit synchronous UDS oscillations with depolarization (Up) and hyperpolarization (Down) states. The UDS are ubiquitously found across species and experimental preparations, and are considered the default activity of many networks [50, 55, 59, 64]. Several studies have suggested that the interactions between cortical regions during UDS are crucial for memory consolidation [26, 93, 126–128]. Impairment of UDS causes learning and memory deficits, while UDS enhancement leads to improvement [129].

Although most cortical areas show synchronous UDS oscillations [93], recent studies have shown that *in vivo* only MECIII, but not LECIII, pyramidal neurons show persistent activity during UDS: events where the neuron's V_m spontaneously persists in the depolarized Up state while the afferent neocortical areas transition to the Down state [94]. The SPA here notably differs from some studies that refer to singular Up states within an isolated network as themselves forms of persistent activity [91]. Depolarizing current injections do not elicit

SPA within MECIII neurons, implicating network rather than intracellular mechanisms. Network models for SPA involve thousands of spiking neurons, and thus tens of thousands of differential equations [130, 131]. This approach trades predictive power for biological realism, as the number of variables are far greater than the number of observables. Mean field models involving few parameters are extensively used to understand UDS dynamics within a local population of neurons [115, 117, 119, 130], but have not been employed to understand large interacting networks and cannot account for major experimental findings.

We found that a simple, mean-field model involving interacting networks of excitation-inhibition can capture the dynamics of SPA during UDS. Our theory also proposed a new phenomenon: spontaneous persistent inactivity (SPI). The theory is detailed in the previous chapter. To test the theory quantitatively, we used the *in vivo* cortico-entorhinal circuit as our model system. Anatomically, the parietal cortex (PAR), a part of the neocortex, serves as an afferent source of input to other neocortical regions, like the frontal (FRO) and prefrontal (PRE) cortices, and to further paleocortical regions like the entorhinal cortex (EC) [132–134]. We thus used the LFP, indicative of average neural activity within a brain region, in the PAR cortex as the afferent reference. Simultaneously, we did whole-cell V_m measurements from anatomically identified pyramidal neurons in the afferent PAR and the efferent FRO, PRE, and EC; as the spontaneous activity of single neurons is tightly linked to the cortical networks in which they are embedded, this allowed us to probe the activity of localized networks within each target region [14]. Both FRO and PRE cortices are implicated in attention, working memory, and memory consolidation [135–140]. Within the EC, the medial (MEC) and lateral (LEC) subdivisions are anatomically and functionally distinct: the MEC contains spatially selective "grid cells" [141], while the LEC is thought to encode objects or experienced time [142, 143]. We focused in particular on the EC layer 3 regions, since MECIII neurons are a major source of input to the hippocampus, show SPA *in vivo*, and are crucial in the generation and maintenance of UDS in the MEC [94, 144].

We detected *in vivo* SPA in MECIII and SPI in both MECIII and LECIII, but not in FRO, PRE, or PAR. Further analysis of these events showed clear agreement with theoretical predictions, as both SPA and SPI showed dependence on neocortical input, were

quantized by neocortical UDS, and resulted in a non-linear amplification of afferent neocortical activity. Further, differences in SPA and SPI across cells could be attributed to differences in excitatory connectivity between and within brain regions. The number of experimental observations explained by our theory are greater than the number of parameters we varied, demonstrating its predictive power. To our knowledge, our study is the first to predict theoretically and detect experimentally the novel phenomena of persistent inactivity, and show that both SPA and SPI not only co-occur but are the result of common network interaction principles.

3.2 The*in vivo* experiment

Details of the experimental procedures are outlined in the Appendix, and are briefly described here. Our theory involves coupled networks, where each network consists of recurrently connected excitatory and inhibitory populations and each network is capable of sustaining its own UDS oscillation. To test the theory quantitatively, we used the *in vivo* cortico-entorhinal circuit as our model system. Mice were lightly anesthetized with urethane to induce robust and steady UDS that were synchronous across the entire neocortex. The local field potential in the parietal cortex (PAR) was measured using a silicon multi-electrode array; this served as our afferent network reference (Fig 3.1). Simultaneously, we did whole-cell V_m measurements from anatomically identified pyramidal neurons in PAR and other neocortical regions like the frontal (FRO) and prefrontal (PRE) cortex and paleocortical regions like the medial and lateral entorhinal cortex, especially layer 3 (MECIII/LECIII).

3.2.1 Detection of UDS, SPA, and SPI

A hidden Markov model was used to classify the data into a binary UDS sequence [145]. Consistent with previous studies, the LFP from PAR and V_m of neurons in the afferent PAR (N=24) and several efferent regions FRO (N=7), PRE (N=13), MECIII (N=57), and LECIII (N=16) showed clear bimodal UDS (Fig 3.2). For subsequent analysis, the amount of SPA (SPI) was defined as the proportion of efferent Up (Down) states which outlasted an

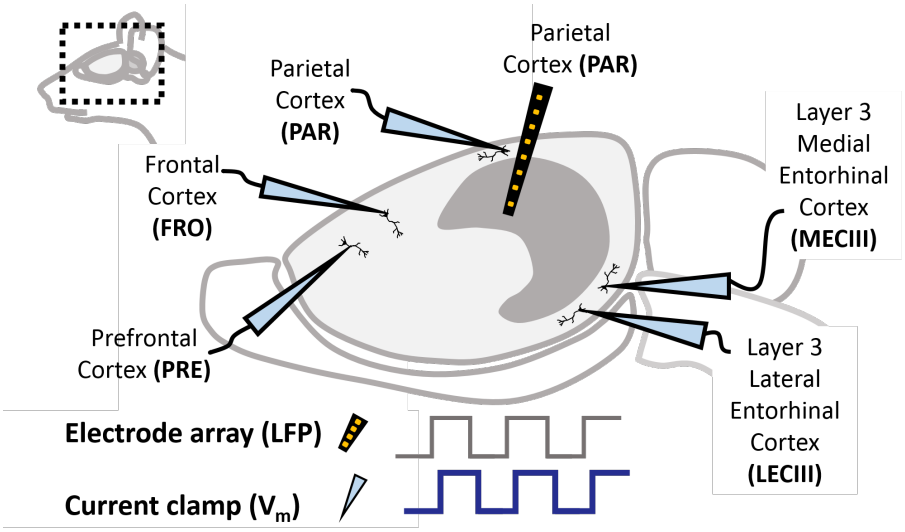

Figure 3.1: Experimental design. Local field potential (LFP) from the parietal cortex was measured using a silicon probe (black). Simultaneously, membrane potential (V_m) was measured using whole-cell patch clamp from an anatomically identified neuron in multiple brain regions.

entire afferent Down (Up) state during an entire experiment. As a first test of the model, we computed the relationship between the PAR LFP and the V_m from PAR pyramidal neurons, which were recorded close by (0.5 mm apart). Since these belong to the same brain region, W_{EXT} is large, and the model predicts complete phase locking, with virtually nonexistent SPA and SPI. This was indeed the case.

We then tested the model, now using FRO and PRE as the efferent. These regions are also in the neocortex, receiving strong inputs from PAR, suggesting large W_{EXT} from afferent PAR [132]. Hence, the model predicted complete UDS synchrony between these areas with virtually no SPA and SPI. This was again confirmed by experiment (Fig 3.3).

Consistent with previous studies, MECIII neurons showed clear instances of SPA, while LECIII neurons did not. In contrast, both LECIII and MECIII neurons showed clear instances of the newly predicted SPI (Fig 3.5). Theory also predicted relative independence of SPA and SPI. Consistently, some MECIII neurons showed both SPA and SPI, only a few seconds apart. Some experiments showed instances of SPA and SPI that were as long as 10 seconds long (Fig 3.4).

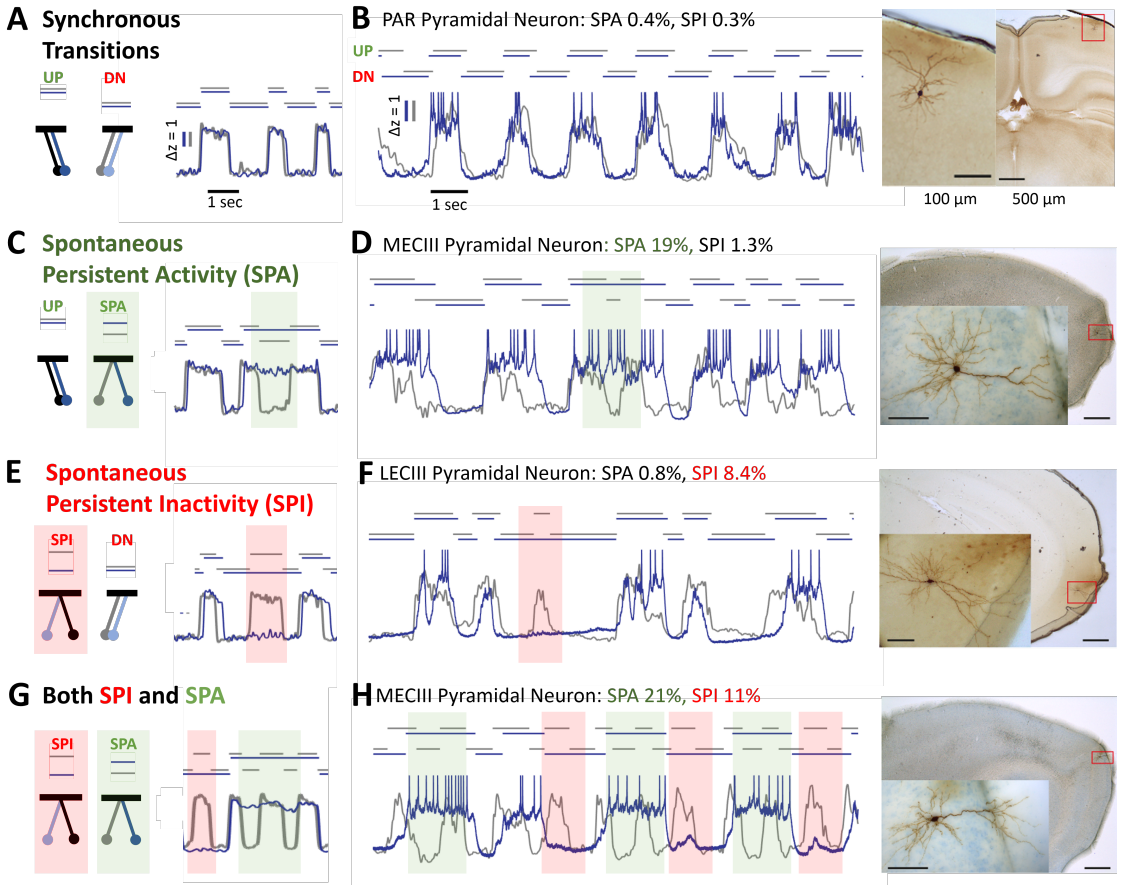

Figure 3.2: Comparison between model output (left) and experimental results. A) The model can reproduce synchronized UDS activity in the two networks (afferent in gray, efferent in blue). The same scale bars for time and amplitude (in z-score) are used for (A-H). B) *In vivo* data matched to simulations of simultaneous UDS in afferent PAR LFP (gray) and efferent V_m (blue), with histological reconstructions (right) of brain region and the patched cell (insets). Here, a PAR neuron's V_m is phase-locked to the PAR LFP, matching theory in (A). Action potentials have been truncated for clarity. The same scale bars for time (1 second), amplitude (z-scores), and length scale (100 μm, 500 μm) are used for all traces and histology. C) Increasing efferent W_{INT} leads to spontaneous persistent activity (SPA, green box), when the efferent network persists in the Up state even when the afferent makes a transition to the Down state. D) Clear SPA (green box) in the V_m of an MECIII pyramidal neuron, matching (C). E) Decreasing W_EXT leads to spontaneous persistent inactivity (SPI, red box), when the efferent network persists in the Down state while the afferent makes a transition to Up state. F) Clear SPI (red box) in the V_m of an LECIII pyramidal neuron, matching (E). G) The same network can exhibit SPA and SPI at different times. H) Both SPA and SPI at different times exhibited by the same MECIII pyramidal neuron, similar to (G).

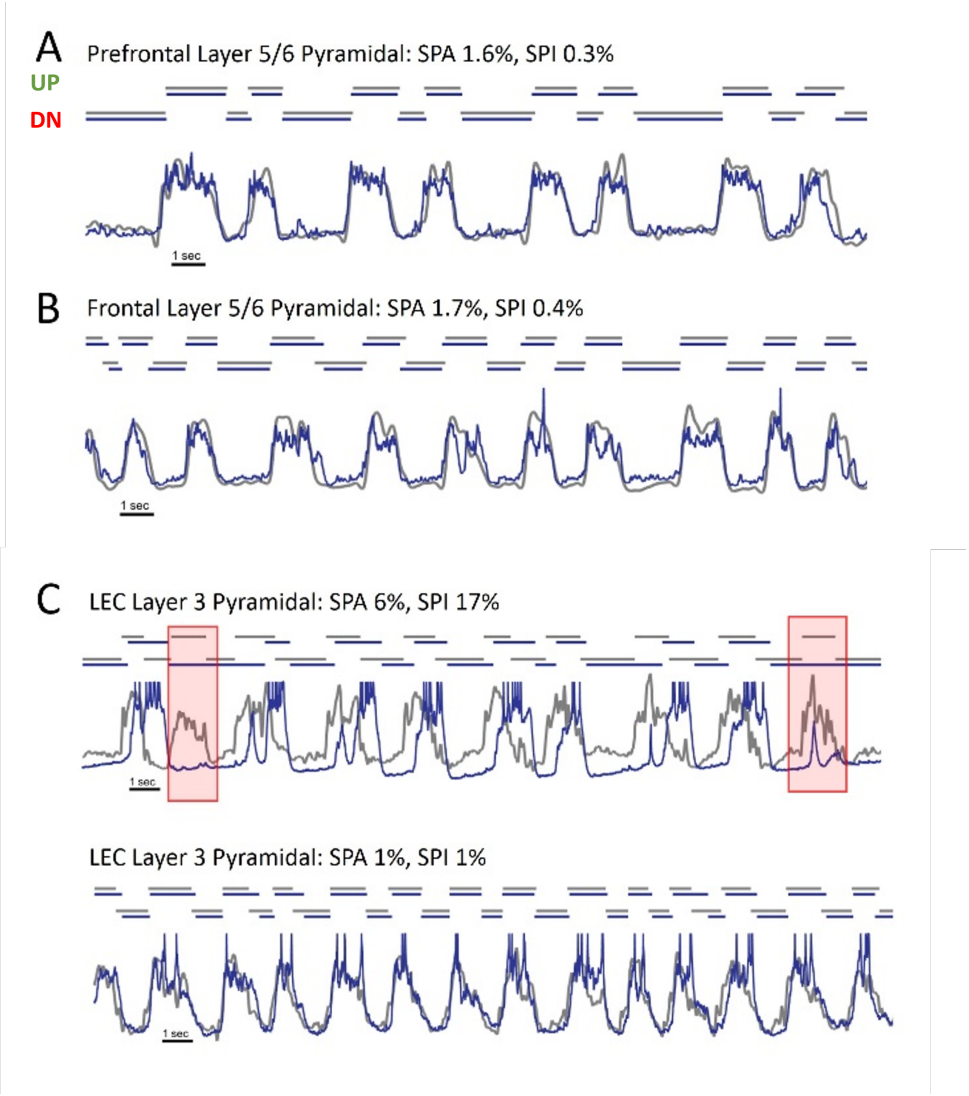

Figure 3.3: Additional examples of experimental traces A) Example trace of the V_m (blue) of a prefrontal cortex layer 5/6 pyramidal neuron, along with simultaneously recorded parietal LFP (gray). Black scale bar at the bottom shows one second time interval, and the detected Up-Down state sequence is shown above for each trace. B) Example trace from frontal cortex layer 5/6 pyramidal neuron. Both neurons (in A and B) exhibited phase-locked UDS to the parietal cortex LFP. C) Two examples of LECIII pyramidal neurons, one showing heightened levels of persistent inactivity (top, red boxes), and the other showing complete phase locking (bottom).

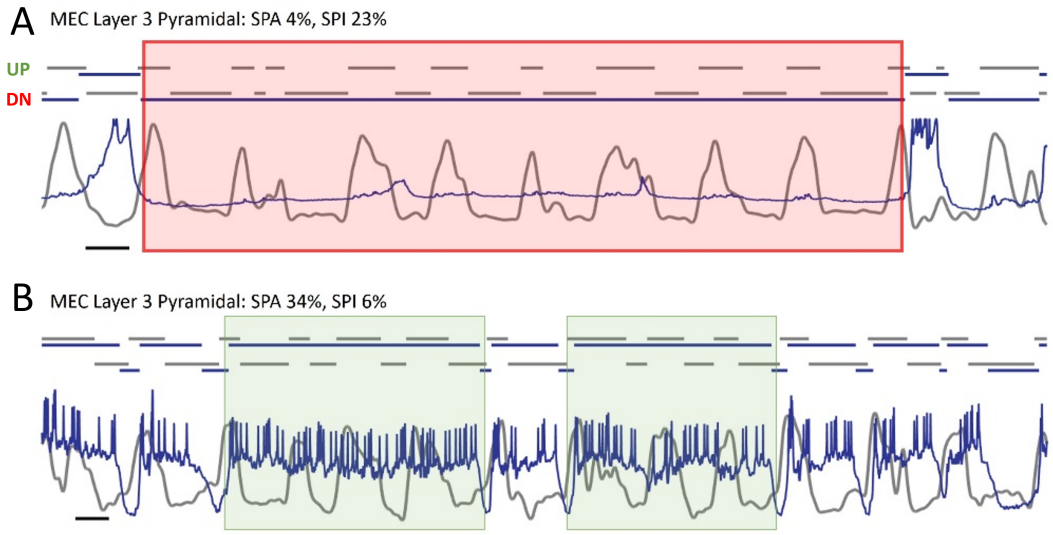

Figure 3.4: Additional examples of experimental traces. A) An example of MECIII neuron showing extremely long persistent inactivity state (red box), lasting over 17.2 seconds. B) An example of MECIII cell showing extremely long persistent activity states (green boxes), lasting 8 and 6 seconds.

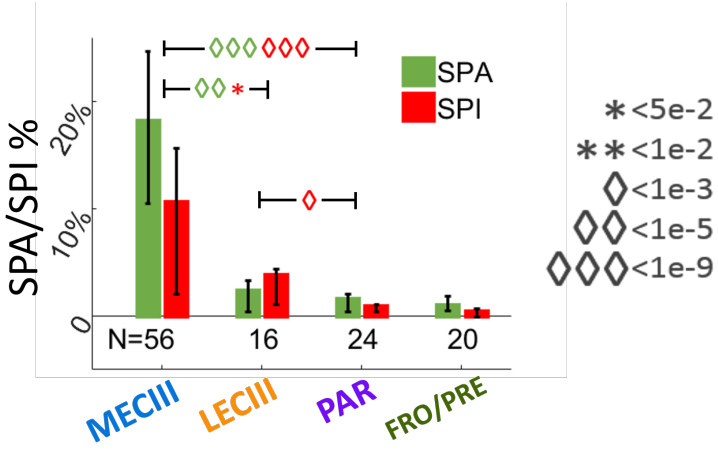

Figure 3.5: Prevalence of SPA/SPI showed significant variation as a function of brain region, with MECIII showing the highest SPA (18.5±7.5%) as well as SPI (10.2±5.3%). LECIII showed diminished SPA (3.3±2.4%) and SPI (5.9±3.1%), while PAR (SPA: 2.6±1.8%, SPI: 1.9±0.7%) and FRO/PRE (SPA: 2.0±0.9%, SPI: 1.3±0.5%) showed even smaller levels. MECIII SPA and SPI levels were both significantly different from both LECIII levels (SPA: $p < 10^{-5}$, SPI: $p < 0.05$) and PAR levels (SPA: $p < 10^{-9}$, SPI: $p < 10^{-9}$), while for LECIII only the SPI level was significantly larger from PAR ($p < 10^{-5}$). Error bars represent ±1 s.t.d, and number of experiments within each brain region is indicated under each bar.

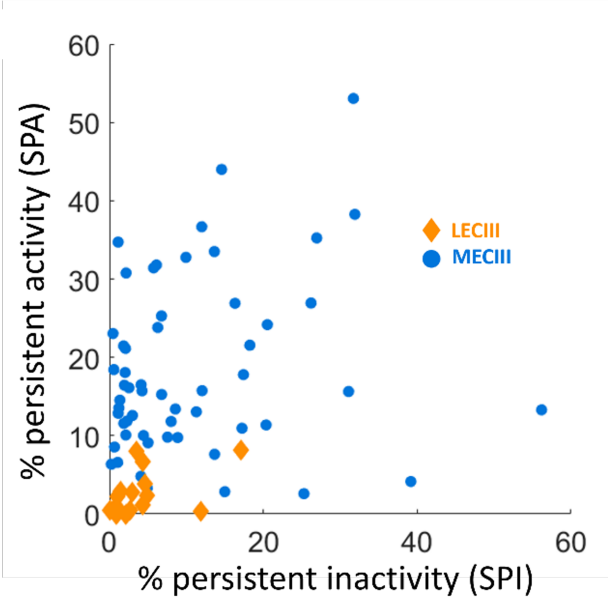

Figure 3.6: The amount of SPA in an entorhinal cell was not significantly correlated with the amount of SPI. Both MECIII and LECIII cells showed varied levels of SPA and SPI in experiment, but there was no significant correlation between SPA and SPI (MECIII: r=0.18, $p > 10^{-1}$; LECIII: r=0.49, $p > 10^{-1}$).

The levels of SPA and SPI within the population of LECIII and MECIII neurons were not significantly correlated to one another (Fig 3.6), consistent with the idea that these two phenomena are the result of independent network parameters. Finally, SPA/SPI levels were not correlated with the duty cycle and the frequency of PAR UDS, indicating that they were not artifacts of differences in brain states across experiments (Fig 3.7).

3.3 Fitting Experiment and Theory

The properties of SPA and SPI not only varied across brain regions, but even between different neurons from the same region. We hypothesized that all of these differences could arise from just two network parameters: the strength of recurrent excitation in the efferent network (W_{INT}) and the strength of external excitatory input to the efferent network (W_{EXT}). To test this idea, we used a two-step approach. First, we simulated all possible networks in this 2D parameter space by varying only W_{EXT} and W_{INT}, while leaving all

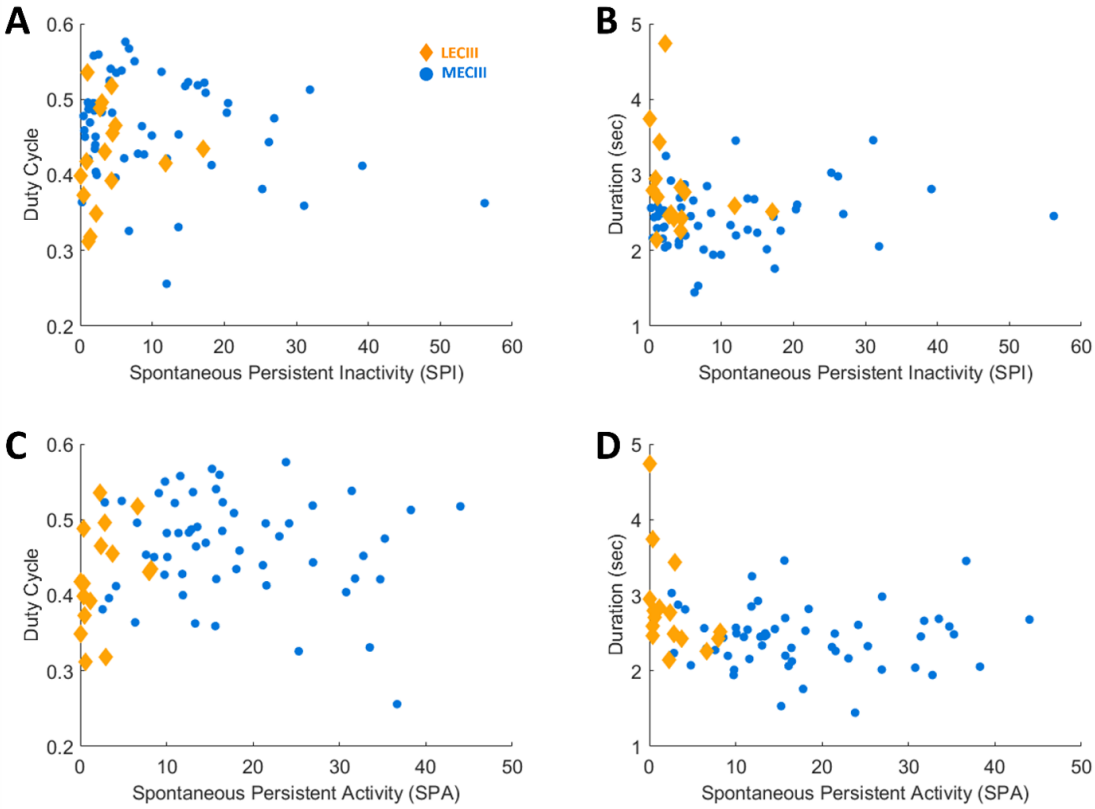

Figure 3.7: The prevalence of SPA or SPI in an experiment was independent of the depth of anesthesia. The depth of anesthesia varies from one experiment to another, and deeper anesthesia produces UDS with longer duration cycles and smaller duty cycle (proportion of the cycle spent in the Up state). Parietal UDS statistics were used to quantify depth of anesthesia of the animal. A) SPI prevalence was not significantly correlated with PAR duty cycle for both LECIII neurons (yellow: r=0.15, $p > 0.1$) and MECIII neurons (blue: r=-0.24, $p > 0.05$). B) SPI was not significantly correlated with mean duration of parietal UDS cycles in the experiment (LECIII: r=-0.27, $p > 0.3$; MECIII: r=0.17, $p > 0.2$). C) Conversely, SPA was not significantly correlated with parietal UDS duty cycle (LECIII: r=0.38, $p > 0.3$; MECIII: r=-0.12, $p > 0.3$) and D) not correlated with mean duration of UDS (LECIII: r=-0.43, $p > 0.05$; MECIII: r=-0.01, $p > 0.9$).

other variables unchanged. Modulating just two free parameters yielded networks with a wide range of both SPA and SPI. Thus, we could estimate the two crucial network variables, W_{INT} and W_{EXT}, by simply computing the amount of SPA/SPI observed experimentally (Fig 3.8). Crucially, we did not match any other properties of SPA and SPI between the model and data. Overall, regions in this (W_{EXT}, W_{INT}) plane with smaller values of W_{EXT} corresponded with higher levels of SPI, and those with larger values of W_{INT} corresponded with higher SPA. While SPA and SPI prevalence across neurons was uncorrelated, the fitted values of W_{INT} and W_{EXT} were significantly negatively correlated, especially for LECIII, indicating differential properties of the networks (Fig 3.9). The two parameter model, thus constrained by experiments, was then used to make several independent, experimentally verifiable predictions, thus providing a large number of quantitative tests of the theory on a cell-by-cell basis.

3.3.1 Differential Connectivity of Cortical Regions

Further, the experimentally constrained model made major predictions about the network connectivity of different brain areas, outlined here and shown in Fig 3.8.

1. Recurrent connectivity W_{INT} within MECIII is greater than within LECIII.
2. The external excitatory input W_{EXT} to MECIII is weaker than to LECIII.
3. The recurrent connectivity W_{INT} within frontal and parietal cortices is weaker than in MECIII.
4. Parietal input W_{EXT} to frontal and prefrontal cortices is greater than to MECIII and LECIII.

There is evidence for some of these predictions in previous experimental work, while others are completely novel and could guide future work. Details are included in the Discussion section of this chapter.

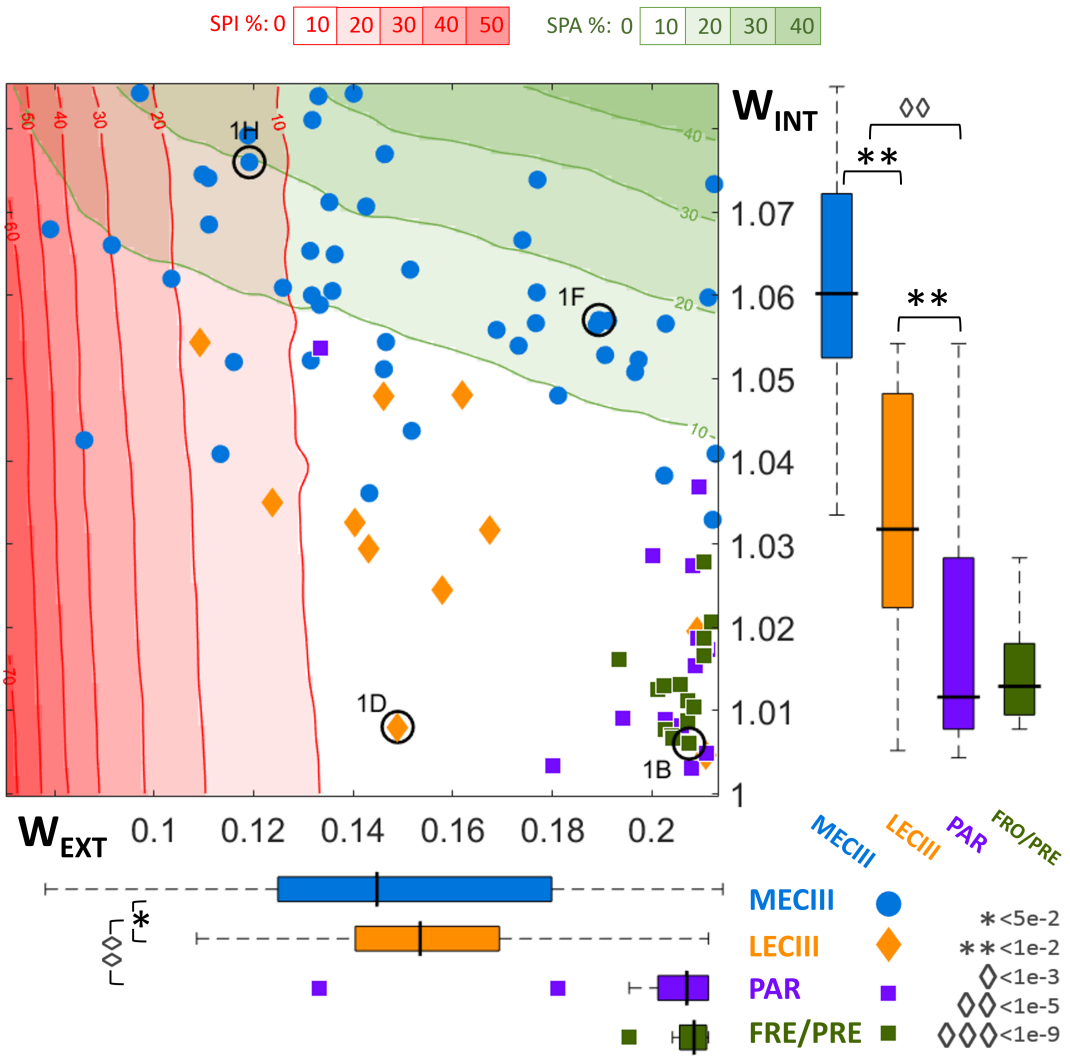

Figure 3.8: The time-averaged prevalence of SPA% (green) and SPI% (red) observed in a single cell were reproduced in the model by varying just two variables, W_{EXT} (x-axis) and W_{INT} (y-axis). The contour lines and shaded areas reveal that W_{EXT} has a greater impact on SPA (nearly horizontal green lines), whereas W_{INT} has a greater impact on SPI (nearly vertical red lines). Each cell is represented by a point (blue circle MECIII, yellow diamond LECIII, violet square parietal (PAR), green square prefrontal/frontal cortices(FRO/PRE)). Locations of the examples cells used in Fig1 are highlighted by the black circles. Bottom: The fitting reveals that W_{EXT} is the largest for FRO/PRE (green, 0.21 $\pm$ 0.005) and PAR (violet, 0.21 $\pm$ 0.01), smaller for LECIII (yellow, 0.15 $\pm$ 0.02), and smallest for MECIII (blue, 0.14 $\pm$ 0.03). W_{EXT} to MECIII was significantly smaller than to LECIII ($p< 0.05$), and both were significantly smaller than to PAR ($p< 10^{-5}$). Box limits and black bar represents middle 50% of data and median, and dotted lines extend to the range, except outliers. Right: The fitting predicts that W_{INT} is the largest for MECIII (1.06 $\pm$ 0.01), smaller for LECIII (1.03 $\pm$ 0.015), and even smaller for PAR (1.01 $\pm$ 0.02) and FRO/PRE (1.01 $\pm$ 0.005). MECIII W_{INT} was significantly larger than LECIII W_{INT} ($p< 10^{-2}$), and both were larger than PAR W_{INT} ($p< 10^{-2}$).

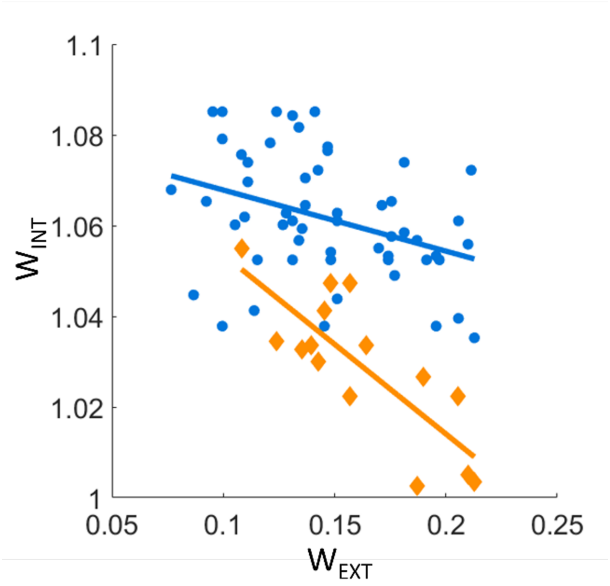

Figure 3.9: Fitted parameters W_{INT} and W_{EXT} were significantly anti-correlated within both MECIII (r=-0.36, p<10-2) and LECIII (r=-0.80, p<10-3).

3.3.2 An alternative fitting strategy

The $W_{EXT} - W_{INT}$ parameter space was divided into a 100-100 grid, and each point was taken as the input into 5 independent simulations of length 1000s. For each experiment, we calculated the "distance" between the experimental data SPA/SPI level and each simulated SPA/SPI level. Let $\Phi_{SPA/SPI}$ denote the proportion of efferent states which were classified as SPA/SPI in the experiment, and $\Psi_{SPA/SPI}$ denote the proportion in a given simulation. The distance between the experiment and any particular simulation is then given by

$$D = \sqrt{(\Phi_{SPA} - \Psi_{SPA})^2 + (\Phi_{SPI} - \Psi_{SPI})^2} \tag{3.1}$$

The simulation with the minimum distance to the experiment was chosen as the best fit. One could also take Φ and Ψ to denote the proportion of afferent LFP states which were classified as 'skipped' by the efferent network, and use this for the distance metric. Results of this fit are shown in Fig 3.10, and are virtually identical to the procedure used in Fig 3.8 and the rest of the dissertation.

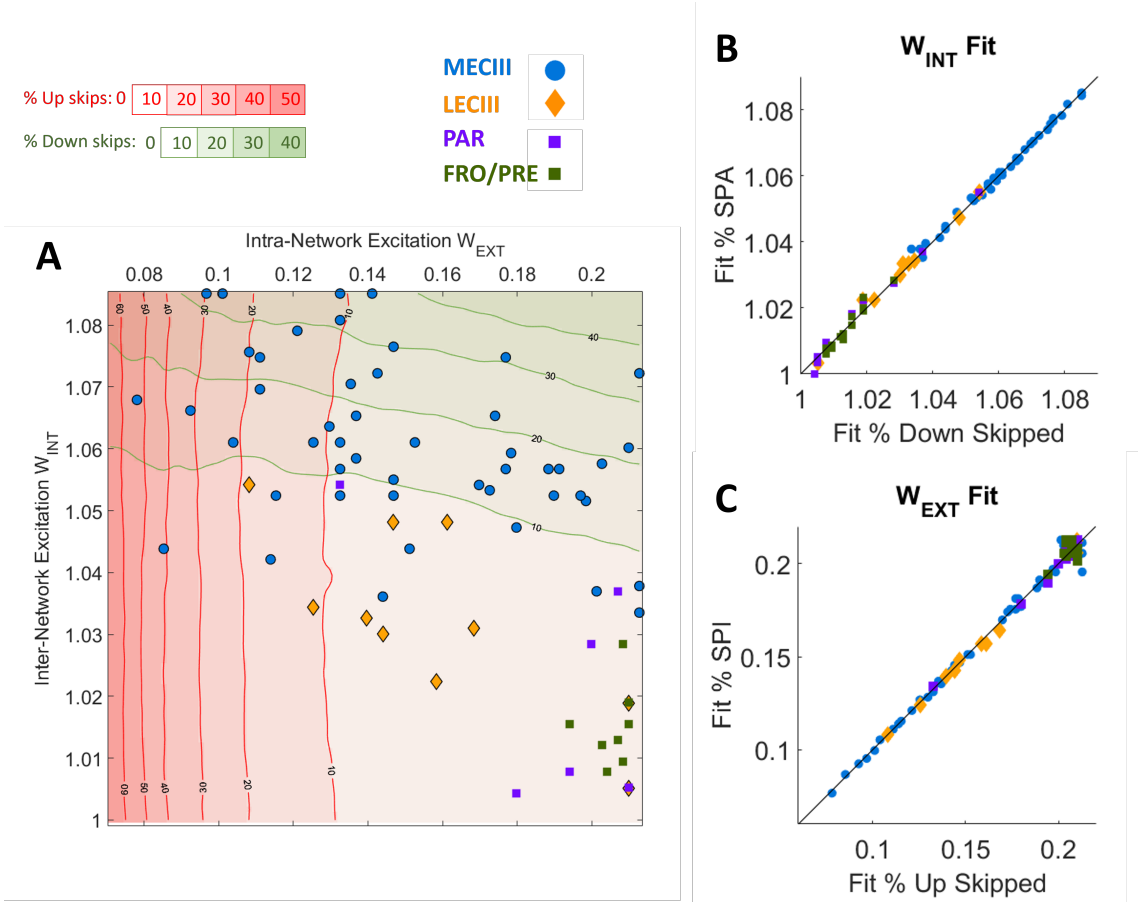

Figure 3.10: Experimental fits to the model were robust over different fitting procedures. In the main text (see Fig 2A), the time-averaged prevalence of SPA and SPI in the efferent states was used to match simulations to the experiment. A) Another method of fitting experimental data to the model is to use the time averaged proportion of afferent states that are "skipped" by the efferent network (skipping afferent Up states leads to SPI, while skipping afferent Down states leads to SPA). Each cell is matched to the simulation space using this metric. The symbols used for each brain region are the same as in Fig 2A. B) Comparing the fits to W_{INT} resulting from this matching scheme (x-axis) to the %SPA/SPI scheme used in the main text (y-axis) reveals that both methods give extremely close values (diagonal line is perfect agreement). C) Comparing the fits to W_{EXT} also shows stark agreement.

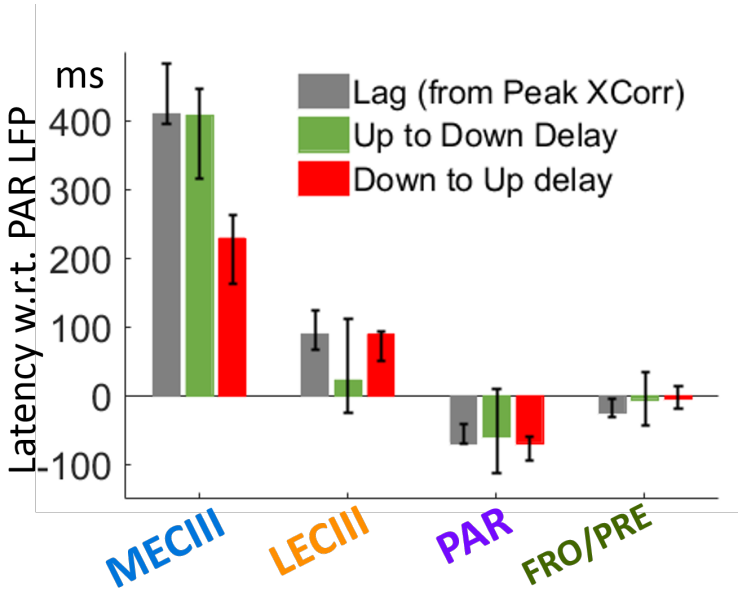

Figure 3.11: The experimentally observed lag between the parietal LFP and efferent MECIII cells was the largest, evidenced by cross-correlation lag (gray, 152 ± 145ms), Up-Down transition latency (green, 401 ± 23ms) and Down-Up latency (red, 223 ± 34ms). The delays for LECIII cells was shorter than those for MECIII cells (xcorr latency 89 ± 22 ms, Up-Down 22 ± 12 ms, and Down-Up 76 ± 13 ms). PAR cells were unique in that they preceded PAR LFP (xcorr latency -54 ± 21 ms, Up-Down -43 ± 34 ms, and Down-Up -58 ± 13 ms).

3.4 Inferred Connectivity predicts Latency between Brain Regions

As a first test to our theory, we investigated the relative timing between networks. If neurons behave like leaky capacitors, the strength of afferent excitatory input should be inversely correlated with the response latency of the efferent network [2, 146]. This was corroborated on a population level *in vivo*, with regions fit to lower values of W_{EXT} having larger latencies to neocortical LFP (Fig 3.11).

3.4.1 The Down-Up transition and W_{EXT}

LECIII cells with greater predicted excitatory input W_{EXT} showed significantly shorter Down-Up transition latency (Fig 3.12). Similar result was found within the population

of MECIII neurons. Further, consistent with model prediction that W_{EXT} from PAR to LECIII is stronger than to MECIII, the population of LECIII neurons showed shorter Down-Up latency than the MECIII population (Fig. 3.12). While W_{EXT} enhances the coupling between the two networks, larger values of W_{INT} make the efferent network more independent of the input. The effect of these competing inputs is state dependent, differentially modulating the efferent Down-Up versus Up-Down transitions. During an afferent Down-Up transition, the efferent network is invariably in the Down state, where recurrent excitation W_{INT} does not contribute. Thus, the latency of the efferent Down-Up transition should be relatively insensitive to W_{INT} but depend strongly on W_{EXT}. This was strongly supported across both LECIII and MECIII populations.

3.4.2 The Up-Down transition and W_{INT}

The situation is reversed for the Up-Down transition, when the efferent network is in the Up state, where recurrent excitation W_{INT} contributes strongly and helps sustain the Up state despite the loss of afferent input, which is in the Down state. Networks with higher W_{INT} have more stable Up states, thereby increasing their "inertia." Thus, the model predicts that that ECIII neurons that have greater predicted W_{INT} should follow the PAR Up-Down transitions with longer latency. This was confirmed for both MECIIII and LECIII. In contrast to Down-Up transitions, the latency of the efferent Up-Down transition should be relatively insensitive to W_{EXT} compared to W_{INT}. This prediction too was strongly supported across individual neurons within MECIII, within LECIII, and across the MECIII vs LECIII ensemble (Fig. 3.12).

These latencies were more correlated with the predicted W_{INT} and W_{EXT} values than with simply the levels of SPA or SPI (Fig 3.12), further supporting the model. Additionally, neurons with greater net excitatory input ($W_{EXT} + W_{INT}$) should have higher firing rate; this was confirmed by experiments, showing greater mean firing rates for MECIII than LECIII, even at the level of individual cells. Further, LECIII neurons' V_m was significantly less depolarized than MECIII neurons (Fig 3.13). The predicted model parameters W_{EXT} and W_{INT} were more strongly correlated with the UDS latencies than the mean firing rates,

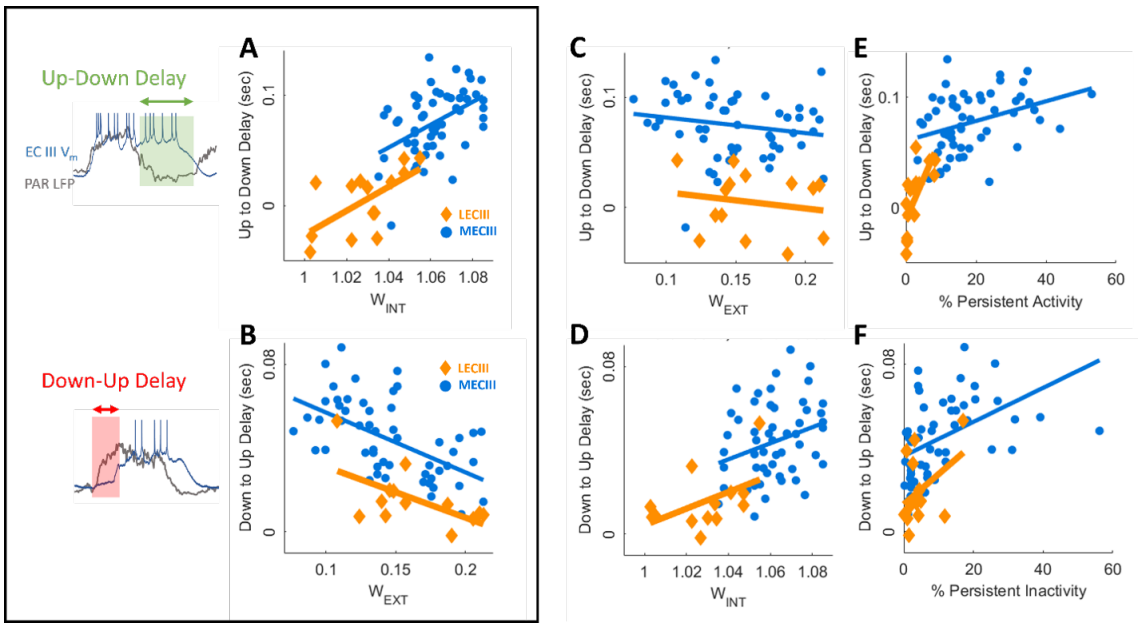

Figure 3.12: Up to Down transition lag between afferent PAR LFP and ECIII V_m is most correlated with recurrent excitation W_{INT}, while the Down to Up transition lag is most correlated with external input strength W¬EXT. A) The internal recurrent excitation W_{INT} increases the stability of efferent network Up state, leading to higher Up-Down delays w.r.t. PAR LFP (MECIII: blue, r=0.47, p$< 10^{-3}$; LECIII: yellow, r=0.63, p$< 10^{-2}$). All delays are reported in units of mean UDS duration. B) W_{EXT} is significantly correlated with the Down to Up Delay (MECIII: r=-0.56, p$< 10^{-5}$; LECIII: yellow, r=-0.60, p$< 10^{-2}$). C) W_{EXT} is negatively correlated with the Up-Down delay, but this is not significant (MECIII: r=-0.17, $p > 10^{-1}$; LECIII: yellow, r=-0.17, $p > 10^{-1}$). D) W_{INT} is positively correlated with the Down-Up delay, but this is significant for the MECIII population (blue, r=0.29, p< 0.05) and not significant for the LECIII population (yellow, r=0.49, $p > 10^{-1}$). E) Previous studies [94] reported a strong correlation between the amount of SPA in a neuron and the Up-Down delay. This is reproduced here. Both MECIII and LECIII populations show significant positive correlation (MECIII: r=0.36, p$< 10^{-2}$; LECIII: yellow, r=0.70, p$< 10^{-2}$). F) Conversely, the amount of SPI in a neuron was correlated with the Down-Up delay. MECIII population showed significant positive correlation (r=0.48, p$< 10^{-3}$), while the LECIII population showed positive but not significant correlation (r=0.42, $p > 10^{-1}$).

further supporting the model and not nonspecific effects.

3.5 SPA and SPI result from non-linear amplification of afferent gamma fluctuations

The above analysis shows that internal W_{INT} and external W_{EXT} excitation strengths are the primary determining factors of the average prevalence of SPA and SPI respectively. However, SPA and SPI are stochastic, varying from cycle to cycle. Can the model capture this stochasticity? Not all afferent Up states are identical: the afferent network is more active during some Up states than others [147]. Similarly, some afferent Down states are more inactive than others. This within-state variability could arise from various processes, ranging from synaptic to neuronal and network. This is reflected in the cortical gamma band power (γ-power, 40-120 Hz), whose magnitude fluctuates considerably across UDS.

3.5.1 Modulation of cortical gamma power during SPA and SPI

To understand the effect of cortical variability on ECIII activity, we modeled the cortical γ-power fluctuations by scaling the afferent input by a memory-less Ornstead-Uhlenbeck process (μ=1, std=0.3), reflecting the coefficient of variation (CV) of the γ-power in the PAR LFP during UDS. According to our theory, the total magnitude of afferent input (UDS with γ-power) should be predictive of the efferent response: afferent Down states with larger γ-power has a greater probability of inducing an Up-Down transition in the efferent network, thus resulting in SPA (Fig 3.14). The converse applies for SPI: an afferent Up state with diminished γ-power is less likely to induce an efferent Down-Up transition, resulting in a larger probability of SPI (Fig 3.15).

This mechanism makes several distinct predictions that we verify as follows. The first prediction is about the magnitude of γ-power during SPA and SPI, in theory and in experiment. The PAR γ-power was significantly larger during Down states which elicited SPA in the ECIII V_m than during the Down states that did not. Conversely, the PAR γ-power was significantly smaller during Up states that induced SPI. The amplitude of the

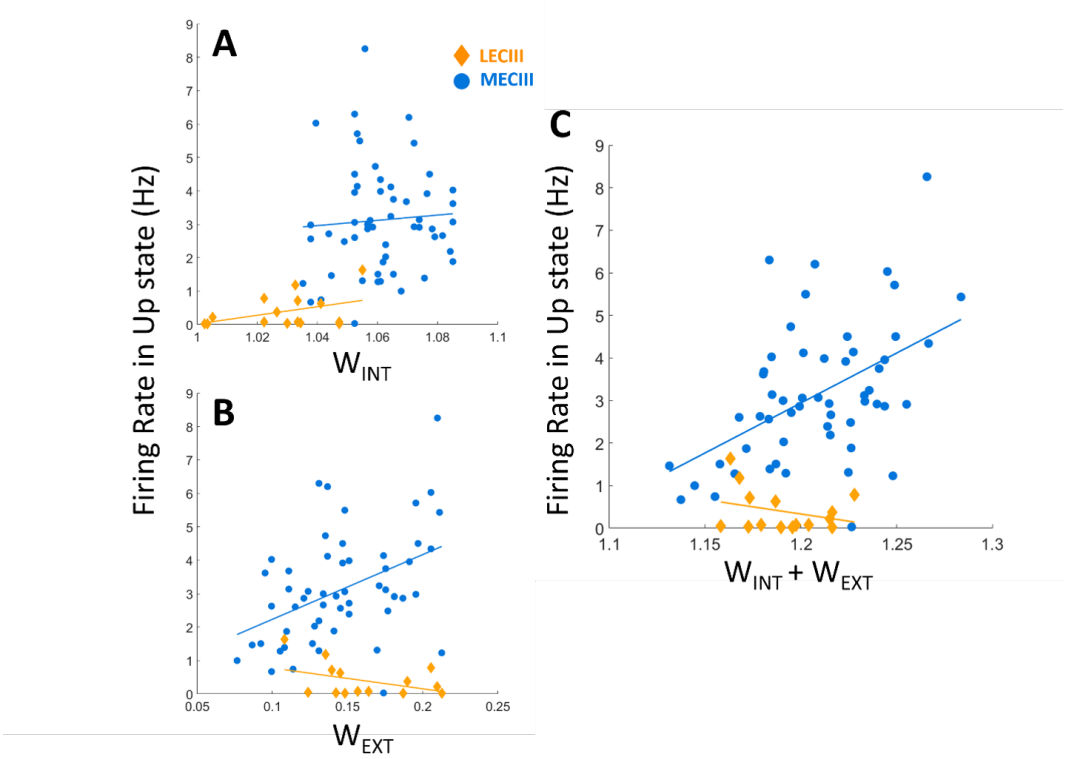

Figure 3.13: Firing rate of MECIII but not LECIII cells was significantly correlated to inferred connectivity parameters. A) The average firing rate of a neuron during the Up state was not significantly correlated with our estimate for the recurrent excitation W_{INT} for either the MECIII (blue: r=0.07, $p > 0.5$) or LECIII (yellow: r=0.42, $p > 10^{-1}$) populations. B) The average firing rate in the Up state was significantly correlated with our estimate for the external input W_{EXT} for only the MECIII population (r=0.43, p$< 10^{-3}$) and not for the LECIII population (r=-0.4, $p > 10^{-1}$). C) To find the total excitatory input into a neuron, we used the sum of our estimates for the recurrent and external excitations $W_{EXT} + W_{INT}$. The MECIII population showed significant positive correlation (r=0.49, p$< 10^{-3}$) while the LECIII population did not show significant correlation (r=-0.29,$p > 10^{-1}$).

unfiltered PAR LFP did not show such significant modulation during ECIII SPA/SPI (Fig 3.16). Thus, fluctuations in the instantaneous cortical γ-power can predict whether a given cortical state will result in SPA or SPI in the efferent network.

3.5.2 Amplification of gamma fluctuations

The second prediction is about the magnitude of γ-power amplification. Our theory predicts that positive afferent γ-power fluctuations during Down states and negative fluctuations during Up states are nonlinearly amplified in the efferent response to generate SPA and SPI, respectively. This amplification cannot be captured by simply taking the difference between the efferent intracellular V_m and afferent extracellular LFP, which by their very nature are orders of magnitude different (Fig 3.17). Instead, we used the ratio of γ-power between the Up and Down states: this is a good approximation, as this ratio was similar between PAR LFP and PAR V_m data, and the γ-power within each state was highly correlated between LFP and V_m data, both within and across PAR experiments (Fig 3.18). The γ-power ratio provided not only a qualitative but a quantitative match between the theoretical predictions and experimental data (Fig 3.19). Specifically, we found that the afferent γ-power fluctuations were amplified by a factor of 3.5 ± 0.2 during SPA and 2.81 ± 0.82 during SPI (Fig 3.20), demonstrating large amplification.

3.5.3 Non-linear dependence of probability on gamma fluctuation size

A third prediction of our theory is about the precise dependence of the probability of SPA/SPI as a function of the afferent γ-power. As previously mentioned, SPA and SPI are binary phenomena, evidenced by the bimodal distribution of MECIII V_m. This bimodality can be naturally described by a binomial random variable. The log-odds of SPA/SPI should depend linearly on the afferent γ-power, i.e. larger probability of SPA(SPI) for larger(smaller) γ-power in the Down(Up) state, and thus the probability distributions should have a sigmoid dependence. This prediction was supported quantitatively between theory and experiment (Fig 3.22). Further, these theoretical predictions were matched quantitatively with experimental data on a cell-by-cell basis. Data from each individual

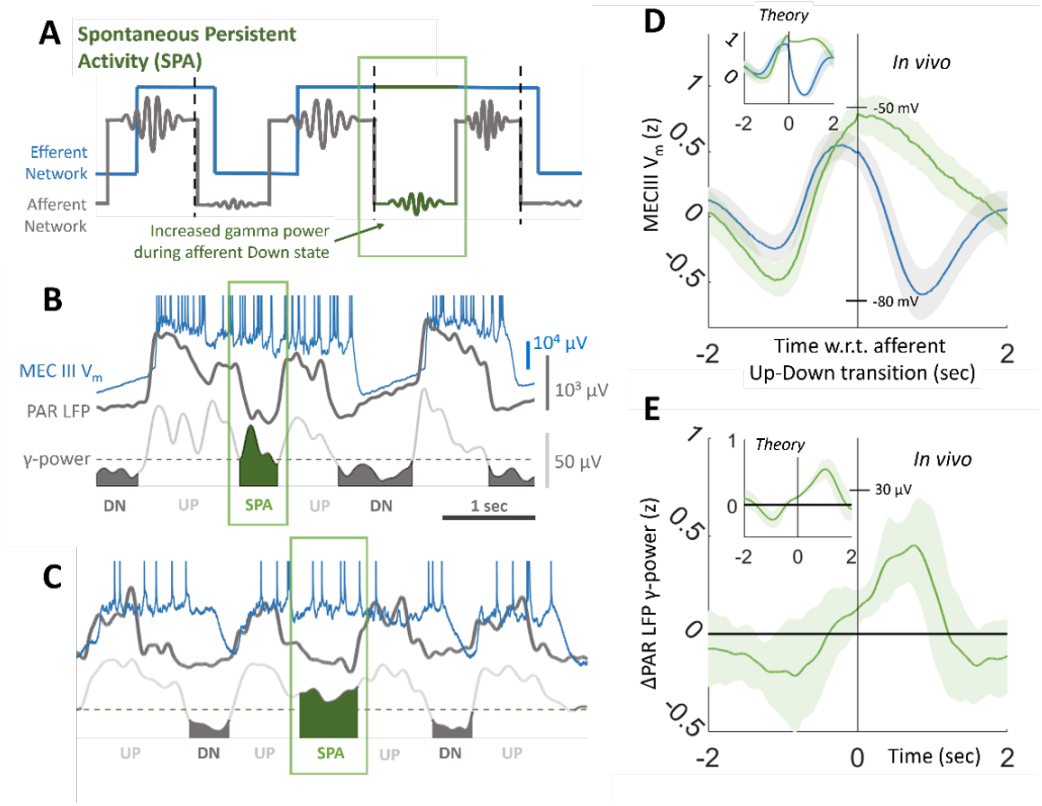

Figure 3.14: Cycle to cycle fluctuations of MECIII SPA are governed by fluctuations in the afferent cortical gamma power in the Down state. A) Afferent network activity varies from cycle to cycle, which manifests as fluctuations in the gamma band (γ: 40-120 Hz) power. Our model predicts that afferent network Down states with higher activity (and thus higher γ-power, green box) are more likely to prevent a synchronous Up-Down transition in the efferent network, resulting in SPA. B-C) Examples from two experiments, showing simultaneous UDS in the afferent PAR LFP (dark gray) and the efferent MECIII V_m (blue), with LFP γ-power shown underneath. The MECIII V_m persists in the depolarized Up state during the PAR Down state with high γ-power (compare green area to other dark gray ones). Note the several orders of magnitude difference in the vertical scales (right) between afferent and efferent voltages. Time scalebar shows 1 sec in B-C. D) Theory (inset) predicts that efferent activity triggered on afferent Up-Down transitions (dotted lines in A) will either persist in the active state (SPA: green) or follow with an Up-Down transition (blue). In agreement with theory, the average V_m of MECIII neurons triggered on Up-Down transitions in the afferent cortex persisted in the depolarized state during SPA (green) compared to synchronous transitions where the neuron goes to a Down state (blue). The maximum difference (20.3±4.1 mV) occurred at a lag of 823 ms and was highly significant ($p< 10^{-8}$). E) Theory (inset) predicts a significant positive difference in afferent activity when triggered on Up-Down transitions that resulted in SPA (green trace in D) vs. those that did not (blue in D). The *in vivo* data confirms this, with significant positive modulation (17 ± 5 μV at lag of 756 ms, $p< 10^{-4}$). Shaded regions here and everywhere represent ±1 standard deviation.

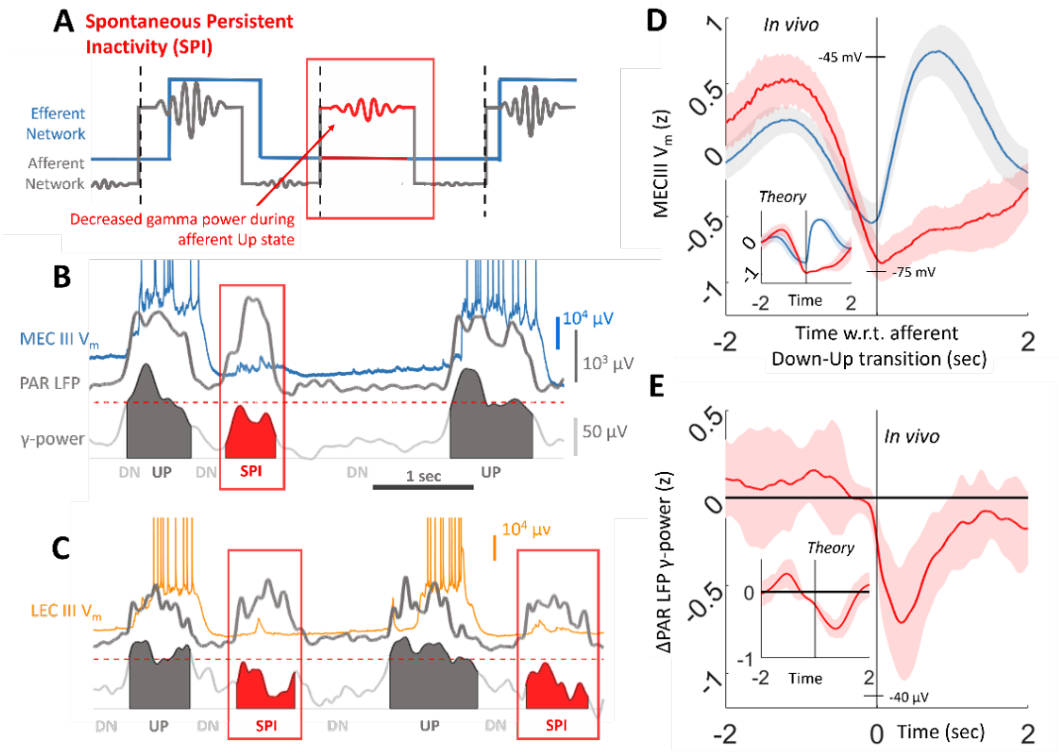

Figure 3.15: Cycle to cycle fluctuations of MECIII SPA are governed by fluctuations in the afferent cortical gamma power in the Up state. A) Afferent network Up states with lower activity (and thus lower γ-power, red box) are less likely to induce a synchronous Down-Up transition in the efferent network, resulting in SPI. This mechanism is symmetric to SPA. B) Example from experiment, showing simultaneous PAR LFP (gray), efferent MECIII V_m (blue), with LFP γ-power shown underneath. The MECIII V_m persists in the hyperpolarized Down state during the PAR Up state with low γ-power (compare red area to other gray ones). Time scalebar shows 1 sec. C) Example of SPI in LECIII V_m (orange) during PAR Up states with low γ-power. Timescale same as B. D) Theory (inset) predicts that efferent activity triggered on afferent Down-Up transitions (dotted lines in A) will either persist in the inactive state (SPI: red) or follow with a Down-Up transition (blue). In agreement with theory, the average V_m of MECIII neurons triggered on Down-Up transitions in PAR LFP persisted in the hyperpolarized state during SPI (red) compared to synchronous transitions where the neuron goes to an Up state (blue). The maximum difference (24.2±5.1 mV) at a lag of 653 ms was highly significant ($p< 10^{-5}$). E) Theory (inset) predicts a significant negative difference in afferent activity when triggered on Down-Up transitions that resulted in SPI (red trace in D) vs. those that did not (blue in D). The *in vivo* data confirms this, with significant negative modulation (-23 ± 10 μV at lag of 345 ms, $p< 10^{-3}$).

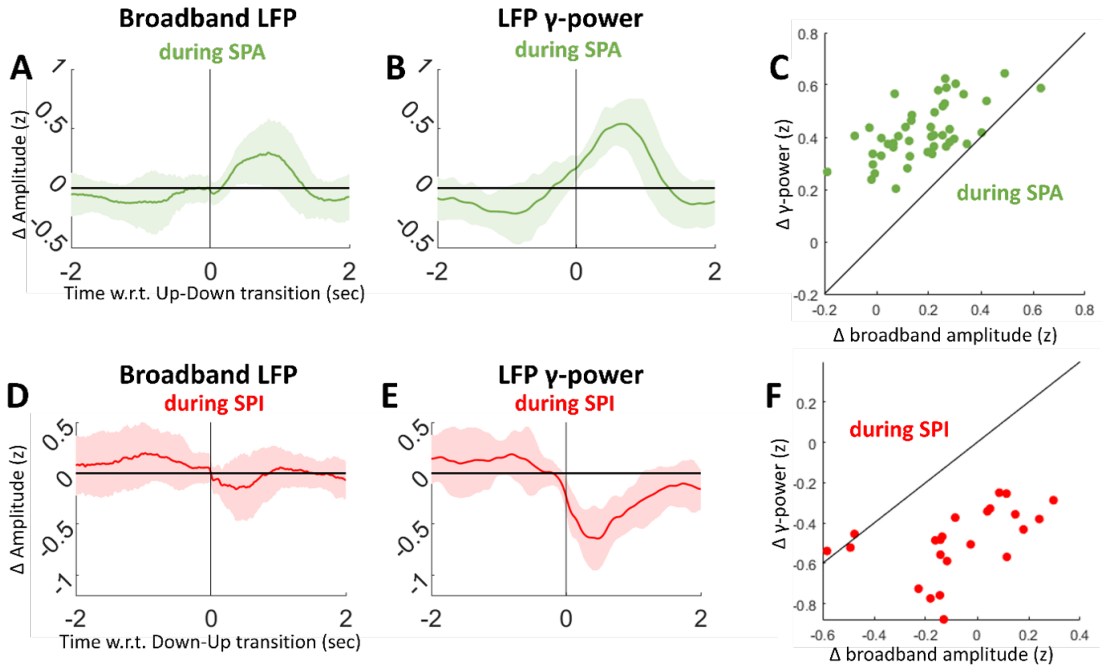

Figure 3.16: Fluctuations in cortical LFP gamma power are larger than fluctuations in LFP amplitude during SPA/SPI. A) The difference in the amplitude (in z-score) of the broadband LFP (high-pass filtered above 0.05 Hz) when triggered on cortical Up-Down transitions that resulted in ECIII SPA vs those that did not shows a significant positive modulation ($p<0.05$). B) Same as Fig 3E. The same procedure shows positive modulation in the afferent γ-power during SPA vs during synchronous transitions. C) During SPA, the modulation of γ-power in the LFP (y-axis) was significantly larger ($p< 10^{-4}$) than the modulation of the amplitude of the LFP (x-axis) on a cell-by-cell basis. Each point represents a single experiment. D) Same as A, but triggered on the Down-Up transition to show the difference in LFP broadband amplitude during SPI vs not. There is no significant difference ($p>0.05$) E) Same as B and Fig 4E, the cortical γ-power shows negative modulation during SPI vs not. F) On a cell-by-cell basis, the modulation in LFP γ-power (y-axis) was significantly more negative ($p< 10^{-4}$) than the modulation in LFP broadband amplitude (x-axis), which itself was not significantly different from zero ($p> 0.05$).

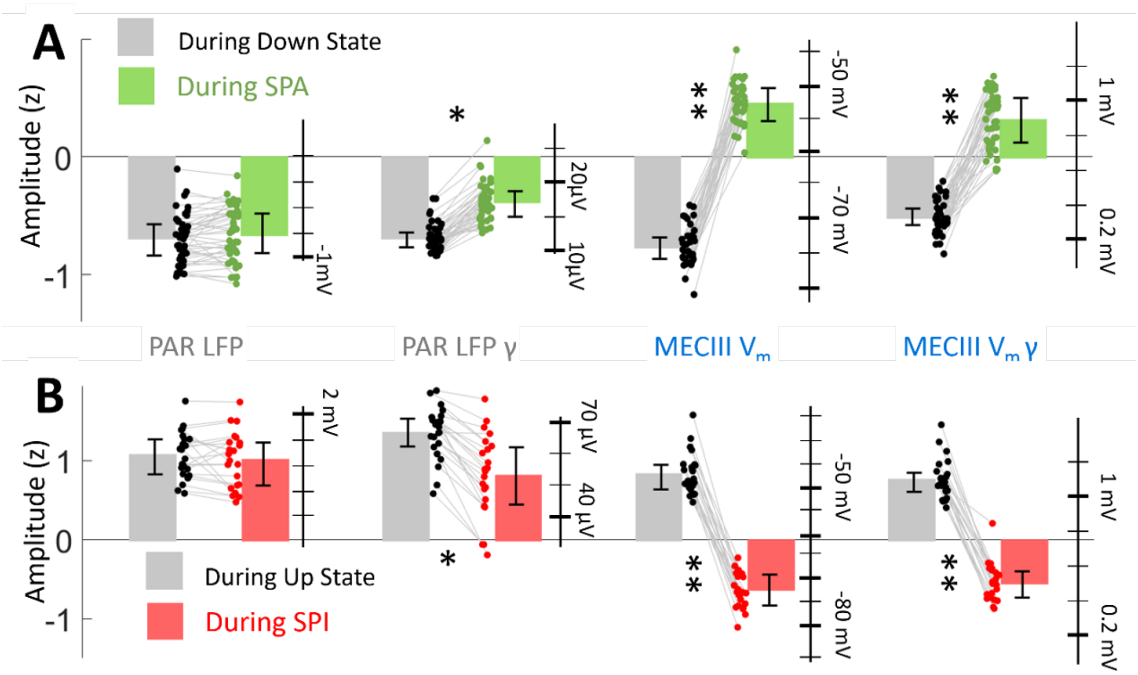

Figure 3.17: PAR LFP fluctuations during SPA/SPI occur within Down/Up states, but MECIII activity switches between Up and Down states. A) During SPA, the average amplitude of parietal LFP (PAR LFP) is not significantly different ($p>0.1$) from the amplitude during normal Down states (normal Down: -0.78±0.17mV, SPA: -0.76±0.22mV). The bars represent averages over all experiments, and individual points represent individual experiments. The global axis on the left represents the quantity in terms of z-score, while the individual axis on the right represents the actual experimental values. The average parietal LFP gamma band power (PAR LFP γ) was significantly higher than during normal Down states (normal Down: 12.1±1.2μV, SPA: 17.3±2.7μV; $p< 10^{-3}$). In the efferent network, the average MECIII membrane potential (MECIII V_m) was significantly negative during non-persistent Down states and significantly positive (in terms of z-score) during persistent activity states, signifying an efferent Up state. The membrane potential was hyperpolarized during normal Down states (-75.8±1.5mV) and depolarized during persistent activity states (-54±2.5mV), and were significantly different ($p< 10^{-7}$). The average gamma power in the MECIII membrane potential (MECIII V_m γ) was significantly higher during SPA states (0.9±0.12mV) than during non-persistent Down states (0.32±0.04mV). B) Same as A, but for SPI and non-SPI Up states. PAR LFP was not significantly different (normal Up: 1.2±0.23mV, SPI: 1.1±0.29mV), but PAR LFP γ-power was significantly lower during Up states which elicited SPI than those that did not (normal Up: 68±4μV, SPI: 53±11μV, $p< 10^{-3}$). MECIII membrane potential (MECIII V_m) was significantly negative during SPI and positive during non-persistent Up states (in terms of z-score), and was hyperpolarized during SPI and depolarized during non-persistent Up states (normal Up: -49.1±4.2mV, SPI: -73.3±5.2mV). The average gamma power in the MECIII membrane potential (MECIII $V_m\gamma$) was significantly lower during SPI states (0.51±0.08mV) than during non-persistent Down states (1.1±0.04mV).

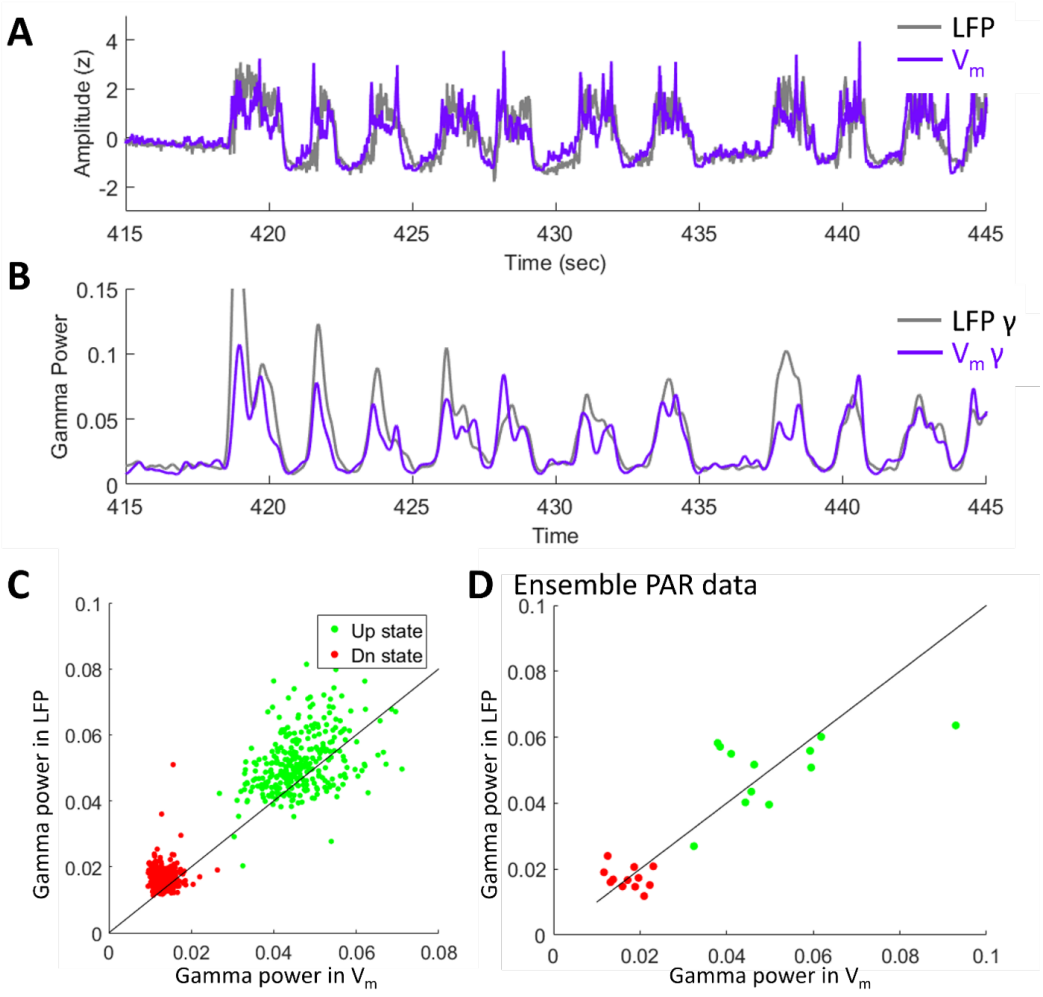

Figure 3.18: Gamma power fluctuations in the membrane potential serve as a surrogate for local network activity. A) LFP from parietal cortex (gray) and membrane potential from a single neuron (purple) in the parietal cortex were z-scored (top) to enable comparison of relative size of fluctuations in the gamma band (γ: 40-120 Hz). Spikes were clipped from the membrane potential trace. B) The traces were filtered in the γ-band and showed similar fluctuations, both in size and duration. Thus, the membrane potential γ-power gives a close estimate of the gamma power in the extracellular LFP. C) Up states had significantly higher γ-power than Down states, but the relative sizes of each was similar between membrane potential and LFP. Each point here corresponds to the average γ-power within a single Up or Down state for the example experiment in A/B. The diagonal line gives perfect agreement. D) Over the ensemble of experiments involving simultaneous recording from parietal LFP and parietal membrane potential, the relative sizes of Up and Down states was similar. Each point represents the average over an entire experiment.

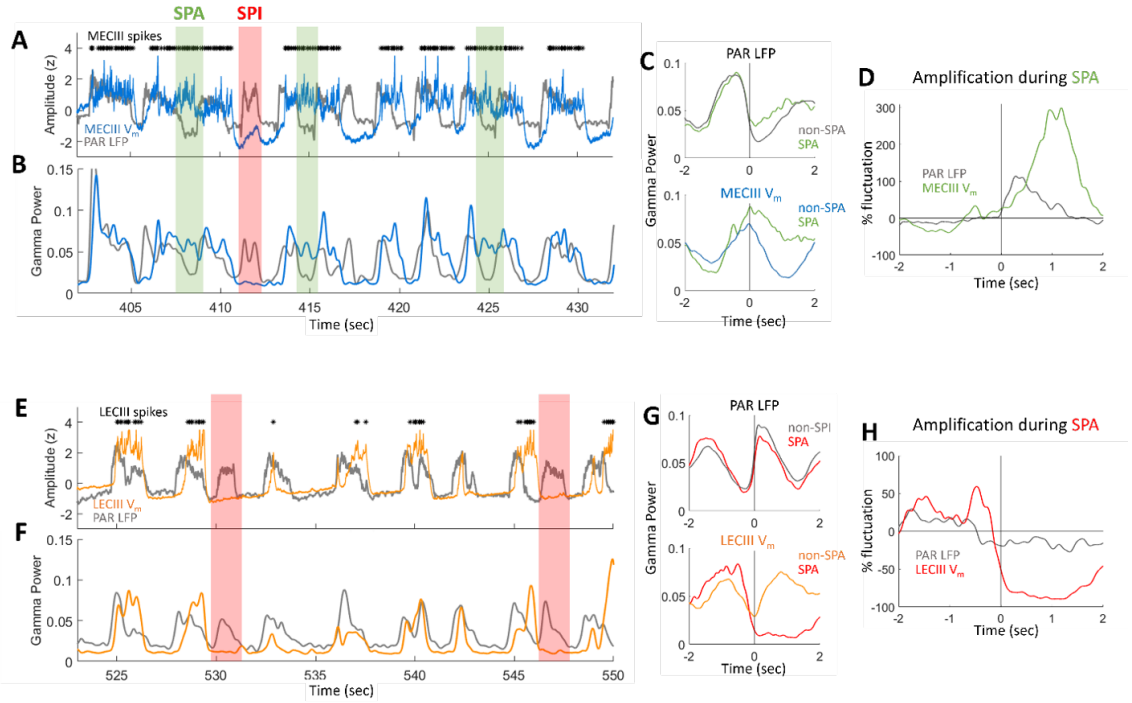

Figure 3.19: Non-linear amplification of MECIII SPA and SPI can be quantified using fluctuations in gamma power. A) Both PAR LFP (gray) and MECIII membrane potential (blue) were normalized by z-score. MECIII spikes were removed for subsequent spectral analysis, and are indicated by the asterisks. B) The traces were filtered in the gamma band (40-120 Hz) and smoothed. Instances of SPA and SPI are highlighted in the green and red boxes, respectively. C) Both gamma power traces were triggered on parietal LFP Up-Down transitions that were followed by efferent SPA (green) and compared with the traces triggered on Up-Down transitions that were followed by an efferent Down state (gray for LFP, blue for V_m). D) To calculate the size of the fluctuation following the transition, the SPA trace (green) was divided by the null, non-SPA trace (gray), and converted to a percent change. In this particular example, the LFP gamma power saw an increase of 100% during SPA, whereas the MEC gamma power saw an increase of 300%. This yields an amplification of 3. E) Same as A, but showing an LECIII neuron (yellow) exhibiting SPI (red boxes). F) The z-scored trace in (E) was filtered in the gamma band and smoothed. G) Both gamma traces were then triggered on parietal LFP Down-Up transitions, and transitions which were followed by SPI were compared against those that were followed by a synchronous Up state. H) The size of the fluctuation was again calculated in a similar fashion to SPA in (D). In this particular example, the LFP gamma power saw a decrease of 20% during SPI, whereas the MEC gamma power saw a decrease of 90%, yielding an amplification of 4.5.

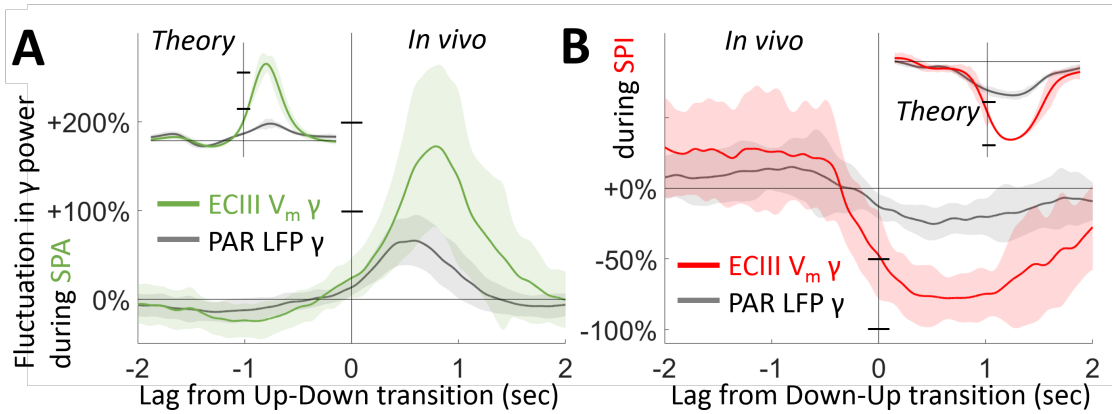

Figure 3.20: A) Theory (inset) predicted that afferent activity (gray) was higher during the Down states that elicited SPA in the efferent network, compared with Down states that did not (same as Fig 3E inset). Due to SPA, the efferent network activity (green) was also significantly higher. The ratio of the efferent to afferent activity modulation, defined as the % increase in activity, termed the amplification factor, was significantly larger than unity (3.5±0.2, $p< 10^{-9}$). *in vivo*, the PAR LFP γ-power was significantly larger (gray: 64±25%, $p< 10^{-4}$) during Down states that elicited SPA in ECIII neurons vs. those that did not (same as Fig 3E). ECIII V_m γ-power was also significantly higher (green: 180±65%, $p< 10^{-5}$), yielding an amplification factor significantly larger than unity (2.81±0.82, $p< 10^{-5}$), in agreement with theory. B) Same as A, but for SPI. Theory (inset) predicted that afferent activity was significantly lower during Up states that elicited efferent SPI vs those that did not (same as Fig 4E inset). Due to SPI, efferent activity (red) was also significantly lower, yielding an amplification factor significantly larger than unity (2.2±0.20, $p< 10^{-10}$). *in vivo*, PAR LFP γ-power was significantly lower (gray: -21±5%, $p< 10^{-4}$) during Up states that elicited SPI vs. those that did not (same as Fig 4E). ECIII V_m γ-power was also significantly lower (red: -70±12%, $p< 10^{-6}$), yielding an amplification factor significantly larger than unity (3.12±0.61, $p< 10^{-5}$), in agreement with experiment.

cell/simulation was well fitted by a sigmoid, supporting our binomial random variable formulation. As expected, the parameters of the sigmoid varied substantially among experiments, based on the degree of SPA and SPI. Remarkably, despite this variability, for a given cell very similar parameters of the sigmoid provided a fit to both the experimental and theoretical results.

The fourth prediction concerns the joint effect of the network variables W_{INT} and W_{EXT} and the afferent cortical γ-power in determining the odds of SPA and SPI. According to the theory, W_{INT} modulates the stability of the efferent Up state, so an increase in W_{INT} would increase the overall odds for the efferent to exhibit SPA by decreasing the threshold γ-power needed in the afferent Down state. The log-odds sigmoid should thus shift to lower values for larger W_{INT}; this is corroborated by the experiments (Fig 3.23). W_{EXT} modulates the coupling of the afferent to the efferent network, so an increase in W_{EXT} would decrease the overall odds for efferent SPI by decreasing the threshold γ-power needed in the afferent Up state. Thus, the log-odds sigmoid for SPI should shift to lower values as $W_{EXT}\neg$ increases. Again, the experiment confirms these predictions quantitatively.

3.6 Quantization

The model predicts that SPA and SPI are all-or-none events. As a result, even though efferent Up/Down state and SPA/SPI durations form a continuous, unimodal distribution, these durations should be quantized in integral units of the afferent UDS cycles (Fig 3.24). To compute this for SPA, segments of the efferent activity trace were extracted around every efferent Down-Up transition, sorted according to the ensuing efferent Up state duration, and assembled into a single matrix (Fig 3.24). The underlying afferent activity matrix for the same time points exhibited alternating bands of UDS, with integer multiples of afferent UDS fitting inside each efferent Up state. The *in vivo* matrix matched strikingly well with model predictions. The same procedure for efferent Down states and SPI produced a similar quantitative match between theory and experiment. The probability distribution of the rescaled state durations for single experiments was significantly multimodal, with peaks

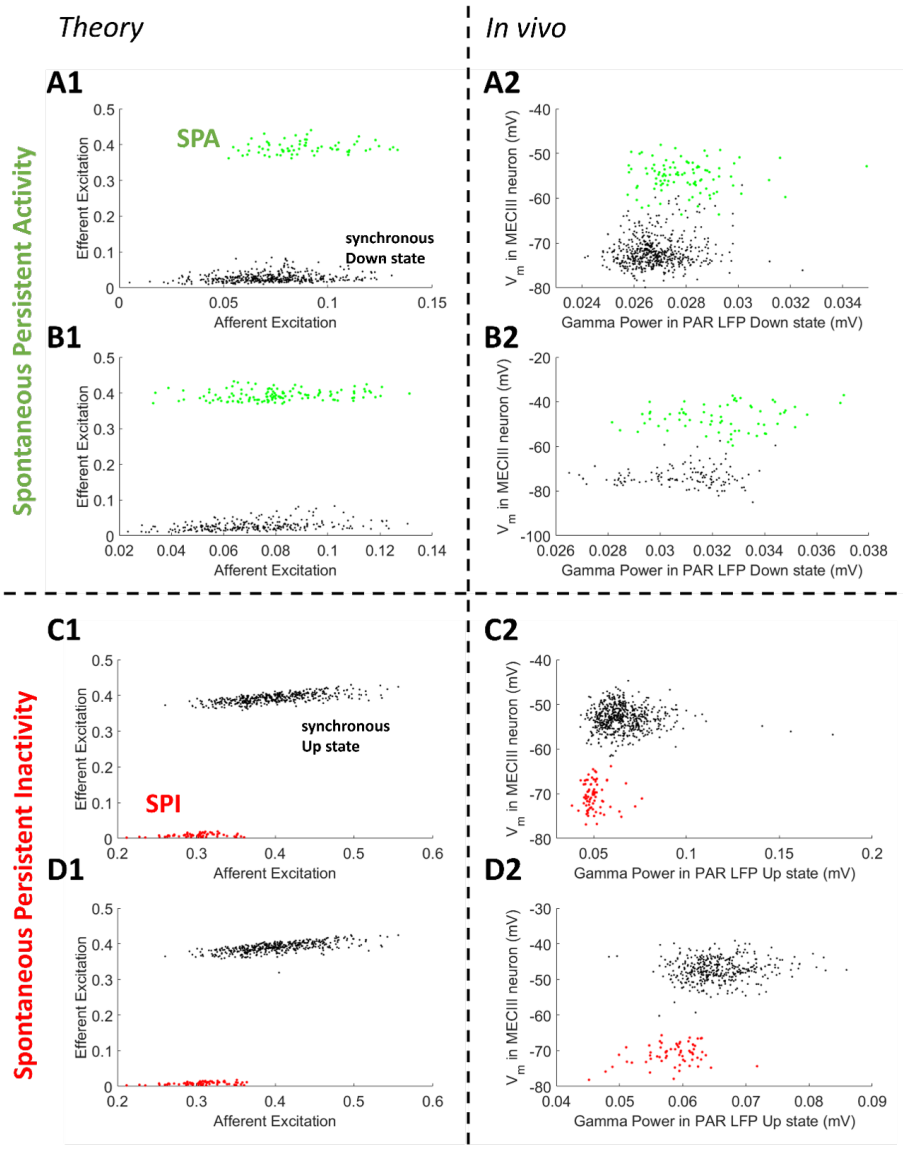

Figure 3.21: Stochastic response of efferent ECIII membrane potential to afferent PAR gamma fluctuations. A1) Simulated response of the efferent network (y-axis) to afferent activity fluctuations (x-axis) shows the stochastic nature of SPA. The theory predicts that for a given afferent Down state, the efferent network exhibits SPA or a synchronous Down state in a discrete, all-or-nothing manner. Thus, Down states with similar activity content can exhibit both SPA and a synchronous Down state within the same experiment. A2) Example from experiment shows probabilistic, all-or-nothing nature of response in the efferent MECIII membrane potential: cortical Down states with similar γ-power can both elicit SPA and a synchronous Down state in an all-or-nothing manner. B1-B2) Another example of SPA, with same convention as A1-A2. C1) Simulated SPI shows that, for afferent Up states with the same activity, the efferent network can both exhibit SPI or a synchronous Up state probabilistically, in an all-or-nothing fashion. C2) The experiment shows similar all-or-nothing, probabilistic response in the membrane potential of the efferent neuron. D1-D2) Another example of SPI in model and experiment.

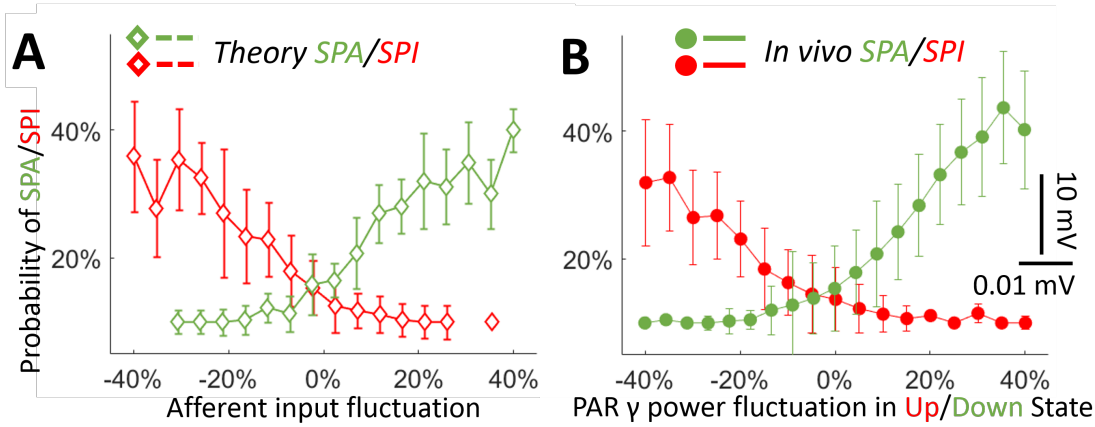

Figure 3.22: A) Theory predicted that, across the ensemble of matched simulations, the probability of efferent SPA increased as a function of the afferent activity during the Down state (green diamond). Conversely, the probability of SPI decreased as a function of afferent activity during the Up state (red diamond). B) In agreement with theory, the probability of ECIII SPA increased as a function of PAR LFP γ-power in the Down state (green circle), and the probability of ECIII SPI decreased as a function of PAR LFP γ-power in the Up state (red circle). The γ-power in Up/Down states were normalized by the average power in each state in every experiment to highlight dependence on fluctuations and compare across different experiments, but axes on the lower right show the true scale of fluctuations.

at the half integers, indicating that the ECIII state transitions were still locked to the PAR LFP transitions, and that the ECIII skipped entire PAR Up/Down states in integer quantities (Fig 3.25, 3.26). Remarkably, this quantization was observed when consolidating the rescaled durations of the Up/Down states over all experiments, further demonstrating the generality of our model.

3.6.1 Departure from Memoryless Bernoulli process

The precise history-dependence of SPA/SPI can provide a further test for our model. One can imagine three scenarios. First, the SPA/SPI are entirely stochastic, in which case their probability distribution would follow a memoryless Bernoulli process, like a sequence of coin flips. Second, SPA/SPI arise due to some change in the overall state of the animal, such that all the SPA/SPI co-occur. However, our theory predicts a third possibility: it should be rarer to have consecutive sets of SPA/SPI compared to singular events. This is because the probability of SPA/SPI is strongly history-dependent. If the network exhibits SPA at

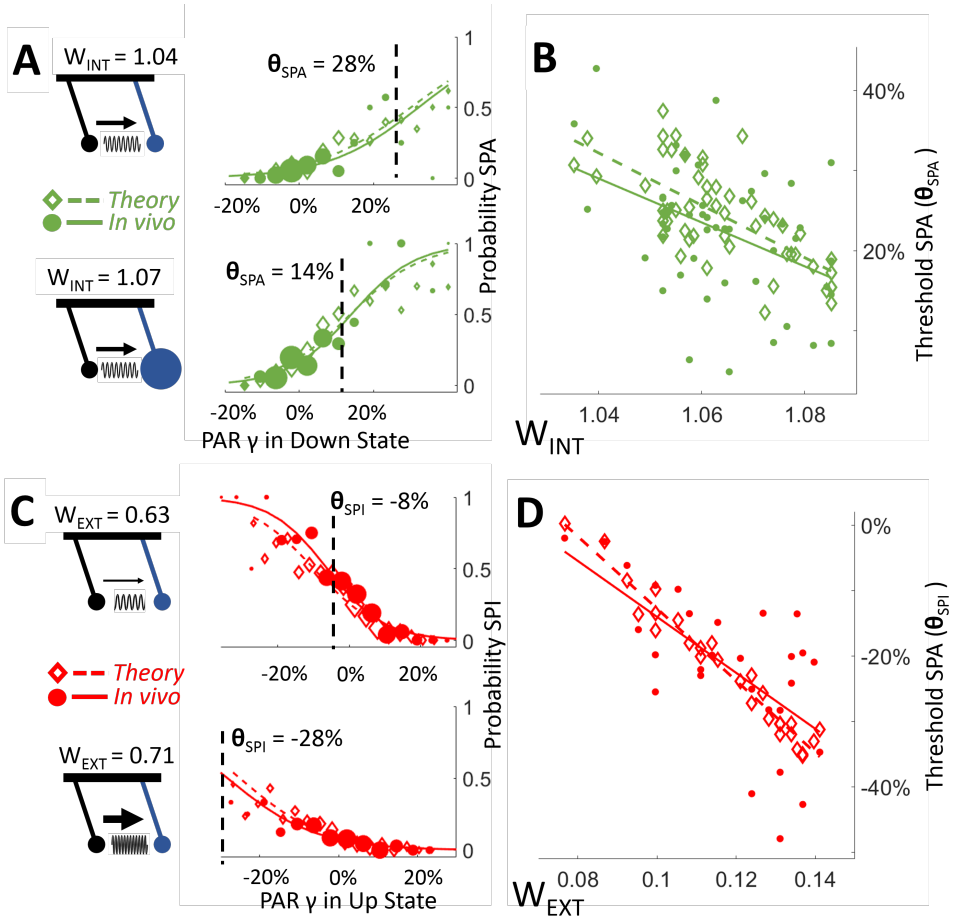

Figure 3.23: A) Examples of two experiments with different fitted W_{INT} values. The dependence of SPA probability on γ-power fluctuations within the experiments (circle) and within matched simulations (diamond) was well-fit by a simple logistic function ($p< 10^{-3}$). The size of each data point is proportional to the number of observations in each γ-power/activity bin. The network with larger "inertia" (higher W_{INT}) is more likely to exhibit SPA for smaller fluctuations in the afferent input during Down states, thereby shifting its sigmoid dependence to the left. This can be quantified by the threshold θ_{SPA} γ-power, measured in units of normalized γ-power fluctuation, where the odds of SPA and not-SPA are equally likely. B) As predicted by the theory (diamonds), *in vivo* (circles) also showed that the larger the internal recurrence W_{INT}, the lower the threshold θ_{SPA}, and the more sensitive the efferent network becomes to positive fluctuations in the afferent Down states. Both theory and experiment were significantly negatively correlated (theory: $p< 10^{-9}$, *in vivo*: $p< 10^{-3}$) C) Examples of two experiments with different fitted W_{EXT} values. The network with larger "coupling" (higher W_{EXT}) is less likely to exhibit SPI for smaller negative fluctuations in the afferent input during Up states. The dependence was well fit by a negative logistic function ($p< 10^{-3}$). θ_{SPI} was the threshold afferent Up state γ-power where SPI and not-SPI are equally likely. D) The theory predicts that θ_{SPI} decreases for increasing W_{EXT}, and this is confirmed with *in vivo* data. Both theory and experiment were significantly negatively correlated (theory: $p< 10^{-8}$, *in vivo*: $p< 10^{-2}$).

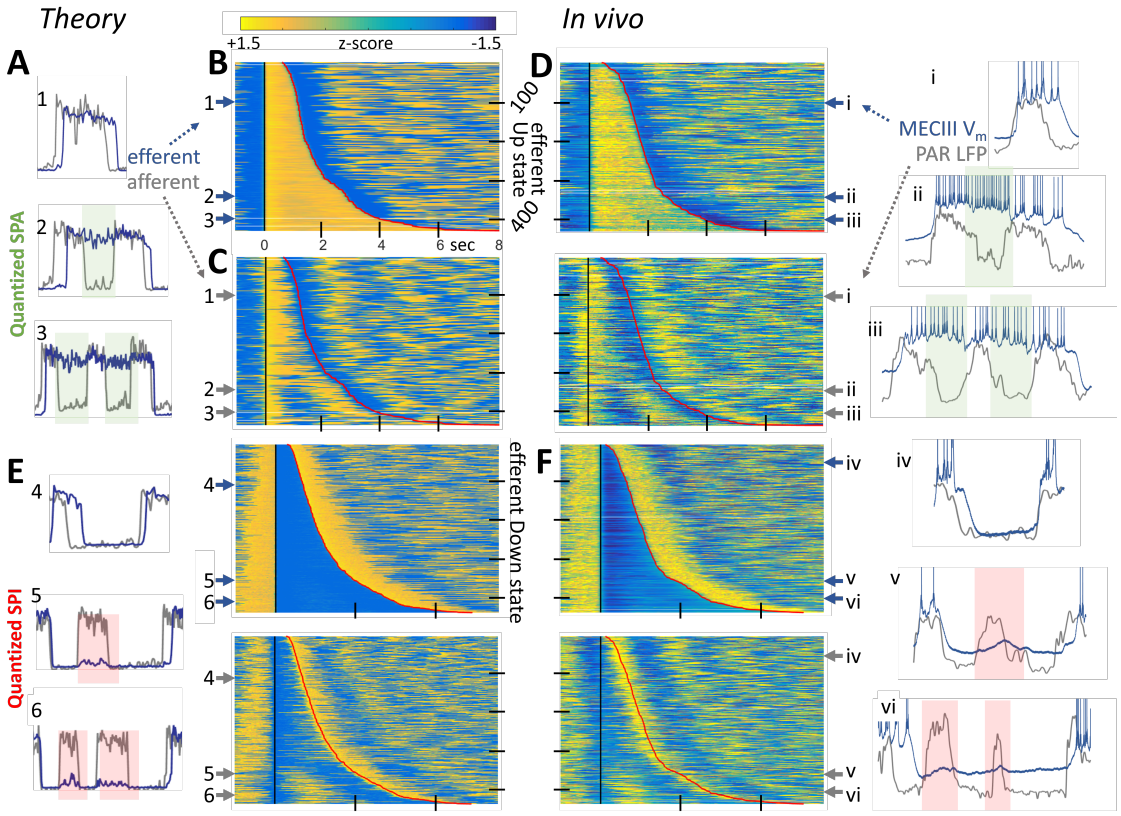

Figure 3.24: Quantization of SPA and SPI in units of afferent parietal UDS cycles results from adaptation, a history-dependent process. A) In the theory, the efferent SPA (blue) span a continuous range of durations, but they are quantized (green boxes, 1,2,3... n) in the units of the number of afferent UDS cycles. B) All efferent Up states were aligned to the efferent Down-Up transition and ordered with increasing duration. C) A second matrix was constructed using the same time points, but using the afferent network activity. The examples (1-3) in (A) correspond to the row numbers in (B/C). Efferent SPA can last 8 seconds, spanning several afferent UDS cycles. Same colorbar axis is used for the amplitude (z-score) for all the panels. D) *in vivo* data from an MECIII neuron validates the theory by showing efferent MECIII Up states (blue) last an integer multiple (i-iii) of afferent PAR LFP UDS cycles (gray). E) Similar to A-D, but for SPI, showing that efferent Down states and SPI show a continuous duration but are quantized (red boxes) in the units of afferent PAR LFP UDS cycles, in theory and F) experiment.

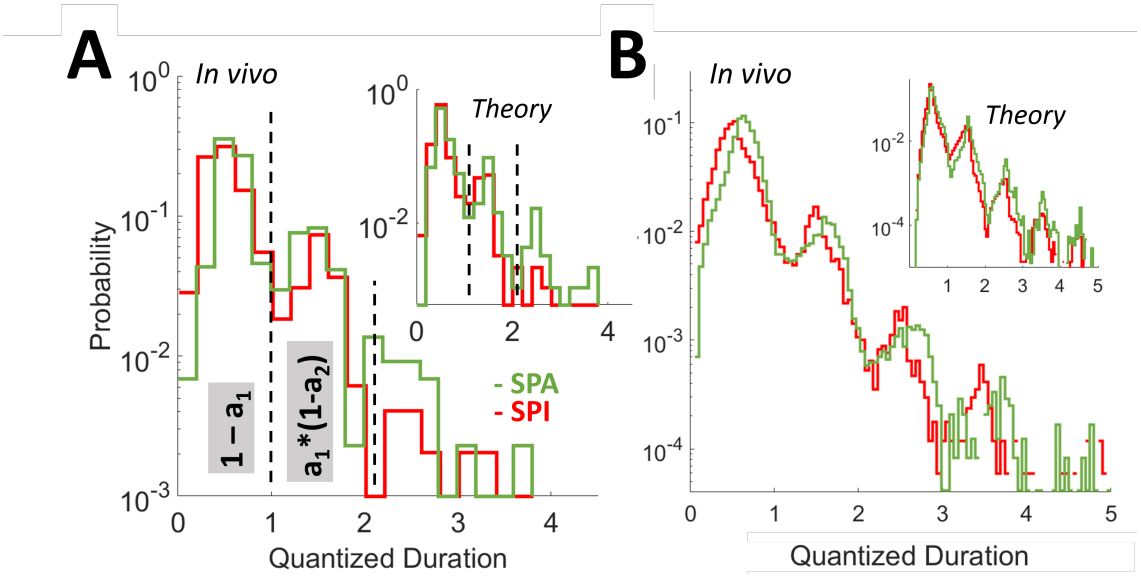

Figure 3.25: A) With time measured in units of the varying afferent UDS cycles, theory (inset) predicted that the distribution of both Up and Down state durations should be multimodal, with peaks at the half integers (reflecting state transitions after an Up/Down state). *in vivo* data showed the predicted multimodality and quantization when MECIII Up/Down state durations were measured w.r.t. variable PAR UDS cycle lengths. B) The multimodal, quantized nature of the distribution was evident even when combining data across all experiments (main) and fitted simulations (inset).

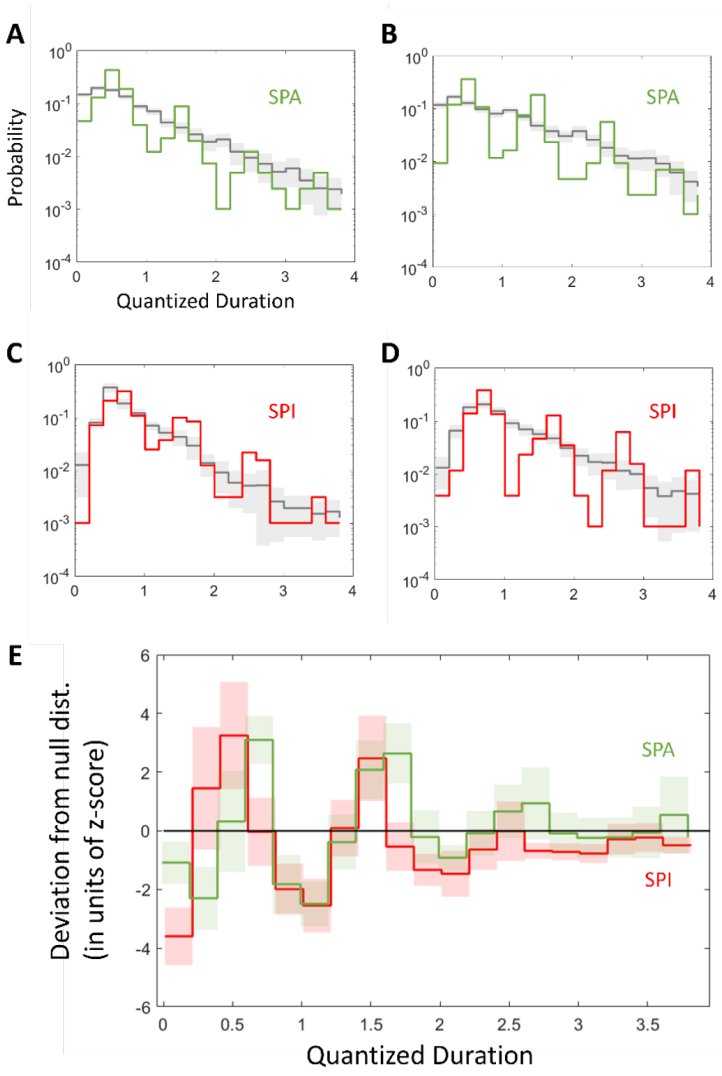

Figure 3.26: Experimental distributions of efferent state length in units of afferent UDS was significantly quantized compared to bootstrap shifted null distributions. A) The distribution of efferent Up state lengths in terms of afferent UDS in the experiment (green) was compared with the same distribution resulting from a random shift of the efferent data (gray). The standard deviation (gray shaded area) of the null distribution was obtained by calculating the distribution from 60 random shifts. The peaks and trough of the real distribution were significantly different from the null. B) Another example of efferent SPA quantization, with corresponding null distribution. C) An example of efferent Down state lengths (red) in terms of afferent UDS also shows significant quantization, different from the null distribution (gray). D) Another example of significant quantization of SPI. E) Taking the difference between the real and null distributions from each experiment and normalizing by the standard deviation in each bin shows that the first trough (at Q.D.=1) and the second peak (at Q.D.=1.5) for both SPA and SPI is significantly different (SPA: first trough p<10-3, second peak p< 10^{-3}; SPI: first trough p< 10^{-3}, second peak p< 10^{-2}) from the null distribution at the population level.

a given afferent Down state, the efferent network's recurrent excitation W_{INT} would be more adapted than usual, reducing the resources needed to sustain SPA in the next Down state, thus reducing the probability of consecutive SPAs. Similarly, the occurrence of SPI at a given afferent Up state would make the efferent network less adapted and hence reduce the probability of consecutive SPIs. To test this prediction, we used the first two modes of the quantized probability distribution (in Fig 3.25) to calculate a_1, the probability of a solitary SPA/SPI, and a_2, the probability that another SPA/SPI occurred given a1 already happened. Here, $a_2 = a_1$ for the first memoryless hypothesis, $a_2 > a_1$ for the second brain-state dependent hypothesis, and $a_1 > a_2$ for the third hypothesis, predicted by our theory. The experiments strongly corroborated our theoretical predictions: the probability of SPA/SPI diminished after the first such event (Fig 3.27). Thus the two network system has a longer-term memory of SPA/SPI due to the adaptation of the recurrent excitation W_{INT} in the efferent network.

3.7 Discussion

3.7.1 A brief history of persistent activity

Persistent activity has been hypothesized to mediate working memory via reverberating activity [34, 109], and has been studied extensively *in vivo*, *in vitro*, and *in silica*. The in vitro experiments and computational studies focus on the role of specific intracellular mechanisms [148–151], while *in vivo* studies focus on network mechanisms of sustained activity during a delay period in many brain regions [113, 139, 152]. Recent studies have shown sustained activity in hippocampal CA1 place cells during navigation [72, 153, 154]. Persistent activity, in the form of sustained depolarization or plateau potentials, has been found in somatic V_m in several brain areas [155–157]. Persistent depolarization and spiking has also been seen in the dendritic V_m of parietal cortex pyramidal neurons during natural sleep and free foraging [158]. Additionally, elevated gamma (γ) power has been found in specific brain areas during working memory [73, 138, 159]. The ubiquity and diversity of persistent activity in different cell types, brain regions, brain state, and behavior supports

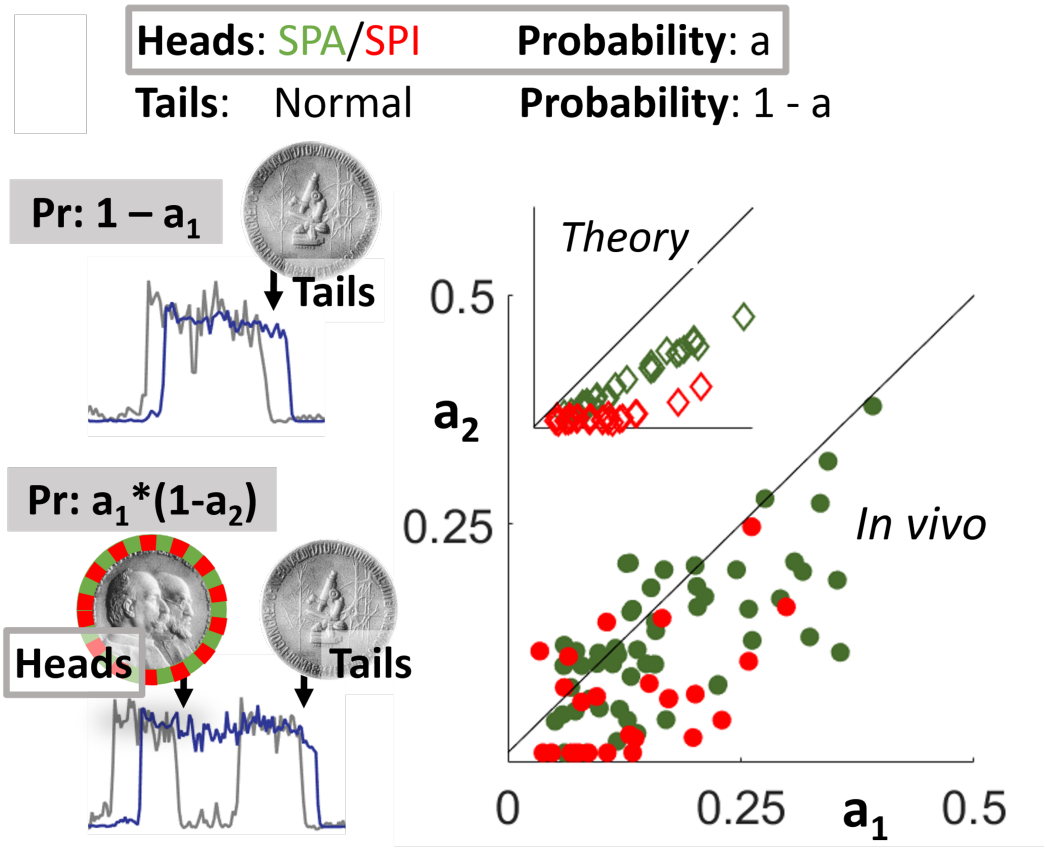

Figure 3.27: To find the precise history-dependence, one can imagine the efferent response to afferent UDS as a sequence of coin flips, as SPA and SPI are all-or-nothing binary events. State transitions in the afferent network destabilize the efferent network, which either persists in its current state, resulting in SPA/SPI (heads, probability Pr=a), or makes a corresponding transition (tails, Pr=1-a). The probability that a given efferent state lasts a single afferent UDS cycle is Pr=$1-a_1$ (the first mode in Fig. 3.25), while the probability that it lasts between 1 and 2 cycles is Pr=$a_1 \cdot (1-a_2)$ (the second mode), where the subscript denotes the nth transition. Unlike a memoryless process (i.e. $a_1 = a_2$) or brain state dependent process (i.e. $a_1 < a_2$), the theory (inset) predicted that the probability of SPA/SPI should decrease when conditioned on SPA/SPI having occurred previously (i.e. $a_1 > a_2$, p< 10^{-16}). This was confirmed in the *in vivo* data (main, p< 10^{-7}) and reflects the underlying long-term memory of the adaptation in the efferent network.

the hypothesis that a common mechanism could apply.

Persistent activity was recently observed in MECIII during UDS *in vivo*. It could not be initiated or terminated by current injections [94], further implicating network mechanisms. Similarly, persistent activity in LECIIII neurons in vitro cannot be perturbed by current injections, but can be influenced by synaptic activation [149]. Thus, we focused on a network based theory of persistent activity with generic neurons. Existing network models show that sustained activity can generated through reverberant excitation and feedback inhibition [160, 161]. These models can explain many experimental observations about stimulus evoked responses, but have not been used to address spontaneous persistent activity in the absence of external sensory input [162]. Models of spontaneous activity have focused on a single network sustaining activity in the Up state [113, 117, 118]. Other studies have modeled interaction between cortical UDS and hippocampal irregular activity, but not studied persistent activity during UDS [163]. Furthermore, these models have not studied the inactive regime.

3.7.2 Summary of Results

The Model

To obtain an analytical understanding of interaction between large networks, and make experimentally testable quantitative predictions, we focused on the cortico-entorhinal interaction during UDS oscillations, using simultaneous LFP from parietal cortex that served as a common afferent reference, along with the membrane potentials measured from anatomically identified neurons in several efferent brain regions. We treated each brain region as a system governed by just three continuous variables, average excitation, average inhibition, and activity-dependent adaptation in only the excitatory population [117–119]. These simplifying assumptions greatly reduced the computational complexity of our theory. But, even this simplified network has 23 independent parameters, which limits quantitative predictions and falsification. Hence, we further simplified the theory using dynamical systems techniques [123] and modeled different brain regions by varying only two biologically rel-

evant parameters: the strength of internal connections W_{INT} within the efferent network and the strength of external input W_{EXT} arising from the afferent parietal cortex, while leaving all the other parameters unchanged. Using only these two variables, we made several quantitatively verifiable predictions about the dynamics of the interaction between these networks. To verify these predictions, we studied the cortico-entorhinal circuit *in vivo*, but under controlled conditions, namely urethane anesthesia. This removed the differential contribution of sensory stimuli and behavior to different networks [7], removed the variation of UDS properties with different sleep stages, made the UDS durations sufficiently large so that persistent activity and inactivity could be detected unequivocally, and made all neocortical areas nearly synchronous. The combination of this simple, two parameter theory and simplified experiment provided quantitative verification of the theory of spontaneous cortico-entorhinal interaction, not only in a region specific fashion, but also in a cell-specific way. Our theory of persistent activity made a surprising prediction, namely the existence of persistent inactivity. In contrast to persistent activity, which involves the efferent network sustaining activity while afferent inputs have shut off, persistent inactivity involves the efferent network sustaining inactivity while afferent input remains active. This has not been reported before in any studies, though there are hints [164, 165]. Dynamical systems analysis revealed the differential roles that the internal efferent excitation W_{INT} and the external input strength W_{EXT} play. Increasing W_{INT} enhanced the ability of the efferent network to sustain activity on its own, increasing the likelihood of persistent activity. On the other hand, decreasing W_{EXT} reduced the ability of the efferent network to initiate an 'Up' state, thereby increasing the likelihood of persistent inactivity. Thus, a combination of theory and experiment about the nature of persistent activity and inactivity can provide powerful insights about the large scale network connectivity across different brain areas *in vivo*.

Testing the theory *in vivo*

In addition to detecting SPI in the experimental data, we confirmed several other model predictions using just two physiological variables, W_{EXT} and W_{INT}, across several brain

regions at the network level and on a cell-by-cell basis. This revealed the nature of large-scale connections between and within several brain regions. Our results predicted that parietal input onto the entorhinal region should be weaker than to the frontal regions. While this has not been directly measured *in vivo*, it is supported by anatomical observations of strong intra-neocortical connections [132, 166, 167]. Within the entorhinal region, the model predicted that parietal input into LECIII was significantly stronger than to MECIII, consistent with anatomical studies [168]. Our analysis found greater amounts of persistent activity in MECIII than LECIII, and the model predicted that this is because the recurrent connections W_{INT} should be larger within MECIII than within LECIII. This is indirectly supported by recent experiments showing greater recurrent connectivity between principal neurons within MECIII than within other MEC layers, and that MECIII network is crucial in the initiation and maintenance of the Up state during UDS *in vitro* in isolated EC slices [144, 169]. Furthermore, the application of acetylcholine to MEC slice preparations *in vitro* causes prolonged Up states in individual cells due to increased overall excitation and more frequent and rhythmic population-wide events, consistent with our hypothesis that persistent Up states are the result of networks having increased internal excitation W_{INT} [170].

The model with above network connectivity not only predicted the prevalence of SPA and SPI in the efferent neurons but also predicted their relative timing to afferent cortical activity [2, 146], at both population-wide and single-cell resolution. Cells with higher predicted W_{EXT}, and thus stronger coupling, exhibited significantly shorter state transition lags, while larger recurrent excitation W_{INT}, and thus stronger "inertia," had longer lags, as expected. The latency patterns were quite different for Down-Up vs Up-Down transitions: the former was more modulated by W_{EXT}, and the latter more by W_{INT}. Our results thus support the hypothesis that the Up state is terminated by internal network mechanisms but is initiated by external input [102, 119]. Taken together, these mechanisms resulted in systematic differences in the response latencies of MECIII and LECIII neurons during Up and Down states, which would influence the information processing in downstream hippocampal neurons [93, 94] and hence the memory consolidation process via spike timing-dependent

plasticity mechanisms [26].

While several studies have focused on persistent activity during working memory tasks, others have focused on the elevated γ-power in the LFP [73]. Our simple theory can unify these two aspects by showing that small fluctuations in the afferent cortical drive, estimated using the instantaneous γ-power, should have a large impact on the occurrence of SPA and SPI in the efferent entorhinal neurons. Specifically, parietal cortex Down(Up) states with larger(smaller) γ-power were significantly more likely to generate SPA(SPI) in both model and data. Crucially, this meant that fluctuations within afferent Up and Down states led to an all-or-nothing response in the efferent network, and the probability of this all-or-nothing response increased non-linearly with the size of the afferent fluctuation, fitted well by a sigmoid dependence. Our model further predicted that the nature of this sigmoid dependence should itself depend on the fitted connectivity parameters: larger internal recurrence W_{INT} should decrease the threshold in the Down state for SPA, while larger external connectivity W_{EXT} should decrease the threshold in the Up state for SPI. These relationships were corroborated by both model simulations and experiment to a remarkable degree of agreement.

The all-or-nothing response with sigmoid probability dependence to afferent input means that the efferent network can non-linearly amplify input fluctuations. During SPA, the efferent network amplifies positive fluctuations in the afferent Down state, while during SPI, the efferent network amplifies negative fluctuations in the afferent Up state. This nonlinear amplification of γ-power could explain the correlations found between γ-power and memory load and provide the mechanism by which discrete oscillatory dynamics manifest working memory through either persistent activity or elevated γ-power [159, 171, 172]. Given the monosynaptic coupling between MECIII pyramidal cells and the hippocampal CA1 network, along with the fact that CA1 inhibition is phase-locked to cortical UDS, this nonlinear amplification of cortical fluctuations could also explain why hippocampal multi-unit activity during UDS shows significant positive modulation during MECIII SPA when compared to an average cortical Up state [94, 106].

As a direct consequence of the underlying physics of the model, the theory predicted that

both SPA and SPI durations, while showing continuous, long-tailed distributions, should also show quantization in the units of afferent parietal cortical UDS cycles. This too was verified experimentally, with quantitative match between theory and experiment. Our model went further to predict that SPA/SPI was highly history-dependent, reducing the probability of consecutive SPA or SPI, and was also confirmed *in vivo*. This further ruled out alternate mechanisms such as stochastic or statewide variables.

3.7.3 Metabolic and Computational Advantage of Persistent Inactivity

While persistent activity has been studied extensively as the mechanism underlying working memory, it is far more energetically expensive than persistent inactivity. Furthermore, the models involving only persistent activity have a limited storage capacity, especially when dealing with memories that require overlapping representations [173–175]. Persistent inactivity introduces a new mechanism to overcome this difficulty. From an information theoretic perspective, a 0 is just as informative as a 1. Hence, a combination of persistent activity and inactivity would be an efficient scheme for storing overlapping memories by multiplexing the representation, which can manifest as γ-band fluctuations [135, 176]. Related, our theory predicted that the same neuron can show SPA and SPI, and this was experimentally confirmed.

3.7.4 Limitations

The long duration of UDS under anesthesia allowed unequivocal detection of both SPA and SPI. But, since SPA and SPI remained unchanged across a range of anesthesia depths, and SPA has been shown in MECIII during drug-free sleep, these results should be broadly applicable [94]. On the other hand, a large number of biological factors that we did not consider could modulate our system wide findings. For example, in addition to the direct inputs from the parietal cortex to EC, there is substantial indirect input via the perirhinal and postrhinal cortices that we did not consider [177]. Recent studies show some cortical inhibitory neurons that remain active during the down state, which can alter the nature of cortical UDS [178]. Finally, hippocampus receives EC input and projects back to EC, and

EC projects back to the frontal cortices; these connections were not included in our model, but could be studied in the future [89]. Despite this, the simple model was able to predict and match a large amount of experimental observations in a quantitative and cell-by-cell manner. Thus, future studies can build on this approach to study SPA/SPI during drug-free sleep.

3.7.5 Conclusions

These results demonstrate that during UDS, the rich dynamics of the entire cortico-entorhinal circuit can be captured in a quantitatively precise fashion using just two variables: the cortico-entorhinal excitation and the recurrent excitation within the entorhinal cortex. Given the direct and indirect pathways linking the entorhinal region to the hippocampus, the decoupling of entorhinal activity from neocortical inputs during SPA and SPI could contribute to selective removal, strengthening, and weakening of memory traces from the hippocampus during slow-wave sleep, thus improving the signal to noise ratio in the space of memories, thereby improving experimentally observed task-related performance. Our theory is sufficiently general and could equally well apply to other networks, e.g. parietal-prefrontal network, where persistent activity is seen during working memory tasks. Recent studies have suggested that γ-oscillations play a crucial role in this process. Our results integrate these findings to show that the γ-power of the input network differentially regulates the persistent activity and inactivity in the efferent network. Thus, a simple, two parameter network and fluctuations could predict more than a dozen experimentally testable phenomena, which were all quantitatively verified *in vivo*. This approach provides a powerful technique to understand the functional connectivity between large networks of neurons.

Chapter 4

SPA and SPI modulate Cortico-Entorhinal-Hippocampal Dialogue *in vivo*

Dialogue between networks of the neocortex, entorhinal cortex, and hippocampus during sleep are fundamental in processes governing memory consolidation and learning. However, a mechanistic understanding of how these brain regions coordinate their activity remains elusive. The recently described spontaneous persistent activity (SPA) and inactivity (SPI) provide a potential substrate for these processes; while the mean-field mechanisms implicated in the generation of SPA and SPI is general and widely applicable, SPA has only been detected in layer 3 neurons on the medial entorhinal cortex (MEC), and SPI in only the layer 3 neurons of both the medial and lateral entorhinal cortex (LEC). Here, we expand on previous investigations and find that SPA and SPI are ubiquitously found in the extended parahippocampal circuit, including neurons in layer 2 of both MEC and LEC, granule cells in the dentate gyrus, and interneurons in the hippocampal CA1 network. Further, we show that cortical high-frequency power not only determines the probability of SPA and SPI but also the fine-timescale coordination between cortical and efferent entorhinal and hippocampal networks during synchronous UDS. Finally, we show that SPA and SPI in entorhinal and hippocampal subpopulations have drastic effects on downstream hippocampal activity; specifically, these subnetworks amplify the signals. These findings could elucidate the mechanism by which coordinated activity across brain regions can lead to memory consolidation and learning.

4.1 Cortico-Entorhinal-Hippocampal Connectivity

Higher order functions, like memory, learning, and cognition, rely on distributed and co-operative activity of multiple large brain networks, distributed in distant regions of the brain. Specifically, neocortical-hippocampal interactions lay at the foundation of information processing for several forms of memory [25, 26, 29, 89, 93, 138]. Memory consolidation is thought to occur during slow-wave-sleep (sometimes called non-rapid eye movement sleep, or NREM sleep), when neocortical networks spontaneously transition between a quiescent "Down" state and an active "Up" state. The hippocampus, on the other hand, shows weak or non-existent correlation to these oscillations [93, 105]. Previous studies have found that when neurons in layer 3 of the medial entorhinal cortex persist in the "Up" state, i.e. exhibit spontaneous persistent activity (SPA), hippocampal circuits are excited at times when neocortical neurons are silent [94]. This finding suggests that MEC firing during UDS may gate the information flow needed for the consolidation of different types of memories and could serve as a source for the observed neocortical-hippocampal decoupling during SWS.

Anatomically, the entorhinal cortex is the major input and output structure of the hippocampal formation, forming the nodal point in cortico-hippocampal circuits [134, 179, 180]. Multimodal, as well as highly processed unimodal sensory inputs converge at the level of neurons in the superficial layers of the entorhinal cortex. This input is then processed by the entorhinal circuit and conveyed to the hippocampal formation by neurons in layer 2 and layer 3 of the entorhinal cortex. These two layers differentially target hippocampal areas: while layer 3 targets the CA1 cell layer directly, layer 2 targets the dentate gyrus, which then feedsforward to area CA3, which in turn feeds forward to area CA1. In turn, the hippocampal formation, especially the CA1 cell layer and the subiculum, are the main source of projections back to the entorhinal cortex, specifically layer 5. Layer 5 neurons in turn project to widespread cortical and subcortical domains in the forebrain. Recent electrophysiological recordings show that cells in MEC are predominantly spatially modulated; in contrast, cells in the LEC care about objects in context [141–143, 181–183]. How these differences in properties of the two subdivisions carry forward to the hippocampus

and back is still a mystery. The ubiquity of connections, along with the demonstrated role of the entorhinal and hippocampal formations in learning and memory, make the cortico-entorhinal-hippocampal circuit and ideal substrate to study complicated network interactions *in vivo*. While extensive studies have been conducted on these brain regions, analysis of simultaneous activity between all four regions, and thus a systematic understanding of how activity propagates from one network to another, is lacking.

4.2 Synchronous and Asynchronous UDS in the extended para-hippocampal region

Details of the experimental procedures are outlined in the Appendix, and are briefly described here. Mice were lightly anesthetized with urethane to induce robust and steady UDS that were synchronous across the entire neocortex. The local field potential in the parietal cortex (PAR), the hippocampal CA1 cell layer (CA1), and the dentate gyrus (DGG) was measured using a silicon multi-electrode array; simultaneously, we did whole-cell V_m measurements from anatomically identified pyramidal neurons in neocortical, paleocortical, and hippocampal regions. In the neocortex, we recorded from pyramidal neurons in superficial layers of the parietal (PAR), prefrontal (PRE), and frontal (FRO) cortices. In the lateral entorhinal cortex, we recorded from fan cells in layer 2 (LECII) and pyramidal cells in layer 3 (LECIII). In the medial entorhinal cortex, we recorded from stellate cells in layer 2 (MECII), pyramidal cells in layer 3 (MECIII), and layer 5 (MECV). Finally, in the hippocampus we recorded from interneurons in CA1 (CA1i), pyramidal cells in CA1 (CA1p) and CA3 (CA3p), and granule cells in the dentate gyrus (DGg). The combination of simultaneous recordings from four locations (the neocortical LFP, V_m from a single neuron in a specific region, hippocampal CA1 LFP, and hippocampal dentate gyrus LFP) during Up-Down states allowed for the analysis of inter-regional dialogue in the absence of sensory stimulus.

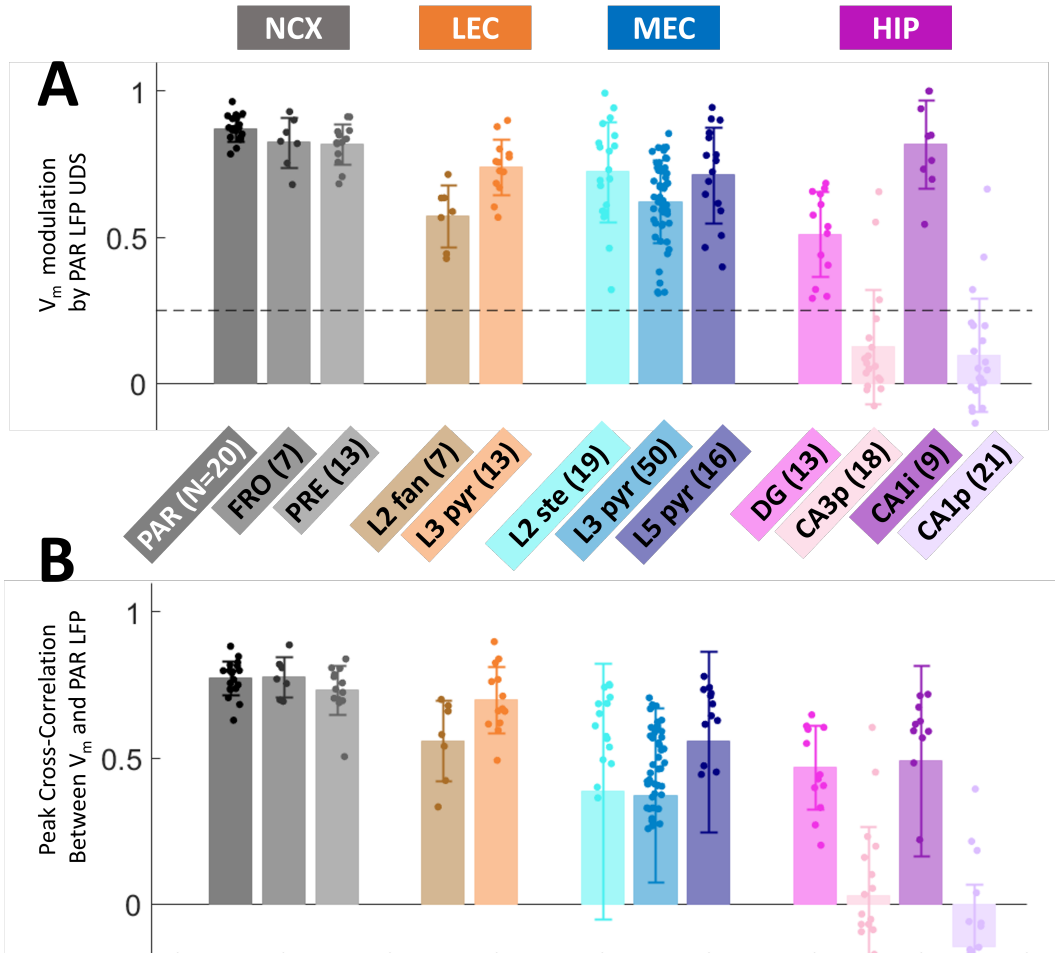

Figure 4.1: Modulation of neuron's V_m during neocortical UDS. A) UDS was detected in PAR LFP, and the modulation was calculated using the amplitude difference between the V_m during Up vs. Down states. Across the neocortical region, Parietal (PAR) neurons showed the highest modulation (0.88 $\pm$ 0.04), followed by Frontal (0.83 $\pm$ 0.09) and Prefrontal (0.82 $\pm$ 0.07). Lateral entorhinal cortex neurons also showed significant modulation (LECII: 0.58 $\pm$ 0.1; LECIII: 0.74 $\pm$ 0.1). Medial entorhinal cortex neurons also showed significant modulation (MECII: 0.73 $\pm$ 0.17; MECIII: 0.63 $\pm$ 0.14; MECV: 0.72 $\pm$ 0.16). Hippocampal neurons had mixed responses. Dentate granule cells (DG: 0.52 $\pm$ 0.15) and CA1 interneurons (CA1i: 0.82 $\pm$ 0.15) showed significant modulation, but CA3 and CA1 pyramidal neurons did not (CA3p: 0.13 $\pm$ 0.2; CA1p: 0.09 $\pm$ 0.2). B) Similar results were found for the peak (either positive or negative) of the cross-correlation between the PAR LFP and V_m of neurons. Neocortical neurons showed the highest correlation (PAR: 0.78 $\pm$ 0.06; FRO: 0.78 $\pm$ 0.07; PRE: 0.73 $\pm$ 0.08), followed by lateral entorhinal neurons (LECII: 0.56 $\pm$ 0.14; LECIII: 0.70 $\pm$ 0.12) and medial entorhinal neurons (MECII: 0.39 $\pm$ 0.44; MECIII: 0.38 $\pm$ 0.30; MECV: 0.56 $\pm$ 0.31). Finally, hippocampal neurons showed mixed modulation, with dentate granule and CA1 interneurons showing significant correlation (DG: 0.46 $\pm$ 0.14; 0.50 $\pm$ 0.32), but CA3 pyramidal neurons showed little to no correlation (0.3 $\pm$ 0.23) and CA1 pyramidal neurons showed weak negative correlation (0.14 $\pm$ 0.21).

4.2.1 UDS modulation in parahippocampal networks

A hidden Markov Model was used to classify the parietal LFP into a binary UDS sequence [145]. The UDS modulation of specific neurons was then found using two methods (Fig. 4.1). First, the peak of the cross-correlation between the broadband parietal LFP and the V_m of each neuron was used to assess UDS modulation. This measure, however, is really a measure of similarity between the LFP in PAR and the V_m of each neuron, and is not necessarily a reflection of the Up-Down modulation. For a more stringent measure, we calculated the amplitude difference, in units of z-score, between the V_m of neurons during those times when the PAR LFP showed an Up state and those times when the PAR LFP showed the Down state. To adjust for the differential timing between the PAR UDS and each neuron's V_m, we used the lag of the peak cross-correlation.

Both methods produced similar results. PAR pyramidal neruons showed the highest modulation to PAR LFP Up-Down states, as expected, since the neuron and the electrode are within the same brain region. Other neocortical areas like FRO and PRE also showed significant modulation, which is expected, given that these neurons are also in the neocortex. In the entorhinal cortex, all neural subtypes showed significant modulation to PAR UDS, but this modulation was significantly weaker than for neocortical neurons. Within LEC, layer 3 pyramidal neurons showed higher modulation compared to layer 2 fan cells. Within MEC, layer 3 pyramidal neurons showed the weakest modulation, and layer 2 and layer 5 cells showed higher modulation. Finally, within the hippocampus, only dentate granule cells and CA1 interneurons showed significant modulation to PAR UDS, consistent with previous studies. CA1 pyramidal neurons showed weak negative modulation, while CA3 pyramidal neurons showed no modulation at the population level. Given these profiles for each neural subtype, we excluded CA1 and CA3 pyramidal neurons from our subsequent analysis of network interactions during UDS. These results are in broad agreement with previous studies [93, 94, 105, 106], but of note is the fact that these studies did not differentiate between layer 2 in MEC vs LEC.

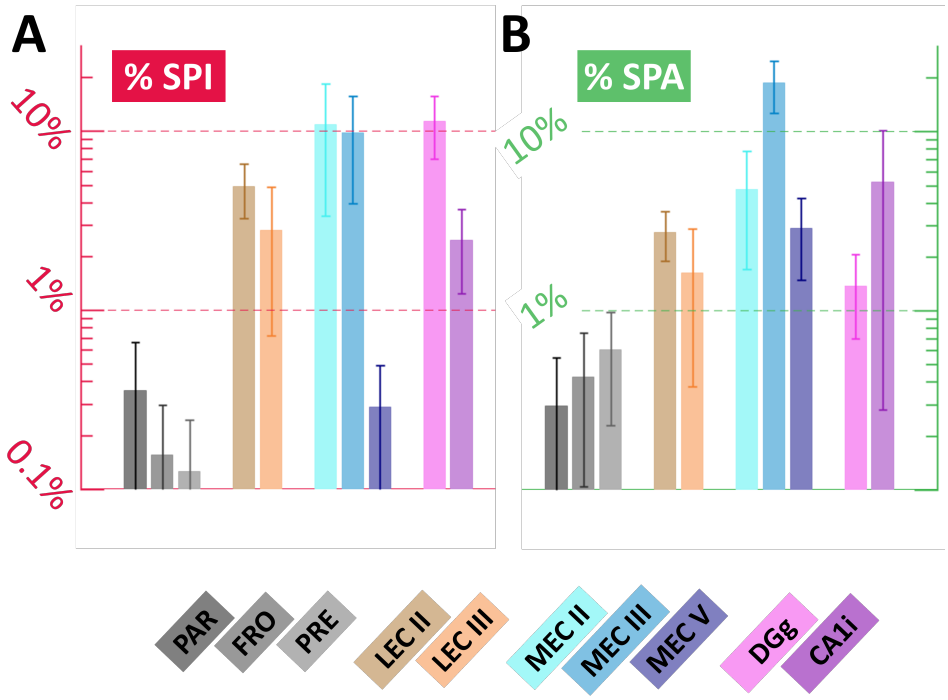

Figure 4.2: SPA and SPI occur in almost all parahippocampal regions. A) The prevalence of SPI within neurons of a population, averaged over each population. Color code is indicated at bottom. Neocortical neurons had the smallest amount (PAR: 0.3±0.2%, FRO: 0.2±0.2%, PRE: $0.2 \pm 0.2\%$). LEC neurons showed significant SPI (LEC II : $8 \pm 2\%$, LEC III: $6 \pm 1\%$), along with superficial layers of MEC (MEC II : $11 \pm 4\%$, MEC III: $10 \pm 5\%$). Deep layers showed virtually no SPI (MEC V: $1 \pm 2\%$). Finally, hippocampal subfields also showed significant SPI (DG : $11 \pm 4\%$, CA1 inter: $3 \pm 2\%$). B)The prevalence of SPA within neurons of a population, averaged over each population. Neocortical neurons had the smallest amount (PAR: $0.3 \pm 0.2\%$, FRO: $0.4 \pm 0.2\%$, PRE: $0.5 \pm 0.2\%$). LEC neurons showed significant SPI (LEC II : $4 \pm 2\%$, LEC III: $2 \pm 1\%$), along with superficial layers of MEC (MEC II : $7 \pm 4\%$, MEC III: $20 \pm 5\%$). Deep layers showed virtually no SPA (MEC V: $2 \pm 2\%$). Finally, hippocampal subfields also showed significant SPA (DG : $2 \pm 4\%$, CA1 inter: $8 \pm 2\%$).

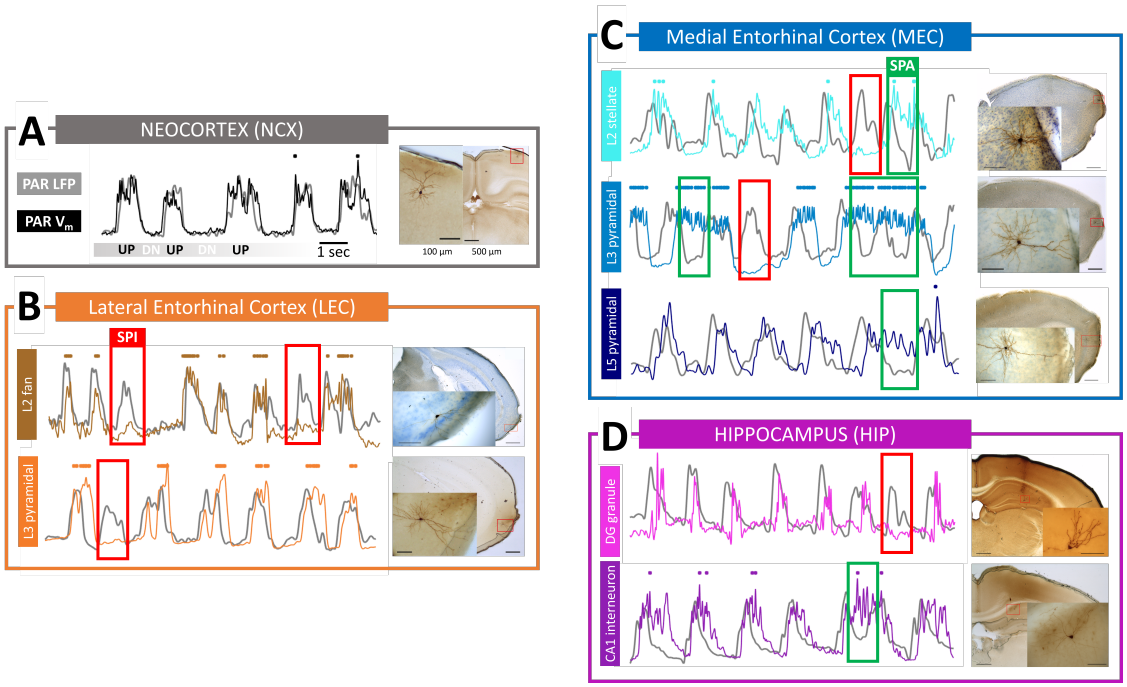

Figure 4.3: SPA and SPI are observed across the entorhinal-hippocampal circuit. A) The simultaneously recorded PAR LFP and V_m from a pyramidal neuron show completely coherent behavior, alternating between Up and Down states. Histology of the neuron is shown on the right, with scale bars indicated. The same scale bar for time (1 second) is used throughout. B) The lateral entorhinal cortex layer 2 fan cells and layer 3 pyramidal cells both show instances of persistent inactivity (SPI, red boxes). C) The medial entorhinal cortex layer 2 stellate cells show both SPI and persistent activity (SPA, green boxes). Same for MEC layer 3 pyramidal cells. MEC Layer 5 pyramidal cells show SPA. D) We focus on the hippocampal subfields which are modulated by cortical UDS. Dentate gyrus granule cells show SPI, and interneurons in CA1 shows SPA.

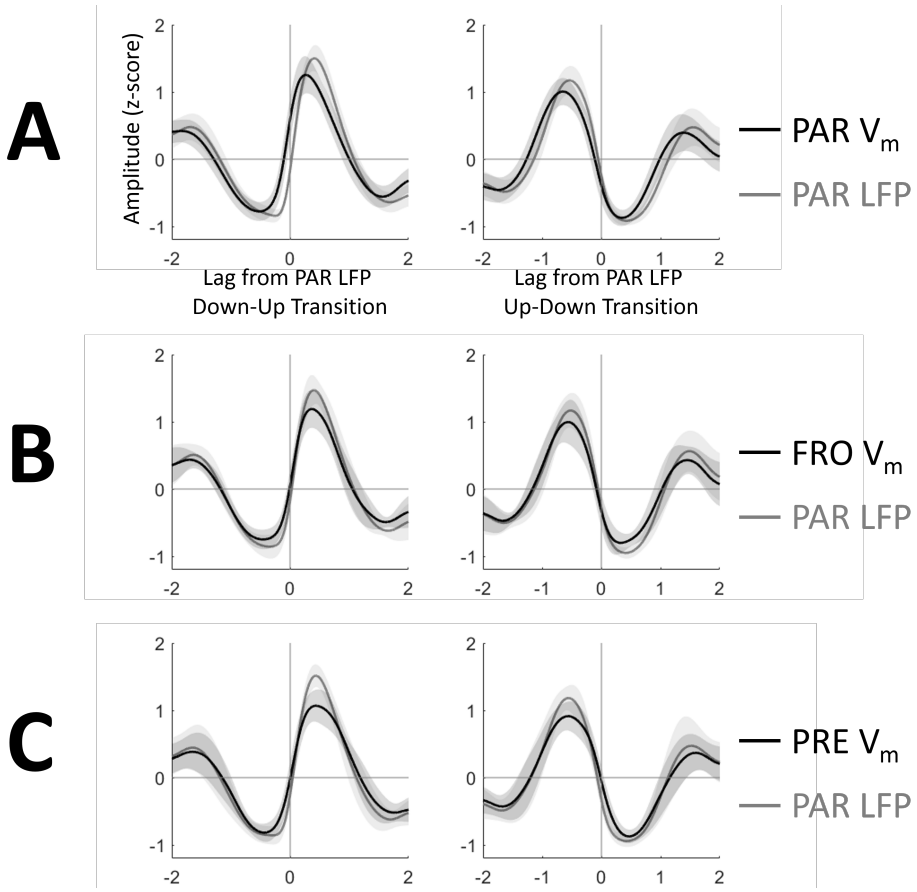

Figure 4.4: Neocortical neurons undergo synchronous transitions with respect to parietal LFP transitions. A) Parietal cortex LFP (gray) and V_m (black) triggered on the LFP Down-Up transition (left) and Up-Down transitions (right) showed synchrony. The parietal cortex V_m preceded the LFP transitions. The average is across all experiments involving parietal cortex V_m. shaded regions indicate ± 1 standard deviation. B) Same as A, but for frontal cortex membrane potential. C) Same as A, but for prefrontal cortex neurons.

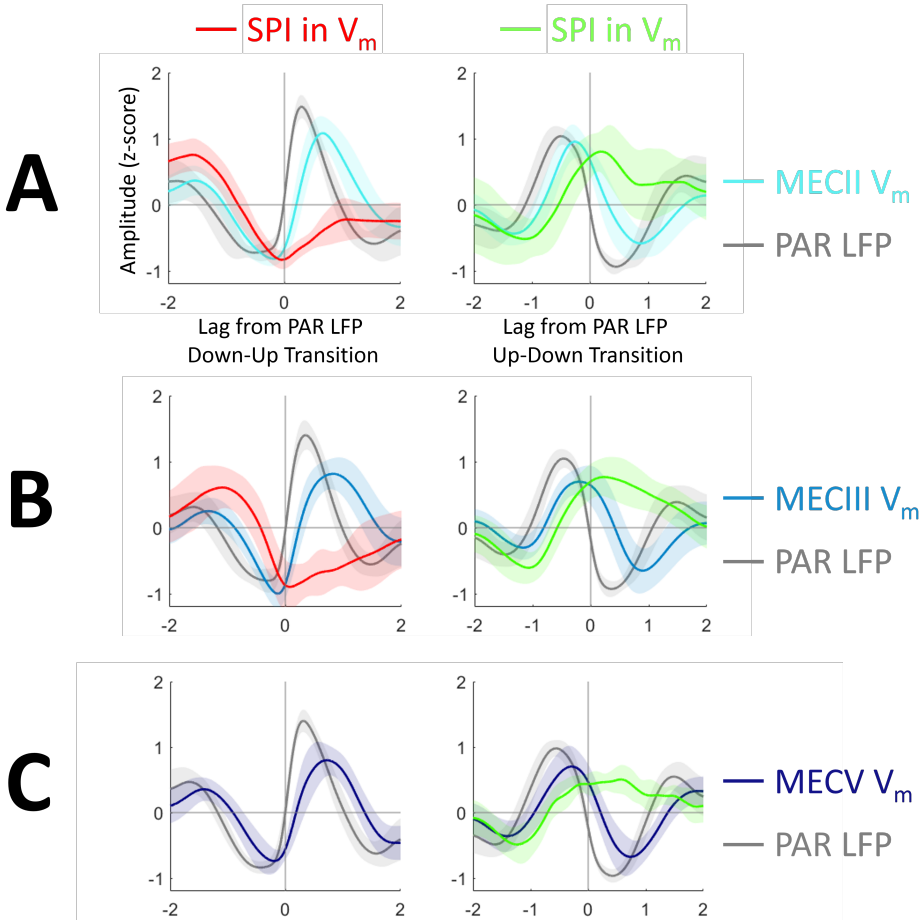

Figure 4.5: Medial entorhinal cortex neurons undergo synchronous transitions with respect to parietal LFP transitions, but can exhibit both SPA and SPI. A) Parietal cortex LFP (gray) and MEC Layer 2 stellate cell V_m (blue) triggered on the LFP Down-Up transition (left) and Up-Down transitions (right) showed synchrony, along with instances of SPI (red) and SPA (green). The membrane potential significantly followed the parietal LFP. B) Same as A, but for MEC Layer 3 pyramidal neurons. This population also shows significant SPI and SPA. C) Same as A, but for MEC Layer 5 pyramidal neurons. This population only shows SPA, not SPI.

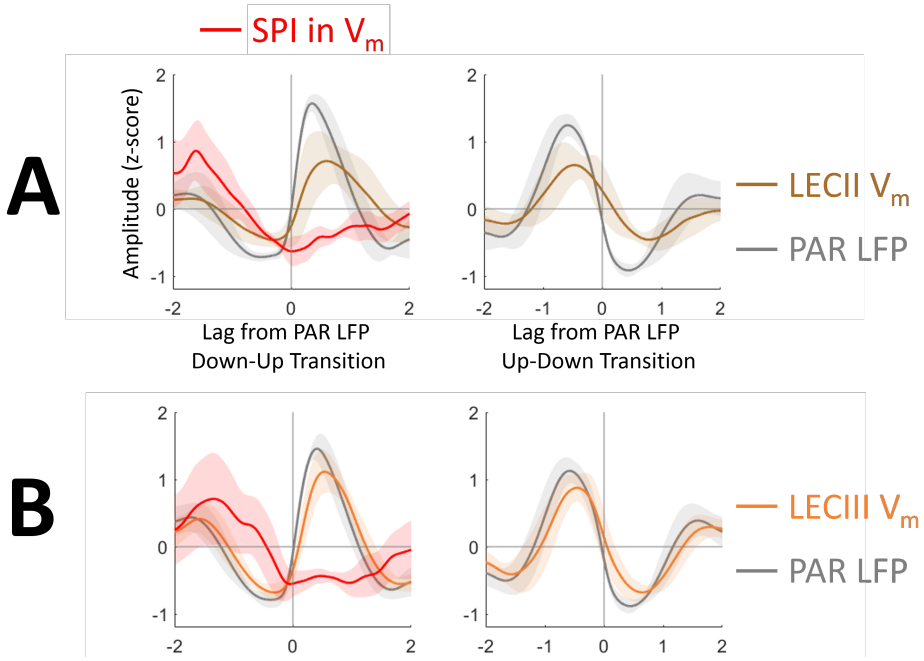

Figure 4.6: Lateral entorhinal cortex neurons undergo synchronous transitions with respect to parietal LFP transitions, but can exhibit SPI. A) Parietal cortex LFP (gray) and LEC Layer 2 fan cell V_m (orange) triggered on the LFP Down-Up transition (left) and Up-Down transitions (right) showed synchrony, along with instances of SPI (red). The membrane potential significantly followed the parietal LFP. B) Same as A, but for LEC Layer 3 pyramidal neurons. This population also shows significant SPI.

4.2.2 SPA and SPI in the extended parahippocampal circuit

Detection of UDS sequences within the V_m of neurons was done using a modified approach from the one used in earlier work, because not all populations expressed bimodal V_m during UDS, and thus using the Hidden Markov Model from earlier gave unreliable results. Instead, UDS sequences were detected in parietal LFP; this was used as a universal clock for the entire experiment. The behavior of V_m during this clock was used to detect SPA and SPI. This new method was employed to expand the applications of our method to neuronal populations which did not exhibit bimodaly distributed V_m but were still modulated by parietal UDS, like DG granule cells and LECII fan cells. Details can be found in the Appendix B.

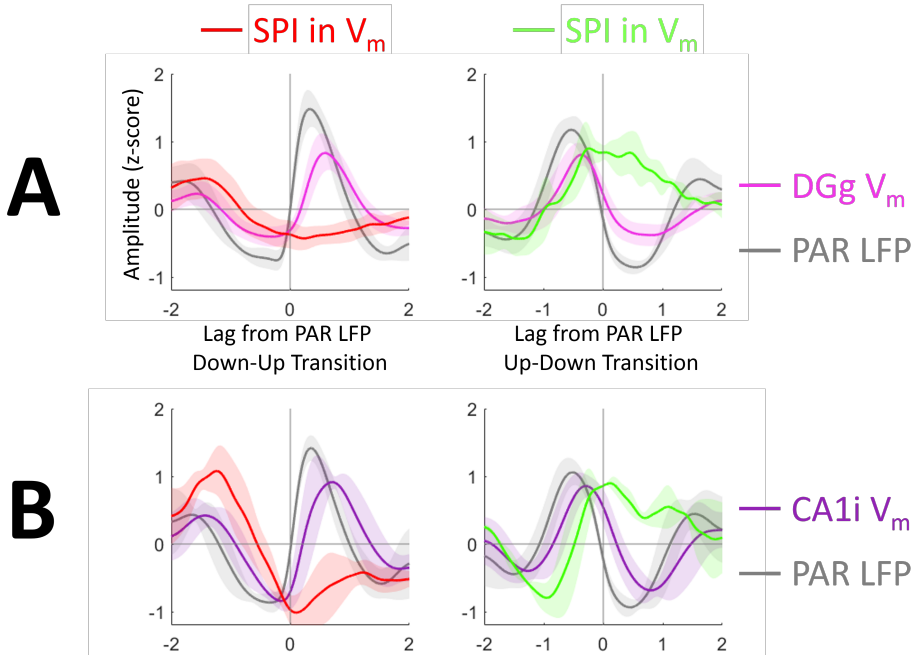

Figure 4.7: Dentate gyrus granule cells and interneurons in CA1 cell layer of the hippocampus undergo synchronous transitions with respect to parietal LFP transitions, but can exhibit both SPI and SPA. A) Parietal cortex LFP (gray) and Dentate Gyrus granule cell V_m (purple) triggered on the LFP Down-Up transition (left) and Up-Down transitions (right) showed synchrony, along with instances of SPI (red) and SPA(green). The membrane potential significantly followed the parietal LFP. B) Same as A, but for CA1 interneurons. This population also shows significant SPI and SPA.

We confirmed the presence of SPA and SPI in MECIII cells, and SPI in LECIII cells; the average prevalence of SPA and SPI found using this new method were comparable to that found using the more stringent, paired UDS method 4.2. In addition to these brain regions, we also found SPA and SPI across the parahippocampal region 4.3. MEC layer II stellate cells displayed both SPA and SPI, sometimes in the same cell. MEC layer V pyramidal cells showed instances of SPA, but rarely SPI 4.5. In the LEC, layer 2 fan cells showed SPI but not SPA, similar to the behavior of layer 3 pyramidal cells4.6. Finally, both dentate gyrus granule cells and CA1 interneurons showed instances of SPA and SPI4.7. Neocortical neurons again showed no SPA or SPI 4.4

4.2.3 Power Spectra and Cross-Region Coherence

To confirm that the UDS oscillations in the brain were present in the V_m across brain regions, we first calculated the power spectrum of each trace 4.8. As expected, all brain regions that were significantly modulated by parietal UDS showed a peak in the delta band (0.5-1 Hz), while CA3 and CA1 pyramidal neurons did not show a significant peak.

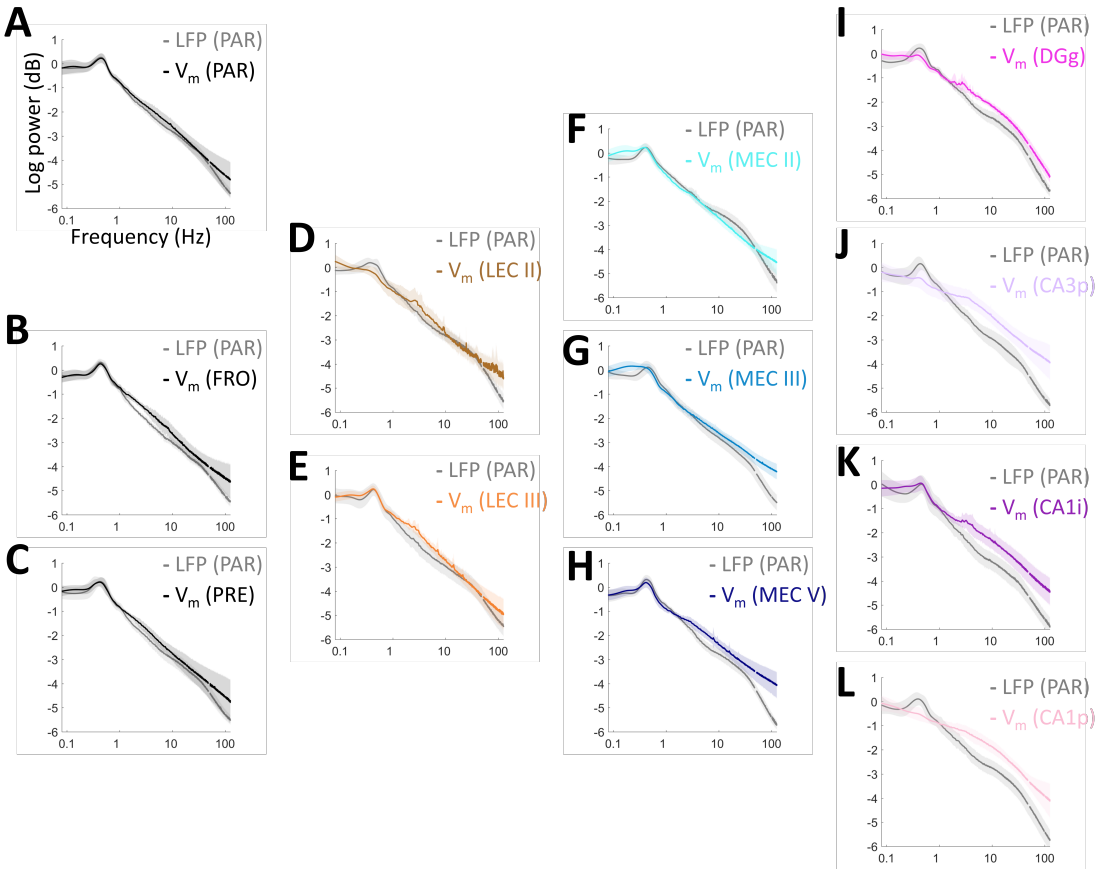

Figure 4.8: Power spectra across all cell populations, along with corresponding parietal LFP power spectra, on log-log scale, showing delta modulation (or lack thereof) in cortex and hippocampus. A) Both parietal cortex LFP and V_m showed a peak in the power spectra within the delta band (<1Hz). Shaded regions represent ±1 s.t.d. B) Same as A, but for frontal cortex neurons. C) Same as A, but for Prefrontal cortex neurons. D) LECII fan cells do not show characteristic peak in delta band. E) LECIII neurons, however, do. F-H) Neurons in MEC layer 2,3, and 5 all show significant peaks in the delta band. Continued on next page.

Figure 4.8: I) Dentate gyrus granule cells show a small peak in the delta band. J) CA3 pyramidal cells show a peak in the delta band, but the peak is not significant, since only about three neurons contribute, while the others show no modulation to the delta band. K) CA1 interneurons show significant peak in the delta band. L) CA1 pyramidal neurons did not show significant modulation in the delta band.

We then calculated the coherence between the parietal LFP and the V_m trace over frequencies ranging from 0.1-100 Hz, and the phase difference within each frequency4.9. Neurons of the neocortex, entorhinal cortex, the dentate gyrus, and CA1 interneurons all exhibited significantly coherent oscillations in the delta band, with the coherence dropping to chance level at higher frequencies. In neocortical neurons, the phase difference decreased with increasing frequency, while for LEC, MEC, and hippocampal neurons with significant coherence, the phase difference increased. This reflects that fact that neoceortical neurons either precede or are coincident with parietal LFP, while entorhinal and hippocampal neurons lag behind. This absolute time lag will manifest as a phase shift at different frequencies; neurons which precede the LFP will show higher phases for higher frequencies [93]. All subpopulations in the cortex were in phase with parietal LFP, but CA1 pyramidal neurons were predominantly out of phase. CA3 and CA1 pyramidal neurons showed highly diminished coherence compared to other cortical neurons, in agreement with the fact that both CA3 and CA1 subpopulations are not modulated by cortical UDS [105].

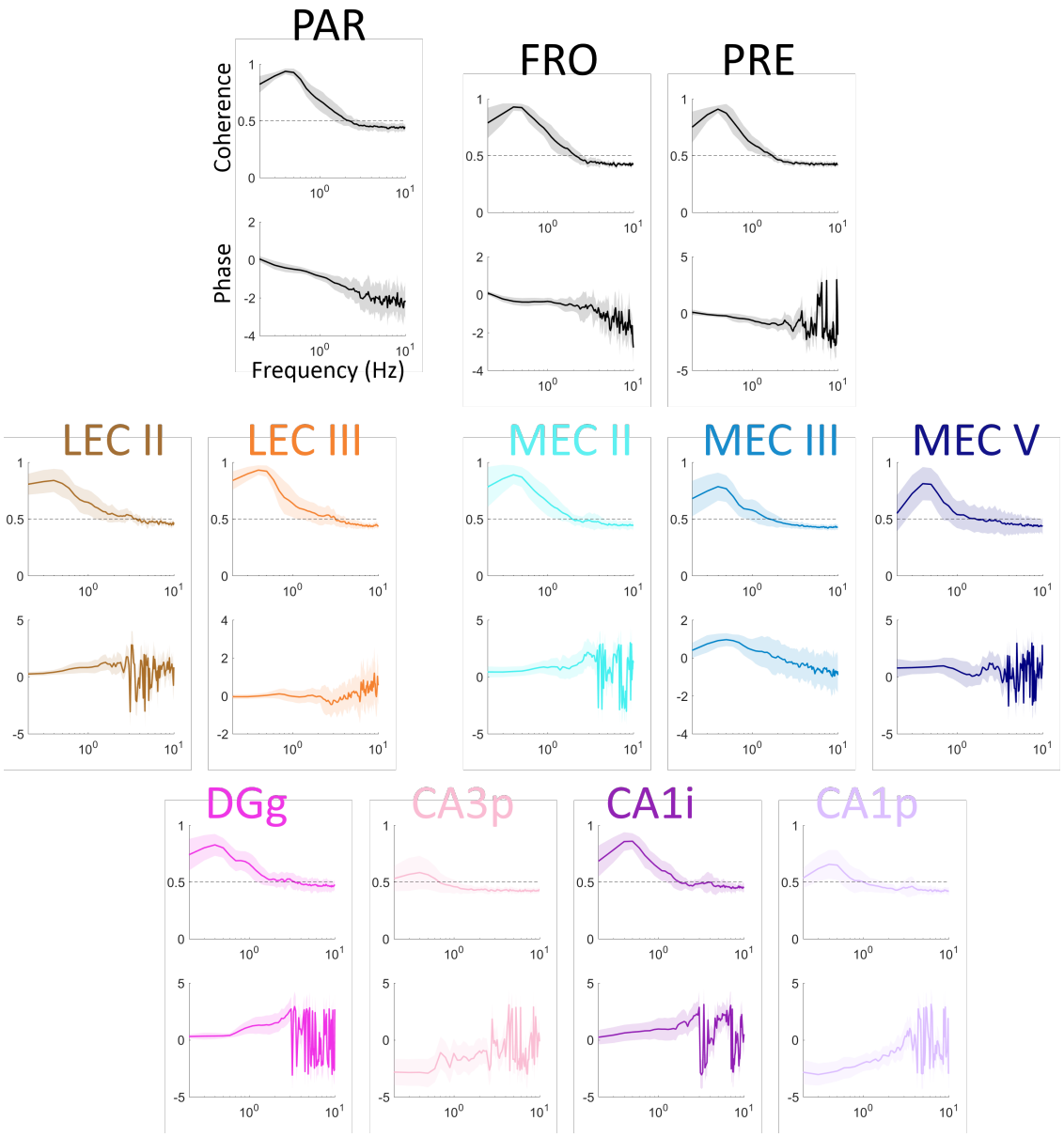

Figure 4.9: Cross-spectral coherence between parietal cortex LFP and populations of neurons in brain regions. A) Top: Parietal cortex neurons were significantly coherent with neighboring LFP from all frequencies lower than 15 Hz. Above this band, the coherence was not significantly different from chance (0.5, dotted line). Bottom: the phase difference between the V_m and the LFP decreased with increasing frequency, indicating that there was a constant time lag between the two signals, with V_m preceding LFP. Shaded regions indicate ± 1 s.t.d. B) Same as A, but for frontal and prefrontal neurons. Both show significant coherence for frequencies below 15 Hz, and a decrease in phase w.r.t. LFP. Continued on next page.

Figure 4.9: C) Same as A, for LEC Layer 2 fan cells and LEC Layer 3 pyramidal cells. Both show significant coherence, but LEC III has significantly stronger coherence to parietal LFP compared to LEC II. The phase increases for LECII fan cells, but not LEC III cells, due to differential lag. D) Cells in MEC layer 2, 3, and 5 all show significant coherence at frequencies below 10 Hz, and increase their phase with frequency, reflecting the fact that MEC neurons significantly lag behind the PAR LFP. E) Hippocampal neurons have mixed responses, varying with subpopulation. Dentate gyrus granule (DGg) cells had significant coherence to parietal LFP below 10 Hz, and the phase increased with frequency in this band. CA3 pyramidal neurons did not show significant coherence. CA1 interneurons showed significant coherence, and the phase increased with frequency. CA1 pyramidal neurons, on the other hand, showed slight coherence in the lower frequency bands, but were out of phase with parietal LFP. The phase also increased with frequency.

4.2.4 Latency between parahippocampal and neocortical activity

To compliment the analysis of spectral coherence, we calculated the transition-specific lag between the parietal LFP and the V_m of neurons in each subpopulation. We confirmed our earlier observations about neocortical neurons and LECIII and MECIII neurons. Further, we found that LECII neurons followed parietal Down-Up transitions at significantly longer lags than LECIII neurons. Additionally, MECII neurons followed PAR Down-Up transitions at a longer lag than MECIII neurons, while MECV neurons followed PAR Down-Up transitions at a shorter lag than MECIII neurons. In the hippocampus, dentate granule cells and CA1 interneurons also followed parietal LFP at similar lags to MEC neurons.

For Up-Down transitions, LECII neurons had similar lags compared with LECIII neurons; both were nearly coincident with parietal LFP Up-Down transitions. In MEC, layer III neurons showed considerably longer Up-Down lags compared to layer II, and still longer than layer V. According to theory, this is due to higher inter-connectivity in the excitatory network. Furthermore, dentate granule cells transitioned to the Down state much sooner than MEC cells, while CA1 interneurons followed with a lag close to that of MEC neurons. These results corroborate those found using the phase-frequency relationship within the coherent bands: namely, those brain areas which preceded the parietal LFP showed decrease in phase with frequency, and vice versa for those regions which followed parietal LFP.

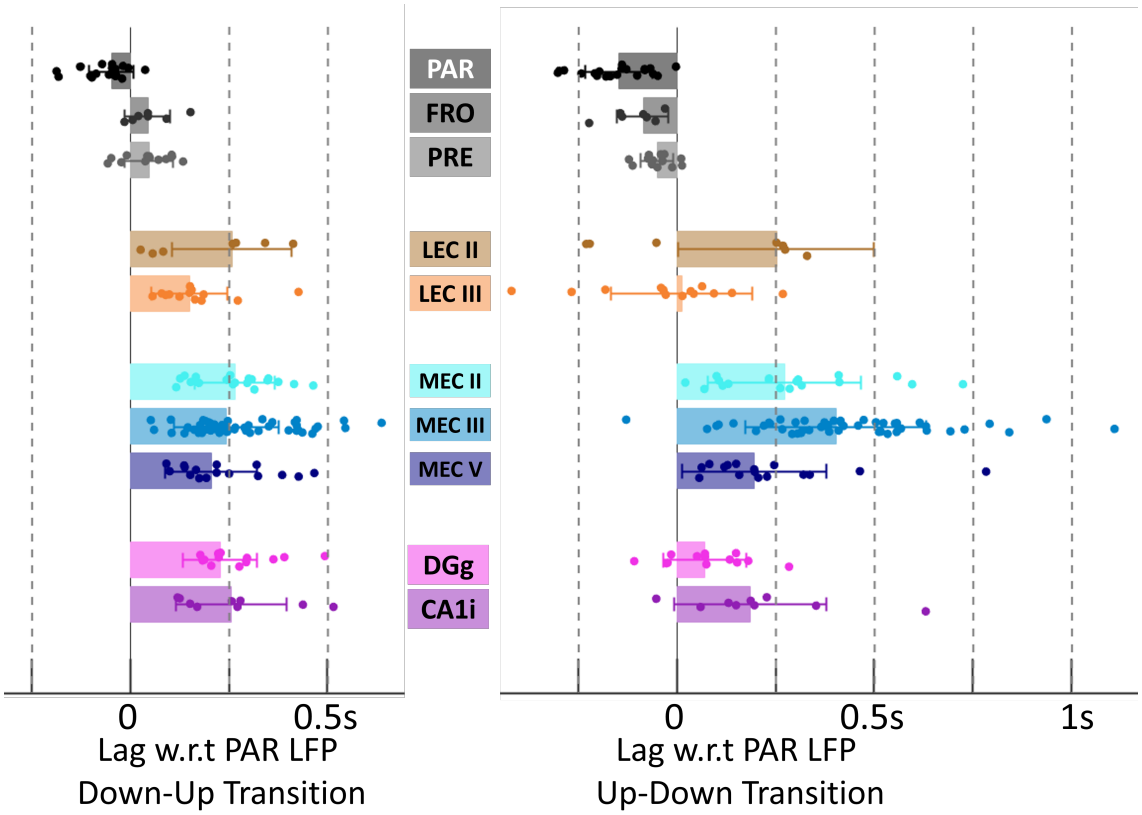

Figure 4.10: Transition lags between parietal LFP and neuronal V_m. Parietal cortex preceded the neighboring LFP for both Down-Up (-50 ± 46 ms) and Up-Down (-167 ± 87 ms) transitions. Frontal cortex neurons followed parietal LFP during the Down-Up transition (26 ± 36 ms) but preceded the Up-Down transition (-71 ± 43 ms). Same with prefrontal neurons (Down-Up: 28 ± 45 ms; Up-Down: -18 ± 12 ms). Lateral entorhinal cortex neurons all followed the parietal LFP, with layer 2 having significantly larger delays than layer 3 (LECII: Down-Up 253 ± 176 ms; Up-Down 250 ± 250 ms; LECIII: Down-Up 172 ± 70 ms; Up-Down 10 ± 167 ms). Medial entorhinal cortex neurons all followed parietal LFP. With Down-Up transitions, the smallest lag occurred in MEC V neurons (235 ± 156 ms), followed by layer 3 (246 ± 135 ms), followed by MEC Layer 2 (265 ± 123 ms). For Up-Down transitions, MEC layer 5 neurons were again with shortest lag (200 ± 189 ms), followed by MEC Layer 2 (261 ± 200 ms) and MEC Layer 3 (403 ± 250 ms). Finally, Dentate Gyrus granule cells and CA1 interneurons also followed parietal LFP, with CA1 interneurons having significantly longer latency (DGg: Down-Up 241 ± 96 ms, Up-Down 89 ± 112 ms; CA1i: Down-Up 251 ± 176 ms, Up-Down 201210 ms).

4.3 Cortical High-Freq Power modulates network interaction strength and timing

Given our theory of cortical interaction, we have shown that SPA and SPI are stochastic events which occur during positive fluctuations in the Down state and negative fluctuations in the Up state. What is the effect of parietal γ-power during synchronous Up and Down states? In the mean field approximation, networks are leaky capacitors; and the larger the input current, the larger the response of the network. Furthermore, the network latency should be shorter. This applies to synchronous Up states as well, and should manifest in the experimental data. To check, we calculated the relationship between parietal gamma power during Up states and the nature of the efferent response.

4.3.1 Timing of synchronous UDS cycles

During an Up state in the parietal cortex, afferent excitation turns on, thereby inducing a Down-Up transition within the efferent neuron. As neuron's are leaky capacitors, the larger the input from the afferent network, the shorter should be the delay to the efferent Down-Up transition. This should manifest within single experiments as well, not just on average, as shown in the previous chapter. This was indeed the case in the *in vivo* data 4.11, where for many cells the lag to the Down-Up transition and the afferent parietal gamma power were significantly negatively correlated.

Across brain regions, cells which exhibited significant correlation between parietal drive and Down-Up transition latency nearly always showed anti-correlation 4.12. The number of cells which showed significant correlation varied across brain regions, however. A majority of cells in the entorhinal cortices showed significant anti-correlation, while only a minority of cells in the neocortex showed anti-correlation. This is despite the fact that entorhinal cortex neurons showed significantly longer lags, on average, to the parietal LFP compared with neocortical neurons. Nearly all cells in the MECIII population showed anti-correlation.

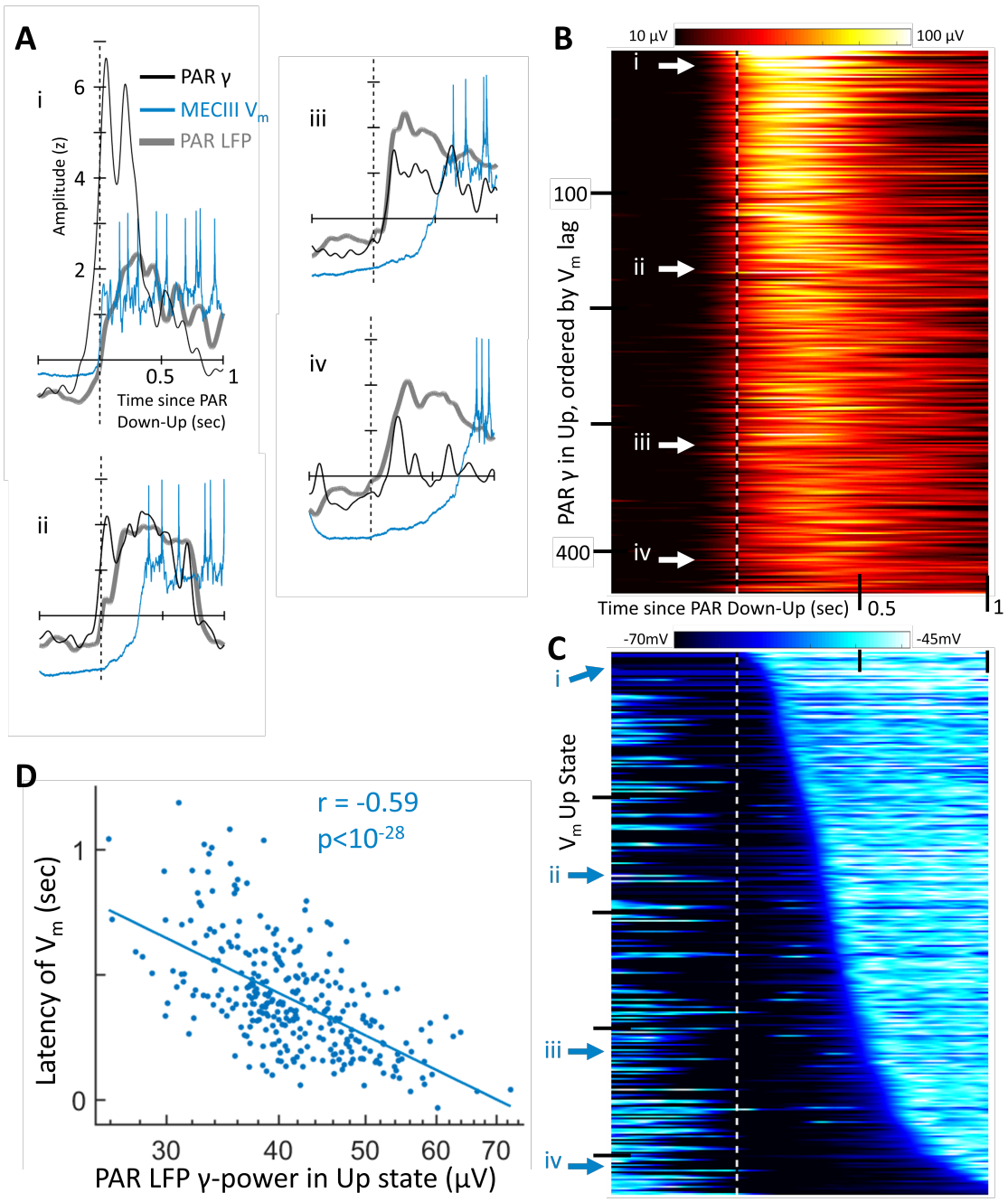

Figure 4.11: Higher gamma power during Up state leads to shorted latencies between afferent drive and efferent Down-Up response. A) Examples from an experiment involving PAR LFP (gray) and MECIII V_m (blue), with the power in the gamma band shown in black. i) For PAR UP states with higher gamma power, the MECIII neuron responds with its own Down-Up transition almost immediately following the PAR LFP Down-UP transition. As the Up state gamma power decreases (ii-iv), the membrane potential lags significantly behind. All data was z-scored across the experiment for display purposes. Continued on next page.

Figure 4.11: B) All data from the parietal LFP gamma power was arranged into a matrix, and aligned by the PAR Down-Up transition. The traces were then ordered by the lag between Down-Up transition in PAR LFP and the same transition in MECIII V_m (shown in C). The traces in (A) are shown as columns in (B) and (C). Clearly, those transitions that induced shorter lags had more gamma power. D) The average gamma power in the PAR LFP during the Up state was plotted against the latency during that transition, showing significant negative correlation.

The converse effect happens during the Up-Down transition, as higher gamma power in the parietal Down state should increase the lag in the efferent network to its own Up-Down transition, since the extra current coming in from the afferent network can help sustain the efferent Up state for longer. This was indeed the case, as nearly all cells which showcased significant correlation showed positive correlation. Unlike the Down-Up transition, the Up-Down transition was far more independent of the parietal drive. In most regions, only a minority of cells showed any correlation; within MEC, layer 3 pyramidal neurons were the most independent. Across populations, dentate granule cells showed the highest likelihood of showing a correlation between parietal drive and the Up-Down latency. We repeated this analysis using the time lag between a parietal transition and when the V_m reached 80% of its peak amplitude during the Up state (or 20% the Down state amplitude for Up-Down transitions), which yielded extremely similar results 4.13.

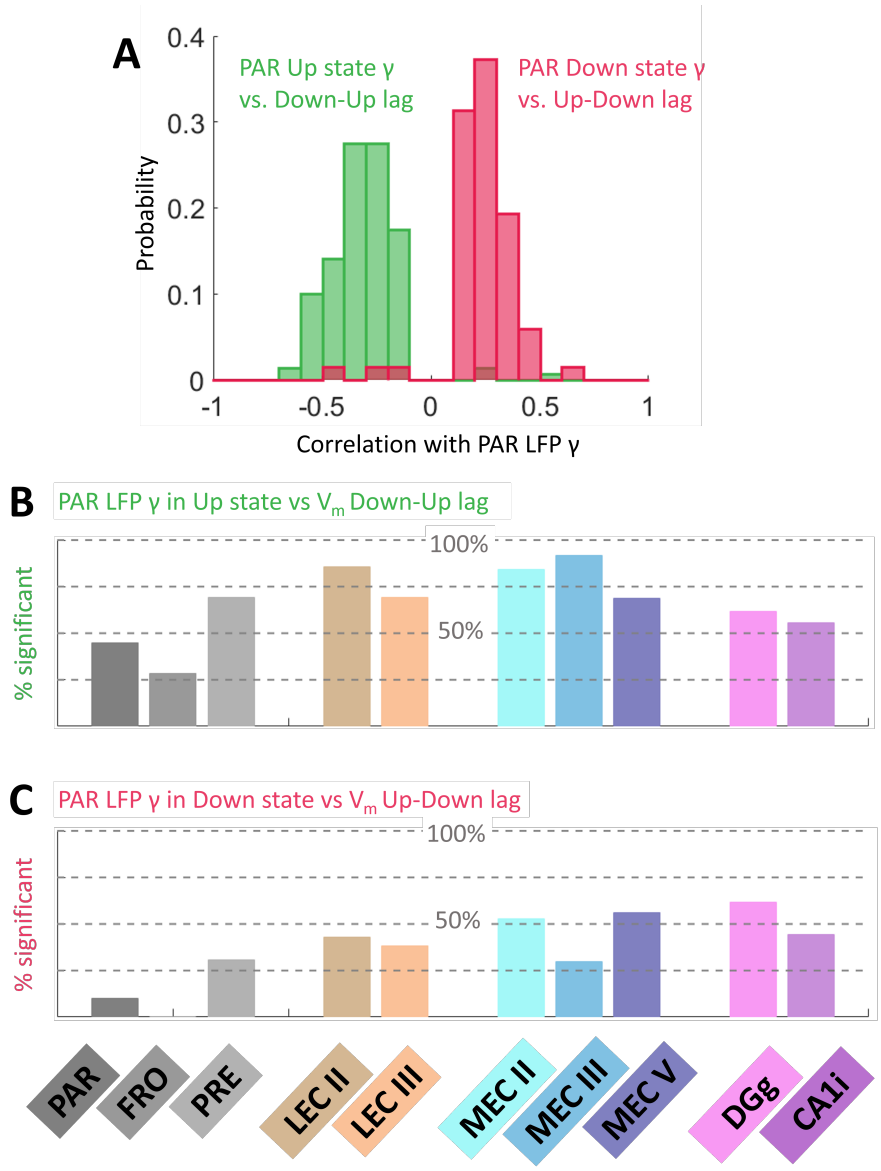

Figure 4.12: Correlation between Timing and Cortical Gamma Drive across neuronal subpopulations A) Across all populations of neurons, significant correlations between the PAR Up state gamma and the V_m Down-Up lag was almost always negative. Conversely, significant correlations between PAR Down state gamma and the V_m Up-Down lag was almost always positive. B) The number of cells which exhibited significant anti-correlation between their Down-Up lag and the PAR gamma drive varied with brain region and cell type. 48% of parietal cells showed significant correlation, only 26% of frontal neurons and 73% of prefrontal neurons showed significant correlation. In LEC, 80% of LECII and 72% of LECIII neurons showed significant correlation. MEC showed the highest correlation, with 82% of MECII cells, 93% of MECIII cells, and 71% of MECV cells showing significant correlation. In hippocampus, 60% of Dentate granule cells and 55% of CA1 interneurons showed significant correlation. Caption continued on next page.

Figure 4.12: C) Same as B, but now for Up-Down lag and gamma drive in the Down state. 10% of parietal cells showed significant correlation, only 0% of frontal neurons and 30% of prefrontal neurons showed significant correlation. In LEC, 40% of LECII and 32% of LECIII neurons showed significant correlation. MEC showed the highest correlation, with 55% of MECII cells, 29% of MECIII cells, and 55% of MECV cells showing significant correlation. In hippocampus, 62% of Dentate granule cells and 45% of CA1 interneurons showed significant correlation.

To further quantify the relationship between afferent drive and the timing of Down-Up transitions, we calculated the slope in the linear relationship between the parietal gamma drive and the timing lag 4.14. We restricted our analysis to only those cells which exhibited significant anti-correlation between the two quantities. MEC III neurons showed the largest negative slope, followed by LEC II neurons, followed by the hippocampal subfields. Further, parietal, MECII, MECIII, and dentate neurons showed a negative correlation between the average lag to the Down-Up transition and the slope of the relationship, which is expected. The other subpopulations did not show significant correlation between the two quantities. Another consequence of the capacitative properties of neurons is that the afferent drive should not only be inversely related to the Down-Up transition lag, it should also be inversely related to the time it takes for the neuron's V_m to transition from the hyperpolarized Down state to the depolarized, active Up state. This was indeed the case in the *in vivo* data, which showed significant negative correlation between the transition time and the parietal LFP gamma among those cells which were significantly correlated 4.15. Conversely, the greater the afferent gamma power in the Down state, the longer the neuron takes to transition from the Up state back into the Down state. Again, this was corroborated by the *in vivo* data, with cells showing positive correlation. Not all cells and subpopulations showed significant correlation, and the Down-Up transition time was more likely to be correlated than the Up-Down transition time.

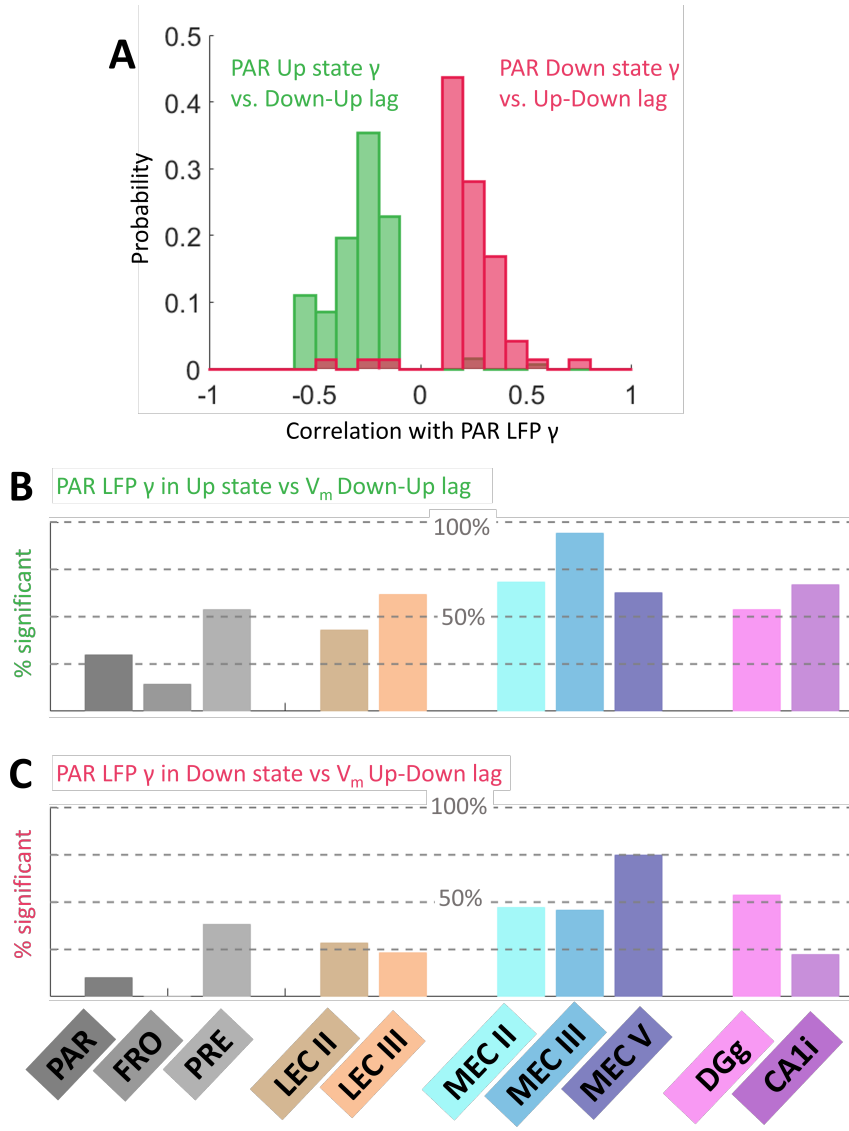

Figure 4.13: An alternate method for quantifying Down-Up and Up-Down lag is to use the delay between the PAR transition and the time when the V_m of a neuron crosses the 80% threshold. A) Similar to the other method, across all populations of neurons, significant correlations between the PAR Up state gamma and the V_m Down-Up lag was almost always negative. Conversely, significant correlations between PAR Down state gamma and the V_m Up-Down lag was almost always positive. B) The number of cells which exhibited significant anti-correlation between their Down-Up lag and the PAR gamma drive varied with brain region and cell type. 27% of parietal cells showed significant correlation, only 14% of frontal neurons and 55% of prefrontal neurons showed significant correlation. In LEC, 45% of LECII and 60% of LECIII neurons showed significant correlation. MEC showed the highest correlation, with 72% of MECII cells, 95% of MECIII cells, and 61% of MECV cells showing significant correlation. In hippocampus, 53% of Dentate granule cells and 70% of CA1 interneurons showed significant correaltion. Continued on next page.

Figure 4.13: C) Same as B, but now for Up-Down lag and gamma drive in the Down state. 10% of parietal cells showed significant correlation, only 0% of frontal neurons and 36% of prefrontal neurons showed significant correlation. In LEC, 26% of LECII and 24% of LECIII neurons showed significant correlation. MEC showed the highest correlation, with 47% of MECII cells, 45% of MECIII cells, and 75% of MECV cells showing significant correlation. In hippocampus, 53% of Dentate granule cells and 23% of CA1 interneurons showed significant correlation.

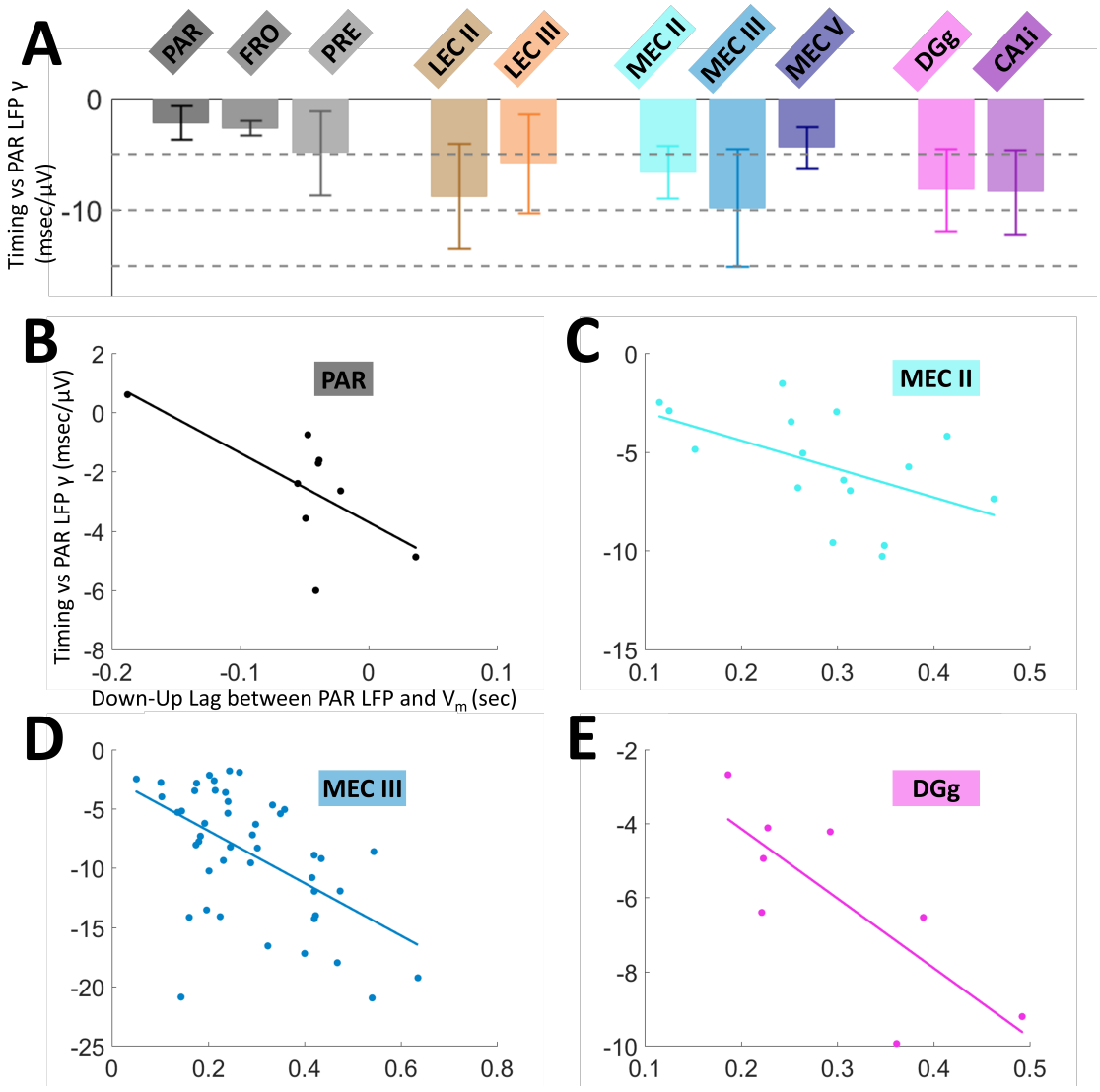

Figure 4.14: Continued on next Page

Figure 4.14: The quantitative relationship between the amount of gamma power in the PAR Up state and the Down-Up transition lag can be captured by the slope, calculated for only those cells with significant correlation A) The largest negative slope occurred for MECIII cells (-10.2 ± 5.1 ms/μV), followed by LECII (-8.1 ± 4.1 ms/μV), followed by Dentate granule (-7.2 ± 4.1 ms/μV) and CA1 interneurons (-7.1 ± 4.0 ms/μV). B) Within some subpopulations, the slope of this relationship was significantly negatively correlated with the average Down-Up lag between the PAR LFP and the V_m Down-Up transition. Within the parietal subpopulation, this lag was significantly negative (r=-0.43, $p < 10^{-2}$). C) Within the MECII population, there was also significant negative correlation (r=-0.31, $p < 10^{-2}$). Similar for D) MECIII neurons (r=-0.41, $p < 10^{-3}$) and E) Dentate Gyrus granule cells (r=-0.34, $p < 10^{-2}$).

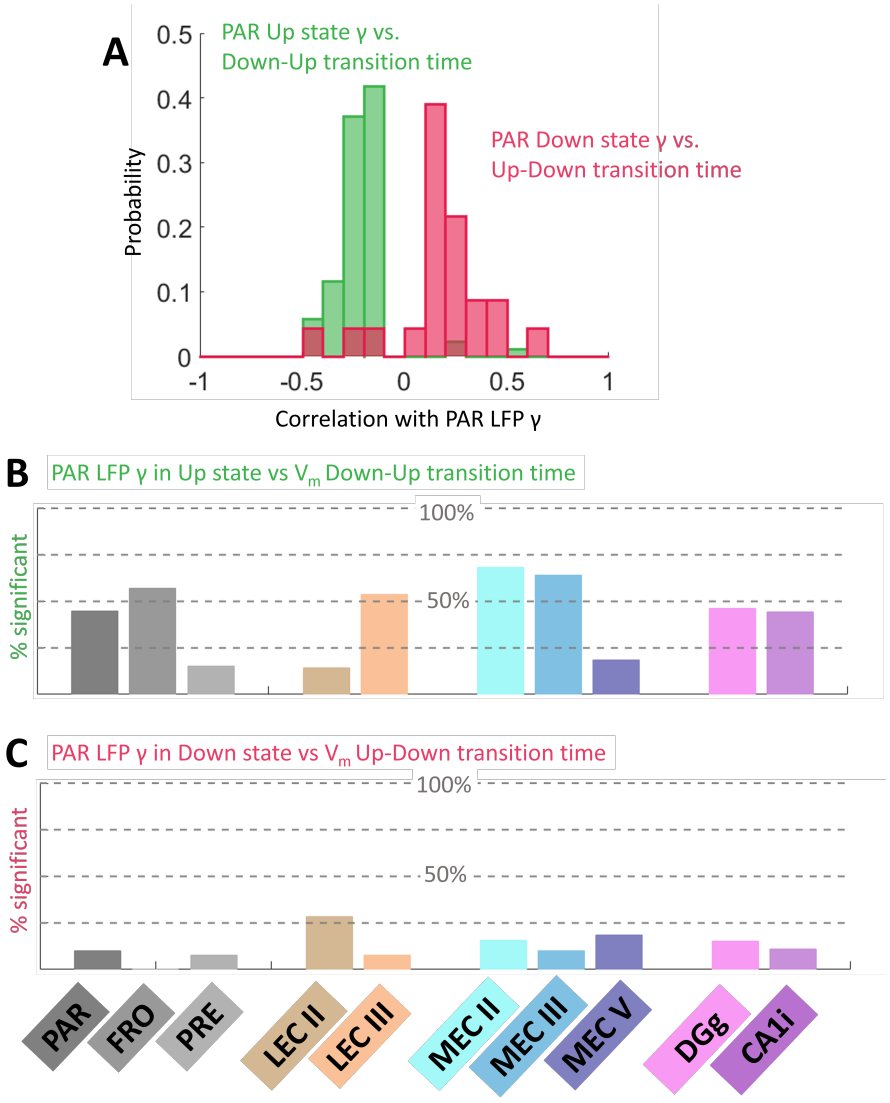

Figure 4.15: Continued on Next Page.

Figure 4.15: The transition time between Down and Up states in the V_m are correlated to the PAR gamma power. A) Across all populations of neurons, significant correlations between the PAR Up state gamma and the V_m Down-Up transition time was almost always negative. Conversely, significant correlations between PAR Down state gamma and the V_m Up-Down transition time was almost always positive. B) The number of cells which exhibited significant anti-correlation between their Down-Up transition time and the PAR gamma drive varied with brain region and cell type. 48% of parietal cells showed significant correlation, only 55% of frontal neurons and 13% of prefrontal neurons showed significant correlation. In LEC, 12% of LECII and 55% of LECIII neurons showed significant correlation. MEC showed the highest correlation, with 68% of MECII cells, 55% of MECIII cells, and 20% of MECV cells showing significant correlation. In hippocampus, 42% of Dentate granule cells and 41% of CA1 interneurons showed significant correlation. C) Same as B, but now for Up-Down transition time and gamma drive in the Down state. Correlation was very rare. 7% of parietal cells showed significant correlation, only 0% of frontal neurons and 5% of prefrontal neurons showed significant correlation. In LEC, 27% of LECII and 5% of LECIII neurons showed significant correlation. MEC showed the highest correlation, with 15% of MECII cells, 10% of MECIII cells, and 18% of MECV cells showing significant correlation. In hippocampus, 12% of Dentate granule cells and 10% of CA1 interneurons showed significant correlation.

4.3.2 Amplitude of synchronous UDS cycles

While the timing between Up-Down and Down-Up transitions for synchronous Up and Down states were correlated and anti-correlated, respectively, to the afferent cortical γ power, this depends highly on the direction of connectivity between the afferent and efferent networks. Specifically, if the individual neurons that are analyzed are *within*, or indeed even $afferent$ to the neocortical UDS, as measured in the parietal cortex, then this correlation should be diminished. This is qualitatively true in our data, since MEC and LEC neurons' transition lags showed higher anti-correlation and correlation to PAR gamma power during the Up and Down states, respectively, compared with the lags of neocortical neurons.

However, the converse should be true for the amplitude of the membrane potential of the neurons. First, the amplitude during the Up state should be positively correlated with the gamma power observed in the parietal LFP, as with higher drive, the neurons should be more depolarized due to larger synaptic excitatory input. Similarly, the amplitude of the

neuron's V_m during the Down state should also be positively correlated with the gamma power observed in the parietal Down state. However, the number of neurons with significant correlation during the Up state should be larger than the number of neurons with significant correlation in the Down state, as the Up state has much higher afferent excitation than the Down state. This was indeed the case (Fig 4.16).

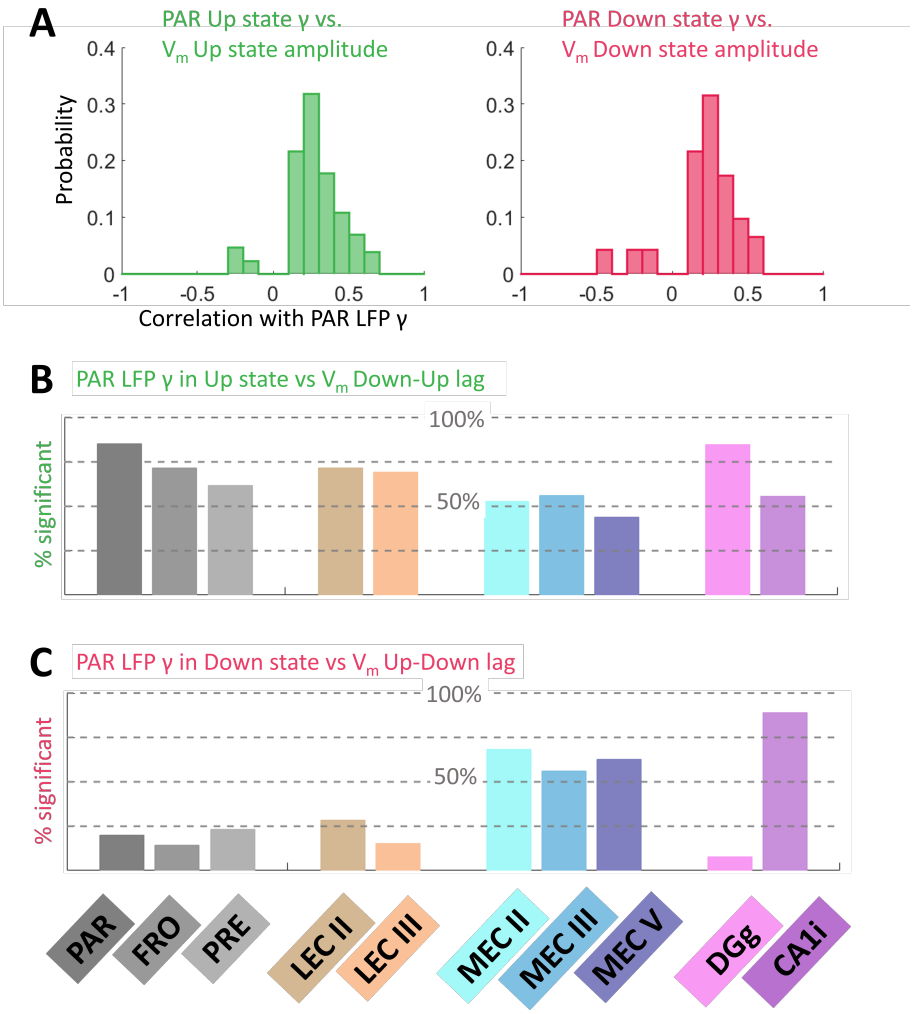

Figure 4.16: The amplitude of the membrane potential in Down and Up states in the V_m are correlated to the PAR gamma power. A) Across all populations of neurons, significant correlations between the PAR Up state gamma and the V_m Up state amplitude was almost always positive. Similarly, significant correlations between PAR Down state gamma and the V_m Down amplitude was almost always positive. Continued on next page.

Figure 4.16: B) The number of cells which exhibited significant correlation between their Up state amplitude and the PAR gamma drive varied with brain region and cell type. 80% of parietal cells showed significant correlation, only 72% of frontal neurons and 61% of prefrontal neurons showed significant correlation. In LEC, 72% of LECII and 70% of LECIII neurons showed significant correlation. MEC showed the correlation, with 52% of MECII cells, 55% of MECIII cells, and 45% of MECV cells showing significant correlation. In hippocampus, 81% of Dentate granule cells and 55% of CA1 interneurons showed significant correlation. C) Same as B, but now for Down state amplitude and gamma drive in the Down state. 20% of parietal cells showed significant correlation, only 15% of frontal neurons and 24% of prefrontal neurons showed significant correlation. In LEC, 27% of LECII and 10% of LECIII neurons showed significant correlation. MEC showed the highest correlation, with 80% of MECII cells, 55% of MECIII cells, and 62% of MECV cells showing significant correlation. In hippocampus, 7% of Dentate granule cells and 84% of CA1 interneurons showed significant correlation.

Interestingly, neocortical neurons showed higher rates of significant correlation compared with paleocortical and hippocampal neurons, during both Up and Down states. This is most likely due to non-linear effects of inhibition that are local to the paleocortical and hippocampal networks, which could be working independent of the afferent cortical drive. Within the neocortex, the balance of excitation and inhibition could be tightly locked to the afferent parietal drive, which is in effect a local network. This might not be the case for paleocortical neurons.

We performed similar analysis for the amplitude of the gamma power within the individual neuron's V_m trace, as this is an approximate measure of the network activity that is afferent to each particular neuron (Fig 4.17). This produced similar results: the gamma power within the V_m was positively correlated with that in the afferent parietal LFP, for both Up and Down states, and neocortical neurons showed higher rates of significant correlation compared with paleocortical and hippocampal neurons.

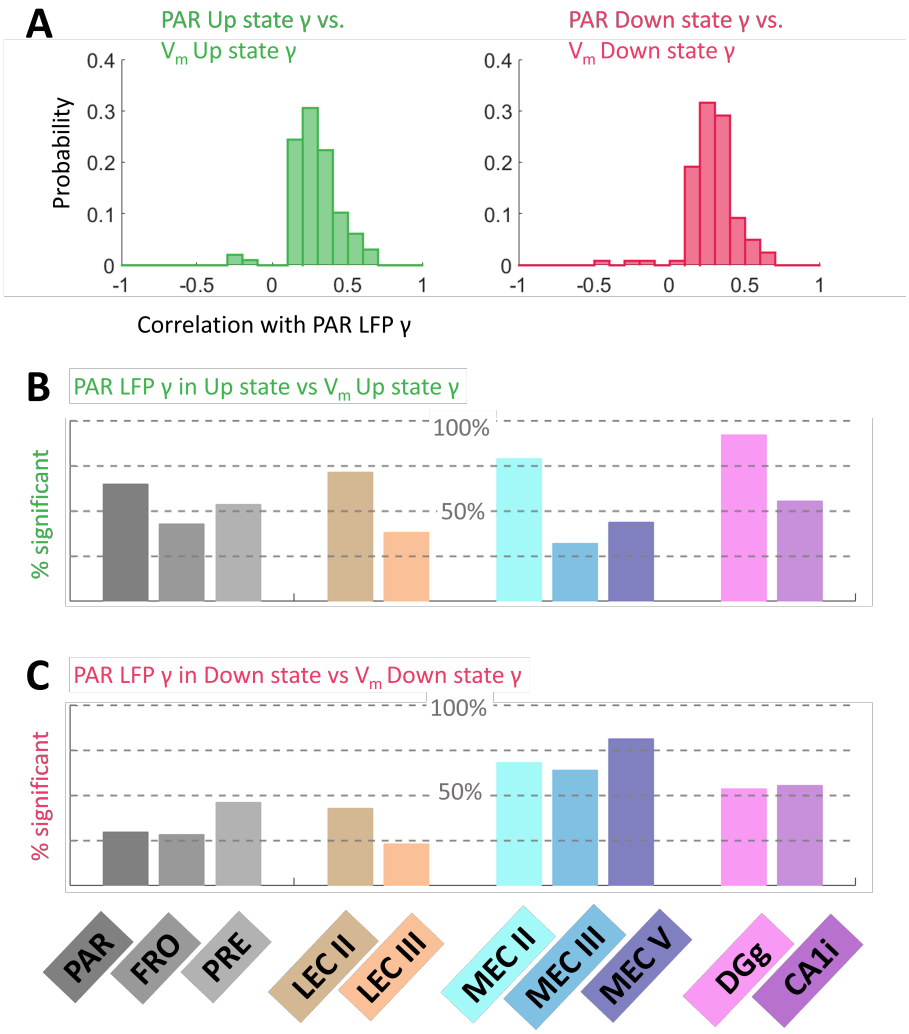

Figure 4.17: The amplitude of the gamma power in the membrane potential in Down and Up states in the V_m are correlated to the PAR gamma power. A) Across all populations of neurons, significant correlations between the PAR Up state gamma and the gamma in the V_m Up state amplitude was almost always positive. Similarly, significant correlations between PAR Down state gamma and the V_m Down gamma amplitude was almost always positive. B) The number of cells which exhibited significant correlation between their Up state amplitude and the PAR gamma drive varied with brain region and cell type. 64% of parietal cells showed significant correlation, only 45% of frontal neurons and 55% of prefrontal neurons showed significant correlation. In LEC, 72% of LECII and 34% of LECIII neurons showed significant correlation. MEC showed the correlation, with 74% of MECII cells, 30% of MECIII cells, and 45% of MECV cells showing significant correlation. In hippocampus, 88% of Dentate granule cells and 55% of CA1 interneurons showed significant correlation. Continued on next page.

Figure 4.17: C) Same as B, but now for Down state gamma amplitude and gamma drive in the Down state. 26% of parietal cells showed significant correlation, only 26% of frontal neurons and 43% of prefrontal neurons showed significant correlation. In LEC, 45% of LECII and 23% of LECIII neurons showed significant correlation. MEC showed the highest correlation, with 70% of MECII cells, 67% of MECIII cells, and 78% of MECV cells showing significant correlation. In hippocampus, 53% of Dentate granule cells and 54% of CA1 interneurons showed significant correlation.

4.4 Amplification of CA1 and Dentate spectral activity due to SPA and SPI

The EC is uniquely positioned as a gateway between the neocortex and the hippocampus, and recently much attention has been shown to how this brain region affects the hippocampal circuits, which are crucial for spatial navigation, memory, and learning. The Up-Down state oscillation presents a unique phenomena by which this link between the neocortex and the hippocampus can be probed, as the events of SPA and SPI are exactly those when the EC decouples from the rest of the cortex. During SPA, the EC is active while the cortex is silent, and during SPI the EC is inactive while the cortex is active. By monitoring the activity in the hippocampus and the dentate gyrus during these events, one can begin deciphering the functional connectivity between these brain regions.

Given their important role in cognition, multiple anatomical studies have established the circuits prevalent within the parahippocampal region. It is now well established that layer two of the EC, both lateral and medial subdivisions, make monosynaptic connections to granule cells in the dentate gyrus. These cells in turn synapse onto CA3 pyramidal cells, which in turn synapse onto CA1 pyramidal cells. Thus, from layer 2 of EC there are three synapses until the CA1 cell layer. On the other hand, layer 3 of EC, both lateral and medial subdivisions, make monosynaptic connections with CA1 pyramidal cells. Thus, only a single synapse separates layer 3 in EC from the CA1 cell layer. Given our theory of SPA and SPI, and the fact that neurons in MECIII amplify afferent cortical activity during these events, this differential connectivity should affect activity of CA1 and dentate gyrus neural populations.

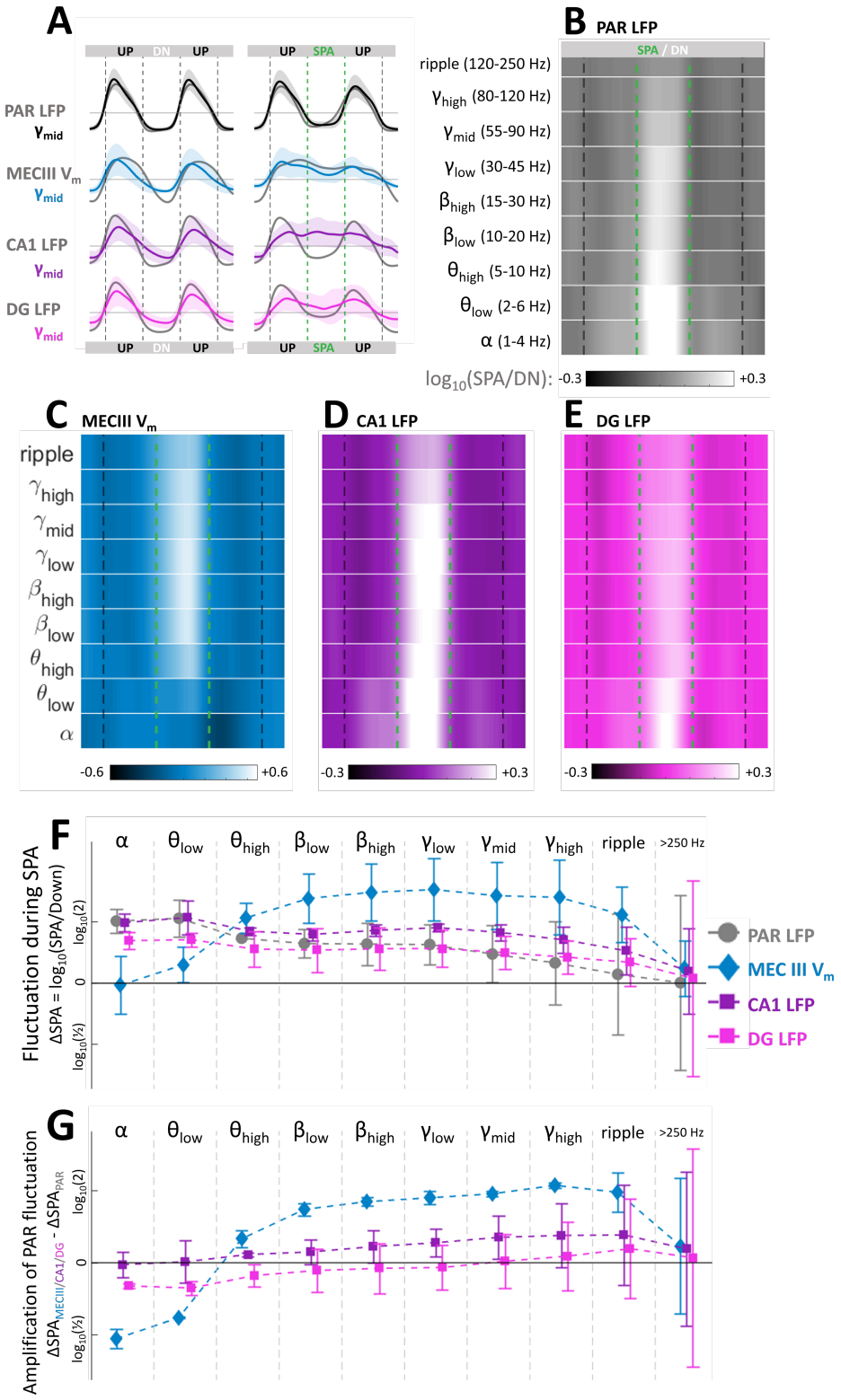

Figure 4.18: SPA in MECIII amplifies cortical activity in CA1 layer during UDS. Continued on next page.

Figure 4.18: A) When comparing PAR LFP Down states which were coincident with MECIII Down states (left) vs those that resulted in SPA (right), the gamma power in the PAR LFP is slightly higher for the latter case (top, black). The MECIII gamma power (blue) was significantly higher, reflecting amplification. Similarly, the gamma power in the CA1 LFP was also significantly higher (purple), and so was the gamma power in the Dentate Gyrus. B) To see how specific bands were amplified by SPA, each relevant band was analyzed separately. The frequency limits are shown on the left. To see modulation, the ratio of power in each band during SPA to the power during normal Down states was taken, and the log computed (see colorbar). All bands were significantly up-regulated during SPA. C) The same procedure was done with MECIII membrane potential; all bands above theta were up-regulated, much higher than the PAR LFP (note the different scale in the colorbar). D) Similarly, the CA1 LFP was examined, showing positive fluctuation. the colorbar is the same as in (A) to allow for comparison. E) Same as D, but for LFP in the dentate gyrus. F) Average fluctuations within each band during SPA for all four brain regions in (B-E) are shown, with error-bars reflecting standard deviation. All four regions experienced positive fluctuation during SPA, with the V_m showing the highest fluctuation. The V_m showed highest fluctuation within the gamma band, while the LFP showed the highest fluctuation within low frequencies. G) To find the average amplification within each band, the fluctuations in (F) within the PAR LFP were subtracted from the fluctuations in V_m, CA1 LFP, and DG LFP. This showed that, for this particular example, while V_m and CA1 LFP activity was amplified greater than 1, there was no amplification in the dentate gyrus.

4.4.1 Spectral signatures of SPA and SPI

We begin by first quantifying how SPA and SPI affect each cortical oscillation band, as these bands are thought to be unique in their function and origin. To compare between the LFP from the parietal cortex, CA1 cell layer, and Dentate Gyrus, and the intracellular V_m, we must first normalize all traces (as the V_m is by design orders of magnitude larger than the extracellular voltages). These traces are then filtered in each of the following bands: α : 1-4 Hz, θ_{low} : 2-6Hz, θ_{high} : 5-10 Hz, β_{low} : 10-20 Hz, β_{high} : 15-30 Hz, γ_{low} : 30-45 Hz, γ_{mid} : 55-90 Hz, γ_{high} : $80-120$ Hz, the ripple band: 120-250 Hz, and the high-frequency (HF) band: >250 Hz. Each of the β, θ, and γ bands were separated into subdivisions to increase spectral resolution. The traces were then aligned with the parietal power traces in their respective bands using the cross-correlation, and then analyzed on a state-by-state basis using the universal parietal UDS clock.

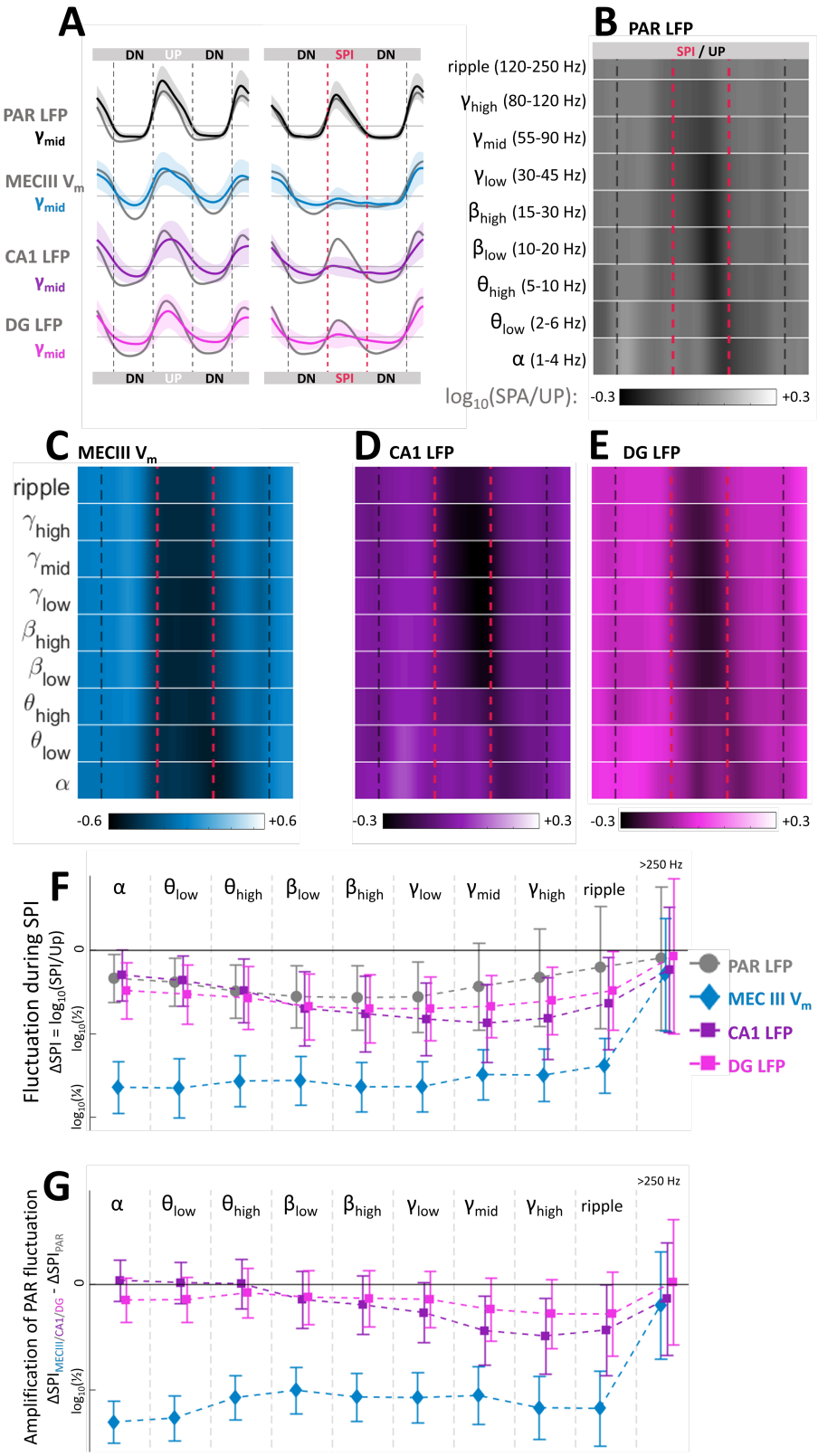

Figure 4.19: SPI amplifies cortical activity in the hippocampus during UDS. Continued on next page.

Figure 4.19: A) When comparing PAR LFP Up states which were coincident with MECIII Down states (left) vs those that resulted in SPI (right), the gamma power in the PAR LFP is slightly lower for the latter case (top, black). The MECIII gamma power (blue) was significantly lower, reflecting amplification. Similarly, the gamma power in the CA1 LFP was also significantly lower (purple), and so was the gamma power in the Dentate Gyrus. B) To see how specific bands were amplified by SPI, each relevant band was analyzed separately. The frequency limits are shown on the left. To see modulation, the ratio of power in each band during SPA to the power during normal Up states was taken, and the log computed (see colorbar). All bands were significantly down-regulated during SPI. C) The same procedure was done with MECIII membrane potential; all bands above theta were down-regulated, much higher than the PAR LFP (note the different scale in the colorbar). D) Similarly, the CA1 LFP was examined, showing positive fluctuation. the colorbar is the same as in (A) to allow for comparison. E) Same as D, but for LFP in the dentate gyrus. F) Average fluctuations within each band during SPI for all four brain regions in (B-E) are shown, with error-bars reflecting standard deviation. All four regions experienced negative fluctuation during SPI, with the V_m showing the highest fluctuation. The V_m showed highest fluctuation within the gamma band, while the LFP showed the highest fluctuation within low frequencies. G) To find the average amplification within each band, the fluctuations in (F) within the PAR LFP were subtracted from the fluctuations in V_m, CA1 LFP, and DG LFP. This showed that, for this particular example, while V_m and CA1 LFP activity was amplified greater than 1, there was amplification in the dentate gyrus to a lesser extent.

As an initial analysis step, we first quantify the scale of fluctuations that occur within the LFP from the cortex and hippocampus and the V_m within neurons during SPA and SPI. To accomplish this, we first extract the power traces within each band, centered around cortical Down states (for SPA) and around cortical Up states (for SPI). These Up and Down states can be partiioned into two categories: those that were coincident in the efferent neuron, and those that were "skipped" by the efferent neuron. The skipped states are the SPA and SPI events. By taking the ratio of the powers between the skipped events vs. those that were coincident, we can quantify the size of the fluctuation that occurs due to the network decoupling. To ease analysis, we use the log-power as our measure; in this case, ratios become differences. As described in Chapter 3, during SPA the cortical LFP power in all bands is higher than during a synchronous Down state. Similarly, during SPI the cortical LFP power in all bands is significantly weaker. These fluctuations are also present within the LFP of CA1 cell layer and dentate gyrus. Unsurprisingly, the fluctuations are larger within the V_m of the efferent neurons, where the SPA and SPI occur.

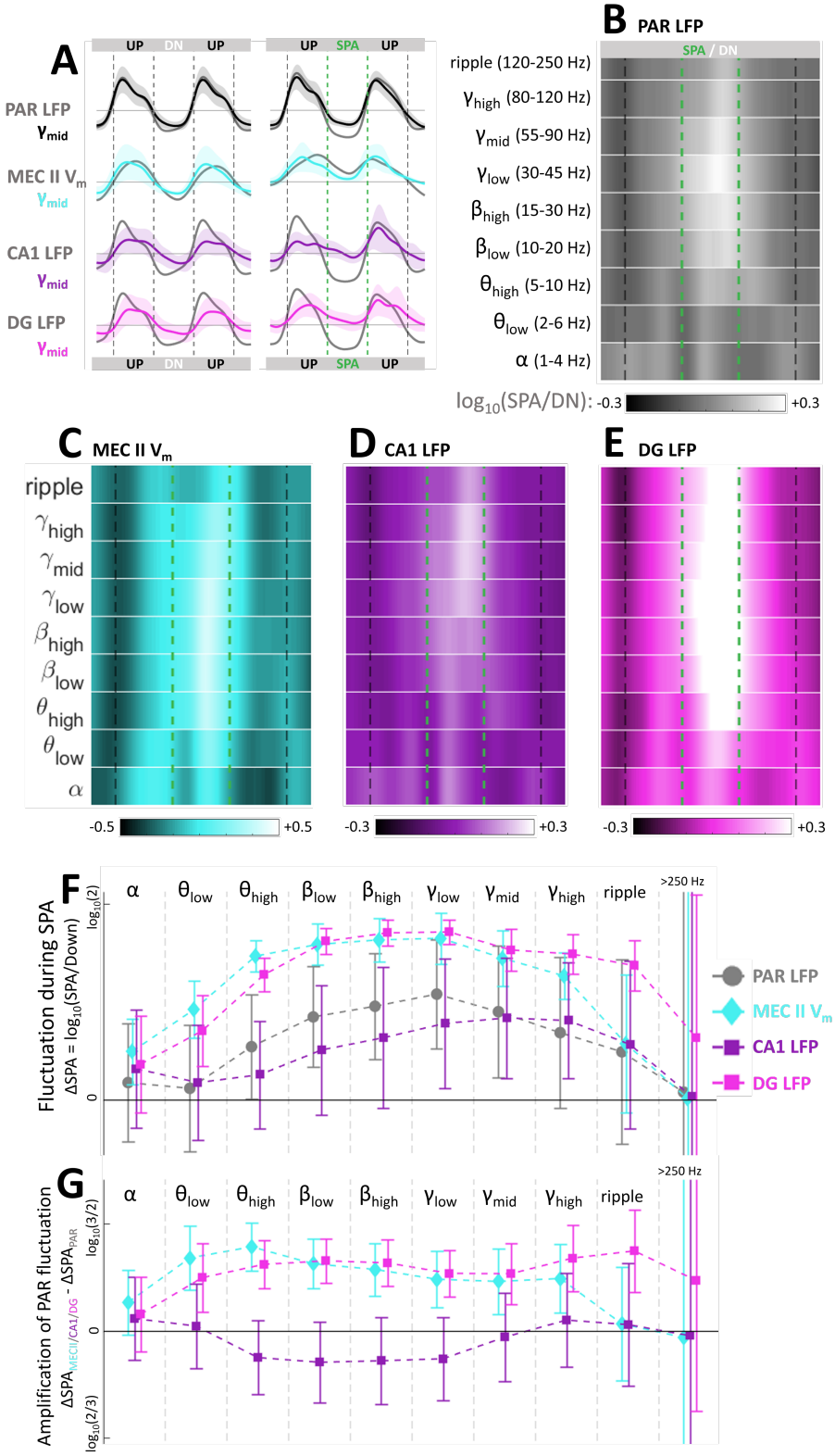

Figure 4.20: SPA in MECII amplifies cortical activity in the dentate gyrus during UDS. Continued on next page.

Figure 4.20: A) When comparing PAR LFP Down states which were coincident with MECII Down states (left) vs those that resulted in SPA (right), the gamma power in the PAR LFP is slightly higher for the latter case (top, black). The MECII gamma power (blue) was significantly higher, reflecting amplification. Similarly, the gamma power in the CA1 LFP was also significantly higher (purple), and so was the gamma power in the Dentate Gyrus. B) To see how specific bands were amplified by SPA, each relevant band was analyzed separately. The frequency limits are shown on the left. To see modulation, the ratio of power in each band during SPA to the power during normal Down states was taken, and the log computed (see colorbar). All bands were significantly up-regulated during SPA. C) The same procedure was done with MECII membrane potential; all bands above theta were up-regulated, much higher than the PAR LFP (note the different scale in the colorbar). D) Similarly, the CA1 LFP was examined, showing positive fluctuation. the colorbar is the same as in (A) to allow for comparison. E) Same as D, but for LFP in the dentate gyrus. F) Average fluctuations within each band during SPA for all four brain regions in (B-E) are shown, with error-bars reflecting standard deviation. All four regions experienced positive fluctuation during SPA, with the V_m showing the highest fluctuation. The V_m showed highest fluctuation within the gamma band, while the LFP showed the highest fluctuation within low frequencies. G) To find the average amplification within each band, the fluctuations in (F) within the PAR LFP were subtracted from the fluctuations in V_m, CA1 LFP, and DG LFP. This showed that, for this particular example, while V_m and DG LFP activity was amplified greater than 1, there was no amplification in the CA1 cell layer.

The fact that V_m fluctuations are larger than the fluctuations within the cortical LFP is in conjunction with the theoretical predictions, since SPA and SPI events occur when the network decouples from the afferent UDS, thereby either staying on or turning off while the afferent network does the opposite. The non-trivial result here is the fact that this fluctuation is also present in the hippocampus, in both the CA1 and DG cell layers. This could be due to the fact that SPA and SPI in the efferent EC brain region is feeding forward into the hippocampus population, and thus during SPA the excitatory currents are larger than during a normal Down state, and similarly during SPI the excitatory currents are smaller than during a normal Up state. Another possibility is that since the cortex, and hence most afferent regions, are already undergoing positive or negative fluctuations during SPA and SPI, these global fluctuations are simple coincident with the hippocampus, which thus displays the same positive or negative change. To discern between these possibilities, we must compare the scale of fluctuations within each population.

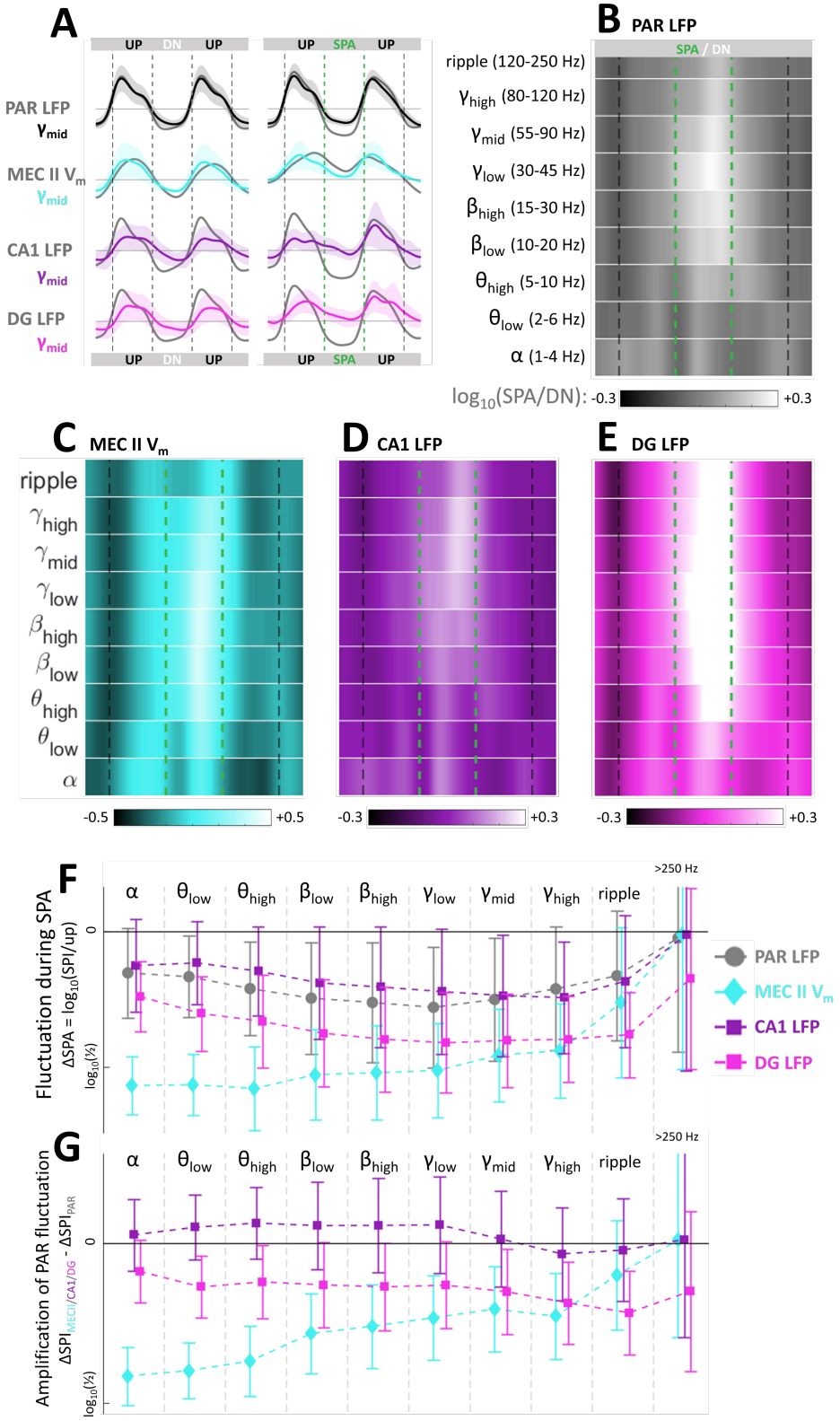

Figure 4.21: SPI amplifies cortical activity in the hippocampus during UDS. Continued on next page.

Figure 4.21: A) When comparing PAR LFP Up states which were coincident with MECII Down states (left) vs those that resulted in SPI (right), the gamma power in the PAR LFP is slightly lower for the latter case (top, black). The MECIII gamma power (blue) was significantly lower, reflecting amplification. Similarly, the gamma power in the CA1 LFP was also significantly lower (purple), and so was the gamma power in the Dentate Gyrus. B) To see how specific bands were amplified by SPI, each relevant band was analyzed separately. The frequency limits are shown on the left. To see modulation, the ratio of power in each band during SPA to the power during normal Up states was taken, and the log computed (see colorbar). All bands were significantly down-regulated during SPI. C) The same procedure was done with MECII membrane potential; all bands above theta were down-regulated, much higher than the PAR LFP (note the different scale in the colorbar). D) Similarly, the CA1 LFP was examined, showing positive fluctuation. the colorbar is the same as in (A) to allow for comparison. E) Same as D, but for LFP in the dentate gyrus. F) Average fluctuations within each band during SPI for all four brain regions in (B-E) are shown, with error-bars reflecting standard deviation. All four regions experienced negative fluctuation during SPI, with the V_m showing the highest fluctuation. The V_m showed highest fluctuation within the gamma band, while the LFP showed the highest fluctuation within low frequencies. G) To find the average amplification within each band, the fluctuations in (F) within the PAR LFP were subtracted from the fluctuations in V_m, CA1 LFP, and DG LFP. This showed that, for this particular example, while V_m and DG LFP activity was amplified greater than 1, there was amplification in the CA1 cell layer to a lesser extent.

4.4.2 Amplification of activity in the V_m of Individual Neurons

As discussed in Ch. 3, during SPA and SPI, positive and negative fluctuations in the afferent γ band power are amplified by the efferent network. We quantified this amplification by taking the ratio of the size of fluctuations in the V_m to the size of the fluctuation within the afferent LFP. If the size is the same, then afferent fluctuations are simply linearly passed onto efferent regions, and there is no amplification. If the ratio is significantly larger than 1, then the efferent network must necessarily have amplified the afferent fluctuation by either sustaining its own activity or negating it. With our new spectral procedure, we can now quantify the amplification within each brain region, within each band. To do this, we take the difference in the log-fluctuation during SPA and SPI. If the difference is 0, then the size of the fluctuation within the afferent parietal LFP and the efferent V_m is the same, and there is no amplification. If, on the other hand, the difference is significantly greater than 0, then the efferent network is indeed amplifying the fluctuations. During SPI, the difference

must be significantly less than 0, since the fluctuations are negative.

We found that all networks which showed significant amounts of SPA amplified the fluctuations above the θ_{high} band (Fig. 4.22). MECIII neurons showed the highest amplification in the γ band, while they showed significant de-amplification in the low frequency bands α and θ_{low}. MECII cells, on the other hand, showed highest amplification in the θ band, while showing lower values of amplification in the higher frequencies. MECII cells, unlike MECIII cells, did not show significant de-amplification in the low frequencies. Finally, both DG granule cells and CA1 interneurons showed highest amplification in the θ bands, with lower amplification at higher frequencies. Interestingly, CA1 interneurons showed de-amplification in the α band, similar to MECIII. DG granule cells, however, did not. Across all spectra and all bands, MECIII cells showed the highest amplification, and that too within the γ band. Above the ripple band, no cell population showed significant amplification.

During SPI, all efferent regions showed amplification of the negative fluctuations in the cortical LFP (Fig. 4.23). MECIII neurons showed the highest amplification in the γ band, similar to its behavior during SPA. Unlike during SPA, there was no band where MECIII showed de-amplification. MECII showed amplification during SPI as well, but not to the magnitude of MECIII. In LEC, both LECII and LECIII showed amplification for all frequency bands, but this amplification was highest for the lower frequencies and for the γ_{low} band within the higher frequencies. Finally, within hippocampus, both $CA1$ interneurons and DG granule cells showed amplification, but DG amplification was significantly larger than CA1 interneurons, for all bands except γ_{high} and the ripple band.

The variability of amplifications between brain regions highlighted in this quantitative fashion show how the intrinsic properties of the networks differ. Within brain regions, there are differences between the laminar structures. Our next focus will be on how these brain regions affect downstream regions, thus giving us insights into the connectivity.

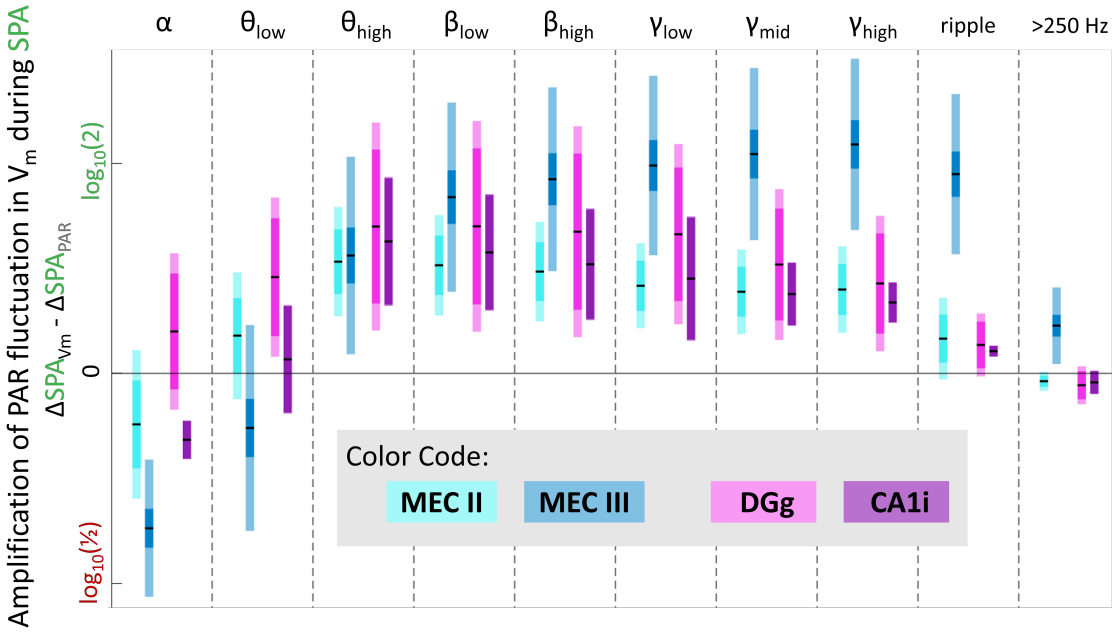

Figure 4.22: SPA amplifies cortical activity fluctuations in the V_m. The amplification factor within each subpopulation of neurons is plotted, averaged over the entire population, for each frequency bin. The colors correspond to each population. MECII neurons show highest amplification in the θ and β bands ($\alpha : -0.06 \pm 0.04, \theta_{low} : +0.05 \pm 0.05, \theta_{high} : +0.15 \pm 0.05, \beta_{low} : +0.14 \pm 0.05, \beta_{high} : +0.13 \pm 0.05, \gamma_{low} : +0.12 \pm 0.05, \gamma_{mid} : +0.11 \pm 0.03, \gamma_{high} : +0.11 \pm 0.04$, ripple: $+0.05 \pm 0.04$, 250Hz: -0.01 ± 0.01). MECIII neurons show highest amplification in the γ bands ($\alpha : -0.16 \pm 0.05, \theta_{low} : -0.05 \pm 0.03, \theta_{high} : +0.15 \pm 0.05, \beta_{low} : +0.23 \pm 0.05, \beta_{high} : +0.26 \pm 0.05, \gamma_{low} : +0.30 \pm 0.05, \gamma_{mid} : +0.31 \pm 0.03, \gamma_{high} : +0.33 \pm 0.04$, ripple: $+0.25 \pm 0.04$, 250Hz: $+0.06 \pm 0.03$). Dentate gyrus neurons show highest amplification in the θ and β bands ($\alpha : +0.05 \pm 0.07, \theta_{low} : +0.13 \pm 0.06, \theta_{high} : +0.25 \pm 0.08, \beta_{low} : +0.23 \pm 0.07, \beta_{high} : +0.23 \pm 0.1, \gamma_{low} : +0.22 \pm 0.1, \gamma_{mid} : +0.15 \pm 0.06, \gamma_{high} : +0.13 \pm 0.04$, ripple: $+0.04 \pm 0.04$, 250Hz: -0.01 ± 0.03). CA1 interneurons show highest amplification in the θ bands ($\alpha : -0.07 \pm 0.02, \theta_{low} : +0.02 \pm 0.1, \theta_{high} : +0.23 \pm 0.08, \beta_{low} : +0.21 \pm 0.07, \beta_{high} : +0.18 \pm 0.1, \gamma_{low} : +0.16 \pm 0.1, \gamma_{mid} : +0.14 \pm 0.06, \gamma_{high} : +0.13 \pm 0.04$, ripple: $+0.04 \pm 0.01$, 250Hz: -0.01 ± 0.01).

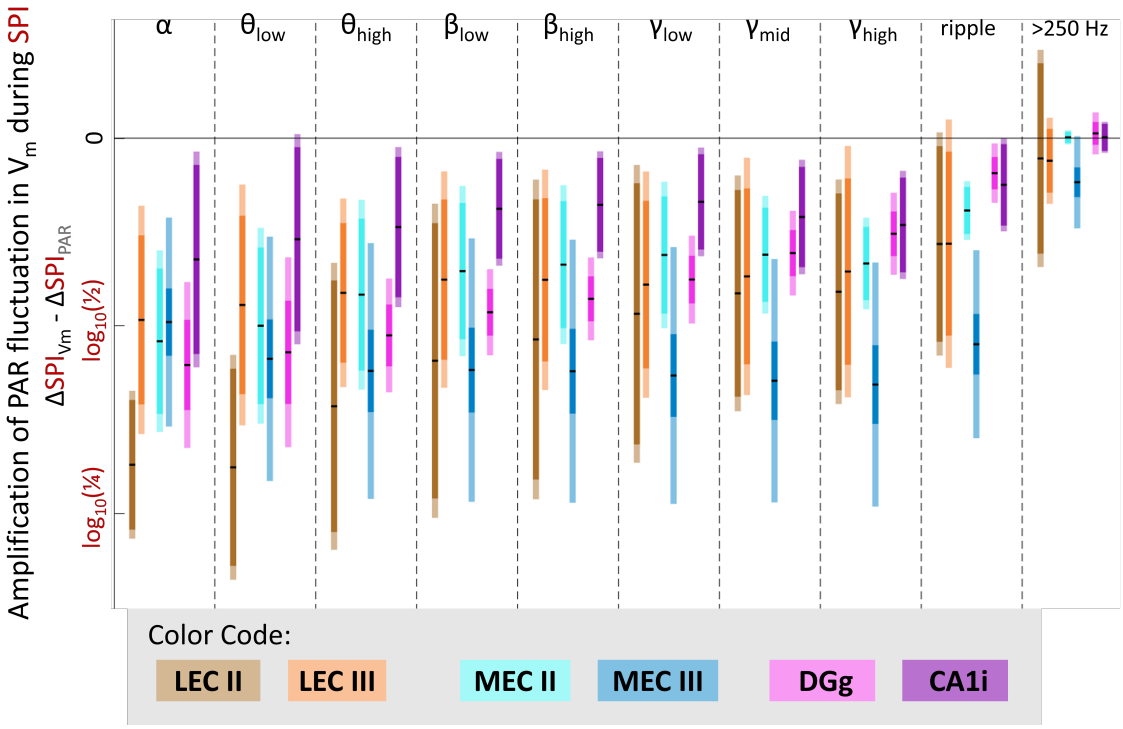

Figure 4.23: SPI amplifies negative cortical activity fluctuations in the V_m. The amplification factor within each subpopulation of neurons is plotted, averaged over the entire population, for each frequency bin. The colors correspond to each population. LECII neurons show highest amplification in the α and θ bands ($\alpha: -0.51 \pm 0.12, \theta_{low}: -0.53 \pm 0.18, \theta_{high}: -0.45 \pm 0.16, \beta_{low}: -0.39 \pm 0.11, \beta_{high}: -0.35 \pm 0.14, \gamma_{low}: -0.31 \pm 0.15, \gamma_{mid}: -0.29 \pm 0.1, \gamma_{high}: -0.26 \pm 0.15$, ripple: -0.21 ± 0.17, 250Hz: -0.01 ± 0.1). LECIII neurons show highest amplification in the α and θ bands ($\alpha: -0.31 \pm 0.12, \theta_{low}: -0.28 \pm 0.18, \theta_{high}: -0.26 \pm 0.16, \beta_{low}: -0.20 \pm 0.11, \beta_{high}: -0.20 \pm 0.14, \gamma_{low}: -0.22 \pm 0.15, \gamma_{mid}: -0.19 \pm 0.1, \gamma_{high}: -0.18 \pm 0.15$, ripple: -0.21 ± 0.17, 250Hz: -0.01 ± 0.04). MECII neurons show highest amplification in the α and θ bands ($\alpha: -0.51 \pm 0.12, \theta_{low}: -0.53 \pm 0.18, \theta_{high}: -0.45 \pm 0.16, \beta_{low}: -0.39 \pm 0.11, \beta_{high}: -0.35 \pm 0.14, \gamma_{low}: -0.31 \pm 0.15, \gamma_{mid}: -0.29 \pm 0.1, \gamma_{high}: -0.26 \pm 0.15$, ripple: -0.21 ± 0.17, 250Hz: -0.01 ± 0.1). MECIII neurons show highest amplification in the γ bands ($\alpha: -0.31 \pm 0.12, \theta_{low}: -0.28 \pm 0.18, \theta_{high}: -0.26 \pm 0.16, \beta_{low}: -0.20 \pm 0.11, \beta_{high}: -0.20 \pm 0.14, \gamma_{low}: -0.22 \pm 0.15, \gamma_{mid}: -0.19 \pm 0.1, \gamma_{high}: -0.18 \pm 0.15$, ripple: -0.21 ± 0.17, 250Hz: -0.01 ± 0.04). Dentate gyrus neurons show highest amplification in the θ and β bands ($\alpha: -0.05 \pm 0.07, \theta_{low}: -0.13 \pm 0.06, \theta_{high}: -0.25 \pm 0.08, \beta_{low}: -0.23 \pm 0.07, \beta_{high}: -0.23 \pm 0.1, \gamma_{low}: -0.22 \pm 0.1, \gamma_{mid}: -0.15 \pm 0.06, \gamma_{high}: -0.13 \pm 0.04$, ripple: -0.04 ± 0.04, 250Hz: -0.01 ± 0.03). CA1 interneurons show highest amplification in the θ bands ($\alpha: -0.07 \pm 0.02, \theta_{low}: -0.02 \pm 0.1, \theta_{high}: -0.23 \pm 0.08, \beta_{low}: -0.21 \pm 0.07, \beta_{high}: -0.18 \pm 0.1, \gamma_{low}: -0.16 \pm 0.1, \gamma_{mid}: -0.14 \pm 0.06, \gamma_{high}: -0.13 \pm 0.04$, ripple: -0.04 ± 0.01, 250Hz: -0.01 ± 0.01).

4.4.3 Amplification of downstream hippocampal activity

So far, we have been concerned with how afferent neocortical activity is amplified by efferent networks localized within the entorhinal cortex and hippocampus. These efferent regions are in turn afferent to the hippocampal subfields of the CA1 cell layer and the Dentate. Thus, by quantifying how the neocortical fluctuations propagate to CA1 and DG, we can quantify how the entorhinal regions feed-forward these fluctuations to downstream hippocampal areas. We will analyze each region, the CA1 layer and the Dentate, separately.

CA1 cell layer

Using a similar procedure as above, we calculated the CA1 amplification during region-specific SPA (Fig. 4.24). The CA1 cell layer activity shows significant amplification during MECIII SPA, but only in the γ band. In all other bands, there was no amplification, meaning that the size of the positive fluctuation was the same as the positive fluctuation exhibited by the cortical LFP. During MECII SPA, however, there was no amplification in any band. This could be reflective of the fact that MECIII neurons are a single synapse away from the CA1 cell layer, but MECII neurons are three synapses away.

When SPA occurred within CA1 interneurons, the amplification was large, sometimes even larger than during MECIII SPA. This is not surprising given than CA1 interneurons are within the CA1 cell layer, and thus embedded within the very network that we are analyzing. During SPA in the DG granule cells, however, CA1 showed significant de-amplification, especially in the β band. This is unexpected, given that DG granule cells are only two synapses away from the CA1 cell layer. Finally, these amplifications were significantly smaller than those found for the actual neuronal V_m, for all bands and regions.

During SPI, CA1 cell layer activity was significantly lower compared to neocortical activity (Fig. 4.25). The CA1 cell layer activity shows significant amplification during MECIII SPI, especially in the high γ band, just like during MECIII SPA. In all other bands, there was no amplification, meaning that the size of the negative fluctuation was the same as the negative fluctuation exhibited by the cortical LFP. During MECII SPI,

however, there was no amplification in any band, just like during MECII SPA.

The CA1 cell layer activity shows significant amplification during LECIII SPI, especially in the low γ band. At lower frequencies, the CA1 activity showed higher amplification than during MECIII SPI. During LECII SPI, however, there was amplification only in the low frequency band.

When SPI occurred within CA1 interneurons, the CA1 activity was significantly larger than during normal Up states. This could be the result of dis-inhibition, since during SPI interneurons would turn off, increasing the excitation within the CA1 cell layer. During SPI in the DG granule cells, however, CA1 showed no effect whatsoever. Finally, these amplifications were significantly smaller than those found for the actual neuronal V_m, for all bands and regions.

Dentate Gyrus

The DG cell layer activity shows significant amplification during MECII SPA, but only in the γ band (Fig. 4.26). In other bands, there was no amplification, meaning that the size of the positive fluctuation was the same as the positive fluctuation exhibited by the cortical LFP. In the low frequency band, however, the DG activity is de-amplified during MECII SPA. During MECIII SPA, there was virtually identical amplification in all bands. This could be reflective of the fact that MECIII neurons do not synapse onto DG, but do innervate and influence MECII cells, which do connect to DG.

When SPA occurred within DG granule cells, the amplification in DG was large, sometimes even larger than during MECIII SPA. This is not surprising given that DG cells are within the DG cell layer, and thus embedded within the very network that we are analyzing. During SPA in the CA1 interneurons, however, DG showed significant amplification, especially in the γ band. This is unexpected, given that CA1 cells are downstream from the DG cell layer. Finally, these amplifications were significantly smaller than those found for the actual neuronal V_m, for all bands and regions.

During SPI, DG cell layer activity was significantly lower compared to neocortical activity (Fig. 4.27). The DG cell layer activity shows significant amplification during MECIII

SPI, especially in the high γ band, just like during MECIII SPA. In all other bands, there was no amplification, meaning that the size of the negative fluctuation was the same as the negative fluctuation exhibited by the cortical LFP. During MECII SPI, however, there was no amplification in any band, just like during MECII SPA.

The DG cell layer activity shows significant amplification during LECIII SPI, especially in the low γ band. At lower frequencies, the DG activity showed higher amplification than during MECIII SPI. During LECII SPI, however, there was amplification only in the low frequency band.

When SPI occurred within CA1 interneurons, the DG activity was significantly larger than during normal Up states. This could be the result of dis-inhibition, since during SPI interneurons would turn off, increasing the excitation within the CA1 cell layer. During SPI in the DG granule cells, however, CA1 showed no effect whatsoever. Finally, these amplifications were significantly smaller than those found for the actual neuronal V_m, for all bands and regions.

4.4.4 Functional Connectivity in the para-hippocampal circuit

Now that we have quantified the effect of region specific SPA and SPI on the activity of the CA1 and DG cell layers, it possible to further compare how each efferent region, specifically in the entorhinal cortex, influences the CA1 and DG populations. This can be done by taking the difference in the amplification factor between the CA1 and DG cell layers for each region, within each band.

The MECII stellate cell population is directly connected to the Dentate Gyrus, but not to CA1. Thus, one would expect that when these cells underwent SPA or SPI, they would preferentially influence the DG activity more than the CA1 activity. This is indeed the case, for both SPA and SPI (Fig. 4.28, 4.29). Interestingly, this asymmetry is largest for the γ and low γ bands, and nearly vanished for low frequencies. In the α and θ bands, there is actually a CA1 bias.

MECIII cells are directly connected to the CA1 cell population, and this is also reflected in our analysis. MECIII cells show nearly non-existent bias between CA1 and DG activities,

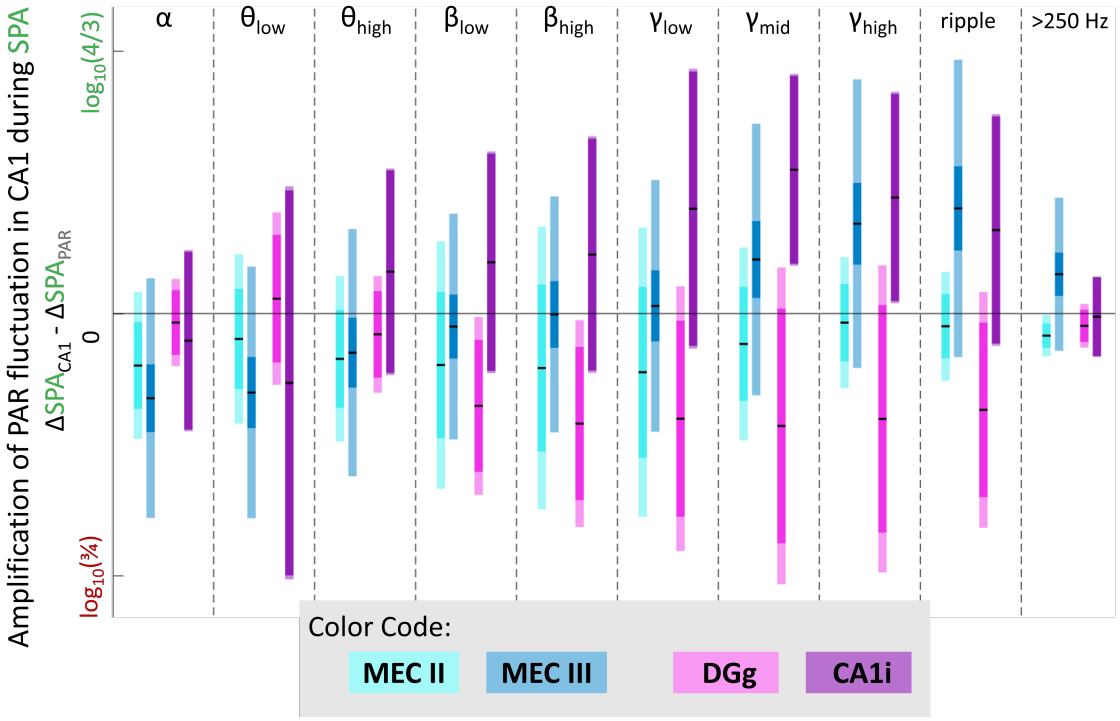

Figure 4.24: When SPA occurs within MEC or hippocampal neurons, the activity feedsforward to the CA1 cell layer. The amplification factor within CA1 due to each subpopulation of neurons is plotted, averaged over all experiments, for each frequency bin. The colors correspond to each population. CA1 showed virtually no amplification during SPA in MECII neurons ($\alpha : -0.06 \pm 0.04, \theta_{low} : -0.02 \pm 0.05, \theta_{high} : -0.02 \pm 0.05, \beta_{low} : -0.1 \pm 0.05, \beta_{high} : -0.03 \pm 0.05, \gamma_{low} : -0.02 \pm 0.05, \gamma_{mid} : -0.01 \pm 0.03, \gamma_{high} : -0.01 \pm 0.04$, ripple: -0.01 ± 0.04, 250Hz: -0.01 ± 0.01). On the other hand, CA1 showed significant amplification during SPA in MECIII neurons, especially in the γ and ripple bands ($\alpha : -0.16 \pm 0.05, \theta_{low} : -0.05 \pm 0.03, \theta_{high} : +0.15 \pm 0.05, \beta_{low} : +0.23 \pm 0.05, \beta_{high} : +0.26 \pm 0.05, \gamma_{low} : +0.30 \pm 0.05, \gamma_{mid} : +0.31 \pm 0.03, \gamma_{high} : +0.33 \pm 0.04$, ripple: $+0.25 \pm 0.04$, 250Hz: $+0.06 \pm 0.03$). During SPA in the dentate gyrus, CA1 LFP showed de-amplification ($\alpha : +0.05 \pm 0.07, \theta_{low} : +0.13 \pm 0.06, \theta_{high} : +0.25 \pm 0.08, \beta_{low} : +0.23 \pm 0.07, \beta_{high} : +0.23 \pm 0.1, \gamma_{low} : +0.22 \pm 0.1, \gamma_{mid} : +0.15 \pm 0.06, \gamma_{high} : +0.13 \pm 0.04$, ripple: $+0.04 \pm 0.04$, 250Hz: -0.01 ± 0.03). Finally, during SPA in CA1 interneurons, CA1 showed significant positive amplification ($\alpha : -0.07 \pm 0.02, \theta_{low} : +0.02 \pm 0.1, \theta_{high} : +0.23 \pm 0.08, \beta_{low} : +0.21 \pm 0.07, \beta_{high} : +0.18 \pm 0.1, \gamma_{low} : +0.16 \pm 0.1, \gamma_{mid} : +0.14 \pm 0.06, \gamma_{high} : +0.13 \pm 0.04$, ripple: $+0.04 \pm 0.01$, 250Hz: -0.01 ± 0.01).

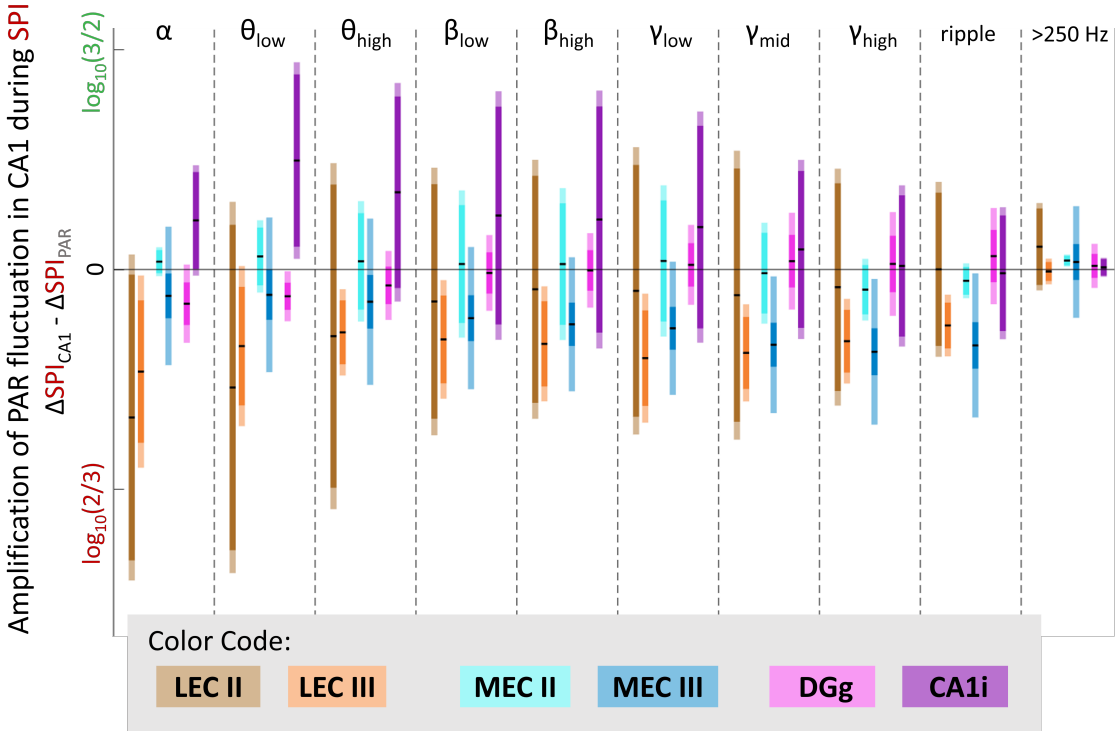

Figure 4.25: When SPI occurs within LEC, MEC, or hippocampal neurons, the activity feedsforward to the CA1 cell layer. The amplification factor within CA1 due to each subpopulation of neurons is plotted, averaged over all experiments, for each frequency bin. The colors correspond to each population. CA1 showed significant amplification during SPI in LECII neurons, but only in the low frequency bands ($\alpha : -0.51 \pm 0.12, \theta_{low} : -0.53 \pm 0.18, \theta_{high} : -0.45 \pm 0.16, \beta_{low} : -0.39 \pm 0.11, \beta_{high} : -0.35 \pm 0.14, \gamma_{low} : -0.31 \pm 0.15, \gamma_{mid} : -0.29 \pm 0.1, \gamma_{high} : -0.26 \pm 0.15$, ripple: -0.21 ± 0.17, 250Hz: -0.01 ± 0.1). During SPI in LECIII neurons, CA1 shows highest amplification in the γ bands ($\alpha : -0.31 \pm 0.12, \theta_{low} : -0.28 \pm 0.18, \theta_{high} : -0.26 \pm 0.16, \beta_{low} : -0.20 \pm 0.11, \beta_{high} : -0.20 \pm 0.14, \gamma_{low} : -0.22 \pm 0.15, \gamma_{mid} : -0.19 \pm 0.1, \gamma_{high} : -0.18 \pm 0.15$, ripple: -0.21 ± 0.17, 250Hz: -0.01 ± 0.04). During SPI in MECII neurons, CA1 shows virtually non-existent amplification ($\alpha : -0.51 \pm 0.12, \theta_{low} : -0.53 \pm 0.18, \theta_{high} : -0.45 \pm 0.16, \beta_{low} : -0.39 \pm 0.11, \beta_{high} : -0.35 \pm 0.14, \gamma_{low} : -0.31 \pm 0.15, \gamma_{mid} : -0.29 \pm 0.1, \gamma_{high} : -0.26 \pm 0.15$, ripple: -0.21 ± 0.17, 250Hz: -0.01 ± 0.1). During SPI in MECIII neurons, CA1 show highest amplification in the γ bands ($\alpha : -0.31 \pm 0.12, \theta_{low} : -0.28 \pm 0.18, \theta_{high} : -0.26 \pm 0.16, \beta_{low} : -0.20 \pm 0.11, \beta_{high} : -0.20 \pm 0.14, \gamma_{low} : -0.22 \pm 0.15, \gamma_{mid} : -0.19 \pm 0.1, \gamma_{high} : -0.18 \pm 0.15$, ripple: -0.21 ± 0.17, 250Hz: -0.01 ± 0.04). Finally, during SPI in dentate gyrus neurons, CA1 shows virtually no amplification ($\alpha : -0.05 \pm 0.07, \theta_{low} : -0.13 \pm 0.06, \theta_{high} : -0.25 \pm 0.08, \beta_{low} : -0.23 \pm 0.07, \beta_{high} : -0.23 \pm 0.1, \gamma_{low} : -0.22 \pm 0.1, \gamma_{mid} : -0.15 \pm 0.06, \gamma_{high} : -0.13 \pm 0.04$, ripple: -0.04 ± 0.04, 250Hz: -0.01 ± 0.03). During SPI in CA1 interneurons, CA1 actually shows positive amplification, possibly because of dis-inhibition ($\alpha : -0.07 \pm 0.02, \theta_{low} : -0.02 \pm 0.1, \theta_{high} : -0.23 \pm 0.08, \beta_{low} : -0.21 \pm 0.07, \beta_{high} : -0.18 \pm 0.1, \gamma_{low} : -0.16 \pm 0.1, \gamma_{mid} : -0.14 \pm 0.06, \gamma_{high} : -0.13 \pm 0.04$, ripple: -0.04 ± 0.01, 250Hz: -0.01 ± 0.01).

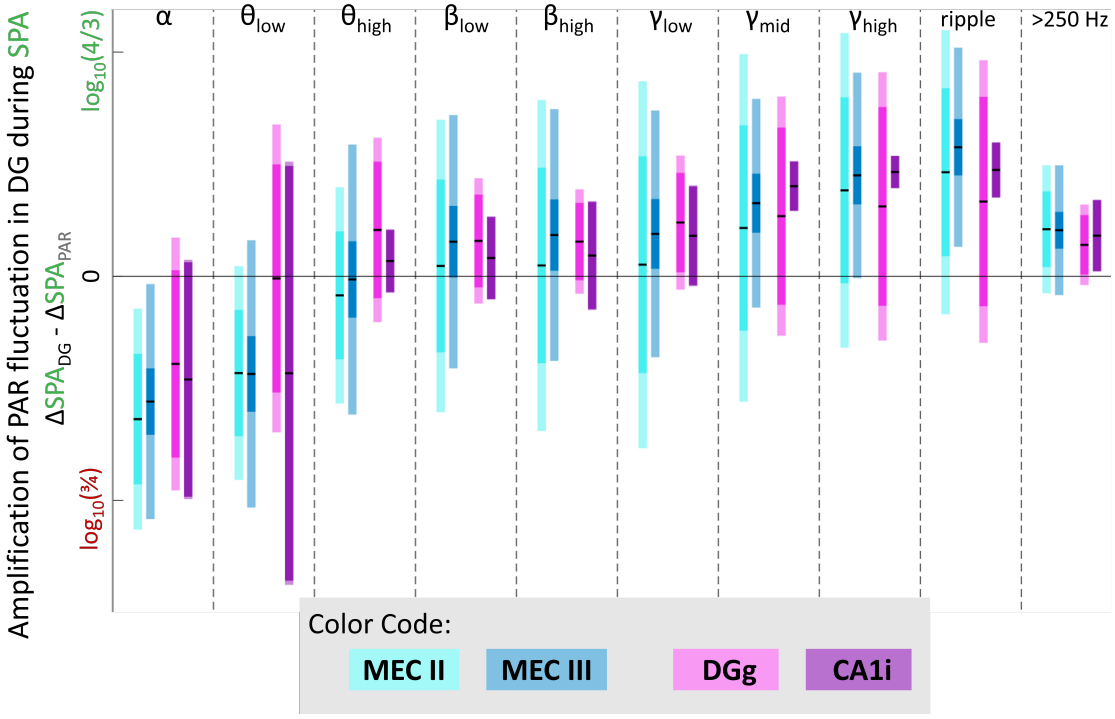

Figure 4.26: When SPA occurs within MEC or hippocampal neurons, the activity feedsforward to the Dentate gyrus granule cell layer. The amplification factor within DG due to each subpopulation of neurons is plotted, averaged over all experiments, for each frequency bin. The colors correspond to each population. DG showed amplification during SPA in MECII neurons, especially in the γ bands ($\alpha : -0.06 \pm 0.04, \theta_{low} : -0.02 \pm 0.05, \theta_{high} : -0.02 \pm 0.05, \beta_{low} : -0.1 \pm 0.05, \beta_{high} : -0.03 \pm 0.05, \gamma_{low} : -0.02 \pm 0.05, \gamma_{mid} : -0.01 \pm 0.03, \gamma_{high} : -0.01 \pm 0.04$, ripple: -0.01 ± 0.04, 250Hz: -0.01 ± 0.01). Similarly, DG showed significant amplification during SPA in MECIII neurons, especially in the γ and ripple bands ($\alpha : -0.16 \pm 0.05, \theta_{low} : -0.05 \pm 0.03, \theta_{high} : +0.15 \pm 0.05, \beta_{low} : +0.23 \pm 0.05, \beta_{high} : +0.26 \pm 0.05, \gamma_{low} : +0.30 \pm 0.05, \gamma_{mid} : +0.31 \pm 0.03, \gamma_{high} : +0.33 \pm 0.04$, ripple: $+0.25 \pm 0.04$, 250Hz: $+0.06 \pm 0.03$). During SPA in the dentate gyrus, DG LFP showed amplification ($\alpha : +0.05 \pm 0.07, \theta_{low} : +0.13 \pm 0.06, \theta_{high} : +0.25 \pm 0.08, \beta_{low} : +0.23 \pm 0.07, \beta_{high} : +0.23 \pm 0.1, \gamma_{low} : +0.22 \pm 0.1, \gamma_{mid} : +0.15 \pm 0.06, \gamma_{high} : +0.13 \pm 0.04$, ripple: $+0.04 \pm 0.04$, 250Hz: -0.01 ± 0.03). Finally, during SPA in CA1 interneurons, DG LFP showed significant positive amplification ($\alpha : -0.07 \pm 0.02, \theta_{low} : +0.02 \pm 0.1, \theta_{high} : +0.23 \pm 0.08, \beta_{low} : +0.21 \pm 0.07, \beta_{high} : +0.18 \pm 0.1, \gamma_{low} : +0.16 \pm 0.1, \gamma_{mid} : +0.14 \pm 0.06, \gamma_{high} : +0.13 \pm 0.04$, ripple: $+0.04 \pm 0.01$, 250Hz: -0.01 ± 0.01).

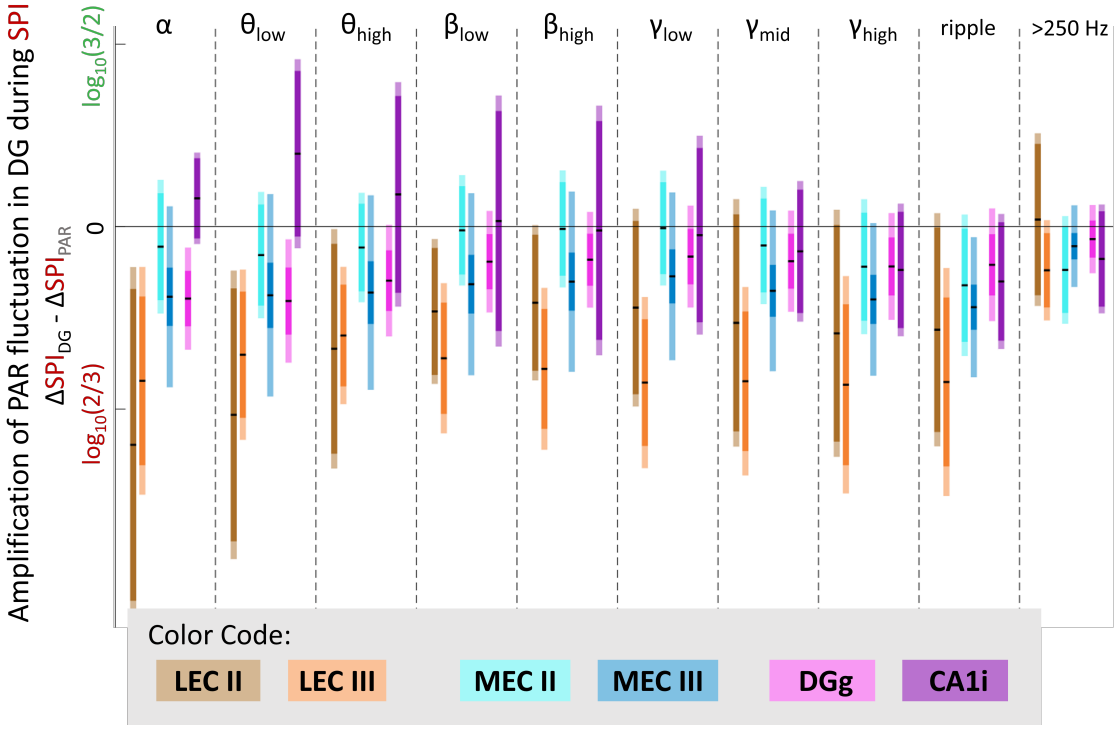

Figure 4.27: When SPI occurs within LEC, MEC, or hippocampal neurons, the activity feedsforward to the Dentate cell layer. The amplification factor within DG due to each subpopulation of neurons is plotted, averaged over all experiments, for each frequency bin. The colors correspond to each population. DG LFP showed significant amplification during SPI in LECII neurons, but only in the low frequency bands ($\alpha: -0.51 \pm 0.12, \theta_{low}: -0.53 \pm 0.18, \theta_{high}: -0.45 \pm 0.16, \beta_{low}: -0.39 \pm 0.11, \beta_{high}: -0.35 \pm 0.14, \gamma_{low}: -0.31 \pm 0.15, \gamma_{mid}: -0.29 \pm 0.1, \gamma_{high}: -0.26 \pm 0.15$, ripple: -0.21 ± 0.17, 250Hz: -0.01 ± 0.1). During SPI in LECIII neurons, DG shows highest amplification in the γ bands ($\alpha: -0.31 \pm 0.12, \theta_{low}: -0.28 \pm 0.18, \theta_{high}: -0.26 \pm 0.16, \beta_{low}: -0.20 \pm 0.11, \beta_{high}: -0.20 \pm 0.14, \gamma_{low}: -0.22 \pm 0.15, \gamma_{mid}: -0.19 \pm 0.1, \gamma_{high}: -0.18 \pm 0.15$, ripple: -0.21 ± 0.17, 250Hz: -0.01 ± 0.04). During SPI in MECII neurons, DG shows virtually non-existent amplification ($\alpha: -0.51 \pm 0.12, \theta_{low}: -0.53 \pm 0.18, \theta_{high}: -0.45 \pm 0.16, \beta_{low}: -0.39 \pm 0.11, \beta_{high}: -0.35 \pm 0.14, \gamma_{low}: -0.31 \pm 0.15, \gamma_{mid}: -0.29 \pm 0.1, \gamma_{high}: -0.26 \pm 0.15$, ripple: -0.21 ± 0.17, 250Hz: -0.01 ± 0.1). During SPI in MECIII neurons, DG show highest amplification in the γ bands ($\alpha: -0.31 \pm 0.12, \theta_{low}: -0.28 \pm 0.18, \theta_{high}: -0.26 \pm 0.16, \beta_{low}: -0.20 \pm 0.11, \beta_{high}: -0.20 \pm 0.14, \gamma_{low}: -0.22 \pm 0.15, \gamma_{mid}: -0.19 \pm 0.1, \gamma_{high}: -0.18 \pm 0.15$, ripple: -0.21 ± 0.17, 250Hz: -0.01 ± 0.04). Finally, during SPI in dentate gyrus neurons, DG shows virtually no amplification ($\alpha: -0.05 \pm 0.07, \theta_{low}: -0.13 \pm 0.06, \theta_{high}: -0.25 \pm 0.08, \beta_{low}: -0.23 \pm 0.07, \beta_{high}: -0.23 \pm 0.1, \gamma_{low}: -0.22 \pm 0.1, \gamma_{mid}: -0.15 \pm 0.06, \gamma_{high}: -0.13 \pm 0.04$, ripple: -0.04 ± 0.04, 250Hz: -0.01 ± 0.03). During SPI in DG interneurons, DG actually shows positive amplification, possibly because of dis-inhibition ($\alpha: -0.07 \pm 0.02, \theta_{low}: -0.02 \pm 0.1, \theta_{high}: -0.23 \pm 0.08, \beta_{low}: -0.21 \pm 0.07, \beta_{high}: -0.18 \pm 0.1, \gamma_{low}: -0.16 \pm 0.1, \gamma_{mid}: -0.14 \pm 0.06, \gamma_{high}: -0.13 \pm 0.04$, ripple: -0.04 ± 0.01, 250Hz: -0.01 ± 0.01).

most likely because when MECIII express SPA or SPI, it propagates through the MECII cells into DG, thus influencing both CA1 and DG populations.

During SPI, LECII and LECIII both show DG bias, but, as predicted by theory and the known anatomical connections, LECII has a stronger influence on DG compared to LECIII, across the spectra. The highest bias, however, occurs in the γ_{low} band, for both LECII and LECIII.

Finally, SPA in the DG shows high bias toward the DG activity, which is expected given that the SPA is occuring within the DG cell layer. However, CA1 interneurons do not show a marked influence on CA1 cell layer, and show virtually no bias towards either DG or CA1. This could be reflective of the fact that MECIII synapses onto CA1 but also only MECII cells. During SPI, this remains unchanged. No matter the band, SPI within DG cells leads to a shut down of the DG cell layer activity.

4.5 Discussion

Neocortical-hippocampal interactions lay the foundation of information processing for many different kinds of memory [184, 185]. During slow-wave-sleep, when memory consolidation is thought to occur, neocortical networks spontaneously fluctuate at low frequencies between Up states and Down states [26, 93, 94]. The hippocampus, however, is only weakly tied to this Up-Down state-related neocortical activity. Thus, a key question is: how might activity be synchronized and coordinated across circuits which are inherently asynchronous? In this present study, we propose that this dialogue occurs during the Up-Down state oscillation through a gating mechanism within the entorhinal cortex. We identify instances of spontaneous persistent activity within several populations of the medial and lateral entorhinal cortex, which are known to provide the majority of input into the hippocampal formation. We provide evidence that these desynchronization events within the entorhinal cortex are the key instances when neocortical information can be either enhanced or suppressed while on its way to the hippocampus. Furthermore, we show that the UDS across the cortex has its own fine temporal structure which is determined by the strength of excitatory afferent

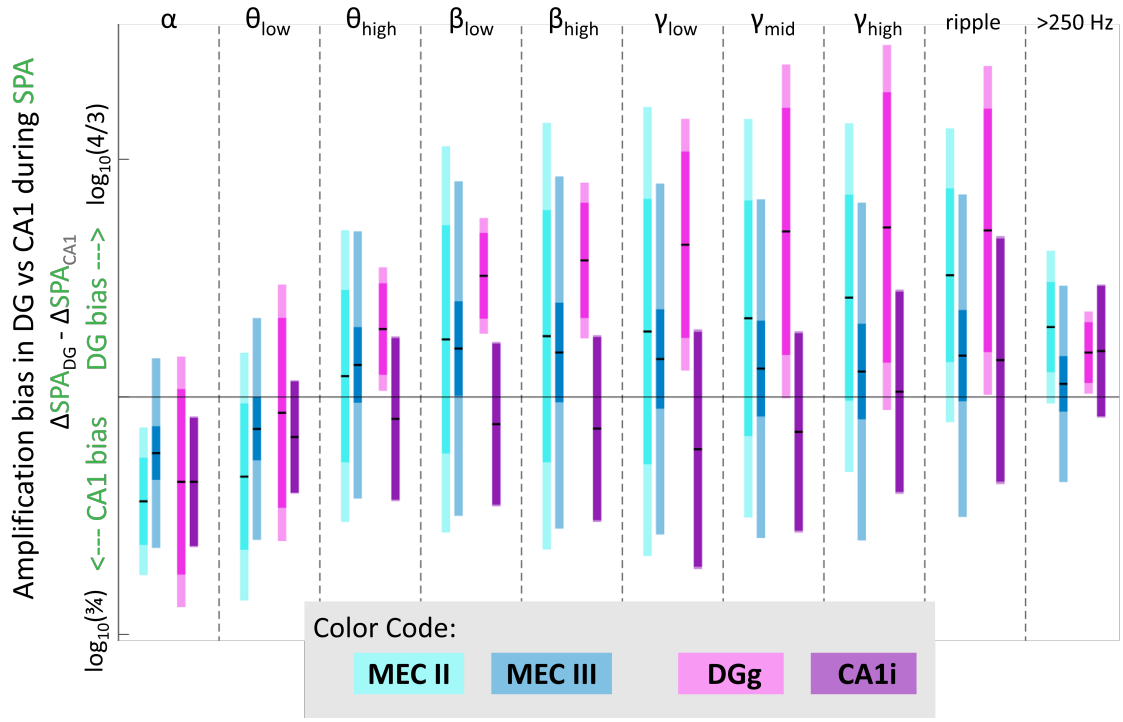

Figure 4.28: When SPA occurs within MEC or hippocampal neurons, the activity feedsforward to both the Dentate gyrus granule cell layer and the CA1 cell layer. The amplification factor within DG can be compared with that within CA1 due to each subpopulation of neurons. This is splotted, averaged over all experiments, for each frequency bin. The colors correspond to each population. During SPA in MECII neurons, DG was preferentially amplified compared to CA1, especially in the γ bands ($\alpha : -0.06 \pm 0.04, \theta_{low} : -0.02 \pm 0.05, \theta_{high} : -0.02 \pm 0.05, \beta_{low} : -0.1 \pm 0.05, \beta_{high} : -0.03 \pm 0.05, \gamma_{low} : -0.02 \pm 0.05, \gamma_{mid} : -0.01 \pm 0.03, \gamma_{high} : -0.01 \pm 0.04$, ripple: -0.01 ± 0.04, 250Hz: -0.01 ± 0.01). On the other hand, DG and CA1 showed similar amplification during SPA in MECIII neurons, with no preferential amplification ($\alpha : -0.16 \pm 0.05, \theta_{low} : -0.05 \pm 0.03, \theta_{high} : +0.15 \pm 0.05, \beta_{low} : +0.23 \pm 0.05, \beta_{high} : +0.26 \pm 0.05, \gamma_{low} : +0.30 \pm 0.05, \gamma_{mid} : +0.31 \pm 0.03, \gamma_{high} : +0.33 \pm 0.04$, ripple: $+0.25 \pm 0.04$, 250Hz: $+0.06 \pm 0.03$). During SPA in the dentate gyrus, DG LFP showed amplification more than CA1 LFP ($\alpha : +0.05 \pm 0.07, \theta_{low} : +0.13 \pm 0.06, \theta_{high} : +0.25 \pm 0.08, \beta_{low} : +0.23 \pm 0.07, \beta_{high} : +0.23 \pm 0.1, \gamma_{low} : +0.22 \pm 0.1, \gamma_{mid} : +0.15 \pm 0.06, \gamma_{high} : +0.13 \pm 0.04$, ripple: $+0.04 \pm 0.04$, 250Hz: -0.01 ± 0.03). Finally, during SPA in CA1 interneurons, DG LFP showed significant positive amplification, but CA1 LFP showed even more. ($\alpha : -0.07 \pm 0.02, \theta_{low} : +0.02 \pm 0.1, \theta_{high} : +0.23 \pm 0.08, \beta_{low} : +0.21 \pm 0.07, \beta_{high} : +0.18 \pm 0.1, \gamma_{low} : +0.16 \pm 0.1, \gamma_{mid} : +0.14 \pm 0.06, \gamma_{high} : +0.13 \pm 0.04$, ripple: $+0.04 \pm 0.01$, 250Hz: -0.01 ± 0.01).

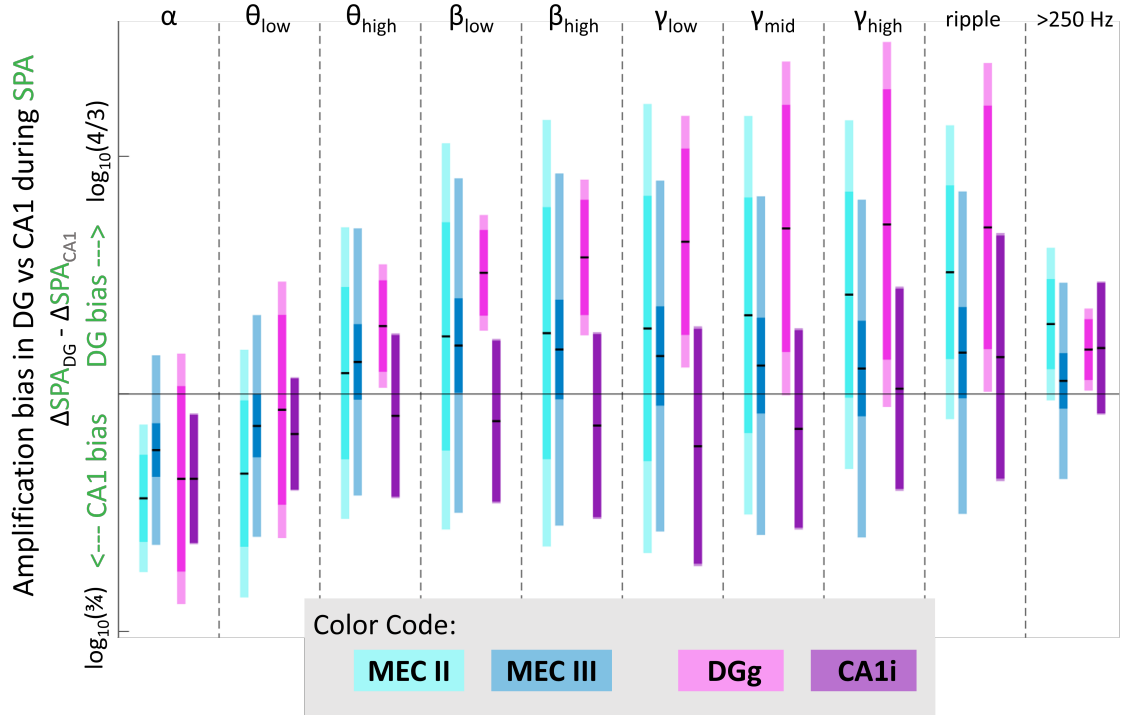

Figure 4.29: When SPI occurs within LEC, MEC, or hippocampal neurons, the activity feedsforward to the Dentate cell layer and CA1 layer. The amplification factor within DG due to each subpopulation of neurons can be compared with the amplification in CA1, and the difference is plotted, averaged over all experiments, for each frequency bin. The colors correspond to each population. DG LFP showed significant amplification during SPI in LECII neurons, significantly more than CA1 LFP ($\alpha: -0.51 \pm 0.12, \theta_{low}: -0.53 \pm 0.18, \theta_{high}: -0.45 \pm 0.16, \beta_{low}: -0.39 \pm 0.11, \beta_{high}: -0.35 \pm 0.14, \gamma_{low}: -0.31 \pm 0.15, \gamma_{mid}: -0.29 \pm 0.1, \gamma_{high}: -0.26 \pm 0.15$, ripple: -0.21 ± 0.17, 250Hz: -0.01 ± 0.1). During SPI in LECIII neurons, DG shows highest amplification in the γ bands, more than CA1 layer ($\alpha: -0.31 \pm 0.12, \theta_{low}: -0.28 \pm 0.18, \theta_{high}: -0.26 \pm 0.16, \beta_{low}: -0.20 \pm 0.11, \beta_{high}: -0.20 \pm 0.14, \gamma_{low}: -0.22 \pm 0.15, \gamma_{mid}: -0.19 \pm 0.1, \gamma_{high}: -0.18 \pm 0.15$, ripple: -0.21 ± 0.17, 250Hz: -0.01 ± 0.04). During SPI in MECII neurons, DG shows more amplification than CA1 ($\alpha: -0.51 \pm 0.12, \theta_{low}: -0.53 \pm 0.18, \theta_{high}: -0.45 \pm 0.16, \beta_{low}: -0.39 \pm 0.11, \beta_{high}: -0.35 \pm 0.14, \gamma_{low}: -0.31 \pm 0.15, \gamma_{mid}: -0.29 \pm 0.1, \gamma_{high}: -0.26 \pm 0.15$, ripple: -0.21 ± 0.17, 250Hz: -0.01 ± 0.1). During SPI in MECIII neurons, DG show highest amplification in the γ bands, but CA1 shows similar amount ($\alpha: -0.31 \pm 0.12, \theta_{low}: -0.28 \pm 0.18, \theta_{high}: -0.26 \pm 0.16, \beta_{low}: -0.20 \pm 0.11, \beta_{high}: -0.20 \pm 0.14, \gamma_{low}: -0.22 \pm 0.15, \gamma_{mid}: -0.19 \pm 0.1, \gamma_{high}: -0.18 \pm 0.15$, ripple: -0.21 ± 0.17, 250Hz: -0.01 ± 0.04). Finally, during SPI in dentate gyrus neurons, DG shows amplification but CA1 does not ($\alpha: -0.05 \pm 0.07, \theta_{low}: -0.13 \pm 0.06, \theta_{high}: -0.25 \pm 0.08, \beta_{low}: -0.23 \pm 0.07, \beta_{high}: -0.23 \pm 0.1, \gamma_{low}: -0.22 \pm 0.1, \gamma_{mid}: -0.15 \pm 0.06, \gamma_{high}: -0.13 \pm 0.04$, ripple: -0.04 ± 0.04, 250Hz: -0.01 ± 0.03). During SPI in DG interneurons, DG actually shows positive amplification, along with CA1 layer ($\alpha: -0.07 \pm 0.02, \theta_{low}: -0.02 \pm 0.1, \theta_{high}: -0.23 \pm 0.08, \beta_{low}: -0.21 \pm 0.07, \beta_{high}: -0.18 \pm 0.1, \gamma_{low}: -0.16 \pm 0.1, \gamma_{mid}: -0.14 \pm 0.06, \gamma_{high}: -0.13 \pm 0.04$, ripple: -0.04 ± 0.01, 250Hz: -0.01 ± 0.01).

current being provided by the neocortical network to the entorhinal network.

To investigate the nature of the Up-Down state oscillation within the cortex and hippocampus, we conducted experiments involving simultaneous recording of four neural subpopulations: the neocortical LFP, the CA1 layer LFP, the DG LFP, and the V_m from specific identified neurons embedded within its own network. Previous studies have shown the presence of spontaneous persistent activity within MECIII pyramidal neurons [94]. The previous chapter provided evidence for why a simple attractor mechanism involving the balance of excitation, inhibition, and adaptation can replicate not only SPA but also propose a new way of encoding memories, namely SPI.

We found that SPA and SPI are found ubiquitously across the entorhinal and parahippocampal region, especially among those subpopulations which were modulated by cortical UDS. We are the first to report the behavior of MEC layer 2 cells and LEC layer 2 cells during *in vivo* UDS; previous studies did not differentiate between the two subdivisions of the EC [93]. This is a crucial distinction, given that the two entorhinal regions differ starkly from one another in both structure and function [89]. We developed a new method of detecting SPA and SPI that did not require the bimodality condition needed earlier to classify V_m traces into a binary sequence [145].

We found that SPA was robustly expressed in not only MECIII pyramidal cells but also MECII stellate cells. These events, where the neuron, and thus the network in which it is embedded, remains depolarized while the rest of the cortex shuts down, has profound consequences on downstream hippocampal neural populations. Indeed, within the hippocampus, both cell populations which were modulated by UDS (the dentate granule cells and CA1 interneurons) showed significant amounts of SPA. These SPA events are most likely due to synchronous SPA events within the MEC, as neither the CA1 layer nor the DG granule cell population have significant recurrent excitatory connections, and pyramidal cells in CA1 are not phase locked to neocortical UDS [105, 106, 186]. Further, the SPA events within MECII cells are most likely themselves the result of the MECIII SPA, since MECII cells cannot support their own UDS oscillations, but MECIII cells can[187]. Related, the fact that MECII has fewer recurrent connections compared to MECIII cells is in agreement with

the theoretical idea that excitatory recurrent connections are crucial in the maintenance and initiation of Up states in the cortex, and can lead to higher rates of SPA [169]. Addition support for this notion comes from the fact that SPA in MECIII involves V_m depolarization of the same magnitude as a "normal" Up state, while in MECII the SPA events are significantly less depolarized compared to synchronous Up states.

We found that SPI was expressed by not only MECIII and LECIII cells, but also MECII and LECII cells. Again, this phenomena is most likely not endogenous of the layer 2 architecture, as both cell populations are dominated by interneurons and inhibition, and rarely form monosynaptic connections between other cells of the same identity [188–190]. SPI was found further down the stream of information in the hippocampus, again in the dentate granule cell population and the CA1 inhibition. Again, these are likely due to a "trickle-down" effect, wherin SPI from the layer 3 EC either directly inhibits CA1 or indirectly moves through layer 2 into dentate gyrus and subsequently CA1 cell layer.

During SPA, previous work has shown that hippocampal circuits are excited, with significantly higher MUA when compared to "normal" Up and Down states [94]. It has thus been suggested that MECIII may gate the information needed for the consolidation of different types of memories. The hippocampus recieves highly processed information from the neocortex and can therefore act as a hub for certain types of memories. It is thought that the hippocampus coordinates memory consolidation by replaying information obtained during the awake state during sleep [25]. Given that the hippocampus indirectly recieves input from most parts of the neocortex, one would expect coordinated neocortical firing to correspond to different levels of hippocampal activity. This however, in not the case. Although Up-Down state fluctuations represent the dominant neocortical network pattern during slow-wave-sleep, the hippocampus exhibits only brief periods of excitation which are only weakly tied to the cortical Up state. These questions were posed by previous studies, which shows that SPA occured within the entorhinal cortex layer 3, especially the medial subdivision, and caused hippocampal MUA to become highly active. The functional role of this release was still unclear.

We found that during SPA in MECII and MECIII and SPI in MECII, MECIII, LECII,

and LECIII, the hippocampal substructures were profoundly affected. The feedforward nature of these connections between the entorhinal and hippocampal structures were also specific to certain bands of oscillations. This is in line with recent findings which suggest that LEC uses the low gamma band to preferentially drive information transfer to the hippocampus, while MEC uses preferentially the high gamma band [191]. Given the differences in the architecture and behavioral functions of the lateral and medial subdivisions, this could indicate that different bands are used for different modes of information about the external world when building memories within the hippocampus.

Hippocampal sharp wave ripples have been implicated in the reactivation of waking firing patterns and memory consolidation [192]. Given our findigns about how activity can be amplified during Down states and suppressed during Up states when the entorhinal population expresses SPA and SPI, hippocampal sharp wave ripples could provide the substrate by which these momentary activations coordinate memory consolidation in parts of the neocortex, especially the prefrontal cortex [137]. The fact that SPA only occurs in the MEC, famous for spatially modulated cells, could mean that sharp wave ripples which occur in the Down state preferentially activate spatially modulated memories at these decoupling times. In contrast, sharp wave ripples that occur during Up states could be involved in encoding non-spatial information.

Chapter 5

3-Hz Rhythm in neurons of LEC Layer 2 and Hippocampal Inhibition

5.1 Introduction: Rhythms During Anesthesia

Hippocampal theta oscillations are of major significance in various cognitive and behavioral processes, such as arousal, attention, exploration of the environment, voluntary locomotion, learning and memory, sensorimotor processing, and REM sleep [71, 193, 194]. Anatomically, the minimal structure needed to trigger and sustain theta activity is the hippocampus and the medial septum. The entorhinal cortex is a major source of input for the hippocampus, and the two divisions of the entorhinal cortex, the lateral (LEC) and medial (MEC), show differential theta modulation. In studies comparing the two regions, the LFP in LEC showed significantly fewer theta oscillations than those in MEC; similarly, single neurons in LEC were significantly less modulated by the theta rhythm than MEC neurons.

Recent studies in sub-gamma (¡30 Hz) oscillations within the hippocampus have shown a new emergent oscillation that is almost half the frequency of theta, called eta (2-4Hz), that emerges within the hippocampus during virtual reality but not during normal behavior. This eta rhythmicity was higher in interneurons than pyramidal neurons within CA1. A prominent rhythm within the same frequency band is also prevalent in hippocampal CA2 pyramidal neurons, but not CA1 pyramidal neurons [195]. Stimulation of the rhythmic neurons at the oscillation frequency showed that the rhythm was not being sustained by

the CA2 neuron or the network in which it was embedded, but instead was coming from upstream, postsynaptic sources.

In this study, we show a new 3-Hz rhythm within the LEC which is not present in the MEC during urethane anesthesia, distinguishing it from the well studies theta rhythms. This rhythm is also present in dentate gyrus neurons and CA1/CA3 inhibition, but not CA1/CA3 excitation. Our results suggest a possible origin for the 3-Hz eta rhythm found in recent studies, and could hint at a larger role for the LEC during navigation of virtual spaces.

5.2 The 3-Hz Rhythm in Membrane Potential

Mice were anesthetized with light urethane dose and simultaneous LFP from the parietal cortex and membrane potential from individual neurons in the para-hippocampal circuit were extracted using methods previously described. Robust Up-Down states were found, along with a conspicuous 3-Hz rhythm that would spontaneously arise and subside, sometimes lasting as long as 100 seconds. These sub-threshold oscillations were found in all regions of LEC, including layer 2 fan cells (N=5), layer 2 multi-form cells (N=6), and layer 3 pyramidal cells (N=12) (Fig. 5.1). These oscillations were also found in hippocampal inhibition, within the CA1 and CA3 interneurons (N=11,12 respectively), but not in hippocampal excitation (Fig. 5.2).

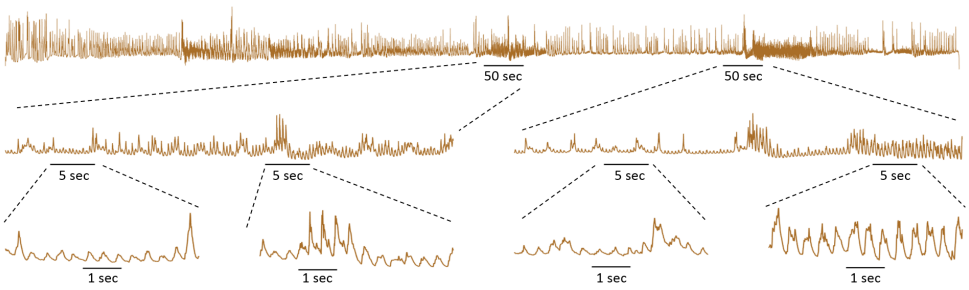

Figure 5.1: Example of prevalent 3Hz rhythm in the membrane potential of an LEC Layer 2 fan cell, under different resolutions on the time axis. Top panel shows entire experiment.

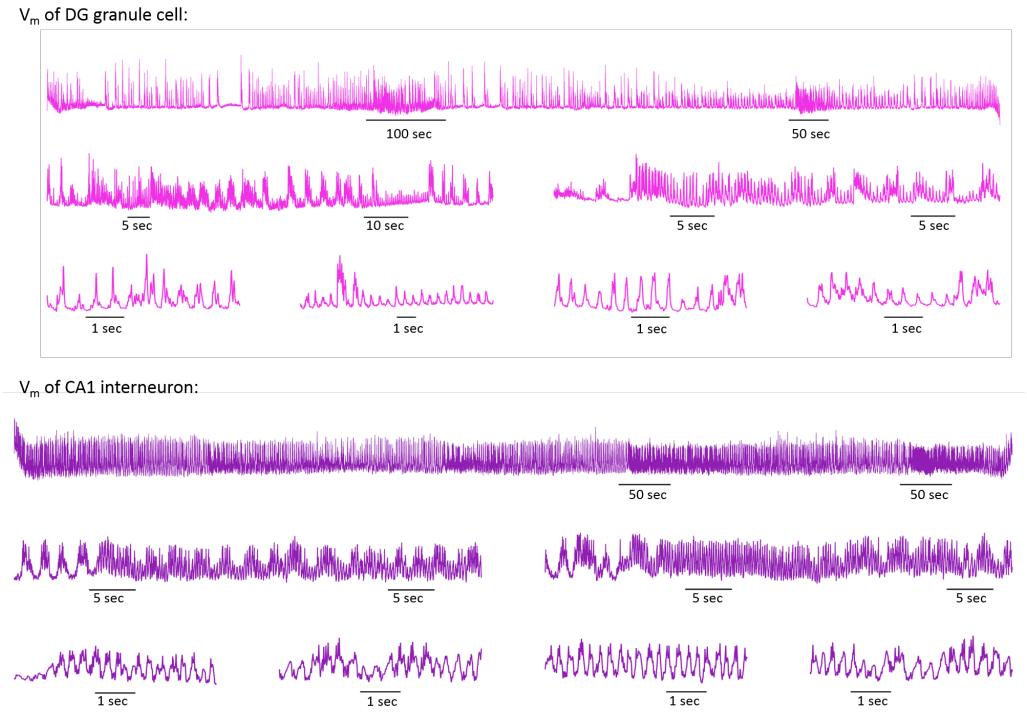

Figure 5.2: Top panel: Same as Fig 5.1, but for a detate gyrus granule cell. Bottom panel: A CA1 interneuron. Both examples show prominent eta oscillation, that is distinguishable from the underlying Up-Down states.

5.2.1 Detection and Quantification

Oscillations are usually detected using autocorrelations, as any prominent rhythmicity will be singled out in this method (Fig. 5.3). This technique exaggerated the prominent Up-Down states which occur during anesthesia, sometimes washing out the 3-Hz rhythm or reducing it only into small bumps riding on top of the larger amplitude 0.5-2 Hz rhythm. To extract this smaller amplitude, higher frequency oscillation, we smoothed the original autocorrelation (Gaussian kernel, s.t.d. 0.1s) and took the second derivative, which effectively enhances oscillations with a factor of ω^2, where ω is the frequency. This resulted in the 3-Hz rhythm getting picked out, and allowed for its unequivocal detection. The noise band was computed using 50 random shuffles, and if the first peak in the 2-4Hz range was larger than 2 s.t.d of the noise distribution, the cell was deemed eta-rhythmic.

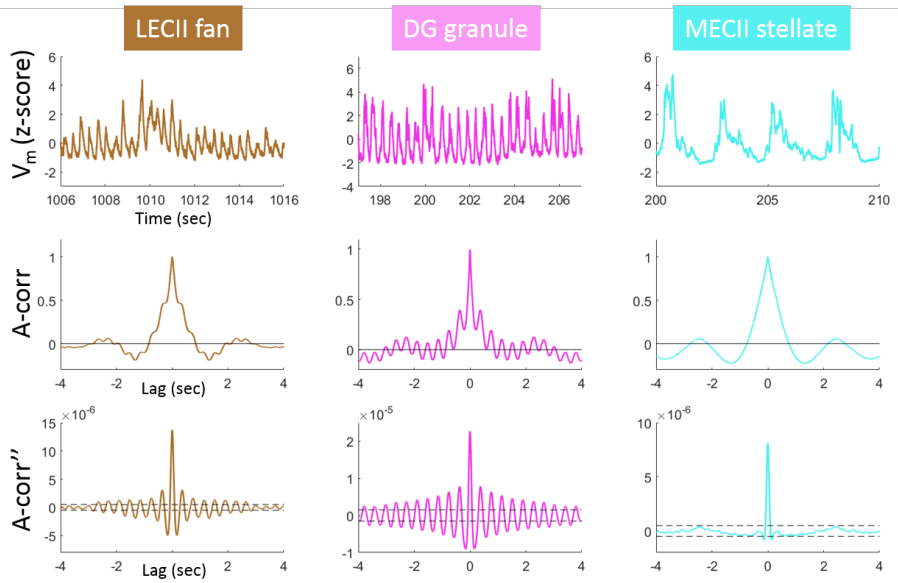

Figure 5.3: Detection of eta-rhythmic cells. To detect the eta rhythm, the following procedure was used. The membrane potential (top row) was used for an auto-correlation (middle row) between lags ±4 seconds. The most prominent oscillation was almost always the Up-Down states, with a frequency between 0.5 and 2 Hz. To detect the higher eta frequency, we took the second derivative of the smoothed auto-correlation (window of 0.1s). The first peak at positive lag was found, and the cell was classified as a 3Hz-rhythmic cell. Here, the LECII fan cell (left column) and Dentate Gyrus granule cell (middle column) show eta rhythmicity, but the MECII stellate cell does not.

5.2.2 Prevalence of 3-Hz Rhythm in Brain Regions

Using this second derivative technique, we identified neurons with rhythmicity in the 2-4 Hz band. No cells in the neocortex showed significant rhythmicity, and virtually no cells within the MEC (Fig. 5.4). The LEC, on the other hand, showed significant rhythmicity, especially in layer 2 (LECII MF: 4/5, LECII fan: 5/6, LECIII pyr: 4/12). In hippocampal areas, the Dentate gyrus granule cells showed rhythmicity (11/12), and the interneurons of CA1 (6/11) and CA3 (8/9) showed rhythmicity. 3Hz rhythm was virtually absent in excitatory neurons (CA1 pyr: 1/15, CA3 pyr: 2/13). The rhythm was incredibly stable across brain regions, with virtually all cells showing the same average frequency (Fig. 5.5).

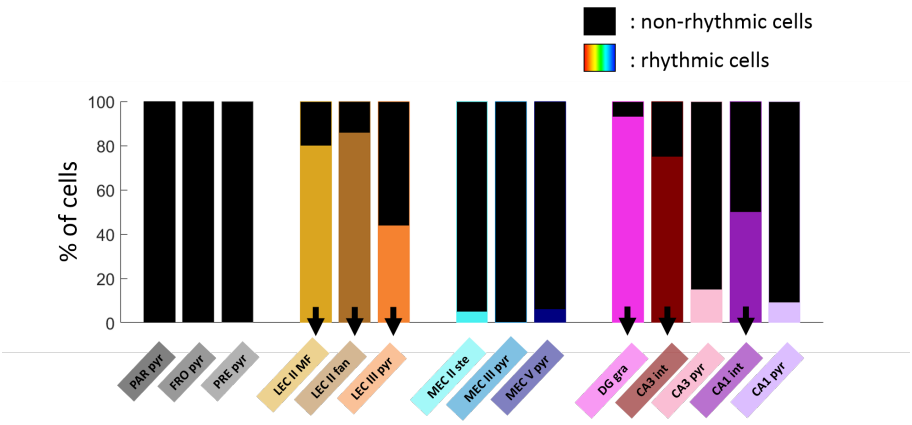

Figure 5.4: Prevalence of 3Hz rhythm within brain regions. The 3-Hz rhythmicity was present in LEC neurons, specially layer 2 (LECII MF: 4/5, LECII fan: 5/6, LECIII pyr: 4/12). The rhythm was completely absent in neocortical areas (PAR, PRE, FRO) and virtually absent in all MEC areas. In hippocampal areas, the Dentate gyrus granule cells showed rhythmicity (11/12), and the interneurons of CA1 (6/11) and CA3 (8/9) showed rhythmicity. 3Hz rhythm was virtually absent in excitatory neurons (CA1 pyr: 1/15, CA3 pyr: 2/13).

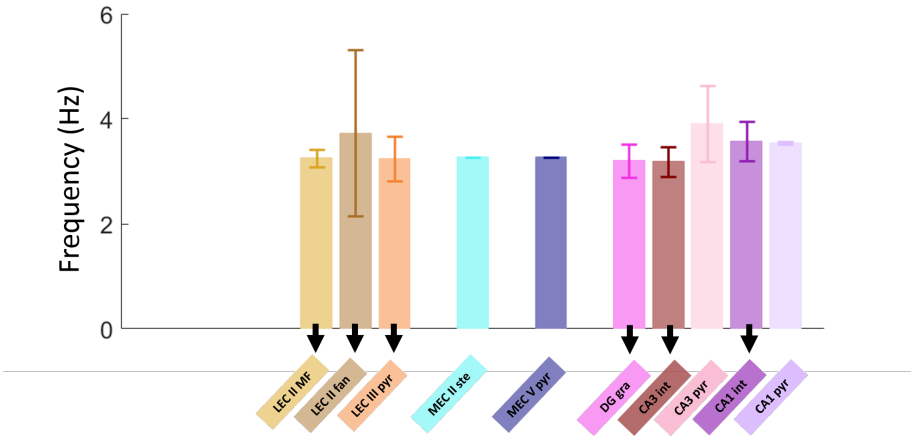

Figure 5.5: Average Eta frequency within brain regions among rhythmic neurons. Only regions of LEC and DG, CA1 interneurons, and CA3 interneurons had significant amounts of rhythmic cells, shown by the vertical arrows. All regions showed very similar rhythms (LEC II MF: 3.1 ± 0.2 Hz, LECII fan: 3.2 ± 0.3 Hz, LECIII pyr: 3.1 ± 0.3 Hz, MECII ste: 3.1Hz, MECV pyr: 3.1Hz, DG gra: 3.1 ± 0.1Hz, CA3 int: 3.1 ± 0.1Hz, CA3 pyr 3.1 ± 0.1Hz, CA1 int: 3.3 ± 0.3Hz, CA1 pyr: 3.23 Hz).

5.3 Eta Epochs

To identify individual oscillating events, we used two approaches. First, the auto-correlogram was computed within 10 second windows, with 5s overlap, and visualized in a matrix (Fig. 5.6). Clear instances of eta-rhythm could be visually detected. To supplement this visual approach quantitatively, we used the wavelet transform. Any given time period was defined as a '3Hz' oscillation epoch if the mean absolute value of its wavelet coefficient between 2-4 Hz exceeded the mean ±2 s.t.d. of the values between 1-100 Hz. The detected events were scrutinized and confirmed by eye and manually rejected if they were erroneously detected.

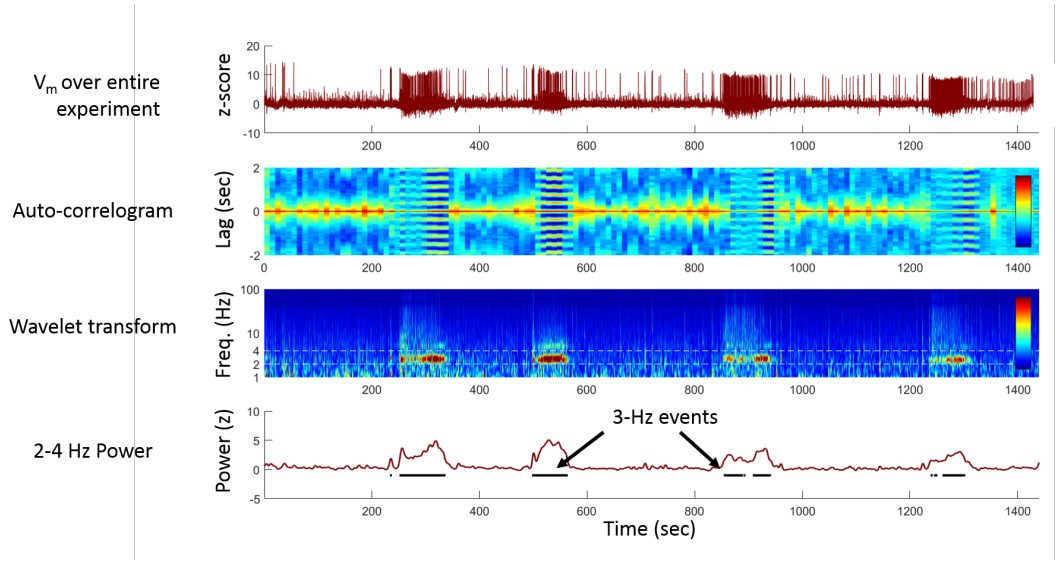

Figure 5.6: Detection of Eta Epochs. The entire experimental trace was first z-scored (top row). The auto-correlogram was taken, and the results visualized (second row). Clear time windows of strong eta rhythmicity is evident. The wavelet transform was also taken to supplement the auto-correlogram (third row). The power in the 2-4 Hz band was used as a measure of eta strength, and eta epochs were identified when it crossed a threshold (fourth row). The detected events were scrutinized and confirmed by eye (using the autocorrelogram) and manually rejected if they were erroneously detected.

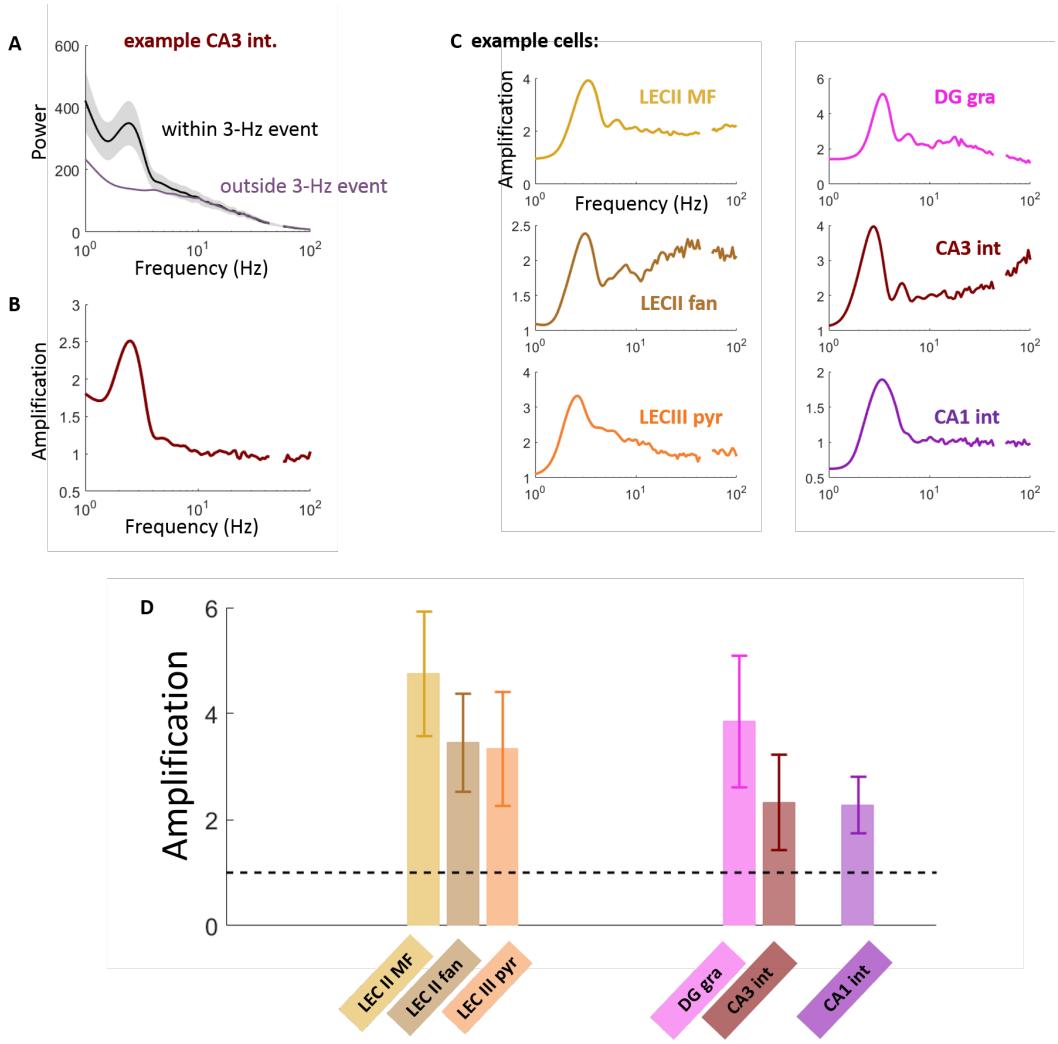

Figure 5.7: Amplification of Eta within Eta epochs. A)An example CA3 interneuron, showing the power spectra within the eta epoch (black) and outside the eta epoch (colored). B) The ratio between the power spectra gives the amplification of each band within the epoch. There is significant amplification in the 2-4 Hz eta band. C) Examples from other brain regions, showing significant amplification of nearly all frequencies during the eta band, but especially eta itself. D) Amplification factors across populations with significant rhythmicity. LEC region showed highest amplification, especially in LEC layer 2 multi-form cells (LECII MF: 4.5 ± 1.4, LECII fan: 3.8 ± 0.8, LECIII pyr: 3.8 ± 0.8). DG granule cells also showed significant amplification, and CA3 and CA1 interneurons showed the lowest amount of amplification (DG: 4.1 ± 1.1, CA3 int: 2.1 ± 0.7, CA1 int: 2.1 ± 0.7)

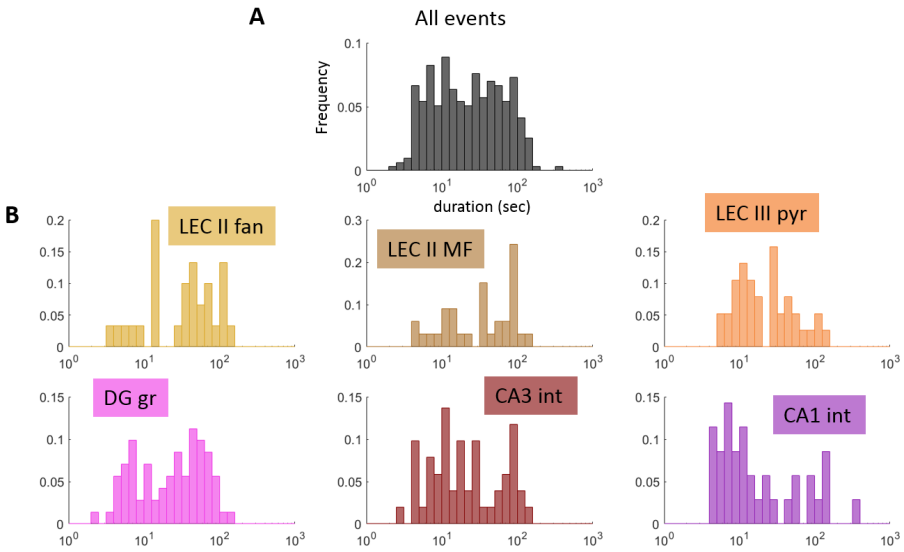

Figure 5.8: Duration of Eta epochs. A) Combined Eta event durations across all cell populations. The durations as a whole is log-normally distributed (mean: 54s, std: 35s). There is a hint of a bimodal distribution. B) Duration of eta epochs within each brain region.

The sub-threshold membrane potential of the neuron showed prominent eta oscillation during the detected epochs. To quantify this effect, we took the ratio of the power spectra (1-100 Hz) between the membrane potentials during the eta epochs and outside the eta epochs (Fig. 5.7). This yielded an amplification factor for each neuron within the eta band. Comparing across brain regions, our analysis showed that the amplification was highest among the population of eta rhythmic LECII multi-form cells, but all LEC regions showed high amplification. DG granule cells also showed similar amplification factors. CA1 and CA3 interneurons, on the other hand, showed significantly decreased amplification during eta epochs. The duration of the epochs was also investigated. Across all cell types and populations, the event durations were log-normally distributed (Fig. 5.8). Within each population, the durations showed a multi-modal distribution, with the events preferentially lasting either 1-10 seconds or 50-100 seconds long. This could be hinting at two different mechanisms for eta generation.

5.4 Discussion

In the present study, we observed a novel 3-Hz rhythm in LEC neurons, Dentate Gyrus granule cells, and interneurons of the hippocampus using whole-cell patch clamp of individual identified neurons. A majority of neurons in the LEC showed rhythmicity, but this was virtually absent in MEC. This rhythm was also present in hippocampal inhibition and Dentate Gyrus granule cells, but not in hippocampal excitatory neurons.

The 3-Hz oscillation found in this study is in close proximity to the minimum frequency of the theta oscillation range [196]. But is the rhythm we found really theta? Given that this rhythm was completely absent in MEC but highly prevalent in LEC, the rhythm we found is most likely not the traditional theta described in previous studies. Theta oscillations comprise large-scale events that recruit the entire hippocampal network, including CA1 and CA3 pyramidal neurons, MEC II stellate cells, and Dentate Gyrus. The rhythm we found here was absent in MEC and hippocampal excitation.

Recent studies have shown a prominent 3-Hz rhythm in CA2 neurons subthreshold membrane potential during urethane anesthesia, but not in CA1 pyramidal neurons [195]. The authors of the study further showed that this rhythm did not occur concurrently with hippocampal theta rhythm in LFP, and that the CA2 pyramidal neurons did not resonate to a 3-Hz current injection. They suggested that the origin of the rhythm lay in circuits upstream from CA2. Taken together with our results, this suggests a close connection between LEC neurons, especially layer 2, and the CA2 circuit, and could be confirmed by future anatomical studies.

Recent studies in behaving animals have shown that while theta is prevalent in real world exploration, a new rhythm, deemed "eta" is prevalent during random foraging in body-fixed virtual reality [71]. The rhythm is further prominent in CA1 interneurons more so than CA1 pyramidal neurons, while the theta rhythm is prominent in both cell populations. The similarity between this rhythm and the one found in our present study suggests that the eta rhythm originates in LEC layer, not MEC. Further studies are needed to support or refute this claim.

Appendix A
Experimental Protocols

A.1 Animals, Surgery, and Histology

Methods were similar to those described previously (15). Briefly, data were obtained from 136 C57BL6 mice aged postnatal day (p)25-43 ($p32\pm1$) weighing 12-21 g (17.5 ± 0.4 g). Mice were anesthetized with urethane (1.64 ± 0.03 g urethane / kg body weight intraperitoneal). Body temperature was maintained at 37°C with the help of a heating blanket. The animals were head-fixed in a stereotaxic apparatus and the skulls exposed. A metal plate was attached to the skull and a chamber formed with dental acrylic, which was filled with warm cerebrospinal fluid. Two 1-mm diameter holes, one for the LFP recordings and one for the whole-cell recordings, were drilled over the left hemisphere and the underlying dura mater was removed.

After electrophysiological recordings, mice were euthanized by transcardial perfusion with 0.1 M phosphate buffer, followed by 4% formaldehyde solution, and 150-200 μm thick brain sections were processed with the avidin-biotin-peroxidase method. Sometimes, a subsequent Nissl stain was applied before embedding. Visualization of biocytin filled neurons allowed for the determination of cell type and recording site (Fig A.1). Unidentified neurons were excluded from analysis. All experimental procedures were carried out according to the animal welfare guidelines of the Max-Plank-Society.

A.2 Electrophysiology and Data Acquisition

Local field potentials (LFPs) were recorded with an 8 site single-shank multisite probe (NeuroNexus Technologies). LFP from layer 2/3 of posterior parietal cortex (2 mm posterior to bregma, 1.5 mm lateral) was used to characterize parietal cortex Up-Down states. *In vivo* intracellular membrane potential (V_m) was recorded in whole-cell configuration by using borosilicate glass patch pipettes with DC resistances of 4-8 MΩ and filled with a solution containing 135 mM potassium gluconate, 10 mM HEPES, 4 mM Potassium Chloride, 10 mM phosphocreatine, 4 mM MgATP, 0.3 mM Na3GTP (adjusted to pH 7.2 with KOH), and 0.2% biocytin for subsequent histological identification. Whole-cell recording configuration was achieved as described previously(89). Relative to bregma, the anteroposterior (AP), mediolateral (ML) and dorsoventral (DV) coordinates of the craniotomies for the V_m recordings were made around -4.5 mm AP and 4 mm ML for MEC; -3.5 to -4 mm AP, 4.5 mm ML and 4 mm DV for LEC; -1.5 to -2 mm AP and 1 mm ML for parietal cortex; 1 to 1.5 mm AP and 1 mm ML for frontal cortex; 2 to 3 mm AP and 0.5 to 1 mm ML for prefrontal cortex.

The average initial series resistance was 46 MΩ, and V_m values were corrected for the estimated junction potential of approximately +7 mV.

The V_m was acquired by Axoclamp-2B (Axon Instruments) and fed into a Lynx-8 amplifier (Neuralynx). The V_m and LFP were recorded by an HS16 preamplifier (Neuralynx) for about 20-40 minutes. The complete recording was used for subsequent statistical analysis. The LFP were sampled at 2 kHz, low-pass filtered below 475 Hz, and amplified 1000-5000 times. The membrane potential was low-pass filtered below 9 kHz, sampled at 32 kHz, and amplified 50-150 times. Simultaneously, the DC value of V_m was recorded by an ITC18 interface (Instrutech) under the control of Pulse software (Heka) or by a Micro1401 with Spike2 software (CED). Some of these DC-coupled data were recorded in discontinuous sweeps of 7 or 10 s, separated by 5 or 2 s, respectively.

A.3 Data preprocessing

All analysis was restricted to subthreshold fluctuations in the membrane potential by removing spikes as follows. The temporal derivative of the bandpass-filtered (100 Hz - 8 kHz) membrane potential signal was computed, and times when this derivative exceeded 10 standard deviations above the mean were taken as spike times. Spike waveforms were then removed by replacing 3 ms of data following the onset of each spike by linear interpolation of adjacent values. To remove the 50 Hz mains hum and its many harmonics, 8-pole bandstop filters were used at 45-55 Hz, 95-105 Hz, 145-155 Hz, 195-205 Hz, 245-255 Hz, and 295-305 Hz.

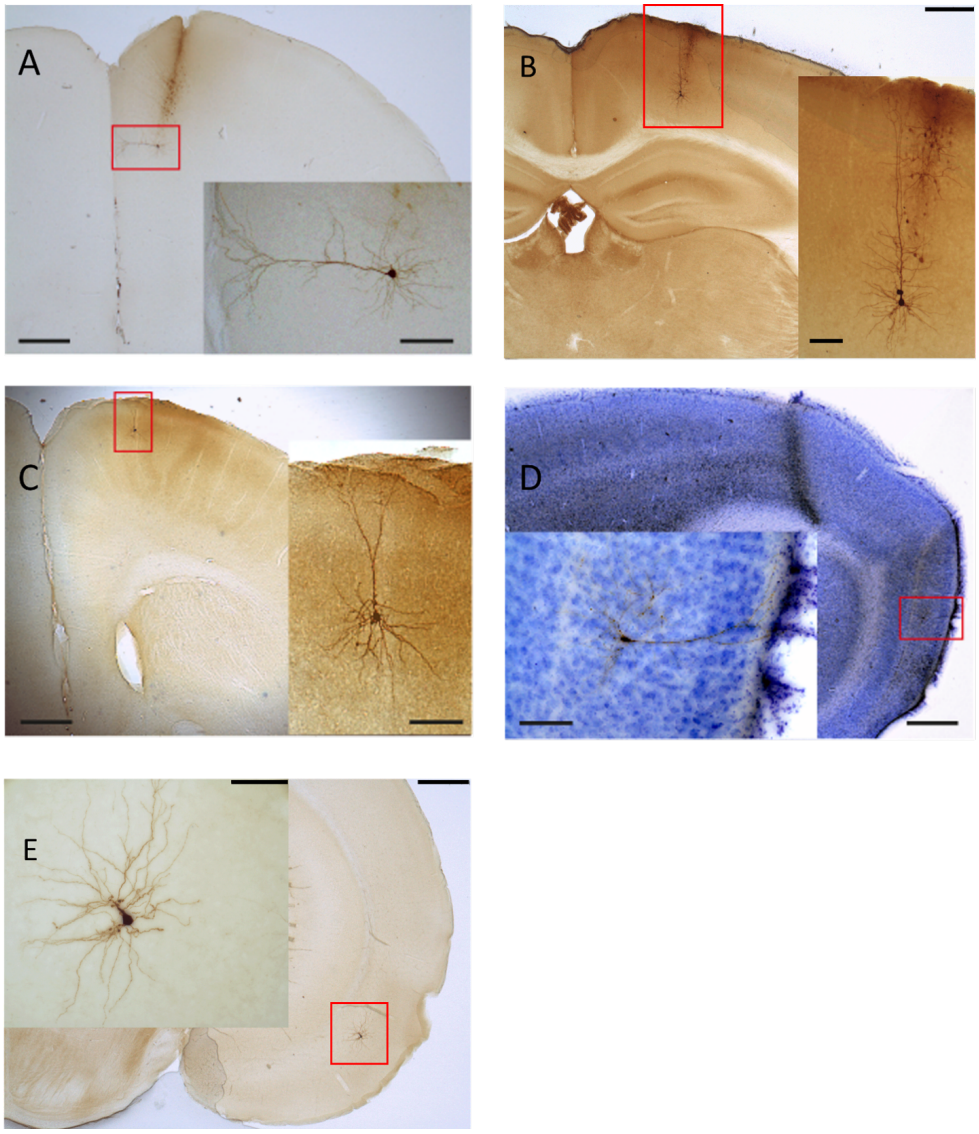

Figure A.1: Histological reconstructions of patched cells allowed for identification of cell type and brain location. A) Prefrontal Cortex Pyramidal Neuron. B) Pareital Cortex Pyramidal Neuron. C) Frontal Cortex Pyramidal Neuron. D) Medial Entorhinal Cortex Layer 3 (MECIII) pyramidal neuron. E) Lateral Entorhinal Cortex Layer 3 Pyramidal Neuron. Scalebars for low and high magnifications are 500 and 100 micrometers, respectively.

Appendix B
Details of Data Analysis

B.1 Explicit-duration Hidden Markov Model detection of Up and Down states

Synchronized epochs, wherein the LFP and cortical V_m undergoes synchronous transitions of Up and Down states (UDS), were selected by locating and eliminating periods of data with desynchronized activity where UDS are absent. Methods from (41) were closely followed. Briefly, the spectrogram of the signal was computed in 15-s overlapping windows using multi-taper methods (Chronux Matlab toolbox) with a time-bandwidth product of 4, and seven tapers. The maximum log power in the range of 0.05-2 Hz and the integral of the log power in the 4-40 Hz range we then used to locate and remove desynchronized epochs in the data. The remaining data exhibited UDS. UDS of both membrane potential and parietal LFP were classified using two state explicit-duration hidden Markov models (EDHMMs). The V_m and LFP were first filtered in the low frequency (0.05-2 Hz) range, and a gaussian observation EDHMM was fit to the filtered signal, with inverse gaussian models of the state duration distributions. The means of the state-conditional gaussians were slowly varying functions of time, where the parameters were estimated over a 50 second window length. We found the maximum likelihood parameter estimates of the EDHMM, and computed the resulting "Viterbi" sequence, which was used to define UDS oscillations.

B.2 Assignment of corresponding neocortical-entorhinal state transitions

Given two UDS sequences, one for the parietal cortex LFP (or network 1 in the simulation) and one for the entorhinal V_m (network 2), the fine temporal relationships and quantized duration was calculated by first assigning each Up/Down state in the V_m to its corresponding set of trigger states in the LFP. This was done through a greedy search algorithm, where in each iteration of the algorithm, the Up/Down state initiations were linked to the closest Up/Down state initiations in the corresponding LFP. Note that this does not guarantee a one-to-one mapping from V_m states to LFP states; those V_m states which map onto more than one LFP state are termed "persistent." The quantized duration of a V_m state was calculated as the number of total LFP states (both Up and Down) that would fit inside a particular V_m state, with each Up and Down state in the cycle contributing to 0.5 units of time (Fig B.1).

B.3 Generalized method of detecting SPA and SPI within membrane potential

While MECIII and LECIII neurons are clearly bimodal, many cells within the larger parahippocampal region are not. This makes detection of clean Up-Down states within the membrane potential trace challenging, thus impeding detection of SPA and SPI events. To address this issue, we sought an alternative method that relied only the UDS sequence in the parietal LFP (B.2).

Up-Down states were detected in the parietal cortex LFP using the same method as described above, and the binary switching defined a universal clock throughout the entire experiment. The lag between the the parietal LFP and the target neuron's V_m was calculated using the peak of the cross-correlation. The V_m trace was then aligned with the parietal LFP, and the LFP and V_m sequences around each Up and Down state were extracted. To detect SPA, all LFP Down states and the previous Up states were selected, and the behavior of the aligned V_m was analyzed. In most cases, the V_m also started in the Up

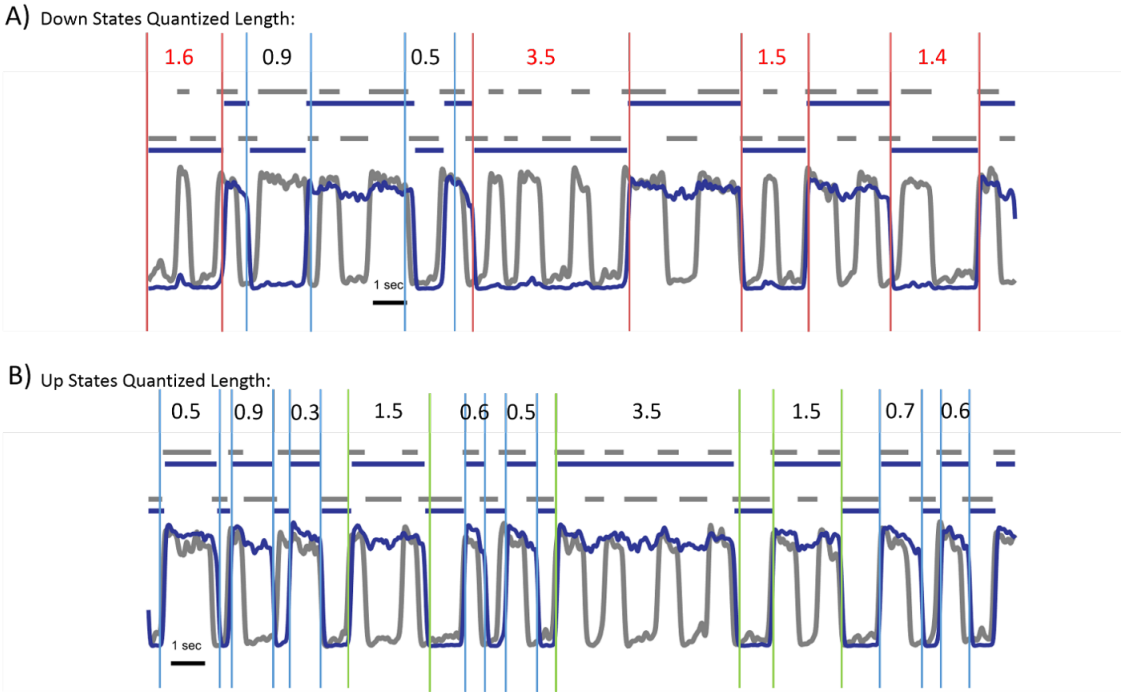

Figure B.1: Counting membrane potential state durations in terms of parietal UDS cycles. A) 'Down' states in the membrane potential (blue trace) are first aligned with the nearest parietal 'Down' state, and the number of LFP 'Down' and 'Up' states this particular membrane potential 'Down' state lasts is counted. Each 'Down' and 'Up' state receives a time length of 0.5 units, a full UDS cycle is thus 1-unit long. The 'Down' states in red represent those that are considered "spontaneous persistent inactivity," since they last for longer than one full UDS cycle. B) Same as A, but for 'Up' states. Those 'Up' states that were identified as persistent activity are highlighted in green.

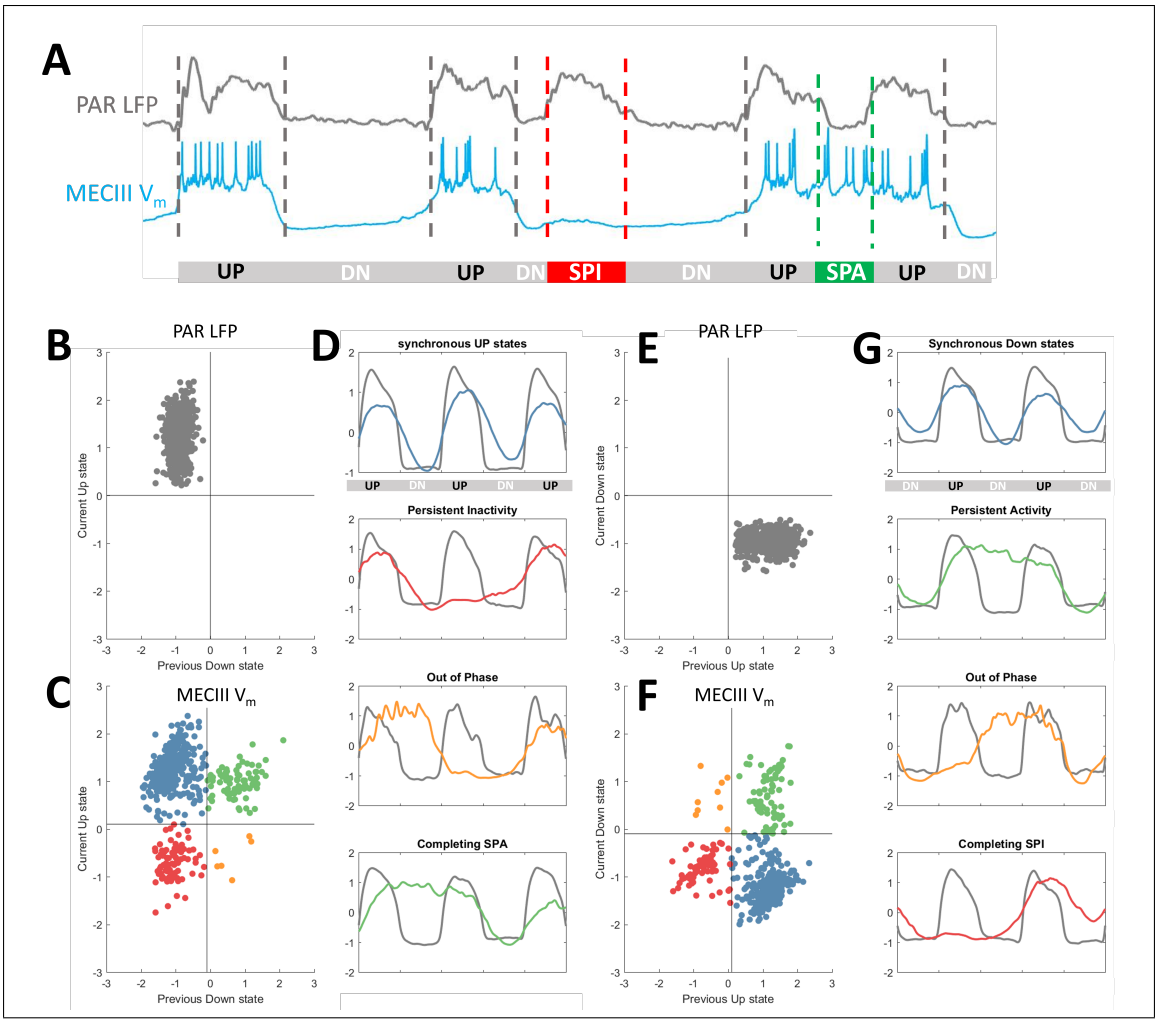

Figure B.2: (Continued on the following page.)

state and transitioned to a Down state, evident by the amplitude of the V_m during those time points. In some cases, the V_m started in the Up state and stayed there; this is SPA. The cases where the V_m started instead in the Down state are discarded.

Similarly, to detect DPI all LFP Up states and the previous Down states were selected, and the behavior of the aligned V_m was analyzed. In most cases, the V_m also started in the Down state and transitioned to a Up state. In some cases, the V_m started in the Down state and stayed there; this is SPI. The cases where the V_m started instead in the Up state are discarded.

Figure B.2: Generalized detection method for SPA and SPI. A) Using the time-lag obtained from the cross-correlation, the membrane potential of the neuron is aligned with the LFP in the parietal cortex, and the Up-Down state sequence in the parietal cortex is used as a universal clock. Up states in the parietal cortex that are accompanied and preceded by hyperpolarization in the V_m are termed SPI, and Down states in the parietal cortex that are accompanied and preceded by depolarization are termed SPA. To detect these states, every Down-Up transition in the parietal cortex is analyzed. The amplitude of the B) parietal LFP and the C) V_m of the target neuron are plotted, with the Down state amplitude on the x-axis and the following Up state amplitude on the y-axis. The target neuron usually does one of three things: it can either undergo a synchronous Down-Up transition (blue), continue in the Down state (red), or have started in the Up state and simply stayed in the Up state (green). The fourth possibility occurs if the V_m is simply out of phase from the parietal UDS (orange). D) To visualize these classes of events, we use the global parietal clock, centered on the UP state. The instances where the V_m persisted in the Down state during a parietal Up state (i.e. the red events) are identified as persistent inactivity (SPI) E) The same procedure was used for the Up-Down transitions. In this case, amplitude of parietal LFP is plotted for Up states (x-axis) and the following down state (y-axis). F) When the V_m is plotted using the same procedure, there are again three prominent possibilities: a synchronous Up-Down transition (blue), a persistent activity state (green), or a completion of SPI. In rare cases, the V_m is out of phase (orange). G) These events can again be visualized using the global PAR UDS clock.

B.4 LFP Amplitude and Gamma Power during Up and Down states

To extract the gamma power in the LFP during UDS, each LFP trace was filtered in the gamma band (40-120 Hz) using 8-pole bandpass filters(90, 91). The amplitude of the Hilbert transform of the signal was used as the gamma amplitude, and was smoothed with a gaussian-convolution of width 100 ms. For every Up and Down state, the gamma power in that state was assigned as the mean value of the power during the middle 80% of the state, thereby removing artifacts from the sharp Up-Down and Down-Up transitions that flank each state. Gamma power in the membrane potential was found by first removing spikes and then using the same technique and parameters. In figures where z-scored amplitude is used, both the broadband and gamma amplitude were z-scored across the entire experiment where UDS was detected.

B.5 *In silico* simulation of LFP and gamma-band activity using mean-field model

To confirm that the activity traces of our mean field model are a realistic approximation of cortical dynamics during UDS, we simulated the LFP using previously established techniques(92). This also allowed us to clarify how activity fluctuations from the UO-process would affect gamma band activity in the LFP. Briefly, the LFP was assumed to be a linear summation of total excitatory and inhibitory currents. Poisson spike trains from an excitatory population (NE = 1000) and inhibitory population (NI = 4000) were generated with a time-varying mean rate parameter for each network, given by the output of the mean-field model described earlier. The excitatory neurons had a peak rate of 3 Hz, and the inhibitory neurons had a peak rate of 10 Hz. Each spike train was convolved with their respective conductance profiles, modeled as a difference of exponentials defined by the rise and decay time constants of AMPA (excitatory, rise time 0.1 ms, decay time 2 ms) and GABA (inhibitory, rise time 0.5 ms, decay time 10 ms) receptors. The resulting time series represent aggregate excitatory and inhibitory conductances. To calculate the current, conductances were multiplied by the difference between the time-varying membrane potential of each neuron (-70 mV in the Down state, -50 mV in the Up state) and the reversal potential of AMPA (0mV) and GABA (-80 mV) receptors. The LFP was the sum of these two currents (Fig S10). The gamma-band activity of the simulated network was then found using the same techniques employed for the in vivo data.

B.6 Sigmoid dependence of SPA/SPI w.r.t. Gamma Power

We followed standard statistical procedures in modeling a dependent Bernoulli random process. As a first order approximation, we assumed a linear relationship between the gamma power in a given state and the log-odds of that particular state being skipped (resulting in persistence) or being synchronously followed. The linear relationship can be written in mathematical form as

$$\log \frac{p}{1-p} = \beta_0 + \beta_1 \gamma \tag{B.1}$$

Where p is the probability that a particular state with afferent gamma content γ is skipped by the efferent network. The "threshold" of this relationship is where the probability of persistent and synchronous transitions are equally likely, i.e. p = 0.5, which occurs at $\gamma_\theta = -\beta_0/\beta_1$. Note that for SPA, $\beta_1 > 0$, since positive fluctuations in the Down state lead to SPA. On the other hand, $\beta_1 < 0$ for SPI, since negative fluctuations in the Up state lead to inactivity.

B.7 Statistics and Hypothesis Testing

Central Tendencies and variability is reported as mean plus/minus standard deviation, unless otherwise noted. All hypothesis tests were performed using two-sided nonparametric Wilcoxon rank-sum tests for equal medians. Wilcoxon signed rank tests were used for paired comparisons or one-sample tests. Correlations were computed using Spearman's rank correlation coefficient. A p-value of less than 0.05 was used for statistical significance.

Bibliography

[1] J. Bardeen, L. N. Cooper, and J. R. Schrieffer. Theory of superconductivity. *Phys. Rev.*, 108:1175–1204, Dec 1957.

[2] A. L. Hodgkin and A. F. Huxley. A quantitative description of membrane current and its application to conduction and excitation in nerve. *The Journal of Physiology*, 117(4):500–544, August 1952.

[3] Marcus E. Raichle and Mark A. Mintun. BRAIN WORK AND BRAIN IMAGING. *Annual Review of Neuroscience*, 29(1):449–476, July 2006.

[4] A.F. Dean. The variability of discharge of simple cells in the cat striate cortex. *Experimental Brain Research*, 44(4), December 1981.

[5] D.J. Tolhurst, J.A. Movshon, and A.F. Dean. The statistical reliability of signals in single neurons in cat and monkey visual cortex. *Vision Research*, 23(8):775–785, January 1983.

[6] A. Arieli, D. Shoham, R. Hildesheim, and A. Grinvald. Coherent spatiotemporal patterns of ongoing activity revealed by real-time optical imaging coupled with single-unit recording in the cat visual cortex. *Journal of Neurophysiology*, 73(5):2072–2093, May 1995.

[7] C. C. H. Petersen, T. T. G. Hahn, M. Mehta, A. Grinvald, and B. Sakmann. Interaction of sensory responses with spontaneous depolarization in layer 2/3 barrel cortex. *Proceedings of the National Academy of Sciences*, 100(23):13638–13643, October 2003.

[8] M. A. Smith and A. Kohn. Spatial and temporal scales of neuronal correlation in primary visual cortex. *Journal of Neuroscience*, 28(48):12591–12603, November 2008.

[9] Edward S. Ruthazer and Michael P. Stryker. The role of activity in the development of long-range horizontal connections in area 17 of the ferret. *The Journal of Neuroscience*, 16(22):7253–7269, November 1996.

[10] Michael Weliky and Lawrence C. Katz. Disruption of orientation tuning visual cortex by artificially correlated neuronal activity. *Nature*, 386(6626):680–685, April 1997.

[11] Tal Kenet, Dmitri Bibitchkov, Misha Tsodyks, Amiram Grinvald, and Amos Arieli. Spontaneously emerging cortical representations of visual attributes. *Nature*, 425(6961):954–956, October 2003.

[12] Brendan K. Murphy and Kenneth D. Miller. Balanced amplification: A new mechanism of selective amplification of neural activity patterns. *Neuron*, 61(4):635–648, February 2009.

[13] Tobias Bonhoeffer and Amiram Grinvald. Iso-orientation domains in cat visual cortex are arranged in pinwheel-like patterns. *Nature*, 353(6343):429–431, October 1991.

[14] M. Tsodyks. Linking spontaneous activity of single cortical neurons and the underlying functional architecture. *Science*, 286(5446):1943–1946, December 1999.

[15] DY Ts'o, CD Gilbert, and TN Wiesel. Relationships between horizontal interactions and functional architecture in cat striate cortex as revealed by cross-correlation analysis. *The Journal of Neuroscience*, 6(4):1160–1170, April 1986.

[16] K.J Friston, C Buechel, G.R Fink, J Morris, E Rolls, and R.J Dolan. Psychophysiological and modulatory interactions in neuroimaging. *NeuroImage*, 6(3):218–229, October 1997.

[17] B. B. Biswal, M. Mennes, X.-N. Zuo, S. Gohel, C. Kelly, S. M. Smith, C. F. Beckmann, J. S. Adelstein, R. L. Buckner, S. Colcombe, A.-M. Dogonowski, M. Ernst, D. Fair,

M. Hampson, M. J. Hoptman, J. S. Hyde, V. J. Kiviniemi, R. Kotter, S.-J. Li, C.-P. Lin, M. J. Lowe, C. Mackay, D. J. Madden, K. H. Madsen, D. S. Margulies, H. S. Mayberg, K. McMahon, C. S. Monk, S. H. Mostofsky, B. J. Nagel, J. J. Pekar, S. J. Peltier, S. E. Petersen, V. Riedl, S. A. R. B. Rombouts, B. Rypma, B. L. Schlaggar, S. Schmidt, R. D. Seidler, G. J. Siegle, C. Sorg, G.-J. Teng, J. Veijola, A. Villringer, M. Walter, L. Wang, X.-C. Weng, S. Whitfield-Gabrieli, P. Williamson, C. Windischberger, Y.-F. Zang, H.-Y. Zhang, F. X. Castellanos, and M. P. Milham. Toward discovery science of human brain function. *Proceedings of the National Academy of Sciences*, 107(10):4734–4739, February 2010.

[18] J. L. Vincent, G. H. Patel, M. D. Fox, A. Z. Snyder, J. T. Baker, D. C. Van Essen, J. M. Zempel, L. H. Snyder, M. Corbetta, and M. E. Raichle. Intrinsic functional architecture in the anaesthetized monkey brain. *Nature*, 447(7140):83–86, May 2007.

[19] M. P. van den Heuvel, C. J. Stam, R. S. Kahn, and H. E. Hulshoff Pol. Efficiency of functional brain networks and intellectual performance. *Journal of Neuroscience*, 29(23):7619–7624, June 2009.

[20] Michael D. Fox and Marcus E. Raichle. Spontaneous fluctuations in brain activity observed with functional magnetic resonance imaging. *Nature Reviews Neuroscience*, 8(9):700–711, September 2007.

[21] F Perrin. A differential brain response to the subject's own name persists during sleep. *Clinical Neurophysiology*, 110(12):2153–2164, December 1999.

[22] Chiara M. Portas, Karsten Krakow, Phillip Allen, Oliver Josephs, Jorge L. Armony, and Chris D. Frith. Auditory processing across the sleep-wake cycle. *Neuron*, 28(3):991–999, December 2000.

[23] W. E. Skaggs and B. L. McNaughton. Replay of neuronal firing sequences in rat hippocampus during sleep following spatial experience. *Science*, 271(5257):1870–1873, March 1996.

[24] Kamran Diba and György Buzsáki. Forward and reverse hippocampal place-cell sequences during ripples. *Nature Neuroscience*, 10(10):1241–1242, September 2007.

[25] Daoyun Ji and Matthew A Wilson. Coordinated memory replay in the visual cortex and hippocampus during sleep. *Nature Neuroscience*, 10(1):100–107, December 2006.

[26] Mayank R Mehta. Cortico-hippocampal interaction during up-down states and memory consolidation. *Nature Neuroscience*, 10(1):13–15, January 2007.

[27] K. L. Hoffman. Coordinated reactivation of distributed memory traces in primate neocortex. *Science*, 297(5589):2070–2073, September 2002.

[28] Adrien Peyrache, Mehdi Khamassi, Karim Benchenane, Sidney I Wiener, and Francesco P Battaglia. Replay of rule-learning related neural patterns in the prefrontal cortex during sleep. *Nature Neuroscience*, 12(7):919–926, May 2009.

[29] Matthew P. Walker and Robert Stickgold. Sleep, memory, and plasticity. *Annual Review of Psychology*, 57(1):139–166, January 2006.

[30] Hong-Viet V. Ngo, Thomas Martinetz, Jan Born, and Matthias Mölle. Auditory closed-loop stimulation of the sleep slow oscillation enhances memory. *Neuron*, 78(3):545–553, May 2013.

[31] Sylvain Chauvette, Josée Seigneur, and Igor Timofeev. Sleep oscillations in the thalamocortical system induce long-term neuronal plasticity. *Neuron*, 75(6):1105–1113, September 2012.

[32] Artur Luczak, Peter Barthó, and Kenneth D. Harris. Spontaneous events outline the realm of possible sensory responses in neocortical populations. *Neuron*, 62(3):413–425, May 2009.

[33] Pierre Maquet, Steven Laureys, Philippe Peigneux, Sonia Fuchs, Christophe Petiau, Christophe Phillips, Joel Aerts, Guy Del Fiore, Christian Degueldre, Thierry Meulemans, André Luxen, Georges Franck, Martial Van Der Linden, Carlyle Smith, and

Axel Cleeremans. Experience-dependent changes in cerebral activation during human REM sleep. *Nature Neuroscience*, 3(8):831–836, August 2000.

[34] D. O. Hebb. *The organization of behavior; a neuropsychological theory*. Wiley, 1949.

[35] Feng Han, Natalia Caporale, and Yang Dan. Reverberation of recent visual experience in spontaneous cortical waves. *Neuron*, 60(2):321–327, October 2008.

[36] Rümeysa İnce, Saliha Seda Adanır, and Fatma Sevmez. The inventor of electroencephalography (EEG): Hans berger (1873–1941). *Child's Nervous System*, March 2020.

[37] G. Buzsaki. Neuronal oscillations in cortical networks. *Science*, 304(5679):1926–1929, June 2004.

[38] Rafael Yuste, Jason N. MacLean, Jeffrey Smith, and Anders Lansner. The cortex as a central pattern generator. *Nature Reviews Neuroscience*, 6(6):477–483, June 2005.

[39] Michael Murphy, Marie-Aurélie Bruno, Brady A. Riedner, Pierre Boveroux, Quentin Noirhomme, Eric C. Landsness, Jean-Francois Brichant, Christophe Phillips, Marcello Massimini, Steven Laureys, Giulio Tononi, and Mélanie Boly. Propofol Anesthesia and Sleep: A High-Density EEG Study. *Sleep*, 34(3):283–291, 03 2011.

[40] Yousheng Shu, Andrea Hasenstaub, Mathilde Badoual, Thierry Bal, and David A. McCormick. Barrages of synaptic activity control the gain and sensitivity of cortical neurons. *The Journal of Neuroscience*, 23(32):10388–10401, November 2003.

[41] M Steriade, A Nunez, and F Amzica. A novel slow (1 hz) oscillation of neocortical neurons in vivo: depolarizing and hyperpolarizing components. *The Journal of Neuroscience*, 13(8):3252–3265, August 1993.

[42] P Achermann and A.A Borbély. Low-frequency (1hz) oscillations in the human sleep electroencephalogram. *Neuroscience*, 81(1):213–222, August 1997.

[43] G Buzsaki, RG Bickford, G Ponomareff, LJ Thal, R Mandel, and FH Gage. Nucleus basalis and thalamic control of neocortical activity in the freely moving rat. *The Journal of Neuroscience*, 8(11):4007–4026, November 1988.

[44] Anton Sirota and György Buzsáki. Interaction between neocortical and hippocampal networks via slow oscillations. *Thalamus and Related Systems*, 3(04):245, December 2005.

[45] Jaime R. Villablanca. Counterpointing the functional role of the forebrain and of the brainstem in the control of the sleep-waking system. *Journal of Sleep Research*, 13(3):179–208, September 2004.

[46] M. Massimini. The sleep slow oscillation as a traveling wave. *Journal of Neuroscience*, 24(31):6862–6870, August 2004.

[47] Carl C. H. Petersen, Amiram Grinvald, and Bert Sakmann. Spatiotemporal dynamics of sensory responses in layer 2/3 of rat barrel cortex MeasuredIn vivoby voltage-sensitive dye imaging combined with whole-cell voltage recordings and neuron reconstructions. *The Journal of Neuroscience*, 23(4):1298–1309, February 2003.

[48] M. H. Mohajerani, D. A. McVea, M. Fingas, and T. H. Murphy. Mirrored bilateral slow-wave cortical activity within local circuits revealed by fast bihemispheric voltage-sensitive dye imaging in anesthetized and awake mice. *Journal of Neuroscience*, 30(10):3745–3751, March 2010.

[49] Ian Nauhaus, Laura Busse, Matteo Carandini, and Dario L Ringach. Stimulus contrast modulates functional connectivity in visual cortex. *Nature Neuroscience*, 12(1):70–76, November 2008.

[50] Marcel Ruiz-Mejias, Laura Ciria-Suarez, Maurizio Mattia, and Maria V. Sanchez-Vives. Slow and fast rhythms generated in the cerebral cortex of the anesthetized mouse. *Journal of Neurophysiology*, 106(6):2910–2921, December 2011.

[51] Ilan Lampl, Iva Reichova, and David Ferster. Synchronous membrane potential fluctuations in neurons of the cat visual cortex. *Neuron*, 22(2):361–374, February 1999.

[52] F. Amzica and M. Steriade. Short- and long-range neuronal synchronization of the slow (1 hz) cortical oscillation. *Journal of Neurophysiology*, 73(1):20–38, January 1995.

[53] M. Volgushev. Precise long-range synchronization of activity and silence in neocortical neurons during slow-wave sleep. *Journal of Neuroscience*, 26(21):5665–5672, May 2006.

[54] F Amzica and M Steriade. Disconnection of intracortical synaptic linkages disrupts synchronization of a slow oscillation. *The Journal of Neuroscience*, 15(6):4658–4677, June 1995.

[55] Maria V. Sanchez-Vives, Marcello Massimini, and Maurizio Mattia. Shaping the default activity pattern of the cortical network. *Neuron*, 94(5):993–1001, June 2017.

[56] Brady A. Riedner, Vladyslav V. Vyazovskiy, Reto Huber, Marcello Massimini, Steve Esser, Michael Murphy, and Giulio Tononi. Sleep homeostasis and cortical synchronization: III. a high-density EEG study of sleep slow waves in humans. *Sleep*, 30(12):1643–1657, December 2007.

[57] M. Steriade, I. Timofeev, and F. Grenier. Natural waking and sleep states: A view from inside neocortical neurons. *Journal of Neurophysiology*, 85(5):1969–1985, May 2001.

[58] M. T. Alkire, A. G. Hudetz, and G. Tononi. Consciousness and anesthesia. *Science*, 322(5903):876–880, November 2008.

[59] S. Chauvette, S. Crochet, M. Volgushev, and I. Timofeev. Properties of slow oscillation during slow-wave sleep and anesthesia in cats. *Journal of Neuroscience*, 31(42):14998–15008, October 2011.

[60] L. D. Lewis, V. S. Weiner, E. A. Mukamel, J. A. Donoghue, E. N. Eskandar, J. R. Madsen, W. S. Anderson, L. R. Hochberg, S. S. Cash, E. N. Brown, and P. L. Purdon. Rapid fragmentation of neuronal networks at the onset of propofol-induced unconsciousness. *Proceedings of the National Academy of Sciences*, 109(49):E3377–E3386, November 2012.

[61] Shuzo Sakata and Kenneth D. Harris. Laminar structure of spontaneous and sensory-evoked population activity in auditory cortex. *Neuron*, 64(3):404–418, November 2009.

[62] I. Timofeev and M. Steriade. Low-frequency rhythms in the thalamus of intact-cortex and decorticated cats. *Journal of Neurophysiology*, 76(6):4152–4168, December 1996.

[63] I. Timofeev. Origin of slow cortical oscillations in deafferented cortical slabs. *Cerebral Cortex*, 10(12):1185–1199, December 2000.

[64] Shimon Marom and Goded Shahaf. Development, learning and memory in large random networks of cortical neurons: lessons beyond anatomy. *Quarterly Reviews of Biophysics*, 35(1):63–87, 2002.

[65] P. GLOOR, G. BALL, and N. SCHAUL. Brain lesions that produce delta waves in the EEG. *Neurology*, 27(4):326–326, April 1977.

[66] Markus Butz, Joachim Gross, Lars Timmermann, Marek Moll, Hans-Joachim Freund, Otto W. Witte, and Alfons Schnitzler. Perilesional pathological oscillatory activity in the magnetoencephalogram of patients with cortical brain lesions. *Neuroscience Letters*, 355(1-2):93–96, January 2004.

[67] Maria V. Sanchez-Vives and David A. McCormick. Cellular and network mechanisms of rhythmic recurrent activity in neocortex. *Nature Neuroscience*, 3(10):1027–1034, October 2000.

[68] Lionel G. Nowak and Jean Bullier. The timing of information transfer in the visual system. In *Extrastriate Cortex in Primates*, pages 205–241. Springer US, 1997.

[69] Emilio Salinas and Terrence J. Sejnowski. Impact of correlated synaptic input on output firing rate and variability in simple neuronal models. *The Journal of Neuroscience*, 20(16):6193–6209, August 2000.

[70] György Buzsáki and Edvard I Moser. Memory, navigation and theta rhythm in the hippocampal-entorhinal system. *Nature Neuroscience*, 16(2):130–138, January 2013.

[71] Karen Safaryan and Mayank R. Mehta. Enhanced hippocampal theta rhythmicity and emergence of eta oscillation in virtual reality. *Nature Neuroscience*, 24(8):1065–1070, June 2021.

[72] Zahra M Aghajan, Lavanya Acharya, Jason J Moore, Jesse D Cushman, Cliff Vuong, and Mayank R Mehta. Impaired spatial selectivity and intact phase precession in two-dimensional virtual reality. *Nature Neuroscience*, 18(1):121–128, November 2014.

[73] Mikael Lundqvist, Pawel Herman, Melissa R. Warden, Scott L. Brincat, and Earl K. Miller. Gamma and beta bursts during working memory readout suggest roles in its volitional control. *Nature Communications*, 9(1), January 2018.

[74] J. Lisman and M. Idiart. Storage of 7 /- 2 short-term memories in oscillatory subcycles. *Science*, 267(5203):1512–1515, March 1995.

[75] J. M. Palva. Phase synchrony among neuronal oscillations in the human cortex. *Journal of Neuroscience*, 25(15):3962–3972, April 2005.

[76] P. Fries. Modulation of oscillatory neuronal synchronization by selective visual attention. *Science*, 291(5508):1560–1563, February 2001.

[77] S. Haegens, B. F. Handel, and O. Jensen. Top-down controlled alpha band activity in somatosensory areas determines behavioral performance in a discrimination task. *Journal of Neuroscience*, 31(14):5197–5204, April 2011.

[78] William A. MacKay and Antonio J. Mendonccą. Field potential oscillatory bursts in parietal cortex before and during reach. *Brain Research*, 704(2):167–174, December 1995.

[79] Xiao-Jing Wang. Neurophysiological and computational principles of cortical rhythms in cognition. *Physiological Reviews*, 90(3):1195–1268, July 2010.

[80] Charles J. Wilson and Philip M. Groves. Spontaneous firing patterns of identified spiny neurons in the rat neostriatum. *Brain Research*, 220(1):67–80, September 1981.

[81] R. Metherate and Scott J. Cruikshank. Thalamocortical inputs trigger a propagating envelope of gamma-band activity in auditory cortex in vitro. *Experimental Brain Research*, 126(2):160–174, May 1999.

[82] Jason N. MacLean, Brendon O. Watson, Gloster B. Aaron, and Rafael Yuste. Internal dynamics determine the cortical response to thalamic stimulation. *Neuron*, 48(5):811–823, December 2005.

[83] Robert N. S. Sachdev, Ford F. Ebner, and Charles J. Wilson. Effect of subthreshold up and down states on the whisker-evoked response in somatosensory cortex. *Journal of Neurophysiology*, 92(6):3511–3521, December 2004.

[84] John J. Tukker, Prateep Beed, Dietmar Schmitz, Matthew E. Larkum, and Robert N. S. Sachdev. Up and down states and memory consolidation across somatosensory, entorhinal, and hippocampal cortices. *Frontiers in Systems Neuroscience*, 14, May 2020.

[85] Garrett T. Neske. The slow oscillation in cortical and thalamic networks: Mechanisms and functions. *Frontiers in Neural Circuits*, 9, January 2016.

[86] David Kleinfeld, Ehud Ahissar, and Mathew E Diamond. Active sensation: insights from the rodent vibrissa sensorimotor system. *Current Opinion in Neurobiology*, 16(4):435–444, August 2006.

[87] A. Agmon and B.W. Connors. Thalamocortical responses of mouse somatosensory (barrel) cortexin vitro. *Neuroscience*, 41(2-3):365–379, January 1991.

[88] Mathew E. Diamond, Moritz von Heimendahl, Per Magne Knutsen, David Kleinfeld,

and Ehud Ahissar. 'where' and 'what' in the whisker sensorimotor system. *Nature Reviews Neuroscience*, 9(8):601–612, August 2008.

[89] Menno P. Witter, Thanh P. Doan, Bente Jacobsen, Eirik S. Nilssen, and Shinya Ohara. Architecture of the entorhinal cortex a review of entorhinal anatomy in rodents with some comparative notes. *Frontiers in Systems Neuroscience*, 11, June 2017.

[90] S. Namiki, H. Norimoto, C. Kobayashi, K. Nakatani, N. Matsuki, and Y. Ikegaya. Layer III neurons control synchronized waves in the immature cerebral cortex. *Journal of Neuroscience*, 33(3):987–1001, January 2013.

[91] E. O. Mann, M. M. Kohl, and O. Paulsen. Distinct roles of GABAA and GABAB receptors in balancing and terminating persistent cortical activity. *Journal of Neuroscience*, 29(23):7513–7518, June 2009.

[92] B. Tahvildari, M. Wolfel, A. Duque, and D. A. McCormick. Selective functional interactions between excitatory and inhibitory cortical neurons and differential contribution to persistent activity of the slow oscillation. *Journal of Neuroscience*, 32(35):12165–12179, August 2012.

[93] Yoshikazu Isomura, Anton Sirota, Simal Özen, Sean Montgomery, Kenji Mizuseki, Darrell A. Henze, and György Buzsáki. Integration and segregation of activity in entorhinal-hippocampal subregions by neocortical slow oscillations. *Neuron*, 52(5):871–882, December 2006.

[94] Thomas T G Hahn, James M McFarland, Sven Berberich, Bert Sakmann, and Mayank R Mehta. Spontaneous persistent activity in entorhinal cortex modulates cortico-hippocampal interaction in vivo. *Nature Neuroscience*, 15(11):1531–1538, October 2012.

[95] Zhe Chen and Matthew A. Wilson. Deciphering neural codes of memory during sleep. *Trends in Neurosciences*, 40(5):260–275, May 2017.

[96] György Buzsáki. Hippocampal sharp wave-ripple: A cognitive biomarker for episodic memory and planning. *Hippocampus*, 25(10):1073–1188, September 2015.

[97] Gideon Rothschild, Elad Eban, and Loren M Frank. A cortical–hippocampal–cortical loop of information processing during memory consolidation. *Nature Neuroscience*, 20(2):251–259, December 2016.

[98] Gabrielle Girardeau, Karim Benchenane, Sidney I Wiener, György Buzsáki, and Michaël B Zugaro. Selective suppression of hippocampal ripples impairs spatial memory. *Nature Neuroscience*, 12(10):1222–1223, September 2009.

[99] N. K. Logothetis, O. Eschenko, Y. Murayama, M. Augath, T. Steudel, H. C. Evrard, M. Besserve, and A. Oeltermann. Hippocampal–cortical interaction during periods of subcortical silence. *Nature*, 491(7425):547–553, November 2012.

[100] Dion Khodagholy, Jennifer N. Gelinas, and György Buzsáki. Learning-enhanced coupling between ripple oscillations in association cortices and hippocampus. *Science*, 358(6361):369–372, October 2017.

[101] Nicolas Maingret, Gabrielle Girardeau, Ralitsa Todorova, Marie Goutierre, and Michaël Zugaro. Hippocampo-cortical coupling mediates memory consolidation during sleep. *Nature Neuroscience*, 19(7):959–964, May 2016.

[102] F. P. Battaglia. Hippocampal sharp wave bursts coincide with neocortical "up-state" transitions. *Learning & Memory*, 11(6):697–704, November 2004.

[103] Thrse M. Jay and Menno P. Witter. Distribution of hippocampal CA1 and subicular efferents in the prefrontal cortex of the rat studied by means of anterograde transport ofPhaseolus vulgaris-leucoagglutinin. *The Journal of Comparative Neurology*, 313(4):574–586, November 1991.

[104] K. Takehara-Nishiuchi. Systems consolidation requires postlearning activation of NMDA receptors in the medial prefrontal cortex in trace eyeblink conditioning. *Journal of Neuroscience*, 26(19):5049–5058, May 2006.

[105] T. T. G. Hahn, B. Sakmann, and M. R. Mehta. Differential responses of hippocampal subfields to cortical up-down states. *Proceedings of the National Academy of Sciences*, 104(12):5169–5174, March 2007.

[106] Thomas T G Hahn, Bert Sakmann, and Mayank R Mehta. Phase-locking of hippocampal interneurons' membrane potential to neocortical up-down states. *Nature Neuroscience*, 9(11):1359–1361, October 2006.

[107] Song-Lin Ding. Comparative anatomy of the prosubiculum, subiculum, presubiculum, postsubiculum, and parasubiculum in human, monkey, and rodent. *Journal of Comparative Neurology*, 521(18):4145–4162, October 2013.

[108] Joel Zylberberg and Ben W. Strowbridge. Mechanisms of persistent activity in cortical circuits: Possible neural substrates for working memory. *Annual Review of Neuroscience*, 40(1):603–627, July 2017.

[109] J. J. Hopfield. Neural networks and physical systems with emergent collective computational abilities. *Proceedings of the National Academy of Sciences*, 79(8):2554–2558, April 1982.

[110] A. Compte. Synaptic mechanisms and network dynamics underlying spatial working memory in a cortical network model. *Cerebral Cortex*, 10(9):910–923, September 2000.

[111] R. Traub and R. Wong. Cellular mechanism of neuronal synchronization in epilepsy. *Science*, 216(4547):745–747, May 1982.

[112] Maxim Bazhenov, Igor Timofeev, Mircea Steriade, and Terrence J. Sejnowski. Model of thalamocortical slow-wave sleep oscillations and transitions to activated states. *The Journal of Neuroscience*, 22(19):8691–8704, October 2002.

[113] Albert Compte, Maria V. Sanchez-Vives, David A. McCormick, and Xiao-Jing Wang. Cellular and network mechanisms of slow oscillatory activity (1 hz) and wave propagations in a cortical network model. *Journal of Neurophysiology*, 89(5):2707–2725, May 2003.

[114] H. S. Seung. How the brain keeps the eyes still. *Proceedings of the National Academy of Sciences*, 93(23):13339–13344, November 1996.

[115] H. R. Wilson and J. D. Cowan. Excitatory and inhibitory interactions in localized populations of model neurons. *Biophys J*, 12(1):1–24, Jan 1972.

[116] David E. Presti. *Foundational Concepts in Neuroscience: A Brain-Mind Odyssey*. Norton, 2015.

[117] Maryam Ghorbani, Mayank Mehta, Robijn Bruinsma, and Alex J. Levine. Nonlinear-dynamics theory of up-down transitions in neocortical neural networks. *Physical Review E*, 85(2), February 2012.

[118] Daniel Levenstein, György Buzsáki, and John Rinzel. NREM sleep in the rodent neocortex and hippocampus reflects excitable dynamics. *Nature Communications*, 10(1), June 2019.

[119] Daniel Jercog, Alex Roxin, Peter Barthó, Artur Luczak, Albert Compte, and Jaime de la Rocha. UP-DOWN cortical dynamics reflect state transitions in a bistable network. *eLife*, 6, August 2017.

[120] Misha V. Tsodyks, William E. Skaggs, Terrence J. Sejnowski, and Bruce L. McNaughton. Paradoxical effects of external modulation of inhibitory interneurons. *The Journal of Neuroscience*, 17(11):4382–4388, June 1997.

[121] W. Rall and C. Hunt. Analysis of reflex variability in terms of partially correlated excitability fluctuation in a population of motoneurons. *The Journal of General Physiology*, 39:397 – 422, 1956.

[122] C. D. GEISLER, L. S. FRISHKOPF, and W. A. ROSENBLITH. Extracranial responses to acoustic clicks in man. *Science*, 128(3333):1210–1211, 1958.

[123] Steven Strogatz. *Nonlinear dynamics and Chaos*. CRC Press, 1994.

[124] Alain Destexhe, Diego Contreras, and Mircea Steriade. Spatiotemporal analysis of local field potentials and unit discharges in cat cerebral cortex during natural wake and sleep states. *The Journal of Neuroscience*, 19(11):4595–4608, June 1999.

[125] Elizabeth A. Clement, Alby Richard, Megan Thwaites, Jonathan Ailon, Steven Peters, and Clayton T. Dickson. Cyclic and sleep-like spontaneous alternations of brain state under urethane anaesthesia. *PLoS ONE*, 3(4):e2004, April 2008.

[126] K. L. Hoffman, F. P. Battaglia, K. Harris, J. N. MacLean, L. Marshall, and M. R. Mehta. The upshot of up states in the neocortex: From slow oscillations to memory formation. *Journal of Neuroscience*, 27(44):11838–11841, October 2007.

[127] A. Sirota, J. Csicsvari, D. Buhl, and G. Buzsaki. Communication between neocortex and hippocampus during sleep in rodents. *Proceedings of the National Academy of Sciences*, 100(4):2065–2069, February 2003.

[128] D. Marr. Simple memory: a theory for archicortex. *Philosophical Transactions of the Royal Society of London. B, Biological Sciences*, 262(841):23–81, July 1971.

[129] Lisa Marshall, Halla Helgadóttir, Matthias Mölle, and Jan Born. Boosting slow oscillations during sleep potentiates memory. *Nature*, 444(7119):610–613, November 2006.

[130] Chi Chung Alan Fung and Tomoki Fukai. Transient and persistent UP states during slow-wave oscillation and their implications for cell-assembly dynamics. *Scientific Reports*, 8(1), July 2018.

[131] Mikael Lundqvist, Albert Compte, and Anders Lansner. Bistable, irregular firing and population oscillations in a modular attractor memory network. *PLoS Computational Biology*, 6(6):e1000803, June 2010.

[132] Suhas Vijayakumar, Jerome Sallet, Lennart Verhagen, Davide Folloni, W. Pieter Medendorp, and Rogier B. Mars. Mapping multiple principles of parietal–frontal

cortical organization using functional connectivity. *Brain Structure and Function*, 224(2):681–697, November 2018.

[133] Menno Witter and Floris Wouterlood. *The Parahippocampal RegionOrganization and Role in Cognitive Function*. Oxford University Press, October 2002.

[134] M.P. Witter, H.J. Groenewegen, F.H. Lopes da Silva, and A.H.M. Lohman. Functional organization of the extrinsic and intrinsic circuitry of the parahippocampal region. *Progress in Neurobiology*, 33(3):161–253, January 1989.

[135] Juri Minxha, Ralph Adolphs, Stefano Fusi, Adam N. Mamelak, and Ueli Rutishauser. Flexible recruitment of memory-based choice representations by the human medial frontal cortex. *Science*, 368(6498):eaba3313, June 2020.

[136] A. Nieder. Representation of the quantity of visual items in the primate prefrontal cortex. *Science*, 297(5587):1708–1711, September 2002.

[137] Ralitsa Todorova and Michaël Zugaro. Isolated cortical computations during delta waves support memory consolidation. *Science*, 366(6463):377–381, October 2019.

[138] Earl K. Miller, Mikael Lundqvist, and André M. Bastos. Working memory 2.0. *Neuron*, 100(2):463–475, October 2018.

[139] P.S Goldman-Rakic. Cellular basis of working memory. *Neuron*, 14(3):477–485, March 1995.

[140] A Baddeley. Working memory. *Science*, 255(5044):556–559, January 1992.

[141] Torkel Hafting, Marianne Fyhn, Sturla Molden, May-Britt Moser, and Edvard I. Moser. Microstructure of a spatial map in the entorhinal cortex. *Nature*, 436(7052):801–806, June 2005.

[142] Albert Tsao, Jørgen Sugar, Li Lu, Cheng Wang, James J. Knierim, May-Britt Moser, and Edvard I. Moser. Integrating time from experience in the lateral entorhinal cortex. *Nature*, 561(7721):57–62, August 2018.

[143] Cheng Wang, Xiaojing Chen, Heekyung Lee, Sachin S. Deshmukh, D. Yoganarasimha, Francesco Savelli, and James J. Knierim. Egocentric coding of external items in the lateral entorhinal cortex. *Science*, 362(6417):945–949, November 2018.

[144] Prateep Beed, Roberto de Filippo, Constance Holman, Friedrich W. Johenning, Christian Leibold, Antonio Caputi, Hannah Monyer, and Dietmar Schmitz. Layer 3 pyramidal cells in the medial entorhinal cortex orchestrate up-down states and entrain the deep layers differentially. *Cell Reports*, 33(10):108470, December 2020.

[145] James M. McFarland, Thomas T. G. Hahn, and Mayank R. Mehta. Explicit-duration hidden markov model inference of UP-DOWN states from continuous signals. *PLoS ONE*, 6(6):e21606, June 2011.

[146] M. R. Mehta, A. K. Lee, and M. A. Wilson. Role of experience and oscillations in transforming a rate code into a temporal code. *Nature*, 417(6890):741–746, June 2002.

[147] A. Compte, R. Reig, V. F. Descalzo, M. A. Harvey, G. D. Puccini, and M. V. Sanchez-Vives. Spontaneous high-frequency (10-80 hz) oscillations during up states in the cerebral cortex in vitro. *Journal of Neuroscience*, 28(51):13828–13844, December 2008.

[148] Alexei V. Egorov, Bassam N. Hamam, Erik Fransén, Michael E. Hasselmo, and Angel A. Alonso. Graded persistent activity in entorhinal cortex neurons. *Nature*, 420(6912):173–178, November 2002.

[149] Babak Tahvildari, Erik Fransén, Angel A. Alonso, and Michael E. Hasselmo. Switching between "on" and "off" states of persistent activity in lateral entorhinal layer III neurons. *Hippocampus*, 17(4):257–263, 2007.

[150] Ruby Klink and Angel Alonso. Ionic mechanisms of muscarinic depolarization in entorhinal cortex layer II neurons. *Journal of Neurophysiology*, 77(4):1829–1843, April 1997.

[151] Michael E. Hasselmo and Chantal E. Stern. Mechanisms underlying working memory for novel information. *Trends in Cognitive Sciences*, 10(11):487–493, November 2006.

[152] Gregor Rainer, Wael F. Asaad, and Earl K. Miller. Selective representation of relevant information by neurons in the primate prefrontal cortex. *Nature*, 393(6685):577–579, June 1998.

[153] Christopher D. Harvey, Forrest Collman, Daniel A. Dombeck, and David W. Tank. Intracellular dynamics of hippocampal place cells during virtual navigation. *Nature*, 461(7266):941–946, October 2009.

[154] Christoph Schmidt-Hieber and Michael Häusser. Cellular mechanisms of spatial navigation in the medial entorhinal cortex. *Nature Neuroscience*, 16(3):325–331, February 2013.

[155] Katie C. Bittner, Aaron D. Milstein, Christine Grienberger, Sandro Romani, and Jeffrey C. Magee. Behavioral time scale synaptic plasticity underlies CA1 place fields. *Science*, 357(6355):1033–1036, September 2017.

[156] Jeremiah Y. Cohen, Sebastian Haesler, Linh Vong, Bradford B. Lowell, and Naoshige Uchida. Neuron-type-specific signals for reward and punishment in the ventral tegmental area. *Nature*, 482(7383):85–88, January 2012.

[157] E. S. Nisenbaum, C. J. Wilson, R. C. Foehring, and D. J. Surmeier. Isolation and characterization of a persistent potassium current in neostriatal neurons. *Journal of Neurophysiology*, 76(2):1180–1194, August 1996.

[158] Jason J. Moore, Pascal M. Ravassard, David Ho, Lavanya Acharya, Ashley L. Kees, Cliff Vuong, and Mayank R. Mehta. Dynamics of cortical dendritic membrane potential and spikes in freely behaving rats. *Science*, 355(6331):eaaj1497, March 2017.

[159] Mikael Lundqvist, Jonas Rose, Pawel Herman, Scott L. Brincat, Timothy J. Buschman, and Earl K. Miller. Gamma and beta bursts underlie working memory. *Neuron*, 90(1):152–164, April 2016.

[160] Guy Major and David Tank. Persistent neural activity: prevalence and mechanisms. *Current Opinion in Neurobiology*, 14(6):675–684, December 2004.

[161] Nicolas Brunel and Xiao-Jing Wang. *Journal of Computational Neuroscience*, 11(1):63–85, 2001.

[162] Xiao-Jing Wang. Synaptic reverberation underlying mnemonic persistent activity. *Trends in Neurosciences*, 24(8):455–463, August 2001.

[163] Pavel Sanda, Paola Malerba, Xi Jiang, Giri P Krishnan, Jorge Gonzalez-Martinez, Eric Halgren, and Maxim Bazhenov. Bidirectional interaction of hippocampal ripples and cortical slow waves leads to coordinated spiking activity during NREM sleep. *Cerebral Cortex*, 31(1):324–340, September 2020.

[164] M. Lemieux, J.-Y. Chen, P. Lonjers, M. Bazhenov, and I. Timofeev. The impact of cortical deafferentation on the neocortical slow oscillation. *Journal of Neuroscience*, 34(16):5689–5703, April 2014.

[165] Roberto de Filippo, Benjamin R Rost, Alexander Stumpf, Claire Cooper, John J Tukker, Christoph Harms, Prateep Beed, and Dietmar Schmitz. Somatostatin interneurons activated by 5-HT2a receptor suppress slow oscillations in medial entorhinal cortex. *eLife*, 10, March 2021.

[166] G. Paxinos. *The Rat Nervous System*. Elsevier, 2004.

[167] R. Douglas, C. Koch, M. Mahowald, K. Martin, and H. Suarez. Recurrent excitation in neocortical circuits. *Science*, 269(5226):981–985, August 1995.

[168] Rebecca D. Burwell and David G. Amaral. Cortical afferents of the perirhinal, postrhinal, and entorhinal cortices of the rat. *The Journal of Comparative Neurology*, 398(2):179–205, August 1998.

[169] Jochen Winterer, Nikolaus Maier, Christian Wozny, Prateep Beed, Jörg Breustedt, Roberta Evangelista, Yangfan Peng, Tiziano D'Albis, Richard Kempter, and Dietmar

Schmitz. Excitatory microcircuits within superficial layers of the medial entorhinal cortex. *Cell Reports*, 19(6):1110–1116, May 2017.

[170] Y. Audrey Hay, Przemyslaw Jarzebowski, Yu Zhang, Richard Digby, Viktoria Brendel, Ole Paulsen, and Vincent Magloire. Cholinergic modulation of up–down states in the mouse medial entorhinal cortex in vitro. *European Journal of Neuroscience*, 53(5):1378–1393, December 2020.

[171] M. W. Howard. Gamma oscillations correlate with working memory load in humans. *Cerebral Cortex*, 13(12):1369–1374, December 2003.

[172] Saeideh Davoudi, Mohsen Parto Dezfouli, Robert T. Knight, Mohammad Reza Daliri, and Elizabeth L. Johnson. Prefrontal lesions disrupt posterior alpha–gamma coordination of visual working memory representations. *Journal of Cognitive Neuroscience*, 33(9):1798–1810, August 2021.

[173] F. Edin, T. Klingberg, P. Johansson, F. McNab, J. Tegner, and A. Compte. Mechanism for top-down control of working memory capacity. *Proceedings of the National Academy of Sciences*, 106(16):6802–6807, April 2009.

[174] Mattia Rigotti, Omri Barak, Melissa R. Warden, Xiao-Jing Wang, Nathaniel D. Daw, Earl K. Miller, and Stefano Fusi. The importance of mixed selectivity in complex cognitive tasks. *Nature*, 497(7451):585–590, May 2013.

[175] Stefano Fusi and L F Abbott. Limits on the memory storage capacity of bounded synapses. *Nature Neuroscience*, 10(4):485–493, March 2007.

[176] Mikael Lundqvist, Pawel Herman, and Earl K. Miller. Working memory: Delay activity, yes! persistent activity? maybe not. *The Journal of Neuroscience*, 38(32):7013–7019, August 2018.

[177] Thanh P. Doan, Maria J. Lagartos-Donate, Eirik S. Nilssen, Shinya Ohara, and Menno P. Witter. Convergent projections from perirhinal and postrhinal cortices

suggest a multisensory nature of lateral, but not medial, entorhinal cortex. *Cell Reports*, 29(3):617–627.e7, October 2019.

[178] Manuel Valero, Tim J. Viney, Robert Machold, Sara Mederos, Ipshita Zutshi, Benjamin Schuman, Yuta Senzai, Bernardo Rudy, and György Buzsáki. Sleep down state-active ID2/nkx2.1 interneurons in the neocortex. *Nature Neuroscience*, 24(3):401–411, February 2021.

[179] Jerome J. Maller, Thomas Welton, Matthew Middione, Fraser M. Callaghan, Jeffrey V. Rosenfeld, and Stuart M. Grieve. Revealing the hippocampal connectome through super-resolution 1150-direction diffusion MRI. *Scientific Reports*, 9(1), February 2019.

[180] Menno P. Witter. Connectivity of the hippocampus. In *Hippocampal Microcircuits*, pages 5–26. Springer New York, 2010.

[181] Albert Tsao, May-Britt Moser, and Edvard I. Moser. Traces of experience in the lateral entorhinal cortex. *Current Biology*, 23(5):399–405, March 2013.

[182] Eirik S. Nilssen, Thanh P. Doan, Maximiliano J. Nigro, Shinya Ohara, and Menno P. Witter. Neurons and networks in the entorhinal cortex: A reappraisal of the lateral and medial entorhinal subdivisions mediating parallel cortical pathways. *Hippocampus*, 29(12):1238–1254, August 2019.

[183] Edmund T. Rolls and Patrick Mills. The generation of time in the hippocampal memory system. *Cell Reports*, 28(7):1649–1658.e6, August 2019.

[184] G. Buzsáki. The hippocampo-neocortical dialogue. *Cerebral Cortex*, 6(2):81–92, 1996.

[185] James L. McClelland, Bruce L. McNaughton, and Randall C. O'Reilly. Why there are complementary learning systems in the hippocampus and neocortex: Insights from the successes and failures of connectionist models of learning and memory. *Psychological Review*, 102(3):419–457, July 1995.

[186] Ivan Soltesz and Attila Losonczy. CA1 pyramidal cell diversity enabling parallel information processing in the hippocampus. *Nature Neuroscience*, 21(4):484–493, March 2018.

[187] Richard J. Digby, Diego S. Bravo, Ole Paulsen, and Vincent Magloire. Distinct mechanisms of up state maintenance in the medial entorhinal cortex and neocortex. *Neuropharmacology*, 113:543–555, February 2017.

[188] Eirik S. Nilssen, Bente Jacobsen, Gunhild Fjeld, Rajeevkumar R. Nair, Stefan Blankvoort, Clifford Kentros, and Menno P. Witter. Inhibitory connectivity dominates the fan cell network in layer II of lateral entorhinal cortex. *The Journal of Neuroscience*, 38(45):9712–9727, September 2018.

[189] Takashi Kitamura, Christopher J. Macdonald, and Susumu Tonegawa. Entorhinal–hippocampal neuronal circuits bridge temporally discontiguous events. *Learning & Memory*, 22(9):438–443, August 2015.

[190] Tora Bonnevie, Benjamin Dunn, Marianne Fyhn, Torkel Hafting, Dori Derdikman, John L Kubie, Yasser Roudi, Edvard I Moser, and May-Britt Moser. Grid cells require excitatory drive from the hippocampus. *Nature Neuroscience*, 16(3):309–317, January 2013.

[191] Antonio Fernández-Ruiz, Azahara Oliva, Marisol Soula, Florbela Rocha-Almeida, Gergo A. Nagy, Gonzalo Martin-Vazquez, and György Buzsáki. Gamma rhythm communication between entorhinal cortex and dentate gyrus neuronal assemblies. *Science*, 372(6537):eabf3119, April 2021.

[192] Joseph O'Neill, Barty Pleydell-Bouverie, David Dupret, and Jozsef Csicsvari. Play it again: reactivation of waking experience and memory. *Trends in Neurosciences*, 33(5):220–229, May 2010.

[193] Benjamin J. Kraus, Mark P. Brandon, Robert J. Robinson, Michael A. Connerney,

Michael E. Hasselmo, and Howard Eichenbaum. During running in place, grid cells integrate elapsed time and distance run. *Neuron*, 88(3):578–589, November 2015.

[194] Joshua Jacobs, Jonathan Miller, Sang Ah Lee, Tom Coffey, Andrew J. Watrous, Michael R. Sperling, Ashwini Sharan, Gregory Worrell, Brent Berry, Bradley Lega, Barbara C. Jobst, Kathryn Davis, Robert E. Gross, Sameer A. Sheth, Youssef Ezzyat, Sandhitsu R. Das, Joel Stein, Richard Gorniak, Michael J. Kahana, and Daniel S. Rizzuto. Direct electrical stimulation of the human entorhinal region and hippocampus impairs memory. *Neuron*, 92(5):983–990, December 2016.

[195] Nobuyoshi Matsumoto, Kazuki Okamoto, Yuki Takagi, and Yuji Ikegaya. 3-hz subthreshold oscillations of CA2 neuronsIn vivo. *Hippocampus*, 26(12):1570–1578, September 2016.

[196] György Buzsáki. Theta oscillations in the hippocampus. *Neuron*, 33(3):325–340, January 2002.